UNIVERSITY OF
BIRMINGHAM

THE MANUFACTURE AND TESTING OF ANODE SUPPORTED Ni-10Sc1CeSZ SOFCs FOR INTERMEDIATE TEMPERATURE OPERATION

BY

NIKKIA MARIE MCDONALD

A thesis submitted to the

University of Birmingham

for the degree of

DOCTOR OF PHILOSOPHY

Centre for Hydrogen and Fuel Cell Research
School of Chemical Engineering
College of Engineering and Physical Sciences
University of Birmingham
Birmingham, England B15 2TT
United Kingdom

DECLARATION

I, Nikkia Marie McDonald, declare that the work presented in this thesis is my own with no help of more than the cited literature.

I also confirm that this work has not been submitted to another examination office, neither in content nor in shape.

_____

Signature (Nikkia Marie McDonald)

Date: 20th January 2017

Place: University of Birmingham, Birmingham, England

ABSTRACT

Developing solid oxide fuel cell (SOFC) systems that operate in lower temperature regimes improves system stability, widens materials selection and lowers performance degradation issues previously observed with higher temperature cells. Thus, there exists much emphasis on the development of SOFCs for intermediate temperature operation. In this work, the development of an intermediate temperature SOFC (IT-SOFC) based on a Ce-doped Scandia-stabilised Zirconia (ScSZ) structure manufactured via screen-printing is outlined. In this thesis we report on the successful manufacture of anode supported 8YSZ baseline cells and cells containing Ni-10Sc1CeSZ anodes supporting 10Sc1CeSZ electrolytes both prepared via die pressing, screen-printing and co-sintering. Commercial 8YSZ and 10Sc1CeSZ reference cells were also tested with results that demonstrated the reliability of the cell testing method. This research aims to demonstrate the viability of 10Sc1CeSZ within an IT-SOFC cell structure and examine the effectiveness of 10Sc1CeSZ on lowering the cell operating temperature.

With dry H_2 as fuel and O_2 from ambient air as the oxidant, the highest performing lab grade and commercial grade YSZ cells obtained OCV values of 1.06V and 1.04V and maximum power density values of 392 mW cm^{-2} and 466 mW cm^{-2} respectively at 800^oC. The commercial 10Sc1CeSZ cells consistently exhibited the highest OCVs > 1.10V of all tested cells due to the highly dense bulk electrolyte supported cell design which also contributed to the lowest cell performances with peak power densities within the range of 90 - 107 mW cm^{-2} observed for all tested cells. The lab grade 10Sc1CeSZ cells outperformed the lab grade YSZ cells during H_2 operation with respect to area specific resistance as values of 0.496 Ω cm^2 and 0.732 Ω cm^2 were obtained for the lab grade 10Sc1CeSZ and lab grade YSZ cells respectively. Despite the lower area specific resistance values, the lab grade 10Sc1CeSZ cell exhibited significantly low OCVs within the range of 0.55V – 0.65V which was the result of a porous, non-homogeneous electrolyte layer.

An improvement in the sintered density of the 10Sc1CeSZ electrolyte with 0.55 mol% Al_2O_3 additions was observed with OCVs within the 0.97 – 1.05V range. The current output for the 0.55 mol% Al_2O_3-10Sc1CeSZ cells was low, peak power densities for the highest performing cell was only 40 mW cm^2 which suggests Al_2O_3 dopant additions had deleterious effects on performance. This can be explained by possible Al_2O_3 segregation at the grain boundaries adversely affecting 10Sc1CeSZ grain boundary conductivity though the specific reason is not clear. Phase stability studies showed single phase cubic ZrO_2 for all of the Al_2O_3 doped 10Sc1CeSZ samples examined, suggesting Al_2O_3

diffused into the ZrO_2 host lattice without any changes to the crystal structure of 10Sc1CeSZ.

Results for the lab grade YSZ and 10Sc1CeSZ tested cells on biogas showed the YSZ system unexpectedly outperformed the 10Sc1CeSZ system with peak power densities of 68.24 mW cm^{-2} and 9.12 mW cm^{-2} at 800^oC for the YSZ and 10Sc1CeSZ cells respectively. Mass spectroscopy data showed minimal methane conversion and low H_2 production and consumption for both the YSZ and 10Sc1CeSZ cells fuelled by biogas, which explained the low current output and large performance losses compared to baseline performance tests on hydrogen where maximum power density values of 180.62 mW cm^{-2} for YSZ and 179.97 mW cm^{-2} for 10Sc1CeSZ were achieved. These preliminary results, though not ideal, demonstrated proof of concept for anode supported SOFCs manufactured via die-pressing and screen-printing and show the potential use of an IT-SOFC based on a 10Sc1CeSZ structure.

There's nothing to stop a man from writing
unless that man stops himself.
If a man truly desires to write,
then he will.
Rejection and ridicule will only strengthen him.
And the longer he is held back
the stronger he will become,
like a mass of rising
water against a dam.
There is no losing in writing,
it will make your toes laugh as you sleep,
it will make your stride like a tiger,
it will fire the eye
and put you face to face with death.
You will die a fighter,
you will be honoured in hell.
The luck of the word.
Go with it, send it…

-- C. Bukowski

For Edwin, Tanisha and Marie…

ACKNOWLEDGEMENTS

To my mother who has been my biggest supporter and without whom I would not have made it this far. There is much more to do. I aim to make you proud.

To my sister, the better of us two, who inspires, teaches and motivates me.

To my advisor, Robert, who pushed me and pushed me and pushed me and pushed when I thought I had nothing left. I sensed that you believed in me. Thank You.

To my 2nd advisor Tim, who gave me access to Met&Mat and shared his ceramics expertise.

To Lina, for explaining the complex in a simple way and for being a model experimentalist.

James, iron sharpens iron. Thanks for always looking out. *head nod*

The BFF. My A1 since Day1.

Amrit, Amrit, Amrit. We have solved the world's problems in about 4 years. Via whats app.

MR. ANTI-EVERYTHING. Anwar, I learned a lot about the world from you. #goals

Iegor, I am an official member of the IPMS team and Kyiv is my city. May you and I meet again.

Prof, the talk helped. And so did the authentic Jordanian dipping seasoning.

Scott, cause you switched off my furnace and sprinkled the office with golden boy charm.

Arvin, you're missed.

VK, you always checked up on me and kept me in the know. My .ppt >> your .ppt

The other half of the Canadian-American connection. Where art though Lydia?

Geoff for breaking the deafening sound of G05 silence and for saying the things most are thinking but in a "crazy Geoff" sorta way.

Fatima, my sister of colour, the TEM images added value to Chapter 6.

Omar, the FIB-SEM visualisations rounded out Chapter 7 rather nicely. Salute.

Many thanks to Professor Vasylyev for the warm welcome, Iegor, Natalia, Alex, Dmitri, Mykola and the IPMS research team in Ukraine for their scholarly feedback and for the bulk conductivity data as all contributed to the work presented in this thesis.

John Hooper and Lynn Draper for pretty much all of it, Aman who informed me of all things Chem Eng/DTC/PhD and Bob for the lab chats and always lending his technical expertise.

Thank You to my examiners Dr. Du and Dr. Kim and my VIVA chair Dr. Al-Duri.

CONTENTS LISTINGS

LIST OF FIGURES

LIST OF TABLES

LIST OF ABBREVIATIONS AND DEFINITIONS

Abbreviation	Definition
α	Powder bulk property
A	Pre-exponential factor
AC	Alternating Current
AFC	Alkaline Fuel Cell
AFL	Anode Functional Layer
ASC	Anode Supported Cell
BET	Brunauer Emmet Teller
CVD	Chemical Vapour Deposition
d	Lattice plane spacing
D	Compact diameter
DMFC	Direct Methanol Fuel Cell
EDX	Energy Dispersive X-Ray Analysis
EIS	Electrochemical Impedance Spectroscopy
ESC	Electrolyte Supported Cell
IT-SOFC	Intermediate Temperature Solid Oxide Fuel Cell
λ	Wavelength of x-ray incident beam
L_o	Initial length
ΔL	Linear dimension change
MCFC	Molten Carbonate Fuel Cell
MIEC	Mixed Ionic and Electronic Conductor
η	Order of diffraction
OCV	Open Circuit Voltage
P	Gas pressure
PD_{max}	Maximum Power Density
P_o	Applied pressure
P_z	Pressure at any depth in the compact
PAFC	Phosphoric Acid Fuel Cell
PEFC	Polymer Electrolyte Fuel Cell
PVD	Physical Vapour Deposition

$\mathbf{R_g}$	Grain resistance
$\mathbf{R_{gb}}$	Grain boundary resistance
$\mathbf{R_{ohm}}$	Ohmic resistance
$\mathbf{R_{tot}}$	Total resistance
S_a	Average surface roughness
S_d	Dry sample weight
S_q	Root mean square of the roughness
S_s	Saturated sample weight
SD	Standard Deviation
SEM	Scanning Electron Microscopy
SOFC	Solid Oxide Fuel Cell
t	Time
TEC	Thermal Expansion Coefficient
TGA	Thermogravimetric Analysis
TPB	Triple Phase Boundary
U	Fuel utilisation
μ	Die wall friction
XRD	X-ray Diffraction
XRF	X-ray Fluorescence
z	Compact height
$\alpha\ (K^{-1})$	Thermal Expansion Coefficient
$A\ (cm^2)$	Cross-sectional area
$ASR\ (\Omega cm^2)$	Area Specific Resistance
$B_d\ (g\ m^{-3})$	Bulk Density
$E\ (V)$	Operating Cell Potential
$E_a(kj\ mol^{-1})$	Activation energy
$E_{Nernst}\ (V)$	Nernst Potential
$E_o\ (V)$	Theoretical reversible cell potential
$F\ (96\,485\ C\ mol^{-1}\ )$	Faraday Constant
$\Delta G\ (J\ mol^{-1})$	Gibbs Free Energy
$\Delta H^o\ (J\ mol^{-1})$	Enthalpy
$I\ (A)$	Current

$I_{0.7}$ $(A\ cm^{-2})$	Current density at operating voltage of 0.7V
k_b $(8.617\ x10^{-5} eV\ K^{-1})$	Boltzmann's constant
l (mm)	Sample thickness
n $(for\ H_2, n = 2)$	Number of electrons in the charge transfer reaction
η_a (V)	Activation polarisation at the anode
η_c (V)	Activation polarisation at the cathode
ρ $(\Omega\ m^{-1})$	Resistivity
ρ $(g\ m^{-3})$	Volumetric mass density
P_o $(tons)$	Pressure at any depth in the compact
P_z $(tons)$	Applied pressure during uniaxial pressing
P_{H_2} (Pa)	Hydrogen partial pressure
P_{H_2O} (Pa)	Water partial pressure
$P_{O_2}^{\frac{1}{2}}(Pa)$	Oxygen partial pressure when cathode is open to ambient air
R $(8.31451\ J\ mol^{-1}\ K)$	Gas Constant
R (Ω)	Resistance
S $(m^2 kg^{-1})$	Average surface roughness
T (C^o, K)	Temperature
ΔT (C^o, K)	Change in temperature
$\sigma(S\ m^{-1})$	Conductivity
v $(mol\ s^{-1})$	Fuel flow rate

PREFACE

The work presented here marks the initial phase of the manufacture of anode supported Solid Oxide Fuel Cells (SOFCs) developed by the Fuel Cell Group of the Doctoral Training Centre in Hydrogen, Fuel Cells and their Applications at the University of Birmingham.

This research considers a specific approach for the fabrication of anode supported SOFC cells made of traditional materials and the transfer of this method to manufacturing anode supported cells using novel, higher performing materials. A comprehensive review of the literature reveals potential for such a method as it incorporates the use of widely known, commonly used materials synthesis and cell manufacturing processes.

There exists much emphasis on the development of SOFCs for intermediate temperature operation and for improved performance on hydrocarbon fuels. Developing SOFC systems that operate in lower temperature regimes improves system stability and lowers performance degradation issues

previously observed with higher temperature cells. Under direct hydrocarbon feed, carbon deposits form on the surface of conventional SOFC anodes, degrading their functionality.

Direct hydrocarbon utilisation in SOFC is a current research trend. While the work being carried out in this area is intensive and vast, there still exists a need for more research to find cheaper, better performing anode catalysts that exhibit performance stability on hydrocarbon fuels over extended lifetimes and at lower temperatures. The emphasis of this thesis is to develop and optimise an intermediate temperature SOFC based on a Ce-doped ScSZ structure, which will both operate at lower temperatures (650-750^{o}C) as well as improve performance on hydrocarbon fuels.

This thesis is comprised of 8 chapters. The first chapter outlines the motivation for alternative energy technologies with an introduction to fuel cells, the principles of SOFC operation, various SOFC cell designs, the practical applications of SOFCs along with the scientific approach and research aims for this project. Chapter 2 defines state of the art materials for conventional SOFC systems, SOFC methods of manufacture and hydrocarbon utilisation in SOFCs. A comparison between the YSZ and 10Sc1CeSZ system and the potential use of a SOFC based on a 10Sc1CeSZ structure is also discussed. Chapter 3 discusses SOFC materials and the research methodology used in this study. Chapters 4 and 5 summarise the experimental approach and present results related to the influence of processing variables on the physical properties of the conventional Ni-YSZ system. Chapter 6 focuses on the manufacture and characterisation of the 10Sc1CeSZ system while Chapter 7 compares the electrochemical performance and microstructural characteristics of the YSZ and 10Sc1CeSZ systems operating on hydrogen and methane fuel. Chapter 8 summarises the achievements and highlights of this research and presents future work recommendations.

CHAPTER 1
INTRODUCTION

This chapter provides a brief introduction to the principles of fuel cell operation and outlines the project rationale for this research thesis.

1.1 OVERVIEW

With oil reserves steadily decreasing and fossil fuels on limited supply, the pressure is on to find replacement sources to supply our current and future energy needs [1]. Large-scale alternative energy demonstration projects are underway and industrialised nations have made the call to develop suitable technologies to gain an edge in the race for a more sustainable energy supply system. The combustion of carbon-based fuels vents harmful CO_2 into the atmosphere, which many argue is largely responsible for the upward shift in the Earth's surface temperature. Fuel cells have garnered much interest as an

alternative solution to conventional energy systems due to their high conversion efficiencies and thus lower specific greenhouse gas emissions.

Sir William Grove introduced the first working fuel cell in 1839 which became known as the "Grove Cell" [2]. Electrodes composed of platinum metal immersed in a beaker of sulphuric acid at room temperature with the upper ends exposed to either hydrogen or air produced a voltage. The first solid-state ceramic ionic conductor was discovered in 1899 by Walther Nernst with its successful conversion into a solid fuel cell by Bauer and Preis in 1937. Fast forward to present day and this same concept, though slightly more developed and sophisticated in its design, has translated into a usable source of power with various applications throughout stationary power, mobile and automotive sectors. With threats to our current energy supply on the rise and increases in world energy demand projected to double by 2050, fuel cells are gradually becoming the technology to meet the energy demands in a shifting market due to their cleaner and more efficient power delivery.

1.2 FUEL CELL TECHNOLOGY

Fuel cells have emerged as one of the most promising energy conversion technologies, due in part, to their potential use in a variety of commercial applications. The rising demand for electrical power allows fuel cells to serve as secondary systems that support power grids during downtime or as the primary power source that provides on-site electricity for home, automotive or consumer electronic use [3], [4]. The use of fuel cells for space and military applications have also been explored [5]. The major advantages of fuel cells include high conversion efficiency, low noise operation, recyclable heat and variable power output independent of unit size [2]. Like batteries, fuel cells are composed of a dense electrolyte in contact with two porous electrodes. These electrochemical devices generate electricity through the use of hydrogen and oxygen but the major difference between fuel cells and batteries is batteries cease to produce electrical energy once the chemical energy is depleted; fuel cells continue to produce power as long as there is a continuous supply of fuel and oxidant [6].

Fuel cells are classified according to operating temperature and charge conducting species of the electrolyte. It is the cell operating temperature that dictates target applications and which materials are best suited for cell component manufacturing. Listed in Table 1.1 is a summary of the different fuel cell types, their charge transporting species and operating temperature range [7]–[9]. The work outlined herein focuses on the development, manufacture and optimisation of lab scale SOFCs. In this thesis, the current study and future outlook of SOFCs will be discussed.

1.2.1 Definition of a Solid Oxide Fuel Cell (SOFC)

Solid Oxide Fuel Cells (SOFCs) are solid-state ceramic energy conversion devices that operate at temperatures 550 - 1000°C [10]. SOFCs have a few advantages over other types of fuel cells relating to their cell design flexibility, variable power output independent of unit size and high temperature operation which renders high efficiency and produces high quality heat usable for co-generation heat and power applications [11].

Table 1.1: Different Classes of Fuel Cells

Fuel Cell	Mobile Ion	Electrolyte	Fuel	Efficiency (%)	T_{op} (°C)
PEFC	H^+	polymer membrane	H_2	45	<100
DMFC	H^+	polymer membrane	CH_3OH/H_2O	45	30-130
AFC	OH^-	KOH	H_2	45	150-200
PAFC	H^+	phosphoric acid	H_2	45-50	180-200
MCFC	CO_3^{2-}	molten carbonate	H_2, CO, CH_4	45-50	650-700
SOFC	O^{2-}	ceramic, YSZ	H_2, CO, CH_4	60	550-1000

SOFCs can operate on both H_2 and hydrocarbon fuels as fuel reforming can occur within the cell stack allowing for the immediate use of existing resources which creates a wider range of fuels that can be considered for SOFC operation. While these advantages make SOFCs one of the most sought after technologies, the technical challenges associated with high temperature operation and the catalytic formation of carbon during hydrocarbon fuel use currently still provide enough scope for research.

The traditional SOFC consists of an oxygen ion conducting Yttria-stabilised Zirconia electrolyte (YSZ), a Ni-ZrO_2 ceramic-metal composite (cermet) anode and a Strontium-doped Lanthanum Manganate (LSM) cathode [12]. These materials are used as they are low in cost and because they adhere rigidly to the chemical and mechanical demands of the cell during fabrication and operation generating high performance yields that make for a simple and efficient fuel cell. The operating principles of an SOFC where hydrogen from methane fuel supplied at the anode side gets oxidised, releasing electrons that are accepted at the cathode is illustrated in Figure 1-1; CO, CO_2, H_2O and heat are by-products of the cell reaction [13].

In a ceramic oxide based fuel cell, oxygen ions serve as the internal charge carrier. The electrons released at the anode where hydrogen is the fuel thus flow through an external circuit and are used to reduce oxygen from air forming the O^{2-} ions [8], [13], [14]. The electrolyte membrane allows O^2

migration between the two electrodes and prevents fuel and air mixing. The cell reactions that occur at each of the electrodes are:

Cathode: $$O_2 + 4e^- \rightarrow 2O^{2-} \quad (1.1)$$

Anode: $$H_2 + O^{2-} \rightarrow H_2O + 2e^- \quad (1.2)$$

Overall Reaction: $$O_2 + 2H_2 \rightarrow 2H_2O \quad (1.3)$$

The rate at which the charge transfer reactions occur is largely dependent upon the ion conducting ability of the electrolyte and how well it can sustain large oxygen partial pressure differences between the electrodes. As this cycle repeats, the electric current generated is ultimately used to supply power.

Further SOFC system development renders benefits that could advance the technology allowing for adoption in certain industries and increased market uptake [15]. Hence, work centred on better understanding SOFC fundamentals, materials development and application, scale up, system design and market penetration have been at the forefront of SOFC research. A more detailed overview of SOFC technology is covered in Chapter 2.

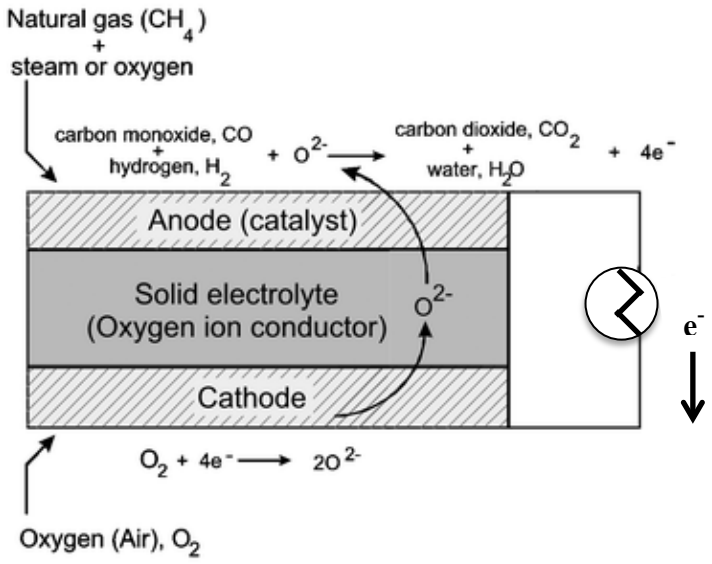

Figure 1-1: Schematic representation of an oxide fuel cell in operation [13]

1.2.2 Solid Oxide Fuel Cell Design

The manufacture of SOFCs has benefitted from a variety of different cell designs, most notably the commercialisation of the tubular SOFC by Westinghouse and the development of the high power output planar stack both pictured in Figure 1-2 [6], [16], [17]. Porous tubes of a large diameter (>15 mm) or small diameter (<5 mm) serve as the structural support onto which SOFC components are deposited and in years past have assumed a variety of different configurations to meet the specific cell operating requirements. Despite the added advantage of a seal less design, rapid start up times and good resistance to thermal cycling with microtubes, development in recent years has focused on the planar design [18]. The planar design, which sees the single cell SOFC components in a planar geometry, is similar to the microtubular cell in that it has adopted different configurations to achieve the performance requirements for a given application [19].

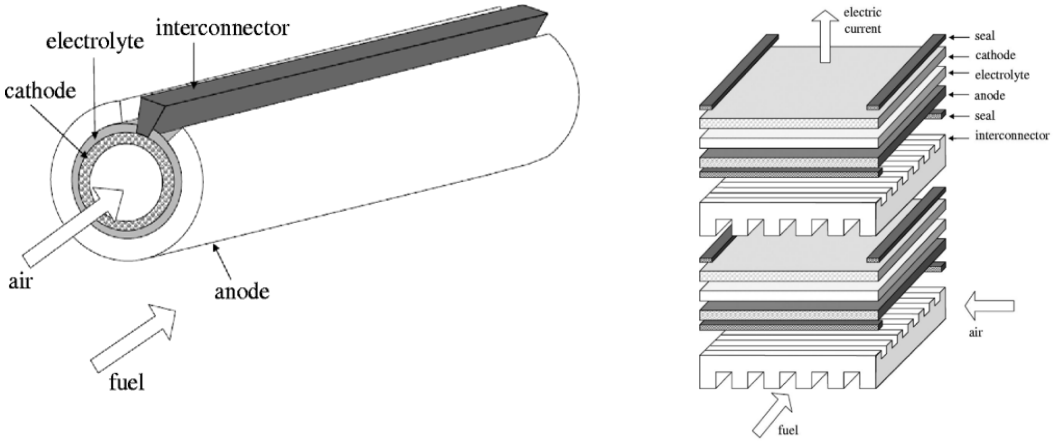

Figure 1-2: Schematic of a SOFC tubular and planar stack cell design [10]

1.2.2.1 Electrolyte Supported Cell (ESC) vs. Anode Supported Cell (ASC) Design

SOFC single cell configurations are grouped as either self-supported or external supported in that one of the cell components serves as the support structure in the self-supported approach while in the external supported configuration a separate support material - metal, metal alloys, interconnect, insulating porous material - is used. Figure 1-3 shows the various SOFC support configurations [11]. The two most common approaches in the planar self-supported configuration have been the electrolyte supported cell (ESC) and anode supported cell (ASC) designs as shown respectively in Figure 1-4. The

vertical representation of the planar ESC pictured first serves to show how the anode thin film (green) covers the same area as the cathode film (black) but on the opposite side of the electrolyte substrate (white). The ESC design contains a bulk electrolyte (150-250 μm) as the structural support with the electrodes applied as thin films while the planar ASC design has the anode as the support layer (200 - 1000 μm) with the electrolyte layer between 5 -20 μm [21]. The ESC design benefits from increased durability and strength brought about by the fully dense bulk electrolyte and does not experience anode re-oxidation problems; the disadvantage of ESCs is the high ohmic resistance (characteristic of ionic conductors), which necessitates high operating temperatures to compensate for these losses. These

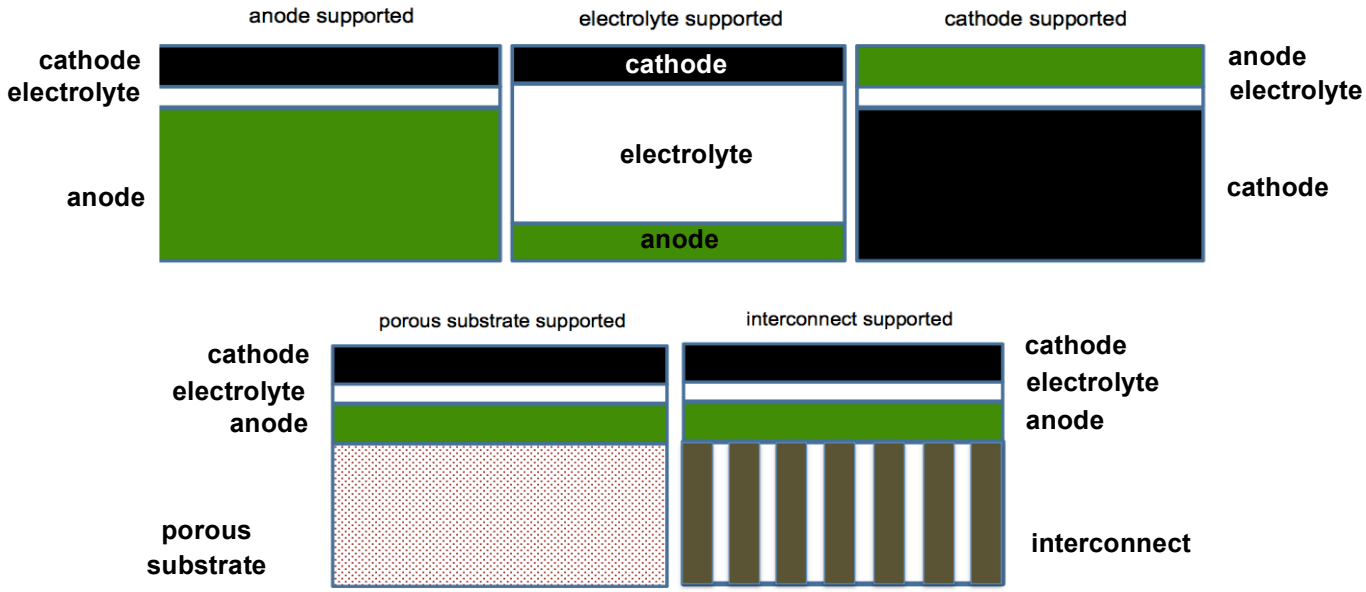

Figure 1-3: Schematic of various SOFC support configurations [11]

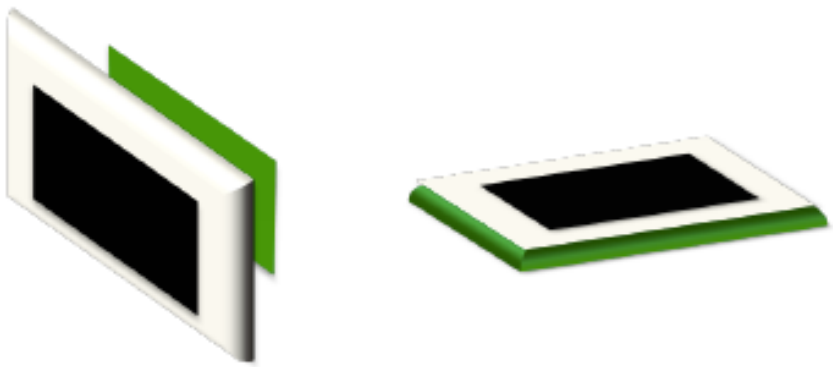

Figure 1-4: ESC and ASC supported planar cell design

require expensive sealant and interconnect materials further driving up cell and operating costs.

Conventional SOFC's use the planar ASC design as the ohmic loss is minimised through the use of a thin electrolyte layer while the electrical conductivity is improved through the use of Ni in the anode support cermet, both of which provide enhanced performance at lower temperatures and allows the use of cheaper materials [20]–[22] . The ASC cell design also takes advantage of better performance in intermediate temperature operating regimes (700 – 850^{o}C), as high operating temperatures are not required for reasonable performance like in the ESC configuration. Benefits of ASCs aside, failure due to anode re-oxidation and concentration polarisation contributions brought about by thicker anode supported substrates are still major concerns [11]. Redox cycling is the process by which the cell is exposed to alternating oxidising and reducing atmospheres, similar to a shut down-start up procedure or fuel interruption caused by an operating failure, which puts the cell at risk of degradation due to anode stresses brought about by repeated cycles of Ni to NiO volume expansion and contraction [23]. The anode microstructure becomes modified and this can result in performance changes and mechanical damage that permeates throughout the entire SOFC [24], [25]. Ultimately, cell configuration and geometry as well as stack design rely heavily on the application and the scale of the system [11]. Several companies and research institutes have adopted the planar ASC configuration where the anode is predominantly tape casted [19].

As this work focuses on the development of intermediate temperature 10Sc1CeSZ cells, to the best of the author's knowledge, there are no commercial manufacturers with available Ni-10Sc1CeSZ anode supported cells based on a screen-printed 10Sc1CeSZ cell structure. Table 1.2, adapted from Tietz and Stöver [19], lists commercial manufacturers who have incorporated the use of 10Sc1CeSZ into their SOFC manufacturing approach which supports the ESC design. This shows the need for more work in this area and this study aims to fill in the gaps. In this work, the ASC design approach for both Ni-YSZ and Ni-10Sc1CeSZ cells was used.

Ni-YSZ and Ni-10Sc1CeSZ substrates were prepared via die pressing despite known limitations placed on minimum thicknesses obtained using this processing route. Care and attention was given to fabricate durable, robust and crack free anode supports without sacrificing mass transport properties. At the start of this work tape casting was not an option due to the lack of equipment. In recent months a tape caster has been purchased and planar, anode supported tapes are the current SOFC design focus. The results of this study lay the groundwork for this next phase of research.

Table 1.2: Manufacturers of ScSZ Cells [19]

Company	Location	Cell Design	Production	Component Material
Fuel Cell Materials	Columbus OH, USA	ESC plates, discs	screen printing tape casting screen printing	Ni-GDC/Ni-YSZ 10ScSZ LSM-GDC
Ningbo Inst	Zhejiang, CN	ESC plates, discs	screen printing tape casting screen printing	Ni-GDC/Ni-YSZ ScSZ LSCF-GDC
Electroscience (ESL)	King of Prussia PA, USA	custom orders not market systems	lamination pressing screen printing tape casting	customised electrodes

1.2.3 Fuel Cell Systems and Their Applications

Fuel cells are more efficient than conventional energy generation systems as they are not limited by the Carnot-Cycle of thermal machines. The advantages of fuel cells from low noise, to variable power output independent of unit size, to design simplicity, makes them suitable for a wide range of stationary and portable applications. When considering their potential use in a given market, fuel cells are grouped according to their power output capabilities. As seen below in Figure 1-5, PEFCs have the widest range of application with the main area of focus directed toward the portable electronics sector and vehicle propulsion. SOFCs have cornered the market for co-generation heat and power applications due to their higher operating temperatures and high-value heat production [26].

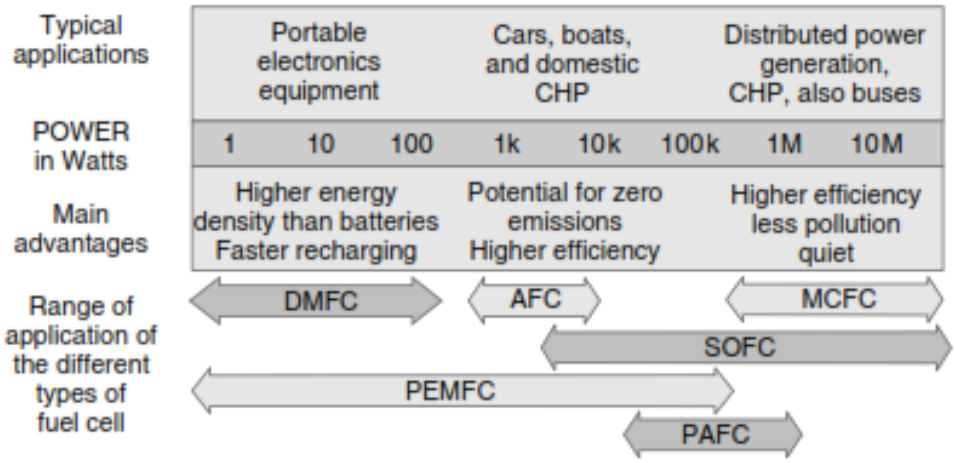

Figure 1-5: A summary of the range of applications of different fuel cells [6]

1.2.4 Fuel Cell Characteristics

Fuel cell performance is determined by measuring the output potential and corresponding current generated by the cell. The operating cell potential E will always be less than the reversible cell potential E_o (if the process is reversible there are no losses) due to irreversible system losses during operation. System losses related to sluggish reaction kinetics at the electrodes, internal cell resistances and fuel transport limitations could all be responsible for the fall in voltage. The theoretical reversible cell potential E_o is equal to the Gibbs free energy where:

$$E_o = \frac{-\Delta G}{2F} \tag{1.4}$$

F is the Faraday constant $96{,}485\ C\ mol^{-1}$ and ΔG is the Gibbs free energy [27]. The two is related to the number of electrons generated in the cell reaction for every 1 *mole* of H_2 used. It is important to note that the Gibbs free energy changes with temperature so for SOFCs where the operating temperature is higher, the ΔG value decreases, reducing the reversible cell potential E_o value and further reducing the E_o and E difference [6].

When no current is running through the fuel cell the voltage measured across the fuel cell is rid of any ohmic losses or internal cell resistances so it can be considered the open circuit voltage (OCV) of the cell. The (OCV) for a SOFC operating on hydrogen is also referred to as the Nernst potential (E_{Nernst}) and defined as:

$$E_{Nernst} = E_o + \frac{RT}{nF}\ln\left[\frac{p_{O_2}^{\frac{1}{2}} p_{H_2}}{p_{H_2O}}\right] \tag{1.5}$$

with E_o as the reversible cell potential, R is the gas constant $8.31451\ \frac{J}{mol\ K}$, T is the temperature in Kelvin, $p_{O_2}^{\frac{1}{2}} p_{H_2}$ and p_{H_2O} are the partial pressures of O_2 at the cathode (when it is exposed to ambient air) and H_2 and H_2O at the anode respectively [27]. As the reversible cell potential E_o falls at elevated temperatures due to changes in ΔG, the E_o at 800°C is 0.98V for a ΔG of -188.6 kJ mol^{-1} (the negative

value denotes an exothermic reaction), thus the measured E_{Nernst} at this temperature will differ due to the varying activity of the reactants and the products which is related to the concentration of the partial pressures of the reactants and products as seen in Equation 1.4.

Once the cell is under load, the circuit is closed and current is produced. This is an irreversible process and the operating cell potential E will be less than the OCV due to system losses mentioned previously. Therefore, the operating cell potential E can be written as:

$$E = E_{Nernst} - IR - \eta_c - \eta_a \qquad (1.6)$$

with R as the cell ohmic resistance, I is the cell current, η_c defines the activation and concentration polarisation at the cathode and η_a defines the activation and concentration polarisation at the anode. The ohmic resistance is the internal resistance of the cell, IR, that measures the resistance of oxygen ion flow through the electrolyte, resistance to current flow from and to the electrodes and contact and leading wire contributions [12]. The operating temperature dictates the ion conducting ability of the electrolyte. Concentration polarisation measures overpotentials caused by gas diffusion processes whilst activation polarisation measures losses due to reaction kinetics at each electrode. A typical $i - V$ curve is pictured in Figure 1-6. The regions of the curve highlight the different contributions to losses in an operating fuel cell and visibly outline how a typical operating cell deviates from the theoretical cell potential. This system diversion from thermodynamic equilibrium dictates the electrochemical performance of the solid oxide fuel cell.

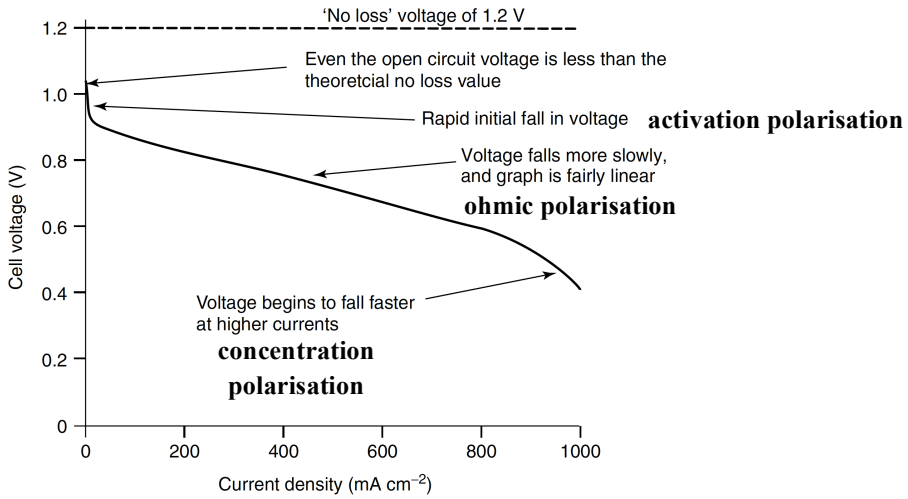

Figure 1-6: A schematic of a fuel cell polarisation curve [2]

1.3 PROJECT RATIONALE

1.3.1 Scientific Approach

1.3.1.1 Doped Ni-10Sc1CeSZ Anodes

As mentioned earlier, the fuel flexibility benefit of SOFCs allows for the immediate use of methane fuels without waiting for a hydrogen economy to be realised. Not to mention, the challenges associated with the production, storage and supply of hydrogen make the crossover to a hydrogen society much slower, and create barriers for widespread implementation of hydrogen based technologies. Developing SOFC systems that operate directly on hydrocarbon fuels eliminates the need for separate fuel reformers and purification systems and allows by-product heat to be recycled back into the cell stack for the purpose of internal reforming. And despite the use of hydrocarbons for SOFC operation coming at an environmental cost (zero greenhouse gas emissions only comes with pure hydrogen use) CO_2 emissions remain lower, heat and power yields are higher all of which sustain interest in further developing and improving SOFC technology.

The fuel variability of SOFCs is an added advantage but the disadvantage of utilising hydrocarbons in a conventional SOFC is the significant loss in cell performance due to low sulphur tolerances and carbon formation on Ni-YSZ anodes [28]–[31]. And because of its low cost and exceptional performance in hydrogen (H_2) and methane (CH_4) environments, Ni-YSZ remains the most developed and most commonly used anode. For the case of CH_4, the simplest hydrocarbon fuel, the formation of carbon can occur via the reaction types listed below [32]:

$$CH_4 \rightarrow C + 2H_2 \quad \text{methane pyrolysis} \quad \Delta H^o_{298K} = 75\,\frac{kJ}{mol} \qquad (1.7)$$

$$2CO \rightarrow C + CO_2 \quad \text{Boudouard reaction} \quad \Delta H^o_{298K} = -175\,\frac{kJ}{mol} \qquad (1.8)$$

At temperatures of 650^{o}C and above, typical SOFC operating temperatures, CH_4 decomposes via pyrolysis making reaction 1.7 dominant whilst at temperatures of 550^{o}C and below, carbon disproportionation of CO as seen in reaction 1.8 is more favourable [6], [33]. Both reactions can occur at various locations throughout the cell and are a product of incomplete hydrocarbon oxidation occurring by different mechanisms within different temperature regimes. The presence of carbon in the cell can clog the anode pores, reduce mechanical integrity due to carbon build up and impair Ni catalytic activity, all of which lead to rapid cell degradation and severe performance losses. Approaches to minimise

Ni-YSZ anode deterioration and mitigate the effect of hydrocarbon utilisation on cell performance include: a) direct/indirect utilisation of CH_4 (converting the fuel to a more usable species externally) b) optimising existing Ni-YSZ anodes or c) formulating new anode materials that are inactive for carbon formation.

While indirect utilisation of CH_4 employs steam reforming ($CH_4 + H_2O$), dry reforming and partial oxidation, steam reforming for SOFCs has proven successful, though a proper balance between temperatures, fuel/steam feed ratios and system pressure is necessary to achieve good fuel conversion efficiencies [34]–[36]. Because steam reforming is a highly endothermic process, high temperature operation (700^{o}C and above) is required to drive the steam reforming reactions making good use of SOFC waste heat during operation, though new challenges are introduced – high gradients in temperature distribution, negative impact of temperature gradients on sealing, and local, thermally activated increased cell degradation - that cannot be ignored.

Optimising current Ni-YSZ anodes by doping with catalysts that suppress carbon formation and operating in stability regions where carbon formation is not thermodynamically favoured is another way to achieve stable, routine long-term SOFC operation. The addition of an oxidation catalyst in the anode to better assist in oxidising the carbon in the fuel, alloying metal catalysts with Ni anodes, or direct substitution of Ni with metals that do not promote solid carbon formation is the focus of a lot of the research in this area.

1.3.1.2 Low Temperature Operation

SOFCs operate in the temperature range 550-1000^{o}C but in recent years research and development aims have focused on reducing operating temperatures to lower system costs, minimise cell performance degradation and improve cell mechanical integrity and durability [37]–[39]. The trade off between good performance observed with high-temperature SOFCs and the longer lifetime perceived with intermediate temperature SOFCs (IT-SOFCs) can be reconciled with a wider selection of cheaper materials that can be considered for use with IT-SOFCs. The major obstacle is finding alternative materials that demonstrate comparable or better performance to those of the current state of the art SOFC [40]. Figure 1-7 summarises the benefits (green) and technical challenges (red) of high temperature operation and hydrocarbon utilisation in SOFCs.

One approach to lowering operating temperature is to enhance the properties of the electrolyte system [38]. Electrolyte material, thickness and deposition method dictate optimal operating temperature

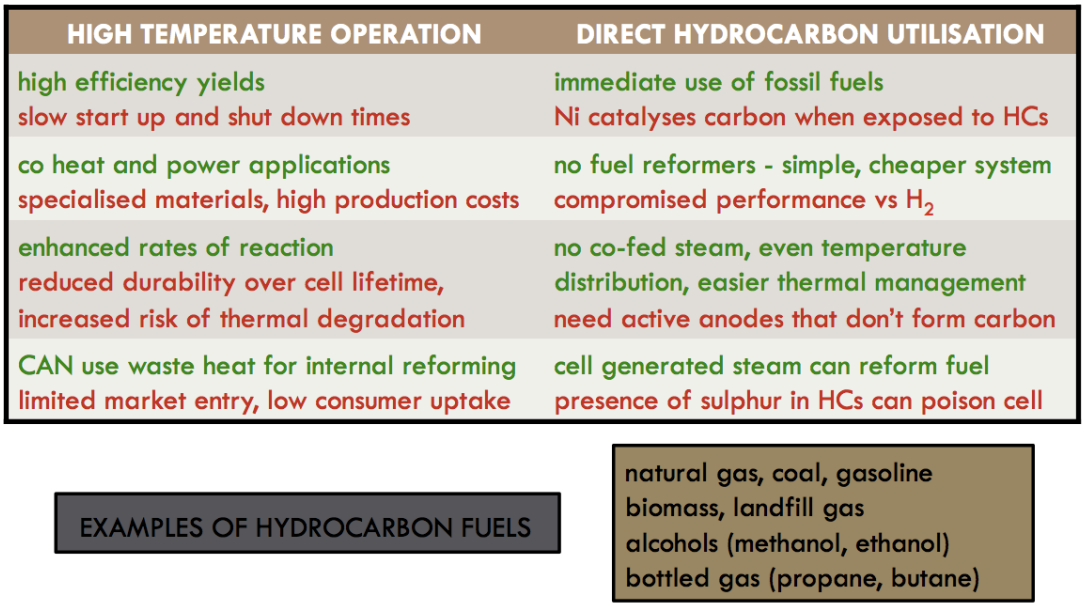

Figure 1-7: Benefits (green) and challenges (red) of high-temperature operation and direct hydrocarbon utilisation in SOFCs

ranges which influence materials selection, cell parameters and processing conditions and determine the fuel cell's placement in a given market and its suitability for a specific application. While reduced temperature operation has its advantages, it has been found to compromise cell reaction kinetics and increase electrode polarisation, electrolyte and overall cell resistances [38]. Careful selection must be given to the most appropriate electrolyte system that yields the target conductivity within the desired temperature regime [41].

A downward shift in the operating temperature of conventional SOFCs requires the use of better performing electrolyte materials [42]. Despite YSZ being the most developed, commonly used electrolyte for SOFCs, a variety of oxide dopants with high solubility's in ZrO_2 can be used. Sc_2O_3 stabilised ZrO_2 (ScSZ) is an alternative to Yttria-stabilised Zirconia (YSZ) electrolytes because Sc_2O_3 has the highest conductivity of all the suitable ZrO_2 dopants [43]–[45]. The higher conducting ScSZ exhibits a lower intrinsic resistance than YSZ at reduced temperature ranges making it an ideal candidate as an alternative IT-SOFC electrolyte material. Figure 1-8 shows the relationship between concentration, radius and conductivity at 1000^{o}C for selected ZrO_2 dopants. This research will explore the use of 10Sc1CeSZ electrolytes based on an anode supported Ni-10Sc1CeSZ structure for intermediate temperature operation on H_2 and CH_4. The added benefit of Ce in the anode to promote CH_4 oxidation

and its impact on performance will be examined.

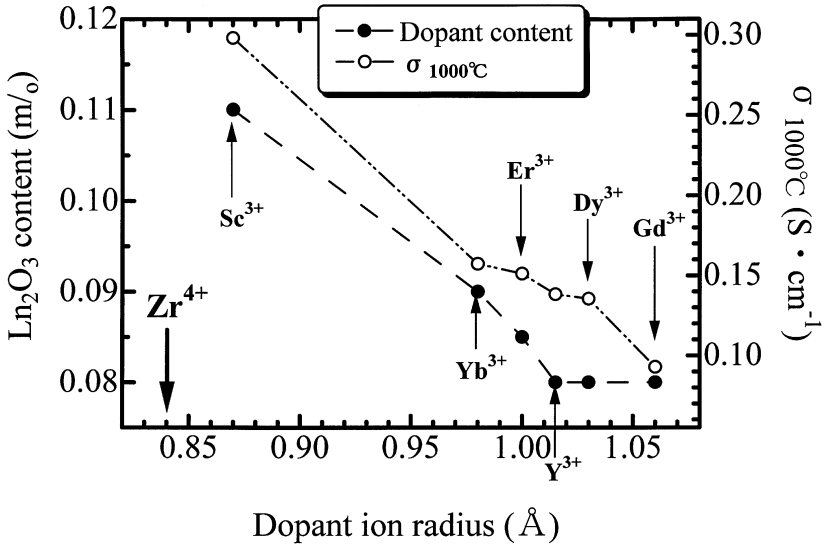

Figure 1-8: Plot of dopant concentration and conductivity as a function of ion radius [46]

1.4 RESEARCH AIMS AND OBJECTIVES

The scope of this work will be to design an intermediate temperature SOFC based on a Ce-doped ScSZ structure for operation on hydrogen and methane. And while much progress has been made towards developing SOFCs for hydrocarbon use based on reformed methane ($CH_4 + H_2O$), there still exists a need to find cheaper, better performing materials that can be either integrated into existing anode structures or used to develop new structures that utilise hydrocarbon fuels directly for enhanced performance stability over extended lifetimes at lower temperatures. The major objectives of this research thesis are summarised below:

i. characterise the starting materials used in the manufacture of anode supported YSZ and 10Sc1CeSZ button cells
ii. develop a ceramic processing route for the starting materials used in the manufacture of anode supported YSZ and 10Sc1CeSZ button cells
iii. develop a standardised procedure for the manufacture of anode supported YSZ and 10Sc1CeSZ button cells
iv. develop a reliable method for the electrochemical testing of anode supported YSZ and 10Sc1CeSZ button cells

v. examine the performance of manufactured and commercial anode supported YSZ and 10Sc1CeSZ button cells on H_2 and CH_4

Preliminary work will be carried out on Ni-YSZ/YSZ/LSM-YSZ anode supported button cells to be used as baseline comparisons followed by cells containing Ni within a 1 mol% Ceria (CeO_2) - 10 mol% Scandia (Sc_2O_3) Stabilized Zirconia (10Sc1CeSZ) matrix. The 1 mol% CeO_2 serves as a mixed conductor and oxidation catalyst for the hydrocarbon fuel. 10Sc1CeSZ will be the electrolyte of choice to lower operating temperature and improve O^{2-} transport to the anode. The manufacturing technique will be screen-printing the anode functional layer and the electrolyte layer as high-quality electrolyte films with thicknesses of 10-15 μm have been successfully fabricated using this processing route [47]–[49]. This adds novelty to the research as anode supported SOFCs based on a 10Sc1CeSZ structure manufactured via screen-printing have yet to be reported to the best of the author's knowledge.

REFERENCES

[1] B. Dudley, *BP Statistical Review of World Energy*, 64th ed., 2015.

[2] EG&G Technical Services, *Fuel Cell Handbook*, seventh ed., University Press of the Pacific, 2004.

[3] G. W. Crabtree, M. S. Dresselhaus and M. V Buchanan, The Hydrogen Economy. *Phys. Today*, 2004. 57 (12): p. 39-44.

[4] D. Carter, M. Ryan and J. Wing, The Fuel Cell Industry Review 2012. *Fuel Cell Today*, 2012. p. 1-52.

[5] U.S. Environmental Protection Agency Combined Heat and Power Partnership, *Technology Characterization – Fuel Cells*. Cat. CHP Technol., 2008.

[6] J. Larminie and A. Dicks, *Fuel Cell Systems Explained*, second ed., John Wiley and Sons, 2003.

[7] V. Ramani, Fuel Cells. *Electrochem. Soc. Interface*., 2006. p. 41-44.

[8] O. Yamamoto, Solid oxide fuel cells: fundamental aspects and prospects. *Electrochim. Acta*, 2000. 45 (15-16): p. 2423-2435.

[9] A. Aricò, V. Baglio and V. Antonucci, Direct Methanol Fuel Cells: History, Status and Perspectives. *Electrocatalysis of Direct Methanol Fuel Cells: From Fundamentals to Applications,* 2009.

[10] S. C. Singhal and K. Kendall, *High Temperature and Solid Oxide Fuel Cells: Fundamentals, Design and Applications*, Elsevier, 2003.

[11] N. Minh, Solid oxide fuel cell technology, features and applications. *Solid State Ionics*, 2004. 174 (1-4): p. 271-277.

[12] N. Q. Minh, Ceramic Fuel Cells. *J. Am. Ceram. Soc.*, 1993. 76 (3): p. 563-588.

[13] R. M. Ormerod, Solid oxide fuel cells. *Chem. Soc. Rev.*, 2003. 32 (1): p. 17-28.

[14] K. Kendall, Progress in solid oxide fuel cell materials. *Int. Mater. Rev.*, 2005. 50 (5): p. 257-264.

[15] S. Hardman, A. Chandan and R. Steinberger-Wilckens, Fuel cell added value for early market applications. *J. Power Sources*, 2015. 287 (1): p. 297-306.

[16] K. Hassmann, SOFC Power Plants, the Siemens-Westinghouse Approach. *Fuel Cells*, 2001. 1 (1): p. 78-84.

[17] L. Blum, W. A. Meulenberg, H. Nabielek and R. Steinberger-Wilckens, Worldwide SOFC Technology Overview and Benchmark. *Int. J. Appl. Ceram. Technol.*, 2005. 2 (6): p. 482-492.

[18] Y. Du, C. Finnerty and J. Jiang, Thermal Stability of Portable Microtubular SOFCs and Stacks. *J. Electrochem. Soc.*, 2008. 155 (9): p. B972-B977.

[19] F. Tietz, H.P. Buchkremer and D. Stöver, Components manufacturing for solid oxide fuel cells. *Solid State Ionics*, 2002. 152–153 (1): p. 373-381.

[20] S. Yang, T. Chen, Y. Wang, Z. Peng, and W. G. Wang, Electrochemical analysis of an anode-supported SOFC. *Int. J. Electrochem. Sci.*, 2013. 8 (2): p. 2330-2344.

[21] L. Blum, L. G. J. (Bert) de Haart, J. Malzbender, N. H. Menzler, J. Remmel and R. Steinberger-Wilckens, Recent results in Jülich solid oxide fuel cell technology development. *J. Power Sources*, 2013. 241 (1): p. 477-485.

[22] N. H. Menzler, J. Malzbender, P. Schoderbock, R. Kauert, and H. P. Buchkremer, Sequential tape casting of anode-supported solid oxide fuel cells. *Fuel Cells*, 2014. 14 (1): p. 96-106.

[23] D. Sarantaridis and A. Atkinson, Redox Cycling of Ni-Based Solid Oxide Fuel Cell Anodes: A Review. *Fuel Cells*, 2007. 7 (3): p. 246-258.

[24] D. Waldbillig, A. Wood and D. G. Ivey, Electrochemical and microstructural characterization of the redox tolerance of solid oxide fuel cell anodes. *J. Power Sources*, 2005. 145 (2): p. 206-215.

[25] A. Faes, A. Nakajo, A. Hessler-Wyser, D. Dubois, A. Brisse, S. Modena and J. Van Herle, RedOx study of anode-supported solid oxide fuel cell. *J. Power Sources*, 2009. 193 (1): p. 55-64.

[26] P. E. Dodds, I. Staffell, A. D. Hawkes, F. Li, P. Grünewald, W. McDowall and P. Ekins, Hydrogen and fuel cell technologies for heating: A review. *Int. J. Hydrogen Energy*, 2015. 40 (5): p. 2065-2083.

[27] E. M. Brodnikovskii, Solid Oxide Fuel Cell Anode Materials. *Powder Metall. Met. C*+., 2015. 54 (3-4): p. 166-174.

[28] M. Gong, X. Liu, J. Trembly and C. Johnson, Sulfur-tolerant anode materials for solid oxide fuel cell application. *J. Power Sources*, 2007. 168 (2): p. 289-298.

[29] A. Atkinson, S. Barnett, R. J. Gorte, J. T. S. Irvine, A. J. McEvoy, M. Mogensen, S. C. Singhal and J. Vohs, Advanced anodes for high-temperature fuel cells. *Nat. Mater.*, 2004. 3 (1): p. 17-27.

[30] S. McIntosh and R. J. Gorte, Direct hydrocarbon solid oxide fuel cells. *Chem. Rev.*, 2004. 104 (10): p. 4845-4865.

[31] C. M. Finnerty, N. J. Coe, R. H. Cunningham and R. M. Ormerod, Carbon formation on and deactivation of nickel-based/zirconia anodes in solid oxide fuel cells running on methane. *Catal. Today*., 1998. 46 (2–3): p. 137-145.

[32] B. De Caprariis, P. De Filippis, A. Petrullo and M. Scarsella, Methane Dry Reforming over Nickel Perovsikite Catalysts. *Chem. Eng. Trans.*, 2015. 43 (1): p. 1-6.

[33] S. Park, J. Vohs and R. Gorte, Direct oxidation of hydrocarbons in a solid-oxide fuel cell. *Nature*, 2000. 404 (6775): p. 265-267.

[34] K. Ahmed and K. Foger, Kinetics of internal steam reforming of methane on Ni/YSZ-based anodes for solid oxide fuel cells. *Catal. Today*, 2000. 63 (2–4): p. 479-487.

[35] J. H. Lunsford, Catalytic conversion of methane to more useful chemicals and fuels: A challenge for the 21st century. *Catal. Today*, 2000. 63 (2–4): p. 165-174.

[36] Y. Wang, F. Yoshiba, M. Kawase and T. Watanabe, Performance and effective kinetic models of methane steam reforming over Ni/YSZ anode of planar SOFC. *Int. J. Hydrogen Energy*, 2009. 34 (9): p. 3885-3893.

[37] K. Acres, Recent advances in fuel cell technology and its applications. *J. Power Sources*., 2001. 100 (1-2): p. 60-66.

[38] A. Tarancón, Strategies for Lowering Solid Oxide Fuel Cells Operating Temperature. *Energies*, 2009. 2 (4): p. 1130-1150.

[39] S. J. Litzelman and J. P. Lemmon, The Promise and Challenges of Intermediate Temperature Fuel Cells. *ECS Trans.,* 2015. 68 (1): p. 39-47.

[40] N. Mahato, A. Banerjee, A. Gupta, S. Omar and K. Balani, Progress in material selection for solid oxide fuel cell technology: A review. *Prog. Mater. Sci.*, 2015. 72 (1): p. 141-337.

[41] P. Charpentier, P. Fragnaud, D. M. Schleich and E. Gehain, Preparation of thin film SOFCs working at reduced temperature. *Solid State Ionics*, 2000. 135 (1-4): p. 373-380.

[42] D. Radhika and A. S. Nesaraj, Materials and Components for Low Temperature Solid Oxide Fuel Cells – An Overview. *Int. J. Renew. Energy Dev.*, 2013. 2 (2): p. 87-95.

[43] O. Yamamoto, Electrical conductivity of stabilized zirconia with ytterbia and scandia. *Solid State Ionics*, 1995. 79 (1): p. 137-142.

[44] J. W. Fergus, Electrolytes for solid oxide fuel cells. *J. Power Sources*., 2006. 162 (1): p. 30-40.

[45] S. Badwal, Zirconia-based solid electrolytes: microstructure, stability and ionic conductivity. *Solid State Ionics*, 1992. 52 (1–3): p. 23-32.

[46] Y. Arachi, H. Sakai, O. Yamamoto, Y. Takeda and N. Imanishai, Electrical conductivity of the ZrO_2 – Ln_2O_3 (Ln=lanthanides) system. *Solid State Ionics*, 1999. 121 (1-4): p. 133-139.

[47] X. Ge, X. Huang, Y. Zhang, Z. Lu, J. Xu, K. Chen, D. Dong, Z. Liu, J. Miao and W. Su, Screen-printed thin YSZ films used as electrolytes for solid oxide fuel cells. *J. Power Sources*., 2006. 159 (2): p. 1048-1050.

[48] C. Xia, F. Chen and M. Liu, Reduced-Temperature Solid Oxide Fuel Cells Fabricated by Screen Printing. *Electrochem. Solid-State Lett.*, 2001. 4 (5): p. A52-A54.

[49] R. Peng, C. Xia, X. Liu, D. Peng and G. Meng, Intermediate-temperature SOFCs with thin $Ce_{0.8}Y_{0.2}O_{1.9}$ films prepared by screen-printing. *Solid State Ionics*, 2002. 152-153 (1): p. 561-565.

CHAPTER 2
SOLID OXIDE FUEL CELL MATERIALS AND MANUFACTURING

This chapter discusses traditional SOFC materials, basics of SOFC operation, SOFC component requirements, manufacturing techniques, the fuelling of SOFCs and the novelty of this research.

2.1 SOFC COMPONENT PROPERTIES AND STATE OF THE ART MATERIALS

This chapter begins with a discussion of the SOFC component materials and their role in the function of SOFCs. An explanation of the cell requirements is given here so the discussion regarding alternate material systems introduced in Chapter 3 and how these systems fulfil or exceed the SOFC component requirements is better understood. Vast and detailed information regarding SOFC component requirements and properties can be found in the literature so these topics will not be discussed in much detail here [1]–[4]. A brief mention of the desired properties and key requirements of each SOFC component will be given in this chapter to better relate SOFC material characteristics to SOFC cell function. A more in-depth discussion regarding traditional SOFC materials, the technical challenges

associated with the use of these materials and alternative material considerations are provided in Chapter 3. Since this thesis discusses research centred on the development and use of alternative electrolyte materials, electrolyte component features and material properties will receive an expanded mention.

2.1.1 8 mol% Y_2O_3-ZrO_2 Electrolyte (8YSZ)

The standard SOFC electrolyte is Zirconia (ZrO_2) doped with 8 mol% Yttria (Y_2O_3) denoted as 8YSZ. 8YSZ has a high oxygen ion conductivity (0.13 S cm^{-1} at 1000°C) and is stable in both oxidising and reducing atmospheres [5], [6]. The electrolyte material must exhibit high oxygen ion conductivity and possess negligible electronic conductivity, be stable in both air and hydrogen-rich environments and have a highly dense structure to prevent fuel mixing. YSZ membranes with theoretical densities > 94% are ideal for SOFC applications [7]. ZrO_2 conductivity is largely controlled by the dopant concentration of the stabilising agent. A variety of dopants at varying dopant levels can be used to introduce oxygen vacancies into the ZrO_2 structure for improved conductivity as seen in Figure 2-1. Because ZrO_2 is a poor oxygen ion conductor due to a low number of oxygen ion vacancies, dopants are introduced to increase the ionic conductivity via increased oxygen ion vacancy concentration and enhanced oxide ion mobility [8]. For Y_2O_3, increases in electrical conductivity are observed up to 8 mol% where the maximum conductivity is reached [9], [10]. The temperature dependence of ZrO_2 as a function of Y_2O_3 content is plotted in Figure 2-2. Further increases in Y_2O_3 concentration do not lead to increases in conductivity because the excess oxide vacancies drive unfavourable interactions between the defects based on the oxygen vacancy association with the dopant cation, leading to lattice strain and vacancy ordering hindering oxygen ion mobility thus decreasing conductivity [4], [5]. Investigating the phase relationship of the Yttria-Zirconia system is rather complex and has been studied by previous researchers [8], [11]–[13]. The industry accepted and widely used Y_2O_3 - ZrO_2 phase diagram cited by several researchers will be referenced in this work [11], [14].

ZrO_2 undergoes phase transformations at different temperatures that have an impact on material properties such as mechanical strength, electrical conductivity and overall system stability. Y_2O_3 additions to ZrO_2 do not just increase vacancy concentration for improved conductivity but can stabilise a given phase to tailor system properties to achieve the desired results for a specific application. Shown in Figure 2-3 is the phase diagram of the Y_2O_3 - ZrO_2 system highlighting the phase transformations that occur in ZrO_2 as a function of temperature and Y_2O_3 dopant levels. According to the phase diagram, pure ZrO_2 exists in the monoclinic phase at room temperature and undergoes the monoclinic to tetragonal phase transition (m → t-ZrO_2) at 1170°C. A two-phase monoclinic-tetragonal region exists between 525°

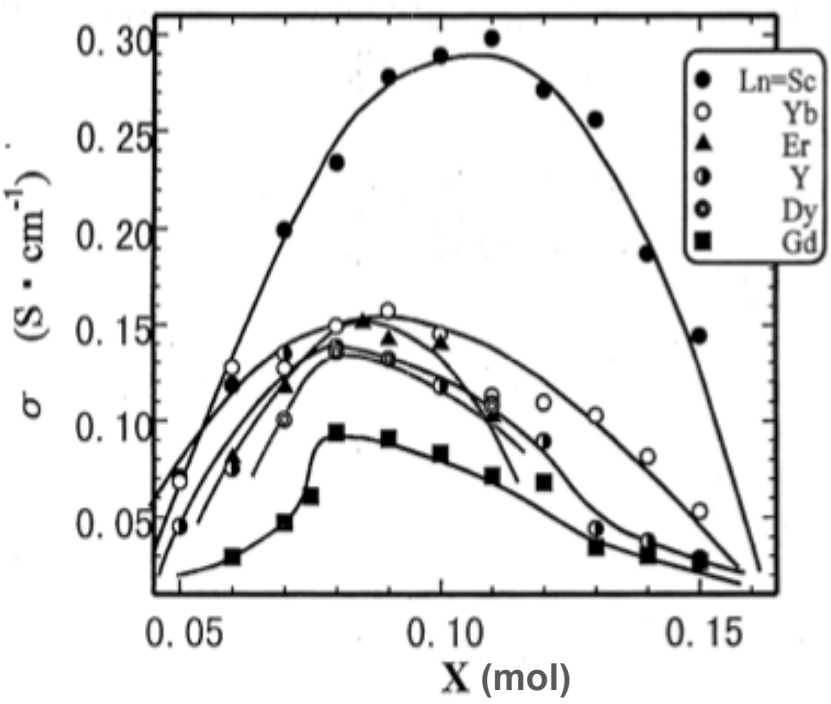

Figure 2-1: Conductivity for the ZrO_2 system as a function of L_2O_3 dopant and L_2O_3 dopant concentration for $(ZrO_2)_{1-x}$ $(Ln_2O_3)_x$ [10]

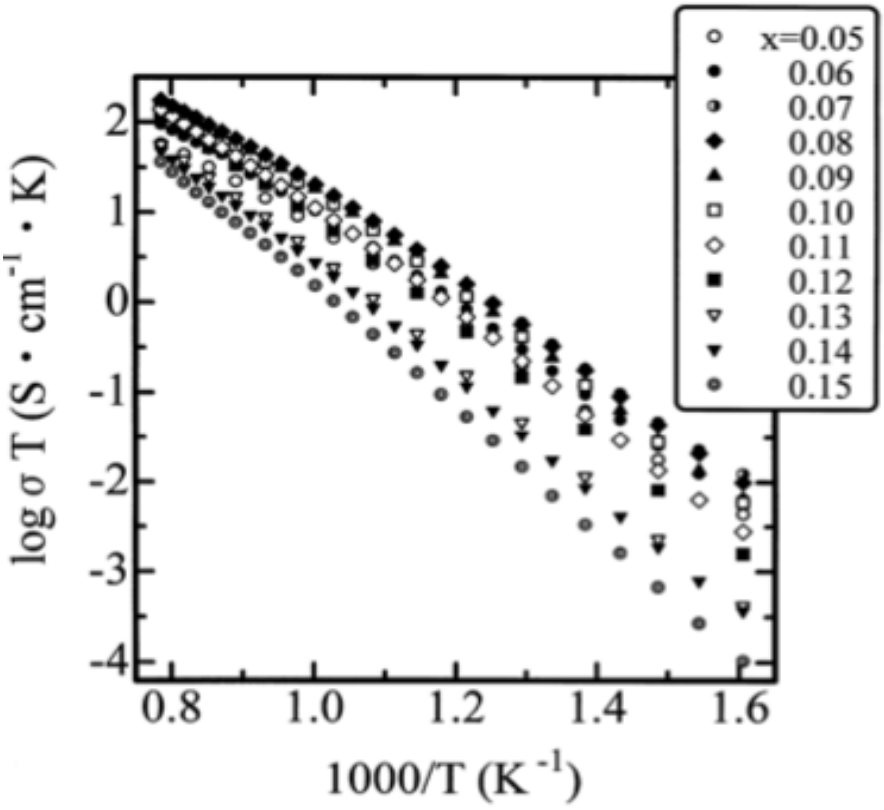

Figure 2-2: Temperature dependence of the conductivity for $(ZrO_2)_{1-x}$ $(Y_2O_3)_x$ [10]

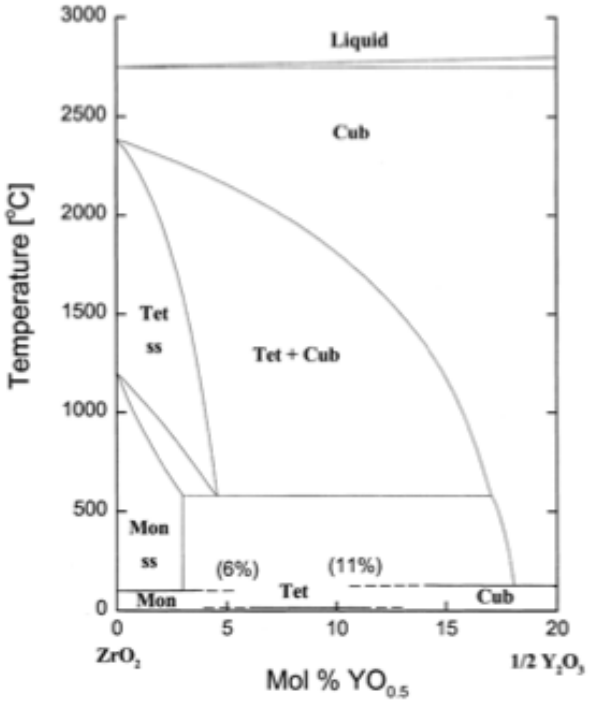

Figure 2-3: Phase diagram of the Y_2O_3-ZrO_2 system [11]

and 1170°C with the two-phase mixture extending into lower temperature regimes as Y_2O_3 dopant levels increase. The phase composition within the 75 - 500°C range and between 2 and 6 mol% Y_2O_3 and 11 and 17 mol% Y_2O_3, is a mixture of monoclinic and cubic phases with tetragonal phase stabilised between 0 - 75°C for these compositions. The tetragonal to cubic phase transition state (t → cZrO_2) for undoped ZrO_2 occurs at 2370°C with the stabilisation of the cubic phase until 2700°C where the liquid phase exists at temperatures above 2700°C.

8YSZ stabilises the higher temperature cubic and tetraganol phases to lower temperatures where a mixture of tetraganol and cubic phases exist between 600°C and 2000°C with a two phase monoclinic and cubic mixture between 75°C and 500°C; 8YSZ is tetraganol at room temperature. And though the phase diagram indicates two-phase cubic mixtures for 8YSZ above 75°C, the cubic phase remains dominant [8] in both regions. Stabilisation of the cubic phase is ideal for YSZ when used in SOFCs as the monoclinic phase of undoped ZrO_2 has very poor conductivity, and the m → t-ZrO_2 transition which occurs at temperatures commonly used during SOFC processing introduces stresses that can lead to cracks and mechanical failure due to the volume changes that accompany the phase transformations [8]. Such transformations could also introduce instability as the two-phase region may have adverse effects on other SOFC components compromising system properties and the overall cell structure. Tetragonal

phase ZrO_2 achieved at lower Y_2O_3 levels is advantageous as increased strength and toughness has been reported [15], [16] but this occurs at the expense of other material properties such as conductivity [17]. Thus, 8 mol% Y_2O_3, the dopant concentration where the maximum conductivity for Y_2O_3 stabilised ZrO_2 is reached, is considered the ideal electrolyte material for SOFCs.

2.1.2 Ni-8YSZ Anode

The state of the art Ni-YSZ anode is the standard anode material due to its low cost and excellent fulfilment of the fuel electrode requirements. Ni is a very good catalyst for the electrochemical oxidation of hydrogen, is low in cost and has good electronic conductivity [18], [19]. The fuel electrode must be durable and physically and chemically stable in cell reducing environments, possess a stable and porous microstructure necessary for the transport of reactants to the reaction sites, high electronic conductivity and in in the case of hydrocarbon fuels, be tolerant to sulphur impurities and reluctant to form solid carbon [1], [18]. Because SOFCs are subjected to operation at elevated temperatures for long times chemical stability and structural integrity are required. Thermal cycling between room temperature and operation temperature similar to a start-up/shut-down procedure along with RedOx cycling where there exists an interruption in the fuel flow similar to an immediate shut down procedure, can have deleterious effects on the SOFC leading to cell degradation and compromised performance or even cell failure [20]–[23]. Lessening the impact of thermal cycling and re-oxidation on the cell component characteristics is essential to achieving a stable and durable SOFC.

The manufacture of Ni-YSZ anodes typically involves the mixing of NiO and YSZ powders instead of Ni metal powders as Ni metal melts at temperatures commonly used for ceramic processing [24]. Since NiO does not form solid solutions with YSZ, the NiO-YSZ composite gets reduced to a Ni-YSZ ceramic-metal (cermet) during cell reduction. This leads to a more porous Ni-YSZ microstructure post reduction due to the volume change associated with the loss of oxygen during the NiO to Ni conversion. And as the thermal expansion coefficient (TEC) of Ni is 1.69×10^{-5} K^{-1} and the TEC of 8YSZ is 1.05×10^{-5} K^{-1} [25], this TEC mismatch coupled with NiO to Ni volume changes during redox cycles can create thermal stresses that result in cell component delamination and cracking during operation. The addition of the YSZ phase in the anode adjusts the TEC for a better match with the electrolyte reducing these stresses, further improving anode-electrolyte adhesion and creating a penetrating and connecting Ni-YSZ framework for ionic and electronic transport as outlined by percolation theory [4], [14], [26]. The addition of YSZ in the anode also offers mechanical strength properties, prevents the sintering of the Ni particles and contributes to the ionic conductivity property of

of the anode [14].

Anode microstructure influences physical properties, impacts cell performance and is strongly dependent on the powder processing method. Figure 2-4 is a schematic which shows the triple phase boundary (TPB) region within a Ni-YSZ anode - the point at which the gas molecules from the fuel feed, oxygen ions from the electrolyte and electrons released to the external circuit intersect and become the active site for the electrochemical reactions. It is essential that continuous contact between the pore, Ni and YSZ phases occur since isolated particles do not contribute to the TPB and therefore cannot make any contributions to the cell performance. Also, increasing the TPB length creates more active sites to participate in the reaction. A carefully controlled anode microstructure obtained with choice materials and fabricated using optimal processing conditions aids in the development of a stable, high efficiency cell with demonstrated performance over extended lifetimes.

2.1.3 LSM-YSZ Cathode

Doped lanthanum manganite ($LaMnO_3$) is a p-type conductor and is the most widely used cathode material in SOFCs due to its high performance and stability in oxidising environments at temperatures of 800-1000^{o}C. Because cathodes operate in oxygen-rich environments, material selection is challenging as base metals cannot be used due to corrosion and noble metals, though corrosion resistant, are too expensive which limits material selection to semi-conductors [4]. The cathode must possess sufficient porosity to facilitate air transport to the reaction sites, be catalytically active for the oxygen reduction reaction, and have high ionic and electronic conductivity to transport electrons and O^{2-} ions produced from the O_2 reduction reaction, maintain chemical and mechanical stability in oxidising environments as well as exhibit stability during thermal cycles [1]. Researchers report LSM-YSZ cathode porosities between 31-34% are suitable for use in SOFCs [28]. Stability with the electrolyte, which is in direct contact with the cathode, is also required.

10-20 mol% Sr-doped $LaMnO_3$ has a good (TEC) match with the standard SOFC electrolyte, Yttria-Stabilised Zirconia (YSZ), and exhibits good ionic and electronic conductivity at higher SOFC operating temperatures of 1000^{o}C which makes it a suitable cathode material that satisfies the component requirements [4]. At operating temperatures of 800^{o}C, the LSM cathode polarisation increases drastically due to poor ionic conductivity so to minimise these resistances LSM is typically mixed with YSZ in a 50:50 wt% ratio to increase ionic conductivity [1]. The addition of YSZ further improves the TEC match with the electrolyte and increases the number of reaction pathways so that a breakdown in the

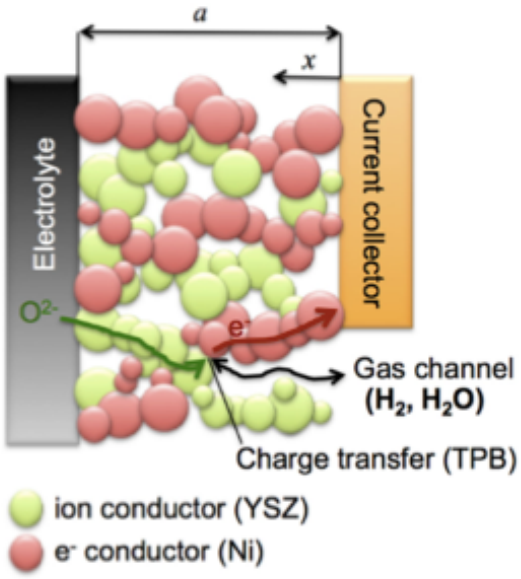

Figure 2-4: The TPB region (point of intersection for O^{2-}, e^- and H_2) where anode electrochemical reactions occur in a Ni-YSZ cermet [27]

reaction process is avoided [29]. Thus, LSM-YSZ is the traditionally used cathode material for SOFCs.

2.2 SOFC MANUFACTURING TECHNOLOGIES

There are a variety of different cell processing techniques used for the fabrication of SOFCs. The fabrication methods listed below are grouped in either one of two categories: mechanical support manufacture or thick film deposition. The cell manufacturing approach is often dictated by the design approach and desired properties of the electrolyte [30] which in recent years has been in the form of a thin film. Screen-printing and tape casting are industry accepted, widely used methods for large scale production of SOFCs with screen-printing being the selected processing technique in this work. To the best of the author's knowledge, no results regarding screen-printed 10Sc1CeSZ electrolyte layers on die pressed Ni-10Sc1CeSZ anode supports has been published which serves as the novelty of this research. Thus, a more detailed explanation about uniaxial pressing and the screen-printing process is provided.

2.2.1 Mechanical Support Manufacture

2.2.1.1 Uniaxial and Isostatic Pressing

Die pressing is a technique used to compact powder into a desired green body shape of a given dimension. For anode supported SOFCs of thicknesses > 0.8 mm, anode supports are typically produced by die pressing [31]. This is because tape casting, the most widely used manufacturing technology for

SOFCs, requires too much drying time for thick (> 0.8 mm) anode supports [31]. In this work, uniaxial "double-action" die pressing was used to fabricate the porous anode support structures.

Powder compaction via pressing can occur by two means: uniaxial pressing or isostatic pressing. Uniaxial pressing applies pressure to powder in a pressing die along a single axis, followed by the ejection of the compact. Single-action uniaxial compaction occurs when the compaction pressure is applied in only one direction while double-action uniaxial compaction occurs when the pressing force is applied in opposing directions [32]. A schematic of single-action vs double-action uniaxial pressing is shown in Figure 2-5. Single-action pressing creates pressure gradients as pressure is only exerted onto the compact by the "top punch" while double-action exerts pressure onto the compact simultaneously by both the top and bottom punches. This serves to create a more balanced pressure distribution to minimise density variations in the green body [33]. And for sample geometries where the height-to-diameter ratio $\left(\frac{z}{D}\right)$ approaches zero, the pressure gradients are even further reduced [34]. This relationship has been defined by Janssen which considers both single-action and double-action compaction [35] and is written in Equation 2.1 where:

$$P_{z=} P_o exp\left(\frac{4\mu\alpha}{D} z\right) \qquad (2.1)$$

P_z is the pressure at any depth in the compact, P_o is the applied pressure, μ is the die wall friction, α is a factor related to the bulk properties of the powder, D is the compact diameter and z is the compact height. When μ is zero, the applied pressure is equal to the pressure at any depth in the compact but as die wall friction increases, the pressure in the compact decreases exponentially with increasing compact depth. And samples with higher $\frac{z}{D}$ ratios see less applied pressure transmitted into the depths of the compact than samples with low $\frac{z}{D}$ ratios that see fewer pressure variations within the compact. The $\frac{z}{D}$ ratio of samples used in this work is 0.04.

Pressure gradients lead to density gradients, which can create stresses and cracks in the compact during sintering as different densification rates occur at different locations throughout the sample [36].

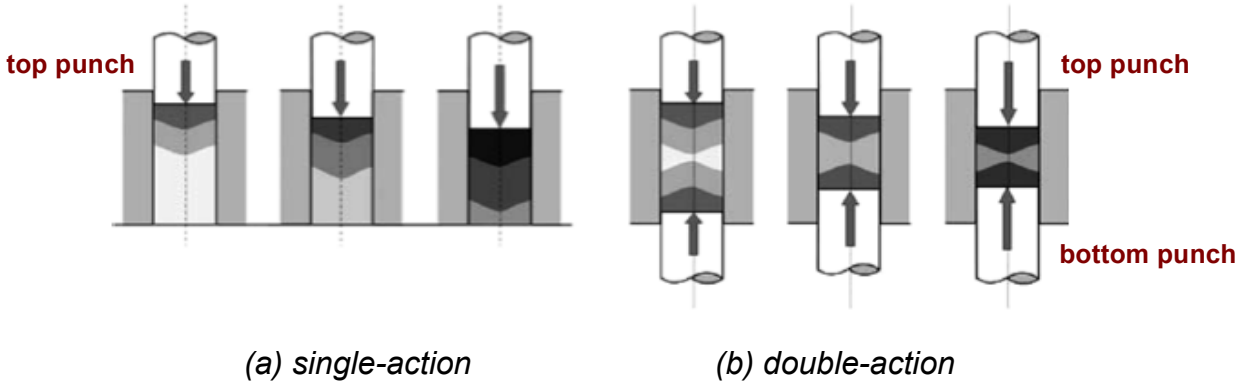

Figure 2-5: Single action and double action uniaxial pressing [33]

And though double-action pressing reduces pressure gradients when compared to single-action pressing, non-uniform densification can still occur during double-action pressing. Friction between the die wall and the powder, incorrect die filling and powder properties such as the presence of agglomerates are all problem sources [33]. Ultimately there are limitations associated with uniaxial pressing that can be overcome with isostatic pressing.

Isostatic pressing involves the application of pressure to a sample in a variety of directions creating equal pressure distribution. This in turn produces a more uniformly dense compact. Isostatic pressing occurs when the sample powder is sealed into a moulding bag and submerged in a liquid - typically glycerine, oils or water - at pressures upward of 400 MPa [33], which compacts the powder, giving it its shape. Upon release of the pressure, the bag is opened and the sample can be removed. This is also advantageous as problems created during the ejection process with uniaxial pressing such as die wall-sample friction and sample expansion during ejection are avoided. And with isostatic pressing, multiple samples can be pressed simultaneously as determined by the size of the moulding bag making it a reliable mass production process.

2.2.1.2 Tape Casting

Tape casting is a conventional ceramic processing route and is the most commonly used manufacturing technique for SOFCs. Tape casting creates "tapes" of a planar shape and has been used for the fabrication of both anode and electrolyte supported SOFCs where the planar approach is best supported by the anode or electrolyte as these components yield the best mechanical stability [37]. Tape casting is the method of choice because membrane thicknesses as low as 100 μm can be obtained [37]

and it is a reproducible, cost-effective method with large scale production possibilities [14]. The slurry, containing the ceramic powder in a given composition along with additives, is fed into the chamber of the tape caster and is flattened onto the surface of a polymer tape by a doctor blade. The doctor blade height and slurry viscosity can be tweaked to yield tapes with the desired thicknesses. The tape is then dried, cut and sintered. For multi-layered SOFCs, subsequent components are cast onto the initial supporting tape and then dried and co-fired. The superior surface quality achievable with tape casted membranes helps to prepare high quality multilayers as a smooth, defect free surface, as is the case when depositing thin electrolytes, aids in the production of dense, leak tight films.

2.2.1.3 Tape Calendaring

Tape calendaring is the process by which planar tapes are produced as a result of mixing a ceramic slurry until it forms a plastic sheet and squeezing this sheet between two rollers until the target membrane thickness is achieved [30]. As is the case with tape casting, the sheet is cut into the desired cell area, dried and fired. Layering separately calendared plastic sheets and simultaneously passing them through rollers in a subsequent rolling step can produce a multi-layered tape. Combining tapes produced via tape casting with those produced via tape calendaring is also viable. Normally, the combined multi-layers are of similar thicknesses as the organic additives present in the slurries are the glue which binds the layers together [31] . Combining thin substrates (<0.5 mm) with thick films (>20 μm) instead of thick substrates (>1.5 mm) with thin films (<20 μm) is a common approach. This ensures good adhesion between the layers. The thickness of tape calendared membranes can reach up to 2 mm [31].

2.2.1.4 Extrusion

Extrusion is a ceramic processing method used to prepare membranes with a variety of different geometries. Tubes, which have been used in the cathode supported design approach commercialised by Siemens [38], were manufactured via extrusion. Ceramic powders are added to a water/polymer base and the mixture is poured into a single open-ended die where an inner rod is used to push the slurry through the tube resulting in the desired shape. The tube is then cut into the appropriate dimensions. The other SOFC components are layered onto the supporting structure using spray coating, dip coating, painting, electrophoretic coating or plasma spraying [37], [39], then dried and sintered accordingly.

2.2.2 Thick Film Deposition

2.2.2.1 Screen-Printing

Screen-printing is a film deposition technique commonly used for the fabrication of SOFC electrolytes [40], [41] although SOFC electrodes have been applied using this technique [42], [43]. Screen-printing inks typically consist of a polymer "vehicle" which serves as a carrier for the powders, solvent, binder, and dispersant. The powder and vehicle are combined in the appropriate ratios to achieve the desired ink properties. Factors such as print speed, the number of print passes, screen mesh count and printer snap-off settings can all be modified to control the printing process while parameters such as powder particle size, powder dispersion and powder packing influence ink rheology [42]. During printing, the ink is forced through the mesh openings of the screen by a rubber squeegee forming a film that adheres to the support structure due to the organic materials in the ink, which give it its "sticky properties".

The squeegee shears the ink from the screen so the flow properties of the ink are crucial for enabling the paste to fill the cavities allowing an easy release of the screen from the substrate surface resulting in good quality prints. This is illustrated in Figure 2-6. The screen-printed inks are dried and then fired to the target temperatures for dense layer sintering. The wet layer thickness is usually 3-4 times greater than the dried layer thickness and the dried layer thickness is usually 1.5-2 times greater than the sintered layer thickness [31]. Solvents and organics evaporate and burn off causing a reduction in layer thickness. Fired layer thicknesses can range from 5-100 μm depending on the printing and ink parameters [31]. In this work, SOFC anode and electrolyte component layers were deposited using screen-printing.

2.2.2.2 Vapour Deposition (PVD, CVD)

Physical Vapour Deposition, commonly referred to as *PVD*, is used to classify Sputtering and Electron Beam Deposition (EB-PVD) techniques as the material transport method for both occurs in the vapour phase without any chemical changes to the material. During EB-PVD, the heated target material is exposed to a high-energy beam while under vacuum which produces atoms of the target material in the gas phase that condense onto the substrate surface until the desired thickness is obtained. In the case of sputtering, the target is typically exposed to an inert gas while under vacuum which releases vaporised atoms that then coat the substrate. Coatings with thicknesses as small as 1-3 μm for both EB-PVD and sputtering can be achieved [30]. For sputtering, the substrate receives material from multiple areas of the

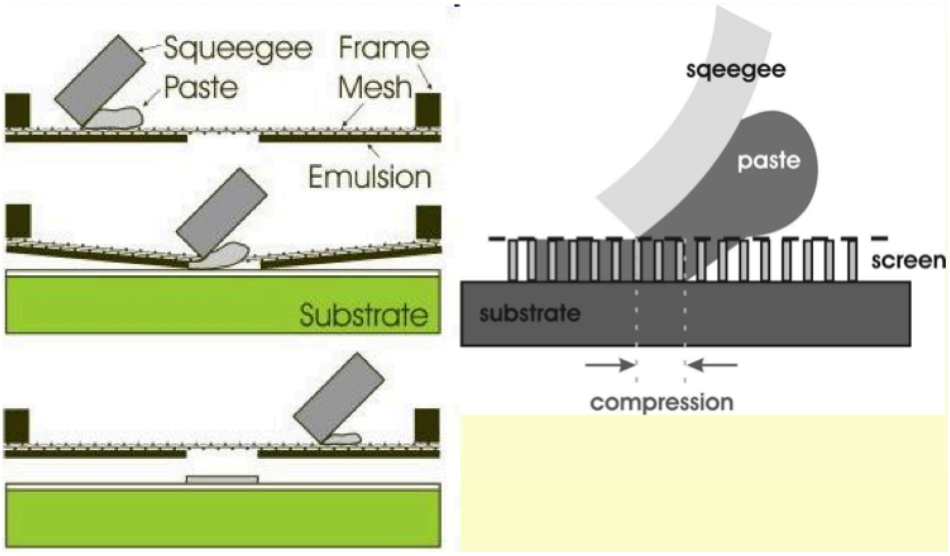

Figure 2-6: Illustration of the screen printing process on a planar substrate [44]

target leading to better coverage while the substrate coverage during EB-PVD is relegated to the direction of the electron beam hitting the target. Conversely, the slow deposition rate associated with sputtering is one of its major limitations [14], [31]. Chemical Vapour Deposition or *CVD* is very similar to PVD in that coatings are deposited onto substrates in the gas phase except during CVD a chemical reaction takes place, facilitated by the use of precursors, on or near the heated substrate resulting in the desired material deposited onto the substrate surface [45]. Though CVD produces film thicknesses of ~5 μm, the expensive cost, high operating temperature and CVD reaction by-products cannot be reconciled [14].

2.2.2.3 Spray Coating

Spray coating can produce film thicknesses in the range of 5-10 μm [30] and involves material deposition by spraying the heated substrate with the powder based solution. Non-homogenous coverage is cause for concern during spray coating, as the spray stream must be properly positioned to ensure even material distribution across the substrate surface. Variables such as spray gun distance, substrate position and even slurry fluidity can aid in improving layer uniformity.

2.2.2.4 Vacuum Slip Casting

During vacuum slip casting, the powder slurry is applied onto the membrane surface after which the sample is placed under vacuum allowing the solvent to be removed leaving solid material on the substrate surface. It is important that the substrate contains sufficient porosity to draw off the excess

liquid allowing for an even homogenous layer to sediment onto the sample surface [31]. The sample is then dried and sintered with layer thicknesses of 1-20 μm achievable.

2.2.2.5 Dip Coating/Spin Coating (Sol-Gel)

Dip and spin coating techniques can make use of powder slurries or sol-gel mediums that contain the powder composition of the material to be deposited in solution that ultimately transforms into a "gel" [46]. The precursor materials used to formulate the gel, typically nitrates or alkoxides, are converted to the desired oxide during heat treatment after coating [4], [14], [31] . The sol-gel mixture is then used to dip or spin coat the substrate to form a film, which is then dried to remove the liquid and sintered to form the dense ceramic [14], [31], [46]. Layer thicknesses of dip and spin coated samples using powder slurries is between 2-10 μm [31] and from 10 nm to 2 μm using sol-gel mixtures [30], [31].

2.3 HYDROCARBON USE IN SOFCs

As stated earlier, SOFC use is closely associated with hydrogen as the primary fuel source due to its high purity and high performance yields under cell operating conditions. But what sets SOFCs apart from other fuel cells is their ability to operate on any fuel that can be reformed to produce hydrogen or oxidised to generate electric current. The main drawback is the formation of carbon when using traditional Ni-based anodes under hydrocarbon fuel operation, which has deleterious effects on cell properties and performance [19], [47], [48]. To maintain the fuel flexibility advantage of SOFCs without sacrificing performance, near term goals call for solid oxide fuel cells that can operate efficiently on natural gas and liquid hydrocarbon fuels.

2.3.1 Hydrocarbon Conversion

The ability of SOFCs to operate on a variety of hydrocarbon fuels allows for the immediate use of existing resources and creates a wider range of fuels that can be considered for SOFC operation. In this section, the discussion of hydrocarbon use will centre around CH_4, the most (stable and) simple hydrocarbon that can be reformed within the cell, a process commonly referred to as internal reforming, and the distinction between indirect utilisation of methane (steam reforming, dry reforming, partial oxidation) and direct utilisation of methane (oxidation of methane) is duly noted.

For the case of CH_4, H_2 can be produced via internal steam or dry reforming and are indicated by Equations 2.2 and 2.3 respectively, where the change in enthalpy indicates highly endothermic reactions for both processes [4]:

steam reforming: $CH_4 + H_2O \rightarrow 3H_2 + CO \quad \Delta H^o_{298K} = 206 \frac{kJ}{mol}$ (2.2)

dry reforming: $CH_4 + CO_2 \rightarrow 2CO + 2H_2 \quad \Delta H^o_{298K} = 247 \frac{kJ}{mol}$ (2.3)

Water vapour and CO_2 comprise the exhaust gases at the anode and with either acting as the oxidant during the electrochemical oxidation of methane both can be re-circulated back into the cell enabling the steam reforming or dry reforming reactions to occur. Alternatively, co-fed steam can be introduced into the fuel stream as part of the steam reforming process. Partial oxidation is the other indirect methane utilisation method where air or oxygen is used as the oxidant to reform the fuel. In the reaction seen in Equation 2.4, oxidation does not proceed to completion, but only partially occurs in the presence of an oxidant and is slightly exothermic while complete oxidation assumes full methane reaction and is shown in Equation 2.5 [4]:

partial oxidation: $CH_4 + \frac{1}{2}O_2 \rightarrow 2H_2 + CO \qquad \Delta H^o_{298K} = -35 \frac{kJ}{mol}$ (2.4)

complete oxidation: $CH_4 + 2O_2 \rightarrow CO_2 + 2H_2O \quad \Delta H^o_{298K} = -890 \frac{kJ}{mol}$ (2.5)

In each of the three processes, 2.2 – 2.4, CH_4 is converted into a mixture of H_2 and CO (syngas), a more usable fuel species for the facilitation of the electrochemical oxidation reactions occurring at the fuel electrode. It is critical to note that generalisations regarding the reaction pathways for hydrocarbon conversion cannot be made as these reaction steps are heavily dependent on anode composition, fuel source and cell testing environment. Lastly, the CO produced by the steam reforming and partial oxidation reactions can recover additional hydrogen depending on the steam content and operating temperature. When this occurs this is referred to as the water-gas shift reaction (WGS) [4], [49]. The WGS is also slightly exothermic and only occurs in the presence of steam so it can take place either alongside or immediately after reactions 2.2 and 2.4:

water gas shift (WGS): $CO + H_2O \rightarrow CO_2 + H_2 \quad \Delta H^o_{298K} = -41 \frac{kJ}{mol}$ (2.6)

Internal steam reforming is a commonly used, well-established self-sustaining process for hydrocarbon conversion that simplifies system design, reduces cost and increases system efficiency [50]. And whilst steam reforming has proven successful, a proper balance between temperatures, fuel/steam ratios, anode composition and system pressure is necessary to achieve good fuel conversion efficiencies and satisfactory power densities under stable operation. For instance, Wang found that high steam/carbon ratios tend to form carbon on Ni-CeO_2 anodes when operating on butane further

emphasising the need to map testing regions where carbon formation is less likely [51]. Indeed, though recycling waste heat and steam to drive the steam reforming reactions has proven advantageous, the internal steam reforming process alone introduces new challenges – high gradients in temperature distributions, thermo-mechanical stresses, uneven temperature distributions creating "cold spots" in the cell, local thermally activated cell degradation and water saturation at the anode - that cannot be ignored. The demands placed on the system also place stringent requirements on the fuel cell components and narrow material choices. Mitigating the challenges associated with steam reforming requires a combination of several different approaches that can produce high fuel conversion yields with minimal detriment to the cell operating system.

2.3.2 Direct Hydrocarbon Utilisation

Direct methane utilisation also known as dry reforming, in theory is the simplest most highly efficient approach to SOFC operation on hydrocarbon fuels. Dry reforming does not require co-fed steam or liberal amounts of by product steam recycled into the cell – the fuel conversion process occurs directly on the anode. In this thesis we open up the meaning of direct hydrocarbon utilisation to preclude steam reforming at start-up but to include low amounts of anode re-circulated steam.

Traditional SOFCs use Ni-YSZ anodes which are by far the best electrocatalysts under H_2 operation but in the presence of hydrocarbon fuels the functionality of Ni-YSZ can degrade severely if unfavourable operating conditions lead to carbon deposition [52]. Coking can occur with the presence of Ni in the anode or also in the gas phase via the methane pyrolysis or the Boudouard reaction, phenomena discussed previously in Chapter 1, Section 1.3.1.1. It has been reported that carbon deposition by means of fuel decomposition most likely occurs at the fuel inlet where there is an abundance of C-H and that higher hydrocarbons have a greater tendency to decompose and form carbon in the gas phase than does CH_4 [53], [54]. The type of carbon formed is controlled by the dominant reaction mechanism type which is heavily influenced by temperature [48]. The C-H-O- triangle in Figure 2-7 shows the regions of coke formation as a function of temperature and C-H-O- ratio [55].

As McIntosh explains [48], graphitic carbon formed by Ni catalysis is chemically different from carbon formed by fuel decomposition. The former tends to dissolve into the anode bulk while the latter aggregates on the surface and can easily be whisked away with steam. Low steam concentrations can remove carbon deposits and prevent anode oxidation whilst high concentrations of pressurised steam across the anode for extended periods can cause further anode sintering and a weakening of the anode structure [56]. The ideal way to minimise anode deterioration is to formulate alternative anodes that are

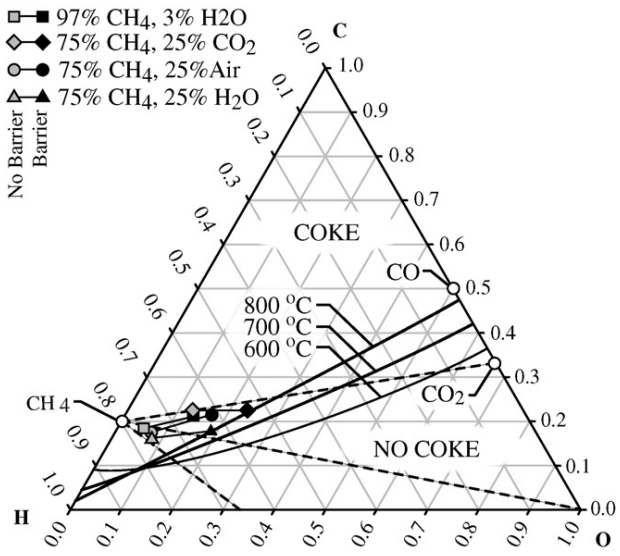

Figure 2-7: Gibbs triangle showing regions of coke formation as a function of temperature and C-H-O ratio [55]

poor catalysts for carbon formation, remove carbon and/or suppress carbon deposition altogether and can utilise the hydrocarbon fuel directly.

Extensive research on the use of either doped Ni-CeO_2 or alloyed Ni-YSZ anodes on both dry and wet hydrocarbons or under steam reforming conditions is still on-going [57]–[59] and a discussion of the results by a few research groups heavily involved in this work has been previously mentioned in the introduction section of this thesis. To our knowledge minimal work has been done on the use of alternative anodes based on a ScSZ structure for either hydrogen or methane utilisation. A review of the literature for research within the last ten years on the fabrication of doped ScSZ anodes operating on methane will be highlighted in Chapter 2, Section 2.5.3.

2.4 ZIRCONIA ELECTROLYTE SYSTEMS

2.4.1 The Ageing of Zirconia Electrolytes

As discussed at the opening of the chapter, since ZrO_2 in its pure form is a poor oxygen ion conductor, oxide dopants are introduced into the ZrO_2 lattice to improve the conductivity via increased oxygen vacancy concentration and enhanced oxygen-ion mobility [8]. Commonly used dopants Sc_2O_3, CaO, MgO, Y_2O_3 are highly soluble in ZrO_2 and because they all have a lower valence than Zr^{+4}, create oxygen vacancies in the host lattice. These dopants stabilise the cubic ZrO_2 phase to lower temperatures preventing phase transformations and ensuring stable conductivities over a wide range of O_2 partial pressures.

Long term testing of cubic stabilised zirconia under cell operating conditions, both Y_2O_3-ZrO_2 and Sc_2O_3-ZrO_2 systems between 8-9 mol%, show ageing and degradation effects in the material properties at elevated temperatures [8], [60]–[62]. Though 8 mol% Y_2O_3-ZrO_2 (8YSZ) is considered fully cubic stabilised zirconia, it actually lay in the cubic-tetraganol two-phase region [8], [11] which implies that this composition is actually a higher conducting metastable tetraganol rich (*t'*) phase [63]. Upon heating for extended times at 1000°C, the tetraganol rich phase (*t'*) breaks down into both cubic rich and tetraganol deficient phases (t) with lower conducting (t) phase precipitates building up over time deteriorating system conductivity [60], [64]; below 700°C no degradation is observed [8]. For 8 mol% stabilised Sc_2O_3-ZrO_2, the magnitude of the conductivity decrease during heating at 1000°C for extended time is higher than stabilised Y_2O_3-ZrO_2 [5] with minimal conductivity changes observed in the Y_2O_3-ZrO_2 system with Y_2O_3 dopant levels between 9-15 mol% [8]. Sc_2O_3-ZrO_2 with dopant levels between 10-11 mol% Sc_2O_3 [65], 9-11 mol% Sc_2O_3 [9], 11-13 mol% Sc_2O_3 [66] and at 11 mol% Sc_2O_3 [67] exhibit stable behaviour with either no reported losses in conductivity for extended times at 1000°C [65], [66] or very low degradation with minimal conductivity changes for extended time at 1000°C [9], [67]. These findings justify the need for alternative electrolyte materials with enhanced properties that demonstrate improved stability at ideally lower temperatures so that these problems may be avoided. Developing electrolytes based on a Sc_2O_3-ZrO_2 structure within the 10-13 mol% composition range provides a viable, alternate processing route for SOFCs .

2.4.2 Scandia Stabilised Zirconia as an SOFC Electrolyte

Sc_2O_3-ZrO_2 systems exhibit superior conductivity properties to Y_2O_3-ZrO_2 systems with even better conductivity and stability in lower temperature regimes. Scandia stabilised zirconia is considered a promising alternative to the traditional 8YSZ electrolyte due to the higher conductivity values of 0.38 S cm^{-1} and 0.159 S cm^{-1} at 1000°C and 800°C respectively for the 8 mol% Sc_2O_3-ZrO_2 composition [67] . In comparison, the 8 mol% Y_2O_3-ZrO_2 system has lower conductivity values of 0.1 S cm^{-1} and 0.03 S cm^{-1} respectively at these same temperatures [68]. The observed increase in conductivity for the Sc_2O_3-ZrO_2 system is due to the smaller dopant radius of the Sc^{3+} ion (0.87 Å) matching more closely with the radius of the Zr^{4+} host ion (0.84 Å) [68] making O^{2-} vacancy migration easier [68]. The 8 mol% Sc_2O_3-ZrO_2 composition has been referenced for the sake of direct comparisons between the conductivities of the Sc_2O_3-ZrO_2 and the Y_2O_3-ZrO_2 systems but unlike 8YSZ which exhibits the highest conductivity at the lowest dopant concentration required to stabilise the cubic phase, Sc_2O_3-ZrO_2 shows maximum conductivity at 10 mol% Sc_2O_3 though cubic phase stabilisation in Sc_2O_3-ZrO_2 is initially observed at 7.5 mol% Sc_2O_3 at 800°C extending through to 22 mol% Sc_2O_3 at 1200°C as seen in the Sc_2O_3-ZrO_2 phase

diagram pictured in Figure 2-8. Literature reveals discrepancies in the phase equilibria of the scandia-yttria system as outlined in numerous studies [69]–[71] but for the purposes of this work, since it has been adequately referenced by previous researchers, the phase diagram as proposed by Spiridonov will be used. Providing an alternative to the current SOFC system through the use of Sc_2O_3-ZrO_2, offers improved system properties and an option for lower temperature operation. The high cost and scarcity of scandia was a hindrance in years past but currently this is no longer an issue, thus, the advantages gained from the use of SOFCs based on a scandia structure continue to keep this class material an attractive option.

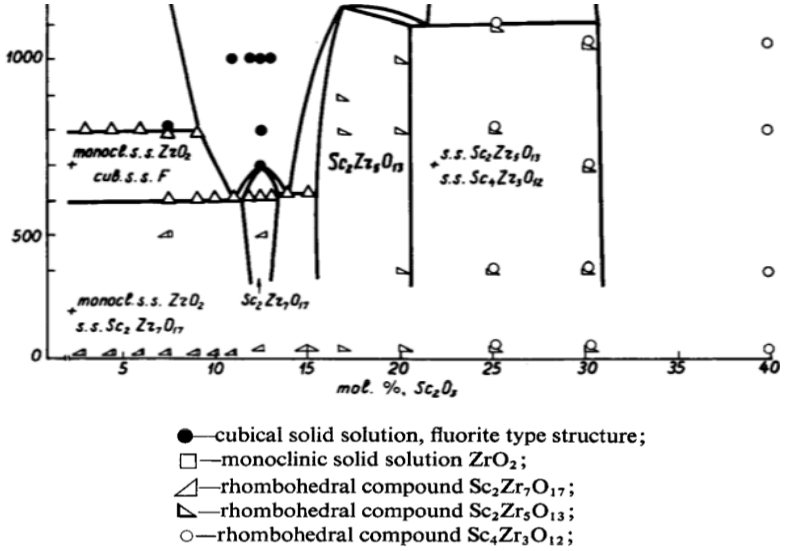

Figure 2-8: Phase diagram of the Sc_2O_3-ZrO_2 system [72]

As discussed in Chapter 1, the demands of high temperature SOFC operation (850 – 1000°C), introduces new challenges such as limited material choices, stack sealing problems, mechanical stress and cell performance degradation which has focused efforts towards the development of intermediate temperature SOFCs (IT-SOFCs, 700 – 850°C) [73]–[76]. The use of an alternative electrolyte with enhanced conductivity properties, as is the case with the Sc_2O_3-ZrO_2 system, could allow for a reduction in operating temperature providing an overall reduction in cell resistance due to the higher conductivity, minimise sealing problems, extend cell lifetimes and mitigate the technical challenges associated with high temperature operation [5], [77], [78]. 10 mol% Scandia (Sc_2O_3) Stabilized Zirconia (10Sc1CeSZ) with 1 mol% Ce addition is the ideal electrolyte composition for IT- SOFCs because the higher conducting cubic phase is dominant at 800°C though the existence of a mixed cubic/rhombohedral (β) phase at this composition [68], [70] with the (β) phase transforming to cubic phase at 1000°C [68] has

been reported.

At even lower temperatures (< 800°C) the cubic phase becomes less stable causing conductivity decreases brought about by the transformation from the higher conducting cubic phase to the lower conducting rhombohedral phase (β) [9], [79], [80]. Small additions of metal oxides, to ScSZ have been shown to suppress this phase transformation stabilising the cubic phase at lower temperatures [68], [79], [81], [82]. CeO_2 as a co-dopant stabilises the cubic phase, although slight changes in conductivity can be seen at 650°C where rhombohedral phase transitions occur [77], [83]. Ceria also acts as an oxidation catalyst promoting the electrochemical oxidation of methane while exhibiting a high resistance to carbon deposition, added benefits to the use of this material, such that hydrocarbon fuel operation remains a viable option [84]–[88]. Despite the absence of defined phase boundaries, the mixed cubic-rhombohedral phase at intermediate temperatures, the rhombohedral phase transition at low temperatures and the slight increase in cost over Y_2O_3-ZrO_2, the use of Sc_2O_3-ZrO_2 is still advantageous and remains of primary interest for use in IT- SOFCs. As mentioned above, the enhanced conductivity and stable properties of 10 mol% Scandia (Sc_2O_3) Stabilized Zirconia (10Sc1CeSZ) with 1 mol% Ce addition make it the material of choice that will be further explored in this thesis. More work is on-going to understand the complexity of the Sc_2O_3-ZrO_2 system to produce phase pure, homogeneous samples well suited for optimal performance under SOFC operating conditions.

2.4.3 The Application of Scandia Stabilised Zirconia as an Electrolyte in an SOFC

A downward shift in the operating temperature of conventional SOFCs requires the use of better performing electrolyte materials. As discussed previously, Sc_2O_3-ZrO_2 has proven to be an ideal candidate for IT-SOFC electrolytes and with more research aimed at achieving phase equilibrium in the Scandia-Zirconia system, manufacturing SOFCs that exhibit good and stable performance built on a Sc_2O_3-ZrO_2 structure is achievable. Researchers have explored the suitability of an SOFC based on a stabilised Sc_2O_3-ZrO_2 electrolyte by performing cell tests using this material [67], [89]–[96]. Other groups have researched the properties of thin film stabilised Sc_2O_3-ZrO_2 electrolytes prepared using electron beam technique and determined its appropriateness as an electrolyte [97]–[100].

Regarding the use of electron beam deposition to prepare the Sc_2O_3-ZrO_2 electrolyte films, researchers have used a 10 mol% Sc_2O_3 electrolyte composition deposited onto either SiO_2 [98], [99] or Ni-ZrO_2 [97], [98], [100] substrates. Andrzejczuk et al. reported [100] dense ScSZ electrolyte films, with relatively high leakage rates initially – $7x10^{-4}$ mbar 1 cm^{-2} s^{-1} that were shown to improve after annealing

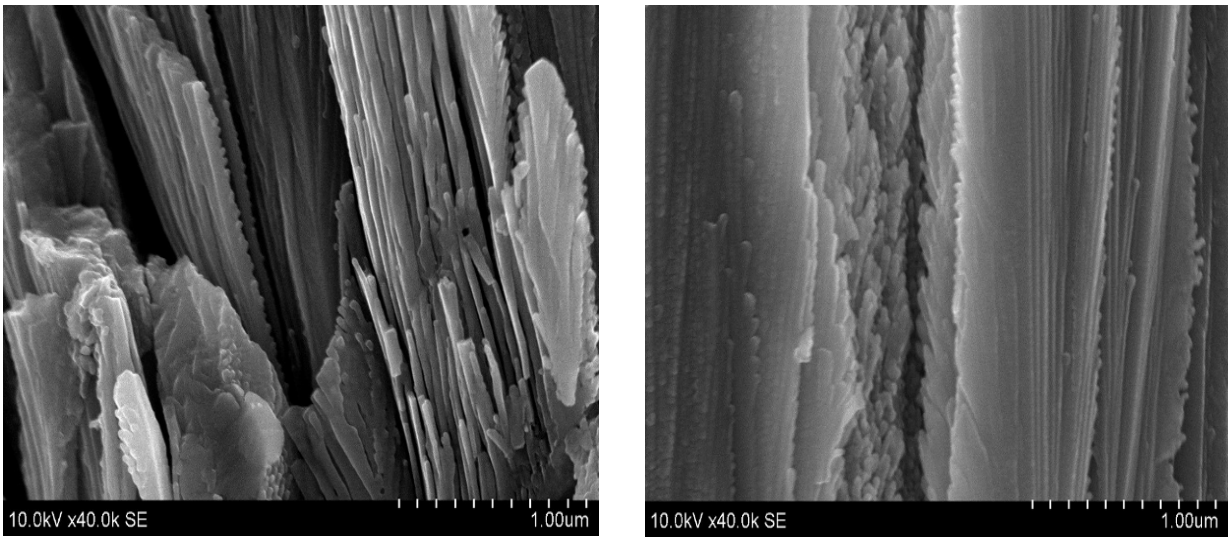

Figure 2-9: SEM image of 10Sc1CeSZ EB-PVD film with columnar cracks [100]

with leakage rates of 9.38 x10^{-5} mbar cm^{-2} s^{-1} yielding dense, homogeneous layers with an area specific resistance (ASR) of 0.65 Ω cm^2. Columnar cracks were visible under electron microscopy as seen in Figure 2-9, which appears to be a reasonable explanation for the high leakage rates. No inter-diffusion between the ScSZ and Ni-YSZ support was observed revealing good adhesion and no cracks. The columnar structure of the film is assumed to be responsible for the high contacting between the electrolyte and anode and the low porosity.

Wilckens et al. [97] prepared full cells based on a Ni-10Sc1CeSZ/10Sc1CeSZ/LSCF structure and carried out materials characterisation to determine conductivity properties for different ScSZ powders at varying p(O_2) for anode optimisation as seen in Figure 2-10. Hardness of the ScSZ electrolyte layers was determined via Vickers indentation tests and yielded values of 3435±1562 MPa, 3035±1048 MPa and 958±350 MPa at loads of P=10 mN, P=100 mN and P=1000 mN respectively. Initial electrical performance tests carried out at Forschungszentrum Juelich Energy Research Institute showed OCV values of 600mV under 1000 ml H_2 at 900^{o}C. Such low OCV numbers suggested leakage through the electrolyte which warranted more investigation so subsequent cell tests were postponed.

Virbukas et al. [99] and Hong and Yoon [98] report cubic phase ScSZ after exposure at temperatures 1000^{o}C [99] and 1400^{o}C [98] with increased e-beam power resulting in increased deposition rates and larger ScSZ clusters. The larger clusters lead to large crystals comprised of smaller sized crystallites. Controlling the e-beam process can yield films with improved properties. Hong

reported film thicknesses between 1.0-2.5 μm with slight columnar structures when deposited on SiO_2 and distinct columns when deposited onto Ni-YSZ substrates as seen in Figure 2-11. The achieved conductivities of $9.46x10^{-3}$ S cm^{-1} at 700°C [98] and $5.52x10^{-2}$ S cm^{-1} at 600°C [99] were slightly lower and higher than previously reported conductivities for ScSZ respectively [9]. These results still support the feasibility of thin film ScSZ electrolytes fabricated by EB-PVD for use in IT-SOFCs.

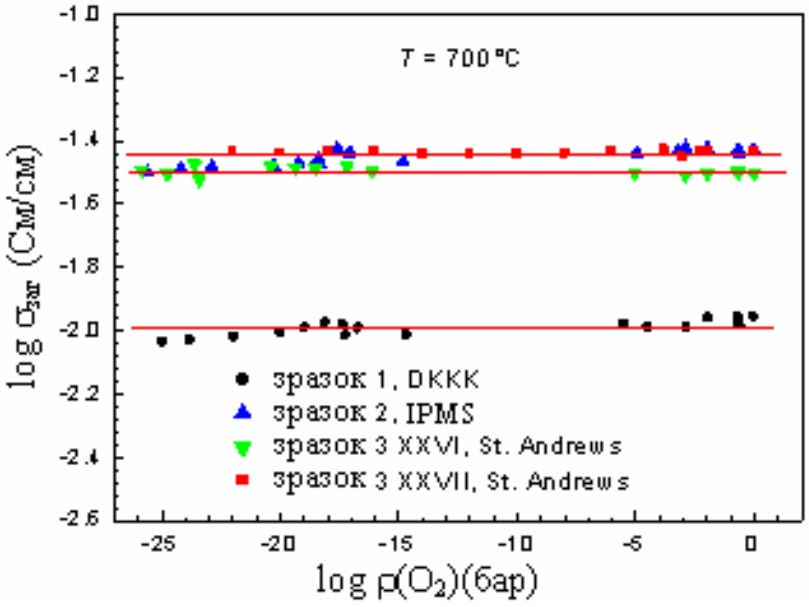

Figure 2-10: Electrical conductivity of different sourced ScSZ powders at varying $p(O_2)$ [97]

Liu et al. reported performance results for a direct carbon fuel cell based on a ScSZ structure adopting an anode supported tubular SOFC configuration fabricated via dip-coating [91]. The cell consisted of a 10.8 cm long Ni-YSZ support tube, with a co-fired NiO-ScSZ anode functional layer, a ScSZ electrolyte and a LSM-ScSZ cathode with an effective cell area of 10.0 cm^2. Peak power values of 104 mW cm^{-2} at 850°C as shown in Figure 2-12 were achieved with carbon black as the fuel source with the lowest R_{ohm} value of 0.71 Ω cm^2 observed at the same temperature. The increasing trend of both R_{ohm} and R_e with decreasing temperature was in agreement with the decrease in peak power density at the corresponding temperatures. These results show promise for operating an SOFC using a ScSZ structure. Lee et al. [89] and Mizutani et al. [67] tested IT-SOFCs based on ScSZ electrolytes using Ni-YSZ anodes and LSCF-YSZ and LSM cathodes respectively. Lee et al. used ScSZ powders in a 8 mol% Sc_2O_3-ZrO_2 composition prepared via glycine nitrate combustion and prepared cells adopting an anode supported design using substrate discs cut from commercial tubes with the cathode applied via

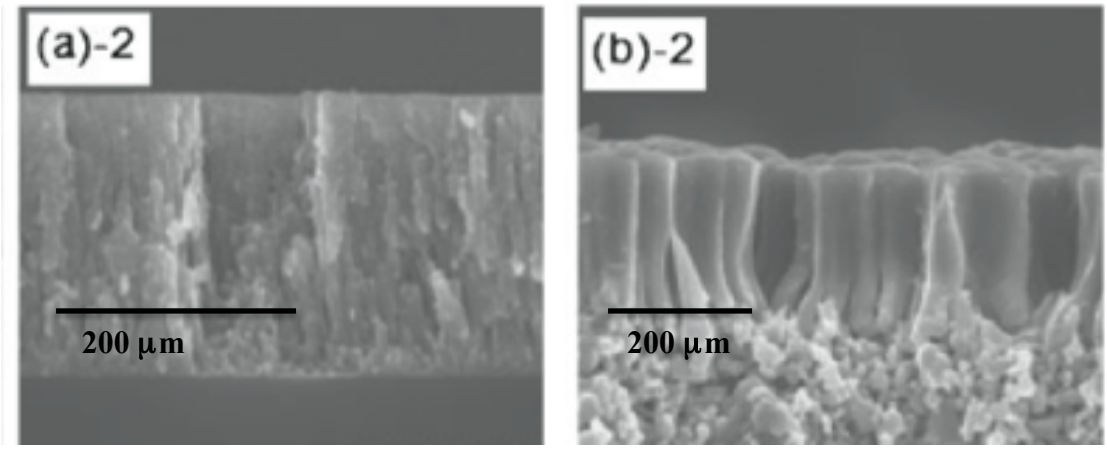

Figure 2-11: ScSZ films deposited by EB-PVD onto (a)-2 SiO_2 and (b)-2 Ni-YSZ supports [98]

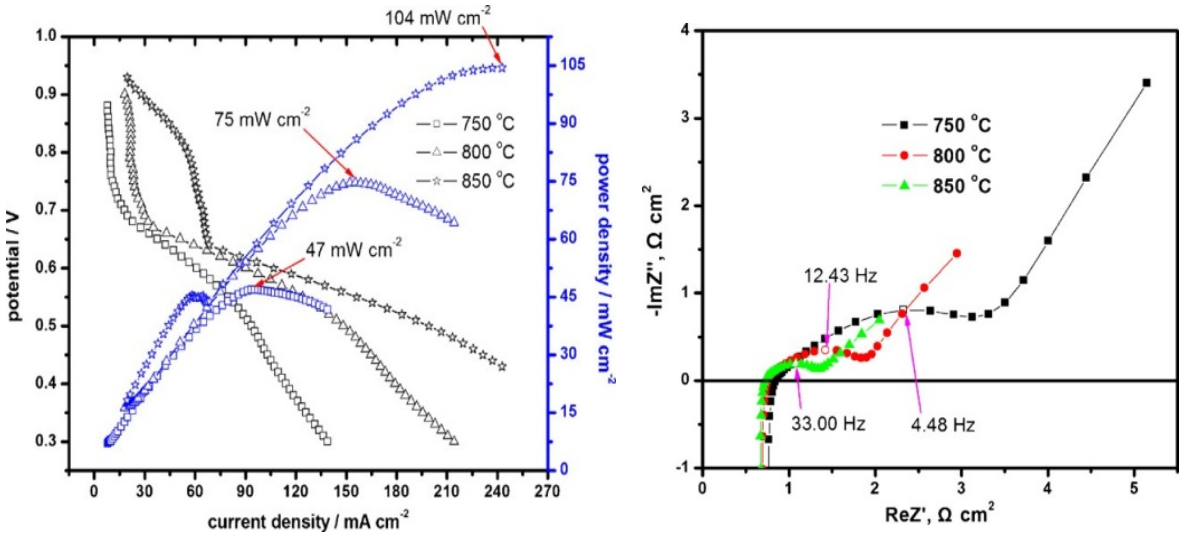

Figure 2-12: Power curves and Nyquist plots for a ScSZ cell fuelled by carbon [91]

screen-printing. The ScSZ electrolyte was 14 µm thick and applied via dip coating. Mizutani et al. used ScSZ powders prepared by sol-gel method in either a 11 mol% Sc_2O_3-ZrO_2 (11ScSZ) or 11 mol% Sc_2O_3-20 wt% Al_2O_3-ZrO_2 (11ScSZ20A) composition that were used to fabricate 250 µm thick electrolyte supported flat plates, though the method of electrode application was not disclosed. Under 3% H_2O-H_2 operation Lee et al. reports OCV values of 0.97V and performance values of 0.362 W cm^{-2} at 750°C for 8ScSZ cells compared to 0.313 W cm^{-2} and 1.03V for 8YSZ cells under the same testing condition as seen in Figure 2-13 (c). Cross-sectional SEM images of the 8ScSZ and 8YSZ cell microstructures are

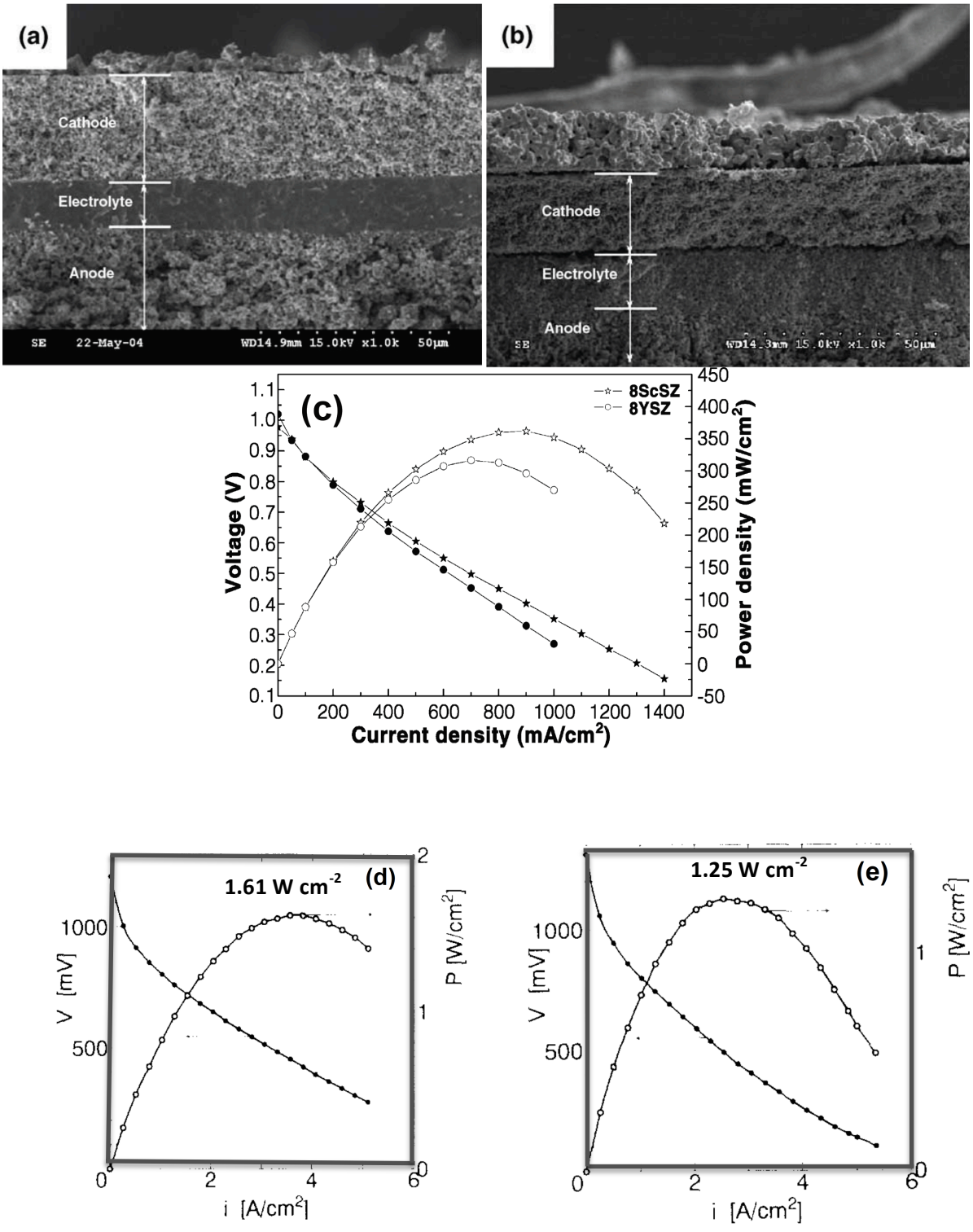

Figure 2-13: Cross-sectional SEM images for (a) 8ScSZ and (b) 8YSZ cells [89]**, (c) performance curves for the 8ScSZ/8YSZ cells** [89]**, (d) performance curves for the 11ScSZ cell and (e) performance curves for the 11ScSZ20A cell** [67]**.**

shown in Figure 2-13 (a) and (b) respectively. Under pure H_2 operation, Mizutani et al. reports peak power values of 1.61 W cm^{-2} and 1.25 W cm^{-2} for the 11ScSZ and 11ScSZ20A cells respectively as seen in Figure 2-13 (d) and (e). The results reported by Lee et al. show the improved performance of the 8ScSZ cell compared to the 8YSZ is attributed to the higher intrinsic conductivity of 8ScSZ while the better OCV value for 8YSZ relates to a more dense electrolyte microstructure when compared to 8ScSZ. For the cells tested by Mizutani et al., the better performance of 11ScSZ over 11ScSZ20A is also attributed to a higher electrolyte conductivity as the conductivity of 11ScSZ20A was found to be comparable to 8YSZ [67].

Cai et al. [90] and Timurkutluk et al. [95] prepared Ni-ScSZ anode supported IT-SOFCs utilising ScSZ electrolytes prepared using commercial powders and deposited via dip coating onto Ni-ScSZ pellets [90] or as a laminar tape onto tape casted Ni-ScSZ substrates [95]. The Pt-ScSZ and LSF-ScSZ/LSF cathodes were applied via slurry coating and screen-printing respectively. Cai et al. tested cells on 3% H_2O-H_2 at 700, 800 and 900^oC and reported peak power values of 1.2V (OCV) and 0.41 W cm^{-2} at 0.8 A cm^{-2} at 900^oC for cell A and 1.1V (OCV) and 0.8 W cm^{-2} at 1.8 A cm^{-2} at 800^oC for cell B. The difference between the two cells is the difference in the co-firing schedule of 1300^oC-5hrs for cell A and 1400^oC-2hrs for cell B. Timurkutluk et al. examined the effects of manufacturing parameters on the performance of tape cased anode supported ScSZ cells. Varying Ni-ScSZ anode functional layer (AFL) thickness and investigating the influence of Gd-doped CeO_2 (GDC) anode infiltration on the performance of tested cells operating on H_2 at 700 – 800^oC with no changes in the ScSZ electrolyte thickness of 10 μm was investigated. Results at 700^oC show increasing AFL thickness decreases performance due to mass transport limitations as pictured in Figure 2-14 (a). The optimised anode structure of 540 μm thick for the support tape and a 135 μm thickness for the AFL achieved a maximum power density of 1.06 W cm^{-2} at 700^oC. The optimised anode with GDC infiltration produced power densities of 1.34 W cm^{-2}, 1.72 W cm^{-2} and 1.89 W cm^{-2} at 700, 750 and 800^oC respectively as shown in Figure 2-14 (b). The improved performance for the GDC impregnated cell is due to an increased number of reaction zones and the enhanced conductivity of the anode brought about by the presence of higher conducting GDC.

Lu et al. [93] and Kobayashi et al. [94] investigated the performance of ScSZ operating on H_2 and H_2 and C_4H_{10} fuels [93]. The ScSZ cells were prepared via tape casting [93] and electrophoretic deposition [94] and deposited onto Cu-Ce-ScSZ anodes and Ni-ScSZ anodes respectively. The LSM-ScSZ [93] and either LSC-ScSZ or Pt-ScSZ [94] cathodes were applied by pasting onto the electrolyte surface with glycerol and by tape casting respectively. Lu et al. reported OCV values of 1.2V with peak

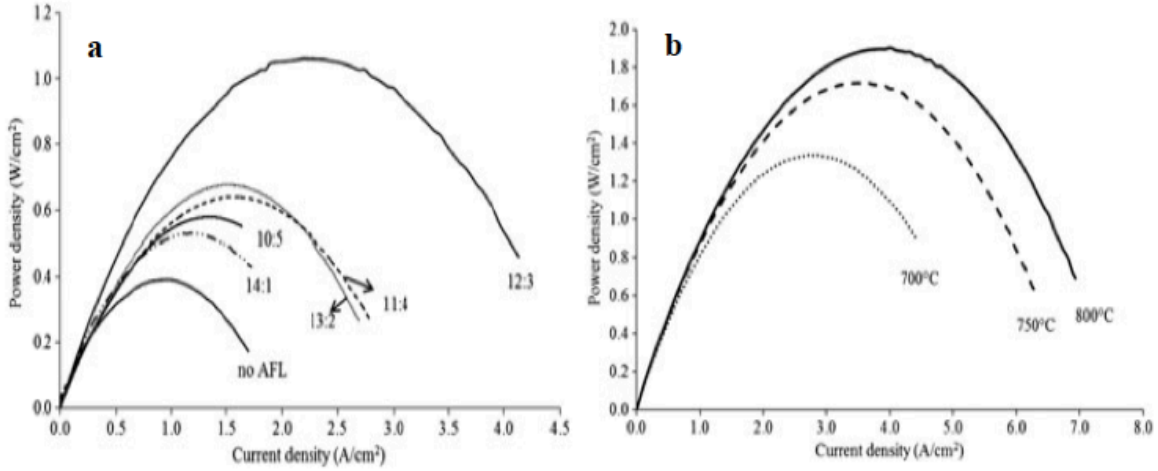

Figure 2-14: (a) Effect of AFL thickness on cell performance at 700°C, (b) power curves of ScSZ cells with GDC infiltration [95]

power densities of 0.29 W cm^{-2} on H_2 at 700°C for the Cu-Ce-ScSZ/ScSZ/LSC-ScSZ cell with a 60 μm thick ScSZ electrolyte. The performance of this cell on C_4H_{10} at 700°C was 0.15 W cm^{-2}, which is reported as similar to data obtained for YSZ cells tested under similar conditions. Kobayashi et al. prepared various cells of 5 μm, 10 μm and 20 μm thick ScSZ layers with reported performance values for the 20 μm cell containing Pt-ScSZ cathode of 1.8 W cm^{-2}, 1.2 W cm^{-2}, 0.4 W cm^{-2} and 0.1 W cm^{-2} at 900, 800, 700 and 600°C respectively. A cross-sectional SEM image of a 10 μm Ni-ScSZ/ScSZ/Pt-ScSZ cell is pictured in Figure 2-15 (a) with the performance curves of the 20 μm cell at 900, 800, 700 and 600°C shown in Figure 2-15 (b). Cell performance data for the ScSZ cell with the LSC-ScSZ cathode could not be obtained due to poor performance brought about by an electrolyte-cathode interaction, even the use of a GDC blocking layer failed to generate results better than the ScSZ/Pt-ScSZ cell.

Cho et al. [96] fabricated intermediate temperature SOFCs composed of thin film ScSZ electrolyte layers deposited via RF sputtering onto Al_2O_3 substrates; the Pt electrodes were also deposited via sputtering. Two cells, each containing 280 nm thick ScSZ electrolyte films, were prepared and tested under H_2 and achieved OCV values of 1.08V and 1.04V and peak power densities of 227 W cm^{-2} and 334 W cm^{-2} at 500°C and 550°C respectively. The polarisation and power density curves for these cells are shown in Figure 2-16 (a). Electrochemical impedance data under different applied voltage conditions was also obtained as seen in Figure 2-16 (b), and the ohmic resistance values of the cells tested at 500°C were 0.340 Ω cm^2 and 0.256 Ω cm^2 at 0.7V and 0.5V respectively. The electrode polarisation resistances

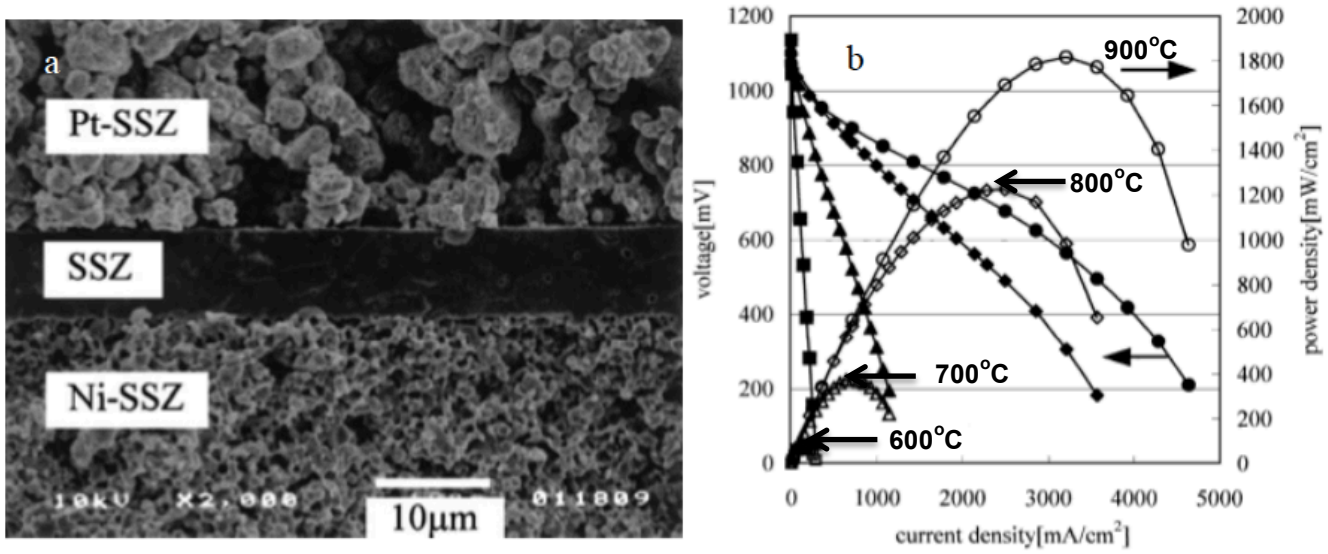

Figure 2-15: (a) Cross-sectional SEM image of Ni-ScSZ/ScSZ/Pt-ScSZ cell, (b) I-V curves for the 20 µm Ni-ScSZ/ScSZ/Pt-ScSZ cell at 900°C, 800°C 700°C and 600°C [94]

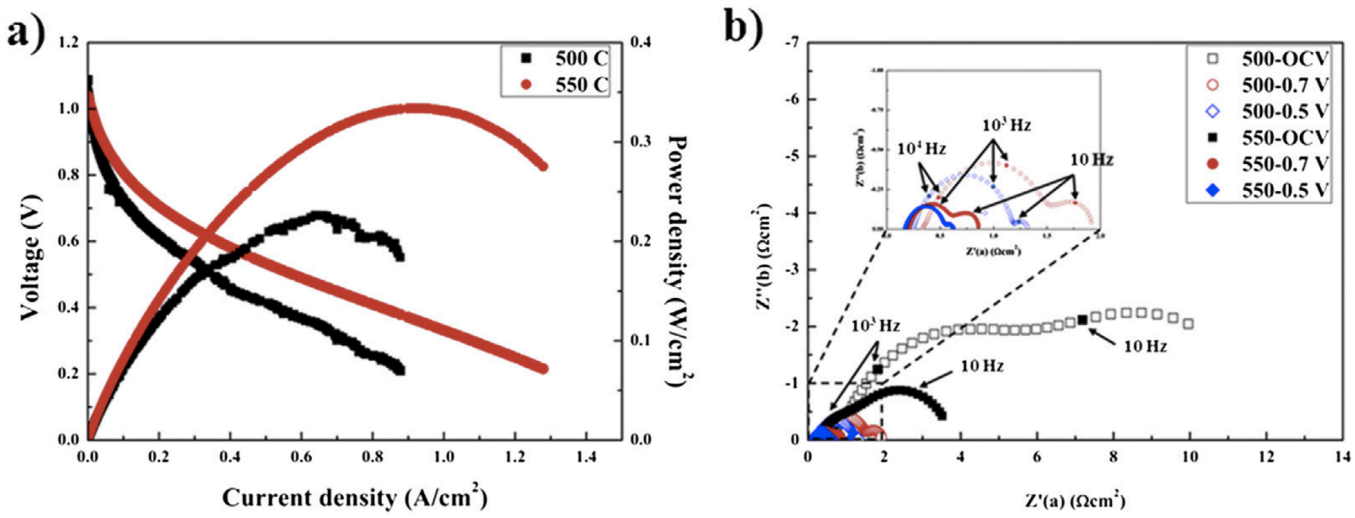

Figure 2-16: (a) Polarisation and power density curves of a Pt/ScSZ/Pt cell tested at 500°C and 550°C under H_2 operation (b) electrochemical impedance data for the ScSZ cell [96]

which correspond to the low frequency x-axis intercepts, changed significantly under different applied voltages at 500°C with values of 1.512 Ω cm^2 and 1.018 Ω cm^2 obtained at 0.7V and 0.5V respectively. The low ohmic resistance values are largely due to the high intrinsic conductivity of ScSZ in addition to the thin electrolyte layer, both of which contributed to the high power density values. The significantly larger electrode polarisation resistances are attributed to sluggish reaction kinetics at the cathode, which is greatly influenced by the applied voltage. Generating electrochemical impedance data at different

applied voltages *allowed the ohmic and electrode polarisation resistances to be clearly separated* [96]. And while this cell did not make use of traditional cermet anodes and ceramic cathodes, these results serve to show the high performance capabilities of an SOFC utilising a ScSZ electrolyte.

These preliminary results demonstrate proof of concept and showcase the promise of ScSZ as an alternative electrolyte material. A summary of these findings can be found in Table 2.1. All cells were fabricated adopting either an electrolyte supported design or an anode supported design with the electrolyte manufactured via dip coating or tape casting. And whilst the research in this area is on-going, nothing has been reported on the fabrication and testing of anode supported IT-SOFCs based on a 10Sc1CeSZ structure fabricated via screen-printing. The research covered in this thesis will implement screen-printing as a deposition method for the 10Sc1CeSZ electrolyte further contributing to the characterisation of the ScSZ system using these findings as an indicator of performance to determine the suitability of this material as an IT-SOFC electrolyte.

2.4.4 Anode Supported SOFCs based on a Ni-ScSZ Support Structure

Much work has been dedicated to understanding fuel reforming and carbon catalysis reactions so new anode materials for use on CH_4 and higher hydrocarbons have been introduced. One way to minimise anode deterioration so hydrocarbon operation remains a viable option is to formulate anodes that are poor catalysts for carbon formation. A review of the work by other research groups shows the focus of materials development based on Ni-ScSZ anodes for operation on hydrocarbon fuels [101]–[107]. Because this work falls outside the scope of this thesis it will not be discussed in much detail here. Research investigating the use of metallic dopants in Ni-ZrO_2 anodes for operation on hydrocarbons can be found elsewhere [108]–[111]. Somalu et al. has investigated the effect of ink rheology and solids loading on the properties of Ni-ScSZ screen-printed anodes [42], [112] with inks containing 28-30 vol% solids producing the most optimised anode layers based on peak conductivity values and mechanical strength values. The work in this thesis will investigate the properties of Ni-10Sc1CeSZ anodes and evaluate its use as a support structure for screen-printed 10Sc1CeSZ electrolyte based cells operating on H_2 and CH_4. Further discussion on Co-doping ScSZ with CeO_2 and the viability of this material as an IT-SOFC is discussed in Chapter 3, Section 3.2.1. Materials research, and repeat cell tests will be carried out to tailor the fabrication methods to the performance requirements of the 10Sc1CeSZ system, making it competitive with the traditional YSZ system.

Table 2-1: Summary of Performance Results for SOFCs Using ScSZ Electrolytes

Author	Cell Design	Electrolyte Fabrication Method	Anode	Cathode	Performance
Lee et al. [89]	ASC	dip coating	Ni-YSZ disc	LSCF-YSZ	0.97sV, 0.362 W cm^{-2} 750°C on 3%H_2O-H_2
Cai et al. [90]	ASC	dip coating	Ni-8ScSZ tape	Pt-8ScSZ	1.2V , 0.41 W cm^{-2} 900°C on 3%H_2O-H_2 1.1V, 0.8 W cm^{-2} 800°C on 3%H_2O-H_2
Liu et al. [91]	ASC	dip coating	Ni-ScSZ tube	LSM-ScSZ	0.95V, 0.104 W cm^{-2} 850°C on carbon black fuel
Timurkutluk et al. [95]	ASC	tape casting	Ni-ScSZ Ni-GDC-ScSZ tape	LSF-ScSZ	1.06 W cm^{-2} at 700°C 1.89 W cm^{-2} at 800°C on H_2
Mizutani et al. [67]	ESC	tapes	Ni-8YSZ	LSM	1.61 W cm^{-2} (11ScSZ) 1.25 W cm^{-2} (11ScSZ w/Al_2O_3) on H_2
Lu et al. [93]	ASC	tape casting	Cu-Ce-ScSZ	LSM-ScSZ	1.2V, 1.80 W cm^{-2} at 900°C on H_2
Wilckens et al. [97]	ASC	EB-PVD	Ni-ScSZ discs	LSCF	0.6V on 1L of H_2 at 900°C
Kobayashi et al. [94]	ASC	electrophoretic deposition	Ni-ScSZ	Pt-ScSZ	1.2V, 0.29 W cm^{-2} at 700°C on H_2 0.15 W cm^{-2} at 700°C on C_4H_{10}
Cho et al. [96]	Al_2O_3 substrate support	RF sputtering	Pt	Pt	1.08V, 227 W cm^{-2} at 500°C 1.04V, 334 W cm^{-2} at 550°C

REFERENCES

[1] A. J. Jacobson, Materials for Solid Oxide Fuel Cells. *Chem. Mater.*, 2010. 22 (3): p. 660-674.

[2] N. Mahato, A. Banerjee, A. Gupta, S. Omar and K. Balani, Progress in material selection for solid oxide fuel cell technology: A review. *Prog. Mater. Sci.*, 2015. 72 (1): p. 141-337.

[3] D. Radhika and A. S. Nesaraj, Materials and Components for Low Temperature Solid Oxide Fuel Cells – An Overview. *Int. J. Renew. Energy Dev.*, 2013. 2 (2): p. 87-95.

[4] M. Kendall and K. Kendall, *High-Temperature Solid Oxide Fuel Cells for the 21st Century-Fundamentals, Design and Applications*, Elsevier, 2016.

[5] J. W. Fergus, Electrolytes for solid oxide fuel cells. *J. Power Sources*, 2006. 162 (1): p. 30-40.

[6] N. Q. Minh, Ceramic Fuel Cells. *J. Am. Ceram. Soc.*, 1993. 76 (3): p. 563-588.

[7] L. J. M. J. Blomen and M. N. Mugerwa, *Fuel Cell Systems*, Springer Science and Business Media, 2013.

[8] S. Badwal, Zirconia-based solid electrolytes: microstructure, stability and ionic conductivity. *Solid State Ionics*, 1992. 52 (1–3): p. 23-32.

[9] S. Badwal, Scandia–zirconia electrolytes for intermediate temperature solid oxide fuel cell operation. *Solid State Ionics*, 2000. 136–137 (1–2): p. 91-99.

[10] Y. Arachi, H. Sakai, O. Yamamoto, Y. Takeda and N. Imanishai, Electrical conductivity of the $ZrO_2 – Ln_2O_3$ (Ln = lanthanides) system. *Solid State Ionics*, 1999. 121 (1-4): p. 133-139.

[11] H. G. Scott, Phase relationships in the zirconia-yttria system. *J. Mater. Sci.*, 1975. 10 (9): p. 1527-1535.

[12] J. Ilavsky and J. K. Stalick, Phase composition and its changes during annealing of plasma-sprayed YSZ. *Surf. Coatings Technol.*, 2000. 127 (2–3): p. 10-129.

[13] M. Yashima, M. Kakihana and M. Yoshimura, Metastable-stable phase diagrams in the zirconia-containing systems utilized in solid-oxide fuel cell application. *Solid State Ionics*, 1996. 86-88 (2): p. 1131-1149.

[14] J. Fergus, R. Hui, X. Li, D. P. Wilkinson and J. Zhang, *Solid Oxide Fuel Cells: Materials Properties and Performance*, CRC Press, 2008.

[15] M. Ghatee, M. H. Shariat and J. T. S. Irvine, Investigation of electrical and mechanical properties of 3YSZ/8YSZ composite electrolytes. *Solid State Ionics*, 2009. 180 (1): p. 57-62.

[16] R. Hannink, Transformation toughening in zirconia-containing ceramics. *J. Am. Ceram*., 2000. 83 (3): p. 461-487.

[17] V. Kharton, F. Marques, and A. Atkinson, Transport properties of solid oxide electrolyte ceramics: a brief review. *Solid State Ionics*, 2004. 174 (1–4): p. 135-149.

[18] E. M. Brodnikovskii, Solid Oxide Fuel Cell Anode Materials. *Powder Metall. Met. Ceram.*, 2015. 54 (3): p. 166-174.

[19] W. Z. Zhu and S. C. Deevi, A review on the status of anode materials for solid oxide fuel cells. *Mater. Sci. Eng. A*., 2003. 362 (1–2): p. 228-239.

[20] Y. Du, C. Finnerty and J. Jiang, Thermal Stability of Portable Microtubular SOFCs and Stacks. *J. Electrochem. Soc.*, 2008. 155 (9): p. B972-B977.

[21] C. M. Dikwal, W. Bujalski and K. Kendall, Characterization of the electrochemical performance of micro-tubular SOFC in partial reduction and oxidation conditions. *J. Power Sources*, 2008. 181 (2): p. 267-273.

[22] W. Bujalski, C. M. Dikwal and K. Kendall, Cycling of three solid oxide fuel cell types. *J. Power Sources*, 2007. 171 (1): p. 96-100.

[23] H. Monzón and M. A. Laguna-Bercero, Redox-cycling studies of anode-supported microtubular solid oxide fuel cells. *Int. J. Hydrogen Energy*, 2012. 37 (8): p. 7262-7270.

[24] W. Huebner, D. M. Reed and H. U. Anderson, Solid oxide fuel cell performance studies: Anode development. *(SOFC VI) Proc. Sixth Int. Symp. Electrochem*. Soc., 1999. 99–19 (1): p. 503-512.

[25] M. Mori, Thermal Expansion of Nickel-Zirconia Anodes in Solid Oxide Fuel Cells during Fabrication and Operation. *J. Electrochem. Soc*., 1998. 145 (4): p. 1374-1381.

[26] D. S. McLachlan, M. Blaszkiewicz and R. E. Newnham, Electrical Resistivity of Composites, *J. Am. Ceram. Soc.*, 1990. 73 (8): p. 2187-2203.

[27] O. Pecho, A. Mai, B. Münch, T. Hocker, R. Flatt and L. Holzer, 3D Microstructure Effects in Ni-YSZ Anodes: Influence of TPB Lengths on the Electrochemical Performance. *Materials*, 2015. 8 (10): p. 7129-7144.

[28] M. Riazat, M. Baniassadi, M. Mazrouie, M. Tafazoli, M. M. Zand., The Effect of Cathode Porosity on Solid Oxide Fuel Cell Performance. *Energy Equip. Syst.*, 2015. 3 (1): p. 25-32.

[29] C. Sun, R. Hui and J. Roller, Cathode materials for solid oxide fuel cells: A Review. *J. Solid State Electrochem.*, 2009. 14 (7): p. 1125-1144.

[30] N. Minh, Solid oxide fuel cell technology - features and applications. *Solid State Ionics*, 2004. 174 (1–4): p. 271-277.

[31] N. H. Menzler, F. Tietz, S. Uhlenbruck, H. P. Buchkremer and D. Stöver, Materials and manufacturing technologies for solid oxide fuel cells. *J. Mater. Sci.*, 2010. 45 (12): p. 3109-3135.

[32] W. D. Kingery, *Ceramic Fabrication Processes*. Technology Press of Massachusetts Institute of Technology, 1958.

[33] R. Oberacker, Part I - Powders. *Ceram. Sci. Technol.*, 2012. 3 (3): p. 1-38.

[34] C. DiAntonio, Characterization and Modeling to Control Sintered Ceramic Microstructures and Properties*: Proc. 106th Annual Meeting of The Am. Ceram. Soc., Ceram. Trans*., 2012. V (157): p. 77-84.

[35] R. M. German, *Particle Packing Characteristics*, Metal Powder Industries Federation, 1989.

[36] S. E. Schoenberg, D. J. Green, A. E. Segall, G. L. Messing, A. S. Grader and P. M. Halleck, Stresses and Distortion Due to Green Density Gradients During Densification. *J. Am. Ceram. Soc*., 2006. 89 (10): p. 3027-3033.

[37] F. Tietz, Components manufacturing for solid oxide fuel cells. *Solid State Ionics*, 2002. 152–153 (1): p. 373-381.

[38] K. Hassmann, SOFC Power Plants, the Siemens-Westinghouse Approach. *Fuel Cells*, 2001. 1 (1): p. 78-84.

[39] N. M. Sammes and Y. Du, Fabrication and Characterization of Tubular Solid Oxide Fuel Cells. *Int. J. Appl. Ceram. Technol.*, 2007. 4 (2): p. 89-102.

[40] P. Von Dollen and S. Barnett, A Study of Screen Printed Yttria-Stabilized Zirconia Layers for Solid Oxide Fuel Cells. *J. Am. Ceram. Soc.*, 2005. 88 (12): p. 3361-3368.

[41] P. Ried, C. Lorenz, A. Brönstrup, T. Graule, N. H. Menzler, W. Sitte and P. Holtappels, Processing of YSZ screen printing pastes and the characterization of the electrolyte layers for anode supported SOFC. *J. Eur. Ceram. Soc.*, 2008. 28 (9): p. 1801-1808.

[42] M. R. Somalu, V. Yufit, I. P. Shapiro, P. Xiao and N. P. Brandon, The impact of ink rheology on the properties of screen-printed solid oxide fuel cell anodes. *Int. J. Hydrogen Energy*, 2013. 38 (16): p. 6789-6801.

[43] J. Piao, K. Sun, N. Zhang and S. Xu, A study of process parameters of LSM and LSM-YSZ composite cathode films prepared by screen-printing. *J. Power Sources*., 2008. 175 (1): p. 288-295.

[44] L. G. J. B. De Haart, *Manufacturing of SOFC Manufacturing of SOFC Contents*. Joint European Summer School for Fuel Cell and Hydrogen Technology, 2013.

[45] J. R. Creighton and P. Ho, *Introduction to Chemical Vapor Deposition (CVD)*. Chem. Vap. Depos., (2001).

[46] L. L. Hench and J. K. West, The sol-gel process. *Chem. Rev.*, 1990. 90 (1): p. 33-72.

[47] A. Atkinson, S. Barnett, R. J. Gorte, J. T. S. Irvine, A. J. McEvoy, M. Mogensen, S. C. Singhal and J. Vohs, Advanced anodes for high-temperature fuel cells. *Nat. Mater.*, 2004. 3 (1): p. 17-27.

[48] S. McIntosh and R. J. Gorte, Direct hydrocarbon solid oxide fuel cells. *Chem. Rev.*, 2004. 104 (10): p. 4845-4865.

[49] J. H. Lunsford, Catalytic conversion of methane to more useful chemicals and fuels: a challenge for the 21st century. *Catal. Today*., 2000. 63 (2–4): p. 165-174.

[50] A. L. Dicks, Hydrogen generation from natural gas for the fuel cell systems of tomorrow. *J. Power Sources*, 1996. 61 (1–2): p. 113-124.

[51] X. Wang and R. J. Gorte, Steam reforming of n-butane on Pd/ceria. *Catal. Letters*., 2001. 73 (1): p. 15-19.

[52] B. Monnerat, L. Kiwi-Minsker and A. Renken, Hydrogen production by catalytic cracking of methane over nickel gauze under periodic reactor operation. *Chem. Eng. Sci.*, 2001. 56 (2): p. 633-639.

[53] C. H. Bartholomew and R. J. Farrauto, *Fundamentals of Industrial Catalytic Processes*, John Wiley & Sons, Inc., 2005

[54] J. R. Rostrup-Nielsen, Production of synthesis gas. *Catal. Today*., 1993. 18 (1): p. 305-324.

[55] M. Pillai, Y. Lin, H. Zhu, R. J. Kee and S. A. Barnett, Stability and coking of direct-methane solid oxide fuel cells: Effect of CO_2 and air additions. *J. Power Sources*., 2010. 195 (1): p. 271-279.

[56] H. He, J. M. Vohs and R. J. Gorte, Carbonaceous deposits in direct utilization hydrocarbon SOFC anode. *J. Power Sources*., 2005. 144 (1): p. 135-140.

[57] S. P. S. Shaikh, A. Muchtar and M. R. Somalu, A review on the selection of anode materials for solid-oxide fuel cells. *Renew. Sustain. Energy Rev.*, 2015. 51 (1): p. 1-8 .

[58] H. Wu, V. La Parola, G. Pantaleo, F. Puleo, A. Venezia and L. Liotta, Ni-Based Catalysts for Low Temperature Methane Steam Reforming: Recent Results on Ni-Au and Comparison with Other Bi-Metallic Systems. *Catalysts, 2013*. 3 (2): p. 563-583.

[59] J. Ayawanna, D. Wattanasiriwech, S. Wattanasiriwech and K. Sato, Electrochemical Performance of Ni1-xCox-GDC Cermet Anodes for SOFCs. *Energy Procedia*, 2013. 34 (1): p. 439-448.

[60] F. T. Ciacchi, K. M. Crane and S. P. S. Badwal, Evaluation of commercial zirconia powders for solid oxide fuel cells. *Solid State Ionics*, 1994. 73 (1–2): p. 49-61.

[61] S. P. S. Badwal, Effect of dopant concentration on electrical conductivity in the Sc_2O_3-ZrO_2 system. *J. Mater. Sci.*, 1987. 22 (11): p. 4125-4132.

[62] I. R. Gibson, G. P. Dransfield and J. T. S. Irvine, Influence of yttria concentration upon electrical properties and susceptibility to ageing of yttria-stabilised zirconias. *J. Eur. Ceram. Soc.*, 1998. 18 (6): p. 661-667.

[63] H. G. Scott, Phase relationships in the zirconia-yttria system. *J. Mater. Sci.*, 1975. 10 (9): p. 1527-1535.

[64] F. T. Ciacchi, S. P. S. Badwal and J. Drennan, The system Y_2O_3-Sc_2O_3-ZrO_2: Phase characterisation by XRD, TEM and optical microscopy. *J. Eur. Ceram. Soc.*, 1991. 7 (3): p. 185-195.

[65] O. Yamamoto, Solid oxide fuel cells: fundamental aspects and prospects. *Electrochim. Acta.*, 2000. 45 (15–16): p. 2423-2435.

[66] C. Haering, A. Roosen and H. Schichl, Degradation of the electrical conductivity in stabilised zirconia systems Part I: yttria-stabilised zirconia. *Solid State Ionics*, 2005. 176 (3–4): p. 253-259.

[67] Y. Mizutani, M. Tamura, M. Kawai, and O. Yamamoto, Development of high-performance electrolyte in SOFC. *Solid State Ionics*, 1994. 72 (1): p. 271-275.

[68] O. Yamamoto, Electrical conductivity of stabilized zirconia with ytterbia and scandia. *Solid State Ionics*, 1995. 79 (1): p. 137-142.

[69] M. R. Thornber, D. J. M. Bevan and E. Summerville, Mixed oxides of the type MO_2(fluorite)-M_2O_3. V. Phase studies in the systems ZrO_2-M_2O_3 (M = Sc, Yb, Er, Dy). *J. Solid State Chem.*, 1970. 1 (3–4): p. 545-553.

[70] R. Ruh, H. J. Garrett, R. F. Domagala and V. A. Patel, The System Zirconia-Scandia. *J. Am. Ceram. Soc.*, 1977. 60 (9–10): p. 399-403.

[71] T.-Y. T. Tzer-Shin Sheu, Jae Xú, Phase Relationships in the ZrO_2-Sc_2O_3 and ZrO_2-ln_2O_3 Systems. *J. Am. Ceram. Soc.*, 1993. 76 (8): p. 2027-2032.

[72] F. M. Spiridonov, L. N. Popova and R. Y. Popil'skii, On the phase relations and the electrical conductivity in the system ZrO_2-Sc_2O_3. *J. Solid State Chem.*, 1970. 2 (3): p. 430-438.

[73] K. Acres, Recent advances in fuel cell technology and its applications. *J. Power Sources*, 2001. 100 (1): p. 60-66.

[74] A. Tarancón, Strategies for Lowering Solid Oxide Fuel Cells Operating Temperature. *Energies*, 2009. 2 (4): p. 1130-1150.

[75] S. de Souza, Thin-film solid oxide fuel cell with high performance at low-temperature. *Solid State Ionics*, 1997. 98 (1–2): p. 57-61.

[76] C. Wang, W. L. Worrell, S. Park, J. M. Vohs and R. J. Gorte, Fabrication and Performance of Thin-Film YSZ Solid Oxide Fuel Cells. *J. Electrochem. Soc.*, 2001. 148 (8): p. A864-A868.

[77] D. Lee, W. Kim, S. Choi, J. Kim, H. Lee, and J. Lee, Characterization of ZrO co-doped with ScO and CeO electrolyte for the application of intermediate temperature SOFCs. *Solid State Ionics*, 2005. 176 (1–2): p. 33-39.

[78] J. T. S. Irvine and P. A. Connor, *Solid Oxide Fuel Cells: Facts and Figures: Past, Present and Future Perspectives for SOFC Technologies*, Springer, 2013.

[79] C. N. Shyam Kumar and R. Bauri, Enhancing the phase stability and ionic conductivity of scandia stabilized zirconia by rare earth co-doping. *J. Phys. Chem. Solids*, 2014. 75 (5): p. 642-650.

[80] Y. Arachi, T. Asai, O. Yamamoto, Y. Takeda, N. Imanishi, K. Kawate and C. Tamakoshi, Electrical Conductivity of ZrO_2-Sc_2O_3 Doped with HfO_2, CeO_2, and Ga_2O_3. *J. Electrochem. Soc.*, 2001. 148 (5): p. A520-A523.

[81] H. A. Abbas, C. Argirusis, M. Kilo, H. D. Wiemhöfer, F. F. Hammad, and Z. M. Hanafi, *Preparation and conductivity of ternary scandia-stabilised zirconia*. *Solid State Ionics*, 2011. 184 (1): p. 6-9.

[82] E. Z. Santos and R. Muccillo, Single Cubic Phase Scandia-Stabilized Zirconia: Stabilization and Aging at 600^{o}C. *ECS Trans.*, 2015. 68 (1): p. 421-427.

[83] Z. Wang, M. Cheng, Z. Bi, Y. Dong, H. Zhang, J. Zhang, Z. Feng, and C. Li, Structure and impedance of ZrO_2 doped with Sc_2O_3 and CeO_2. *Mater. Lett.*, 2005. 59 (19–20): p. 2579-2582.

[84] E. P. Murray, T. Tsai,and S. A. Barnett, A direct-methane fuel cell with a ceria-based anode. *Nature*, 1999. 400 (6745): p. 649-651.

[85] X.-F. Ye, B. Huang, S. R. Wang, Z. R. Wang, L. Xiong and T. L. Wen, Preparation and performance of a Cu–CeO_2–ScSZ composite anode for SOFCs running on ethanol fuel. *J. Power Sources*, 2007. 164 (1): p. 203-209.

[86] C. J. Laycock, J. Z. Staniforth and R. M. Ormerod, Biogas as a fuel for solid oxide fuel cells and synthesis gas production: effects of ceria-doping and hydrogen sulfide on the performance of nickel-based anode materials. *Dalton Trans.*, 2011. 40 (20): p. 5494-5504.

[87] X.-F. Ye, S. R. Wang, Q. Hu, J. Y. Chen, T. L. Wen and Z. Y. Wen, Improvement of Cu–CeO_2 anodes for SOFCs running on ethanol fuels. *Solid State Ionics*, 2009. 180 (2–3): p 276-281.

[88] A. Trovarelli, *Catalysis by Ceria and Related Materials*. Imperial College Press, 2002.

[89] D. Lee, I. Lee, Y. Jeon, and R. Song, Characterization of scandia stabilized zirconia prepared by glycine nitrate process and its performance as the electrolyte for IT-SOFC. *Solid State Ionics*, 2005. 176 (11–12): p. 1021-1025.

[90] Z. Cai, T. N. Lan, S. Wang and M. Dokiya, Supported Zr(Sc)O_2 SOFCs for reduced temperature prepared by slurry coating and co-firing. *Solid State Ionics*, 2002. 153 (2002): p. 583-590.

[91] R. Liu, C. Zhao, J. Li, F. Zeng, S. Wang, T. Wen and Z. Wen, A novel direct carbon fuel cell by approach of tubular solid oxide fuel cells. *J. Power Sources*, 2010. 195 (2): p. 480-482.

[92] H. Gu, R. Ran, W. Zhou and Z. Shao, Anode-supported ScSZ-electrolyte SOFC with whole cell materials from combined EDTA–citrate complexing synthesis process. *J. Power Sources*, 2007. 172 (2): p. 704-712.

[93] C. Lu, Development of intermediate-temperature solid oxide fuel cells for direct utilization of hydrocarbon fuels. *Solid State Ionics*, 2004. 175 (1–4): p. 47-50.

[94] K. Kobayashi, I. Takahashi, M. Shiono and M. Dokiya, Supported $Zr(Sc)O_2$ SOFCs for reduced temperature prepared by electrophoretic deposition. *Solid State Ionics*, 2002. 152–153 (1): 591-596.

[95] B. Timurkutluk, C. Timurkutluk, M. D. Mat and Y. Kaplan, Development of high-performance anode supported solid oxide fuel cell. *Int. J. Energy Res.*, 2012. 36 (15): p. 1383-1387.

[96] G. Y. Cho, Y. H. Lee, S. W. Hong, J. Bae, J. An, Y. B. Kim and S. W. Cha, High-performance thin film solid oxide fuel cells with scandia-stabilized zirconia (ScSZ) thin film electrolyte. *Int. J. Hydrogen Energy*, 2015. 40 (45): p. 15704-15708.

[97] R. Steinberger-Wilckens, M. Lugovy, and D. Klein, *Development of Sofc Based on Scandia Doped Zirconia Ceramics.* Fundamentals and developments of fuel cells conference (FDFC 2008).

[98] Y. S. Hong and H. H. Yoon, Preparation of Scandia-Stabilized Zirconia Electrolyte Thin Films for Intermediate Temperature-Solid Oxide Fuel Cells by Electron Beam Vapor Deposition. *Japanese J. Appl. Phys.*, 2011. 50 (1): p. 01BE 01-09.

[99] D. Virbukas, G. Laukaitis, J. Dudonis, O. Katkauske and D. Milčius, Scandium stabilized zirconium thin films formation by e-beam technique. *Solid State Ionics*, 2011. 184 (1): p. 10-13.

[100] M. Andrzejczuk, O. Vasylyev, M. Brychevskyi, L. Dubykivskyi, A. Smirnova, M. Lewandowska, K. J. Kurzydłowski, R. Steinberger-Wilckens, J. Mertens and V. Haanappel, Structural features and gas tightness of EB-PVD 1Ce10ScSZ electrolyte films. *Mater. Sci.*, 2012. 30 (3): p. 170-179.

[101] Y. Shiratori, T. Oshima and K. Sasaki, Feasibility of direct-biogas SOFC. *Int. J. Hydrogen Energy*, 2008. 33 (21): p. 6316-6321.

[102] K. Ke, A. Gunji, H. Mori, S. Tsuchida, H. Takahashi, K. Ukai, Y. Mizutani, H. Sumi, M. Yokoyama and K. Waki, Effect of oxide on carbon deposition behavior of CH_4 fuel on Ni/ScSZ cermet anode in high temperature SOFCs. *Solid State Ionics*, 2006. 177 (5–6): p. 541-547.

[103] H. Kishimoto, K. Yamaji, T. Horita, Y. Xiong, N. Sakai, M. E. Brito and H. Yokokawa, Feasibility of liquid hydrocarbon fuels for SOFC with Ni–ScSZ anode. *J. Power Sources*, 2007. 172 (1): p. 67-71.

[104] H. Sumi, K. Ukai, Y. Mizutani, H. Mori, C. Wen, H. Takahashi and O. Yamamoto, Performance of nickel-scandia-stabilized zirconia cermet anodes for SOFCs in 3% H_2O-CH_4. *Solid State Ionics*, 2004. 174 (1–4): p. 151-156.

[105] B. Huang, S. R. Wang, R. Z. Liu and T. L. Wen, Preparation and performance characterization of the Fe–Ni/ScSZ cermet anode for oxidation of ethanol fuel in SOFCs. *J. Power Sources*, 2007 167 (2): p. 288-294.

[106] B. Huang, X. F. Ye, S. R. Wang, H. W. Nie, J. Shi, Q. Hu, J. Q. Qian, X. F. Sun and T. L. Wen, Performance of Ni/ScSZ cermet anode modified by coating with $Gd_{0.2}Ce_{0.8}O_2$ for an SOFC running on methane fuel. *J. Power Sources*, 2006. 162 (2): p. 1172-1181.

[107] M. R. Somalu, V. Yufit, D. Cumming, E. Lorente and N. P. Brandon, Fabrication and characterization of Ni/ScSZ cermet anodes for IT-SOFCs. *Int. J. Hydrogen Energy*, 2011. 36 (9): p. 5557-5566.

[108] L. Troskialina, *Improved Performance of Solid Oxide Fuel Cell Operating on Biogas Using Tin Anode-Infiltration,* PhD Thesis, University of Birmingham, 2016.

[109] J. Myung, S.-D. Kim, T. H. Shin, D. Lee, J. T. S. Irvine, J. Moon and S.-H. Hyun, Nano-composite structural Ni-Sn alloy anodes for high performance and durability of direct methane-fueled SOFCs. *J. Mater. Chem. A*, 2015. 3 (26): p. 13801-13806.

[110] H.-C. Tsai, S. I. Morozov, T. H. Yu, B. V Merinov and W. A. Goddard, First-Principles Modeling of Ni_4M (M = Co, Fe, and Mn) Alloys as Solid Oxide Fuel Cell Anode Catalyst for Methane Reforming. *J. Phys. Chem. C*., 2016. 120 (1): p. 207-214.

[111] A. Benyoucef, D. Klein, C. Coddet and B. Benyoucef, Development and characterisation of (Ni, Cu, Co)-YSZ and Cu-Co-YSZ cermets anode materials for SOFC application. *Surf. Coatings Technol*., 2008. 202 (10): p. 2202-2207.

[112] M. R. Somalu, V. Yufit and N. P. Brandon, The effect of solids loading on the screen-printing and properties of nickel/scandia-stabilized-zirconia anodes for solid oxide fuel cells. *Int. J. Hydrogen Energy*, 2013. 38 (22): p. 9500-9510.

CHAPTER 3
MATERIALS AND METHODS

This chapter discusses the materials and preparation process for the manufacture and testing of anode-supported Ni-ZrO_2 SOFCs.

3.1 SOLID OXIDE FUEL CELL COMPONENT MATERIALS

As discussed previously in Chapter 2, the state of the art SOFC is based on a porous Ni-YSZ cermet anode, a dense YSZ electrolyte and an LSM-YSZ composite cathode [1], [2]. These material choices best fulfil SOFC component requirements with chemical and thermal stability in oxidising and reducing environments, good conductivity, high catalytic activity and sufficient mechanical strength properties – all characteristics of a performing SOFC. Due to its low cost, good electronic conductivity and high catalytic activity for hydrogen oxidation, Ni is considered the best catalyst of all materials considered [3]. $0.08(Y_2O_3)$-$0.92(ZrO_2)$ is the most widely used YSZ composition for SOFC electrolytes

due to its stability and high ionic conductivity at elevated temperatures over a wide range of oxygen partial pressures though a variety of oxide dopants with high solubilities in ZrO_2 can be used [4], [5]. The Sr-doped $LaMnO_3$ ($La_{1-x}Sr_xMnO_3$) cathode (LSM) is a p-type conducting oxide at high oxygen partial pressures (p_{O_2}) and exhibits a higher electronic conductivity than undoped $LaMnO_3$ [6]. In oxygen rich environments and at temperatures > 700°C, LSM conductivity is stabilised though conductivity decreases significantly in reducing environments [5]–[7]. Due to cost as well as compatibility with YSZ electrolytes, LSM is the cathode material of choice. Interconnects serve as the contact by which multiple cells are electrically joined in series to form stacks for a given desired power output. The most common interconnect material Strontium and Vanadium doped Lanthanum Cobaltite (LSCV) is used because of its compatibility with other cell components, good conductivity and stability in cell testing environments [5]. Because the research in this study was conducted on single cells, extensive information regarding interconnect research and development will not be provided. Table 3.1 lists the state of the art SOFC component materials in the first column with the alternative class of materials chosen for this study listed in the last column.

Table 3.1: State of the Art SOFC Component Materials [1], [2], [5], [8]

Anode	**Requirements**	**Advantage over Ni-YSZ**
$Ni(Y_2O_3)_{0.08}$ - $(ZrO_2)_{0.92}$ (Ni-YSZ)	good TEC match with YSZ good $\sigma_{electronic}$ good porosity stability in H_2 atmosphere active for H_2 oxidation redox stability	Ni-10Sc1CeSZ higher σ_{ionic} contribution from 10Sc1CeSZ Ce is a CH_4 oxidation catalyst, Ni-10Sc1CeSZ can be used on both H_2 and CH_4 fuels
Electrolyte	TEC match with electrodes	**Advantage over YSZ**
$(Y_2O_3)_{0.08}$ - $(ZrO_2)_{0.92}$ (YSZ)	high σ_{ionic}, low $\sigma_{electronic}$ dense and leak tight stability in test atmosphere	10Sc1CeSZ σ_{1000} (0.30 Scm^{-1}) - ScSZ σ_{1000} (0.13 Scm^{-1}) - YSZ reduced T_{op} due to higher σ
Cathode	good TEC match with YSZ	**Advantage over LSM-YSZ**
$La_{0.8}Sr_{0.2}MnO_3$ (LSM-YSZ)	mixed $\sigma_{electronic}$, σ_{ionic} good porosity stability in O_2 atmosphere active for O_2 reduction	LSCF higher $\sigma_{electronic}$, (MIEC) has reaction pathways over entire cathode surface = more TPB points
Interconnect	dense	
$LaCrO_3$ (LSCV)	compatibility with SFC components	

3.2 MATERIAL CHOICES FOR INTERMEDIATE TEMPERATURE SOLID OXIDE FUEL CELLS (IT-SOFCS)

The high operating temperature of SOFCs drives degradation, slows down startup time, and places stringent requirements on the choice of fuel cell materials. Research trends focused on the development of SOFCs that operate in intermediate temperature regimes (700-850^{o}C) predominate, with an emphasis on simplifying the manufacturing process [9] in order to produce cost-effective, high performance fuel cell systems that extend the current reach of SOFC commercialisation and widen their scope of use in green energy markets [10]–[12]. Careful selection must be given to the most appropriate material systems that yield the target properties within the specified temperature range. At present this remains a challenge, as there is no wide range of alternate materials fully developed for intermediate temperature operation. A few have been studied and are briefly outlined below.

3.2.1 Electrolytes

One approach to lowering the operating temperature is to enhance the ionic conductivity of the electrolyte system. Steele introduced the use of Gadolinia doped Ceria ($Ce_{0.9}Gd_{0.1}O_{1.95}$ - GDC) electrolytes for operation in the 500-700^{o}C range with GDC peak conductivity observed at 20-25 mol% Gadolinia, reporting consistently higher conductivities over both ScSZ and YSZ systems at and below 600^{o}C [5], [13]–[15]. The $Ce_{0.9}Gd_{0.1}O_{1.95}$ composition, however, has been shown to demonstrate better stability than the $Ce_{0.8}Gd_{0.2}O_{1.95}$ composition at low oxygen partial pressures [16]. It is important to note that GDC is a mixed ionic-electronic conductor and at high oxygen partial pressures is primarily an ionic conductor but at low oxygen partial pressures Ce^{4+} is easily reduced to Ce^{3+} introducing electronic conductivity that predominates at higher SOFC operating temperatures > 650^{o}C [4], [5], [17]. This electronic conductivity can flow through the electrolyte even at OCV conditions causing further deviations from theoretical OCV values lowering the cell's potential placing limitations on the maximum achievable voltage. This makes GDC a less suitable choice as an intermediate temperature SOFC electrolyte and excluded altogether for high SOFC operating temperatures.

Samaria doped Ceria (SDC) is another material in the class of doped ceria electrolytes with the $Sm_{0.2}Ce_{0.8}O_{1.9}$ composition exhibiting the highest conductivity of 0.023 S cm^{-1} at 600^{o}C amongst all the CeO dopants [18] due to the large number of oxygen vacancies and the smallest radius mismatch between the Sm^{3+} and Ce^{4+} ions resulting in increased O^{2-} vacancy migration. The conductivity of the SDC system is composition dependent with sintering conditions heavily influencing conductivity properties. The problem of Ce^{4+} to Ce^{3+} reduction in low oxygen partial pressure environments at elevated temperatures remains a concern though the use of doped ceria electrolytes at temperatures below

650^{o}C remains a viable option.

Doped lanthanum gallate ($La_{0.9}Sr_{0.1}Ga_{0.8}Mg_{0.2}O_3$-LSGM) is another electrolyte material considered for IT-SOFCs as the ionic conductivity is higher than that of both ScSZ and YSZ between 200 and 800^{o}C and comparable to that of GDC within the same temperature range [6], [13], [15], [19], [20]. And unlike ceria electrolytes where Ce^{+4} reduces to Ce^{3+} in low oxygen partial pressures, LSGM remains stable in such environments and is compatible with conventional lanthanum manganite (LSM) and low temperature lanthanum cobaltite (LSCF) cathodes, though some Mn diffusion into LSGM [21] and inter-diffusion between LSCF and LSGM has been reported [4], [6], [13], [15], [19], [22]. Preparing phase pure LSGM for some compositions remains a challenge as $SrLaGa_3O_7$ and $La_4Ga_2O_9$ secondary phases for the $La_{0.8}Sr_{0.2}Ga_{0.8}Mg_{0.2}O_3$ system have been detected in the grain boundaries while the $La_{0.9}Sr_{0.1}Ga_{0.8}Mg_{0.2}O_3$ system produces almost phase pure material [23]. The phase purity of LSGM is heavily dependant on stoichiometry so it is important that the composition of this material is controlled. Regarding electrolyte-anode stability, the chemical compatibility between LSGM electrolytes and Ni-based anodes is compromised as LSGM reacts quickly with Ni resulting in the formation of $LaNiO_3$ insulating phases which give rise to high anode overpotentials that quickly increase with time in addition to La loss during half-cell co-firing both of which lower cell performance [1], [4], [5], [15], [24]. Other disadvantages including poor mechanical strength and the high cost of GaO [20] made LSGM unsuitable for this study.

Sc_2O_3 stabilized ZrO_2 (ScSZ) is an ideal candidate as an IT-SOFC electrolyte because Sc_2O_3 has the highest conductivity of all the ZrO_2 dopants. A comparison of the temperature dependent conductivities for the different oxygen ion conductors is shown in Figure 3-1. The mismatch between the host Zr^{+4} and dopant Sc^{3+} radius is the least, minimising dopant-vacancy interaction and reducing the barrier to O^{2-} vacancy migration which leads to higher conductivities [15], [25], [26]. Ageing both the YSZ and ScSZ systems at 1000^{o}C for 1000hrs leads to disruptions in conductivity with 9-11 mol% Sc_2O_3-ZrO_2 showing small conductivity decreases when compared with 7.0-9.0 mol% Sc_2O_3-ZrO_2, which had conductivity losses much larger than 8 mol% Y_2O_3-ZrO_2 which were also greater than losses observed for Y_2O_3-ZrO_2 systems at higher Y_2O_3 concentrations [4], [15], [27], [28]. Increasing dopant levels suppresses degradation with no conductivity decreases observed for Sc_2O_3-ZrO_2 doped with 11-13 mol% Sc_2O_3 [29].

For the 10 mol% ScSZ system, where the conductivity maximum is reached, a mixture of dominant cubic and rhombohedral (β) phase exists [25], [30] with the (β) phase transforming to cubic

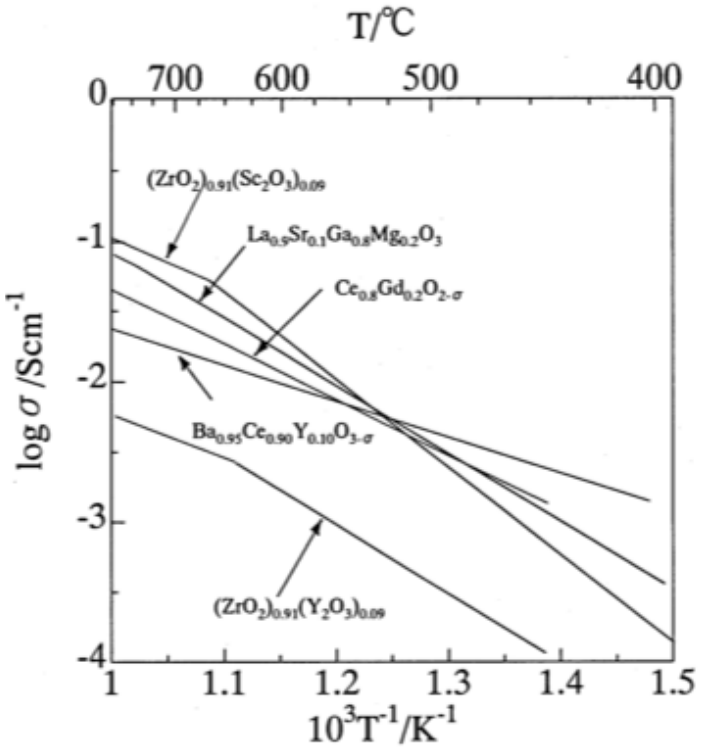

Figure 3-1. Conductivity as a function of temperature for different oxygen ion conductors [4]

phase at 1000°C [25]. Co-doping ScSZ with CeO_2 has been shown to stabilise the cubic phase to temperatures below 1000°C, though phase transitions from cubic to the lower conducting rhombohedral phase (β) are observed at temperatures of 600°C and below [15], [16], [28], [31]–[35]. The choice of CeO_2 as a co-dopant is well suited because the cubic phase is stabilised until 1500°C [36]–[38] and also because CeO_2 acts as an oxidation catalyst for hydrocarbon fuels exhibiting a high resistance to carbon deposition [2], [39]–[41], so fuel flexibility is an added benefit. The multicomponent phase and instability of the ScSZ system remains a focus of interest for researchers [42]–[44] as the problems outlined in previous studies regarding phase transitions during ageing and upon cooling [25], [34], [37] persist, limiting extensive development of this system for IT-SOFC applications.

After careful consideration of all electrolyte candidate materials and despite the phase stability setbacks of the Sc_2O_3-ZrO_2 system, ZrO_2 doped with 10 mol% Sc_2O_3 and 1 mol% CeO_2, was the intermediate temperature electrolyte composition chosen for this study. The electrolytic properties of this material are a best match for the cell test conditions explored in this research along with knowledge contributions to be gained related to the performance of intermediate temperature anode supported 10Sc1CeSZ cells. Results published by researchers who have extensively studied the properties of ScSZ co-doped with CeO_2 and assessed its suitability as an alternative electrolyte material for IT-SOFCs have

been presented. As this work focuses on the fabrication and testing of 10Sc1CeSZ cells manufactured via screen-printing, extensive research related to the influence of dopant composition on system properties can be verified in the literature and will not be duplicated here. Published work shows 10 mol% ScSZ co-doped with 1 mol% CeO_2 possesses the highest ionic conductivity and exhibits good stability in both oxidising and reducing environments under extended, intermediate temperature conditions [45]. Thus, the performance of this system on H_2 and CH_4 will be studied in this work.

3.2.2 Anodes

Doped strontium titanate ($SrTiO_3$), a mixed ionic and electronic conductor (MIEC) that exhibits electronic conduction at low oxygen partial pressures, has garnered substantial interest and has been studied extensively to determine its appropriateness for use as a fuel electrode in SOFCs [46]–[53]. Literature reports that (La,Sr) doped $SrTiO_3$ bodes well as an alternative anode material as different compositions allows various approaches to be considered for achieving the properties best suited for SOFC application. The interest in $SrTiO_3$ was born out of a need to address the coking problem with Ni-based anodes as well as the reactivity problem between LSGM electrolytes and Ni-based anodes. $SrTiO_3$ also provides redox stability in anodes [48], [54]. $SrTiO_3$ performance though, is compromised when compared against Ni-YSZ anodes due to high anode polarisation and poor catalytic activity in the ceramic [55]. The use of bilayers, $SrTiO_3$ anode composites and catalyst dopants have been added to the cell structure to reduce anode polarisation and improve performance [46], [53], [56]–[58]. The data surrounding $SrTiO_3$ anodes is encouraging but is not of interest in this work as the use of LSGM electrolytes and the testing of SOFCs under oxidation-reduction conditions are not explored here.

Doped Ni-YSZ, Ni-GDC and Ni-ScSZ anodes are all alternative anode systems of interest and have been proposed for better compatibility with GDC and ScSZ electrolytes. They enhance sulphur tolerance while suppressing carbon deposition during hydrocarbon operation [59]. Investigating the use of metal alloys in Ni-ZrO_2 and Ni-CeO_2 anodes that do not catalyse the formation of carbon but that have found to be less catalytically active than Ni have been explored [60]–[64]. Use of Ni-ScSZ anodes based on a ScSZ cell structure for hydrocarbon operation has been studied in depth [65]–[69] but the use of Ni-ScSZ anodes for intermediate temperature operation deserves more attention [70], [71]. Based on the chosen 10Sc1CeSZ composition for the ScSZ system, Ni-10Sc1CeSZ was selected as the anode material.

3.2.3 Cathodes

Alongside the introduction of doped lanthanum manganate cathodes ($La_{1-x}Sr_xMnO_3$), doped

lanthanum cobaltite cathodes ($La_{1-x}Sr_xCoO_3$) have also been proposed for SOFC use especially at intermediate temperatures [5]. Sr is a commonly used dopant as it has a similar ionic radius to La [72]. $La_{1-x}Sr_xMnO_3$ and $La_{1-x}Sr_xCoO_3$ share the same ABO_3 crystal structure and possess defects (oxygen and La deficiency or excess) that are heavily dependent on system temperature, oxygen partial pressure and material composition, which significantly influence system conductivity [5], [72]. The doping of both $LaMnO_3$ and $LaCoO_3$ systems creates excess Mn^{4+} and Co^{4+} cation vacancies when the Sr^{2+} divalent acceptor atom replaces the La^{3+} trivalent host as seen in expressions 3.1 and 3.2 respectively [5], [6], [73]:

$$LaMnO_3 \longrightarrow La_{1-x}^{3+}Sr_x^{2+}Mn_{1-x}^{3+}Mn_x^{4+}O_3 \qquad (3.1)$$

$$LaCoO_3 \longrightarrow La_{1-x}^{3+}Sr_x^{2+}Co_{1-x}^{3+}Co_x^{4+}O_3 \qquad (3.2)$$

These cation vacancies (electron holes) then become the primary charge carries in these p-type conductors. $La_{1-x}Sr_xCoO_3$ is slightly different from $La_{1-x}Sr_xMnO_3$ as it is a mixed ionic and electronic conductor (MIEC) that exhibits higher electronic and ionic conductivity than $LaMnO_3$ [73]. For the $La_{1-x}Sr_xCoO_3$ system, Sr doping increases oxygen vacancy concentration further increasing its TEC ($20x10^{-6}$ K^{-1}) which is in contrast to the $La_{1-x}Sr_xMnO_3$ system as Sr doping produces no oxygen vacancies but results in a lower TEC ($11x10^{-6}$ K^{-1}) [72], [74]. The benefit of having a (MIEC) cathode is the various pathways which the electrochemical reactions can take as they are not limited to the cathode-electrolyte surface as is the case with $LaMnO_3$ but can also occur at any open pore surface within the cathode [72]. This reduces cathode polarisation losses improving performance. Figure 3-2 is a pictorial representation of the three cathode types and the different possible reaction pathways as reported by Sun et al. [72]. For $La_{1-x}Sr_xCoO_3$, there has also been the substitution of Fe on the B-site for cobalt in the $LaCoO_3$ system which has further improved performance as written in expression 3.3 [6]:

$$La_{1-x}\,Sr_xCo_{1-y}Fe_yO_3 \qquad (3.3)$$

A major difference between $LaMnO_3$ and $LaCoO_3$ is that $LaCoO_3$ is more reactive with YSZ electrolytes and forms $SrZrO_3$ and $La_2Zr_2O_7$ insulating phases at elevated temperatures $\geq$ 800°C [4], [5], [27], [73], [75]. The compositional dependence for the formation of $SrZrO_3$ and $La_2Zr_2O_7$ phases in $La_{1-x}Sr_xMnO_3$ cathodes, brought about by Mn and Sr migration respectively, is rather complicated but can be minimised

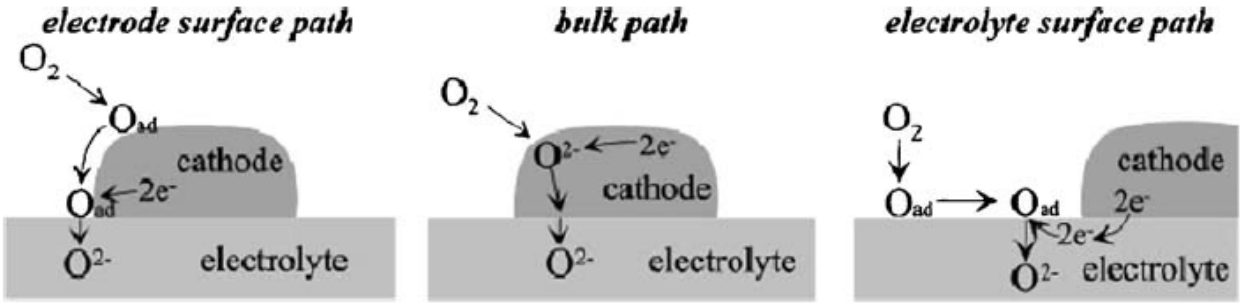

Figure 3-2: Reaction pathways for a cathode p-type conductor (a - LSM), a MIEC (b - LSCF) and a composite cathode (c - LSM-YSZ) [72]

where x<0.3 [5], [76] and when fabrication temperatures are kept below 1300°C [5], [6]. The greater TEC of $La_{1-x}Sr_xCoO_3$ creates a greater TEC mismatch with YSZ than what exists for $La_{1-x}Sr_xMnO_3$ which can cause sintering stresses during firing, creating new concerns [6]. Despite these drawbacks, intermediate temperature SOFCs typically use $La_{1-x}Sr_xCo_{1-y}Fe_yO_3$ (LSCF) cathodes as their superior peformance over $La_{1-x}Sr_xMnO_3$ cathodes in this temperature regime outweighs their negative properties. And because no significant zirconate phase formation between YSZ electrolytes and $LaCoO_3$ cathodes has been reported when doped CeO_2 interlayers are used, cell structures based on this combination have been developed [4], [77]. In this work, LSCF cathodes deposited over a GDC interlayer film were used for the ScSZ SOFC system.

3.2.4 Anode Porosity

Electrode microstructure is very critical to the performance of SOFCs. In the case of anode supported SOFCs, it is necessary to develop anode structures that are porous enough to efficiently transport reactant gas to the reaction sites and remove fuel by-products without sacrificing strength or increasing anode polarisation [16]. Pore size, pore count, pore morphology and pore distribution all have an impact on anode microstructure influencing anode substrate strength, sintering behaviour, conductivity and permeability so it is crucial to fabricate structures that yield the desired anode properties.

Researchers have fabricated anodes incorporating the use of different pore formers and different pore former content to determine the relationship between the characteristics of the starting powders, the sintered structure and properties that effect overall cell performance [78]–[82]. Jin et al. [82] studied the influence of flour and graphite on the microstructure of NiO-YSZ anodes and found a rapid increase in cell resistance when porosity levels exceeded 55% with the particle morphology of the different pore

formers heavily influencing the size and distribution of the pores formed in the anode microstructure. It was shown that the weight loss profiles of the samples containing flour exhibited a faster sintering shrinkage that produced large, non-uniformly distributed pores which may compromise mechanical stability while the graphite samples had a much slower decomposition producing smaller, more uniform pores. Cells were prepared using graphite as the pore former of choice due to the higher surface area of the smaller pores leading to enhanced electrochemical reactions at the TPB.

Yu et al. [80] studied the relationship between pore volume content and the size and morphology of starting NiO and YSZ powders and the influence of these factors on the electrical properties and final microstructure of the anode. Changing carbon black levels from 40% vol to 13% vol resulted in a more porous structure (79% theoretical density) when the combination of coarse YSZ and fine NiO powders were used (CF-13) compared with denser microstructures for the 40% vol anode samples (86% theoretical density) prepared with both fine NiO and YSZ powders (FF-40). The conductivities of both CF-13 and FF-40 samples were comparable. For the CF-13 sample, the finer NiO particles surrounding the coarse YSZ powders created a continuous Ni phase as were observed for the FF-40 sample, which aided in enhanced conductivity. And despite lower carbon levels for the CF-13 samples resulting in higher porosities, the degree of densification observed for the NiO-YSZ composites is dominated by the sintering kinetics of the starting materials. Finer powders have increased contact and more energy to rearrange and move facilitating mass transport and pore removal unlike coarser powders, which in this study were isolated inhibiting neighbouring particle-particle contact thus reducing densification. The trend of increasing porosity with increasing levels of carbon black was observed for both sample sets with similar decreases in vol% Ni though the magnitude of the increase was higher for the CF samples.

Sarikya et al. showed a direct relationship between the distinct features of different pore former particles (flake graphite, PMMA, spheroidal graphite, sucrose and polystyrene) and the resultant pore structures formed in the fired ceramic [78]. It was also found that polymer based pore formers decomposed quickly and completely by 400^{o}C while the burnout procedure for graphite pore formers occurred more slowly and at higher temperatures resulting in lower bulk porosities for the polymer pore former samples compared with the graphite samples. Virkar reports gradual decreases in ASR as porosity increases with ASR changes from 0.156 Ω cm^2 to 0.074 Ω cm^2 observed for minimum and maximum porosities of 32% and 76% respectively as well as an increase in current density from 352 mA cm^{-2} to 783 mA cm^{-2} for the same porosity levels where carbon was used as a pore former [79]. A range of materials – rice starch, potato starch, carbon black and graphite – have been previously used as anode

pore formers [27], [83] in SOFC manufacture and in this work the use of tapioca starch and wheat flour, both market grade powders and carbon black (Vulcan) were explored.

3.3 SOFC RAW MATERIALS

Provided in Table 3.2 is a list of the raw materials used in the manufacture and testing of the anode supported SOFCs used in this study. The material classification, use and manufacturer name are given.

3.4 SOFC BUTTON CELL MANUFACTURE

3.4.1 Ni-ZrO_2 Substrate Fabrication

As seen in Figure 3-3, Ni-ZrO_2 anode supported fuel cells were prepared by combining NiO (Novamet-A) powder with:

- ✓ 8YSZ (TZ-8YS, Tosoh) in a 70:30 wt% NiO:YSZ ratio
- ✓ 10Sc1CeSZ (DKKK or IPMS) in a 70:30/60:40 wt% NiO:10Sc1CeSZ ratio
- ✓ 10 wt% pore former
- ✓ 3 wt% Oxalic Acid (Sigma-Aldrich) as surfactant
- ✓ 5 wt% PVB (Pioloform BL-16, Wacker) as binder

The starting powders were wet milled in ethanol and placed on a horizontal rotating ball mill and milled overnight at 180 rpm using spherical (3 mm and 15 mm) and cylindrical (3/8") ZrO_2 beads. The ball milling step was implemented for efficient powder mixing and to break up any agglomerates in the as-received powders. Media beads of the same composition as the material to be mixed were used as this minimises contamination. The chosen milling speed considered the jar diameter and the diameter of the rollers to ensure milling action where the media balls tumble and fall from the top of the container as the jar rotates crushing the powders. Very high speeds can cause the media to line the container walls without any contact with the powders while too low speeds can prevent the media from cascading down on the powders both resulting in ineffective milling. The volume of the container used was at minimum 30% larger than the total volume of the powder, media and solvent so there existed sufficient space for rolling. Wet milling was chosen over dry milling as it has a greater propensity to crush hard agglomerates with the amount of solvent added enough to form fluidal slurry. While milling time can only be determined by trial and error for a specific system, in this work, overnight milling was sufficient for good powder mixing and homogeneity. The powder slurry was stir dried while heated at 60^{o}C to

Table 3.2: SOFC Raw Materials

Source	Material	Classification	Use
Novamet	NiO-A	anode powder	bulk/active anode
Pi-Kem	NiO	anode powder	bulk/active anode
Tosoh	TZ-8YS	electrolyte powder	electrolyte film
IPMS	10Sc1CeSZ	electrolyte powder	electrolyte film
DKKK	10Sc1CeSZ	electrolyte powder	electrolyte film
FCM	GDC-10	electrolyte powder	blocking layer
Sigma Aldrich	α-Al_2O_3	powder	sintering aid
Praxair	LSM	cathode powder	cathode film
Praxair	LSCF	cathode powder	cathode film
Vulcan	carbon	pore former	bulk anode
Market	tapioca starch	pore former	bulk anode
Market	wheat flour	pore former	bulk anode
Sigma Aldrich	Oxalic Acid	surfactant	bulk anode
Wacker	Pioloform BL-16	PVB binder	bulk anode
Heraeus	V-737	vehicle	printing inks
Shanghai Institute of Synthetic Resins	DAD87	Ag paste	wire contacts cell sealant current collector
Fiaxell	M_Grid	Au Grid	current collector
Aremco	Ceramabond 552-VFG	ceramic sealant	cell sealant
Almath		alumina tube	cell testing tube
Scientific Wire Company	Ag spool	0.25mm Ag wires	cell leading wires
NIMTE (CAS)	YSZ	anode supported button cells	commercial reference cell
NIMTE (CAS)	10Sc1CeSZ	electrolyte supported button cells	commercial reference cell

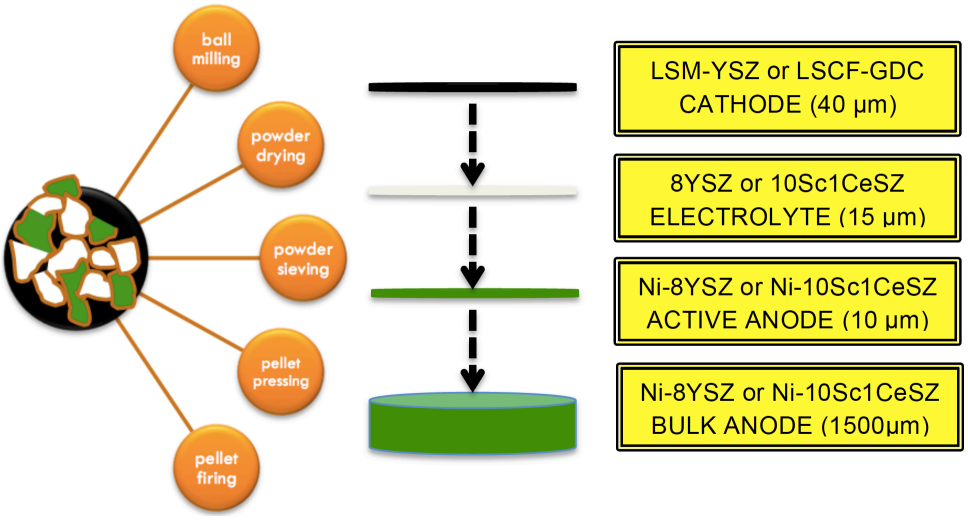

Figure 3-3: Ni-ZrO_2 anode substrate manufacture and cell design approach

prevent powder segregation then ground and sieved using a 32 μm mesh screen. The sieved powder was uniaxially compacted under a pressure of 5.5 ton cm^{-2} to form 35 mm diameter discs. The discs were pre-fired in air at 1°C/min to 325°C and 500°C respectively, where they dwelled at each temperature for one hour to burn off organic additives and then heated at 3°C/min to target sintering temperatures ranging from 1000 to 1200°C where they were held for 2, 4, 6 or 8hrs and then cooled at 5°/min to room temperature.

3.4.2 Preparation of Ni-YSZ/Ni-10Sc1CeSZ Single Cells

The microstructure of the Ni-YSZ anode is heavily influenced by the properties of the starting powders, the NiO:YSZ ratios and the manufacturing method of the anode component. As mentioned in Chapter 2, Section 2.12 the general anode requirements are [2]:

i. good TEC matches with the electrolyte
ii. good electronic conductivity >100 S cm^{-1}
iii. good ionic conductivity >10 mS cm^{-1}
iv. chemical and thermal stability in the test environment and with other cell components (electrolyte, interconnect)
v. catalytic activity for fuel oxidation
vi. creation of the TPB reaction zone, the site for the cell reactions
vii. sufficient porosity for fuel transport and removing reacted gas
viii. tolerance against thermal and RedOx cycling such that anode functionality and structural integrity is not compromised

To sustain good conductivity, a minimum of 30% Ni by volume in the Ni-YSZ anode cermet is required [84]–[86]. Below this value the Ni-YSZ system behaves as a more or less pure ionic conductor as evidenced by the large, abrupt drop in conductivity at 30 vol% Ni for two Ni-YSZ systems prepared with different YSZ powders as seen in Figure 3-4. These findings are supported by the concept of percolation threshold an idea supported by percolation theory, a mathematical model used to explain the connectivity and creation of a continuous framework of a component within a binary system or random environment [87].

Percolation theory analyses the network connectivity of a system and predicts that ~30 vol% Ni is the percolation threshold for the Ni phase and suggests this is the volume fraction of Ni required to create an interconnected conducting pathway through the Ni metal phase [88], [89]. Results reported by

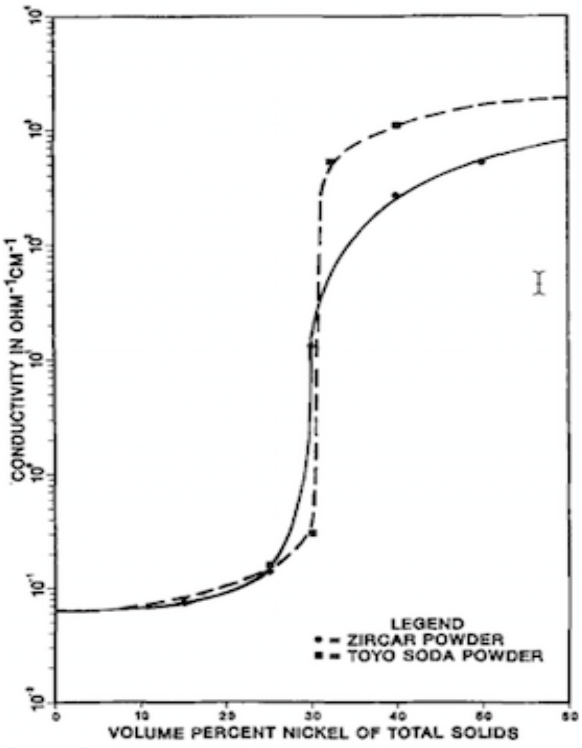

Figure 3-4: Conductivity curve of Ni-YSZ cermets at varying Ni solids content [84]

Kawashima et al. confirm the findings of Dees et al. which show a dramatic increase in conductivity for Ni-volume fractions exceeding 32% suggesting a change in the conduction mechanism to electronic conduction through the Ni phase from ionic conduction through the YSZ phase where much lower conductivity is observed [84], [88], [90]. Because the conductivity of Ni is much higher than the conductivity of YSZ the main conduction path will be through the Ni phase as long as it is continuous [84]. Kawashima et al. also found that "*at the percolation threshold, only 20% of the total Ni participates in the conduction cluster formation, and 80% of the Ni particles in the TPB cannot act as the anode. For Ni volume fractions above 44%, 90% of the total Ni particles participate in forming the TPB.*" Lee et al. [89] varied the Ni content in Ni-YSZ anodes from 10 to 70 vol% and reported similar findings to those of Dees and Kawashima with sharp conductivity increases at 32 vol% Ni with gradual increases in conductivity above 35% vol Ni. Koide et al. reported the percolation threshold at 40 vol% Ni for Ni-YSZ samples where the Ni content varied from 31 to 87 vol% with the highest power output obtained for the 87:13 Ni-YSZ sample. Koide also showed reduced ohmic resistance and polarisation increases with increased Ni content. These findings show the electrical behaviour of Ni-YSZ anodes is strongly influenced by Ni content.

3.4.2.1 NiO-ZrO_2 Substrate Volume Ratios

A fixed 70:30 wt% NiO-YSZ (68:32 vol% NiO-YSZ) composition for the Ni-YSZ anode substrates was selected based on percolation theory, the published findings of Ni levels that promote good conductivity, the requirement of adequate mechanical strength and a good TEC match with the electrolyte. This ratio has also been used by previous researchers who report good TPB distribution at the anode-electrolyte interface and sufficient anode porosity which yielded low ohmic resistance and good performance [79], [86]. The 70:30 wt% NiO-10Sc1CeSZ composition was initially used for the Ni-10Sc1CeSZ support pellets but poor strength during handling and manufacturing was observed so the composition ratio was changed to 60:40 wt% NiO-10Sc1CeSZ (57:38 vol% NiO-10Sc1CeSZ). Researchers also report minimum polarisation losses [91] and power density values greater than 300 mW cm^{-2} [92], [93] for anode supported Ni-YSZ cells using the 60:40 wt% composition.

3.4.2.2 NiO-ZrO_2 Anode Functional Layers

The use of anode substrates for the SOFC ASC configuration serves to maintain the mechanical integrity and durability of the anode though large support thicknesses can contribute to concentration polarisation losses as fuel transport through thick supports may be compromised. There also exists the risk of discontinuity in the electronic conduction path through the Ni phase due to the presence of pores and the overall coarse microstructure thus the use of anode functional layers (AFLs) into the ASC design has been proposed [90], [94], [95]. The use of AFLs is designed to create a finer microstructure with many active sites where the gaseous phase, Ni phase and YSZ phase meet and the electrochemical reactions take place. Increasing the number of active sites for fuel oxidation through the use of AFLs can reduce the activation polarisation [79] and ohmic resistance [96]. The activation polarisation is a function of the concentration of electroactive species and the charge transfer resistance of those species in the TPB region so the greater the number of active sites the lower the activation polarisation. And as the ohmic resistance consists of the internal cell resistance, which includes the contact resistance at the interface between the electrodes and electrolyte, the ohmic resistance decreases as the contact between the anode-electrolyte at the interface is improved which is achieved through the use of AFLs. Other studies show decreased concentration polarisation and the highest power density of 0.73 W cm^{-2} for a SOFC prepared with a 20 μm thick AFL layer [97]. The improved performance was due to more reaction sites created by the AFL and sufficient transport of the gaseous species to the reactant sites due to the enhanced AFL microstructure. Cells prepared with AFLs that are too thick can result in low fuel permeation.

Researchers have shown the use of AFLs do not extend the reaction zone through the thickness of the support nor does it limit the active region to the anode-electrolyte interface; it lengthens the reaction area away from the anode-electrolyte interface into the depths of the anode [95], [98]–[100]. AFLs are also printed onto the coarse anode supports to provide a smoother surface upon which to deposit the electrolyte layer for improved adhesion and densification [96]. Examining the influence of varying AFL compositions [101], [102] and thicknesses [92], [97], [103]–[105] on anode microstructure and SOFC electrochemical performance falls outside the scope of this work but is something other researchers have studied. Based on the improved performance of the use of AFLs found in literature coupled with the surface roughness results reported in Chapter 5, Section 5.4.1, NiO-YSZ AFLs were integrated into the fabrication process [98], [106].

Ni-YSZ or Ni-10Sc1CeSZ (AFLs) were screen-printed onto their respective anode supports using a DEK Model 248 screen printer and 50:50 wt% solids loading inks. Previous studies show ASC SOFCs with NiO-YSZ AFL compositions within the 50:50 – 60:40 wt% range yielded good power densities and low anode polarisation so this was the basis for the 50:50 wt% composition used here [101], [107]. The inks were made by combining the powders with a terpeniol based vehicle (Heraeus V-737) and mixed using a three-roll mill (Exakt 50). Every cell contained two anode functional layer (AFL) prints where each print was followed by a 15 min ambient air dry and a 15 min oven dry in air at 120^{o}C.

3.4.2.3 YSZ/10Sc1CeSZ Electrolyte Layers

Screen-printed YSZ or 10Sc1CeSZ films were deposited onto their respective anode substrate/AFL cell structure using inks prepared similarly to the anode inks. Three electrolyte layers were printed per cell and followed the same drying schedule as the AFL prints. Both YSZ and 10Sc1CeSZ electrolyte inks had a solids loading of 40 vol% as this was the highest obtainable loading that yielded printable inks. A study of ink viscosity and ink printability was carried out and a more detailed discussion of these results can be found in Chapter 5, Section 5.7.3. The half-cells were co-fired at 1400^{o}C-4hrs in air using a 3^{o}C/min ramp rate up and a 5^{o}C/min ramp rate cool down to obtain the desired anode and electrolyte microstructures. During the manufacture of anode supported SOFCs, two high-temperature sintering steps are typically used: anode-electrolyte co-firing to achieve full electrolyte density followed by a lower temperature cathode-sintering step. Co-firing is a simple process that has been shown to produce high-quality ceramic multilayers but is not without its challenges. Mitigating these challenges through the use of a single step co-firing method has also been proposed [9]. Because each component in the multilayer has different shrinkage properties (anode support, anode functional

layer, electrolyte layer) it is important to select anode support processing conditions that yield partial sintering so during the co-sintering stage shrinkage mismatches between all components in the half-cell are minimised. Previous researchers report co-firing Ni-ZrO_2 anode/ZrO_2 electrolyte bilayers at 1400^{o}C-4hrs to achieve fully dense electrolyte films [108]–[111]. The co-sintering temperature profile for the YSZ and 10Sc1CeSZ half-cells is shown in Figure 3-5.

For the Ni-10Sc1CeSZ cells, 2 Gd_2O_3-CeO_2 (GDC) interlayer prints (GDC-10, Fuel Cell Materials) were screen-printed onto the 10Sc1CeSZ electrolyte films for improved adhesion of the LSCF-GDC cathodes and to serve as a blocking layer for the prevention of LSCF-10Sc1CeSZ reactions. GDC layers were deposited using inks prepared similarly to the anode and electrolyte inks**.** As discussed earlier in section 3.2.3, zirconate resistive phases have been known to form and have adverse effects on cell properties and performance when using doped lanthanum cobaltite cathodes ($La_{1-x}Sr_xCoO_3$) in direct contact with ZrO_2 electrolytes so a GDC barrier layer [112] is oftentimes used to intercept these reactions. SOFCs with GDC interlayers take advantage of the high ionic conductivity contribution of GDC and may also benefit from improved cell performance due to lower electrode polarisation and enhanced electrochemical reactions when doped CeO_2 interlayers are used as reported previously [113]–[115]. Table 3.3 summarises the printing conditions for the Ni-ZrO_2 half cells.

3.4.2.4 LSM-YSZ/LSCF-GDC Cathode Layers

Brush painting of the LSM-YSZ (LSM:$La_{0.8}Sr_{0.2}MnO_2$) cathodes was limited to a stenciled section of the fired Ni-YSZ/YSZ half cells and fired at 1175^{o}C-3hrs followed by paint brushed LSM layers fired at 1125^{o}C-3hrs [116]. For the 10Sc1CeSZ system, (LSCF: $La_{0.6}Sr_{0.4}Fe_{0.2}Co_{0.8}O_3$). LSCF-GDC cathodes followed by pure LSCF current collector layers were applied and fired at 975^{o}C-3hrs and 925^{o}C-3hrs respectively [117]. To maintain consistency in the application of the cathode layers, the same paintbrush, the same-stenciled area and the same number of brush strokes remained constant. Figure 3-6 summarises the manufacturing process and features a cross-sectional optical image of a Ni-YSZ/YSZ/LSM-YSZ/LSM anode supported single cell. The distinct microstructures of the different SOFC component layers are visible. YSZ and 10Sc1CeSZ system microstructures are discussed further in Chapters 5 and 6.

3.5 SOFC TESTING AND ANALYSIS

3.5.1 Cell Mounting and Sealing

In preparing the cells for testing, silver (Ag) paste (DAD87, Shanghai Institute of Resins) applied

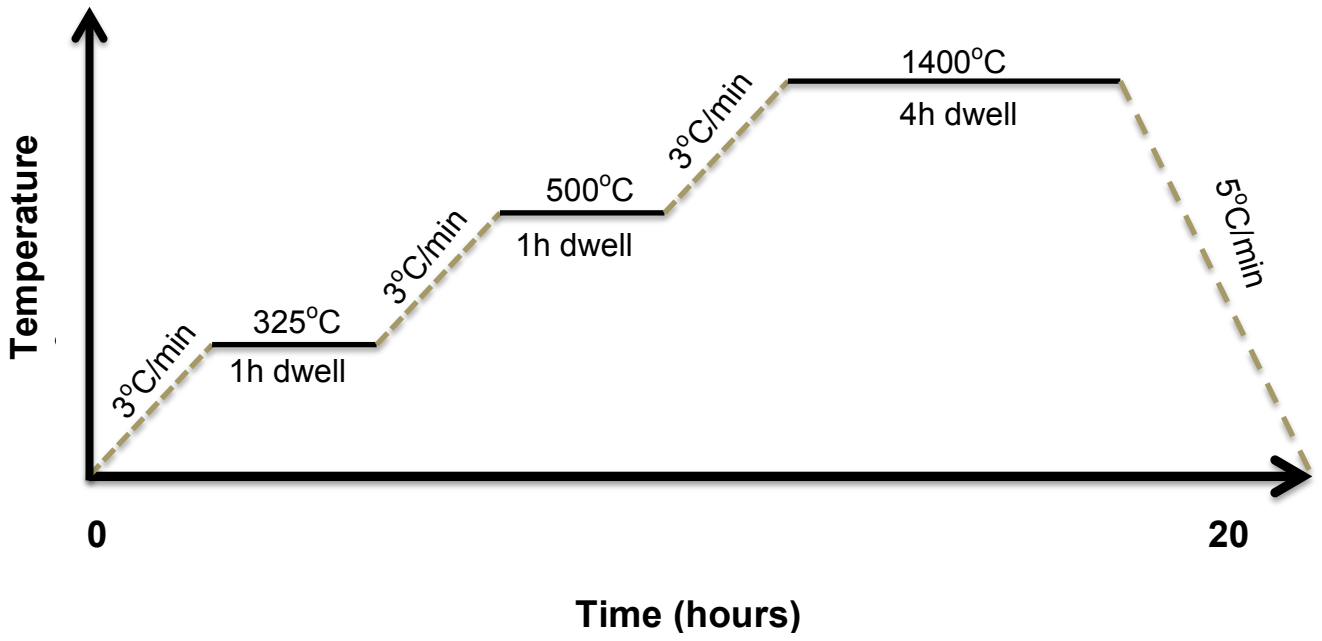

Figure 3-5: Co-firing schedule for the Ni-YSZ/Ni-10Sc1CeSZ half cells in air

Table 3.3: Summary of Screen-Printing Conditions for SOFC

SOFC COMPONENT	PRINTING CONDITIONS FOR SOFC COMPONENT LAYERS			
		INK LOADING	FIRED LAYER THICKNESS	DRYING
ANODE	Ni-YSZ	33% solids by volume	2 layers, 12µm	EACH PRINTED LAYERS: dried 15 min in ambient air then oven dried 15min in air at
	Ni-10SC1CeSZ	33% solids by volume	2 layers, 12µm	
ELECTROLYTE	YSZ	40% solids by volume	3 layers, 15µm	
	10SC1CeSZ	40% solids by volume	3 layers, 15µm	
BLOCKING LAYER	GDC	30% solids by volume	2 layers, 8µm	
CATHODE	LSM-YSZ	30% solids by volume	paintbrushed, 15µm	
	LSM	28% solids by volume	paintbrushed, 25µm	
	LSCF-GDC	30% solids by volume	paintbrushed, 15µm	
	LSCF	28% solids by volume	paintbrushed, 25µm	

in the form of a bull's eye was applied to the cathode side as well as to the anode side for enhanced current collection. Most work in literature cite the use of a Pt or Au mesh current collector in contact with both electrode surfaces for better quality current collection [60], [118], [119]. Ag paste was used in this work due to the low cost. The cells consisted of a 1 mm anode support, a 12 µm anode functional layer (AFL), a 15 µm electrolyte layer and a 40 µm thick cathode with an active cell area of 2.5 cm^2.

A series of sealing trials were carried out to determine the best sealant for attaching the SOFC

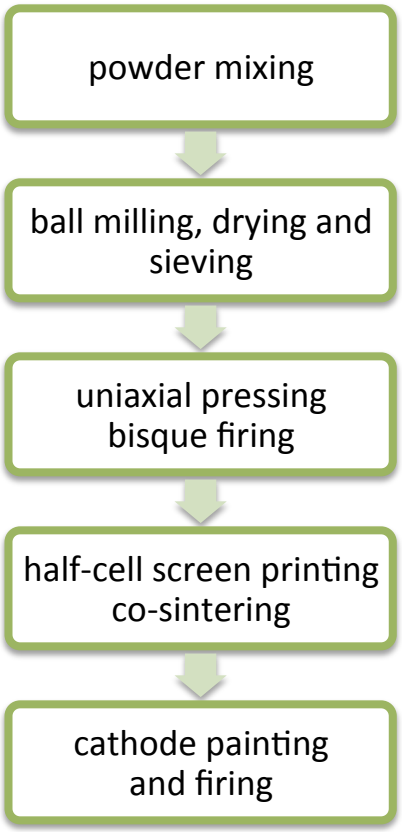

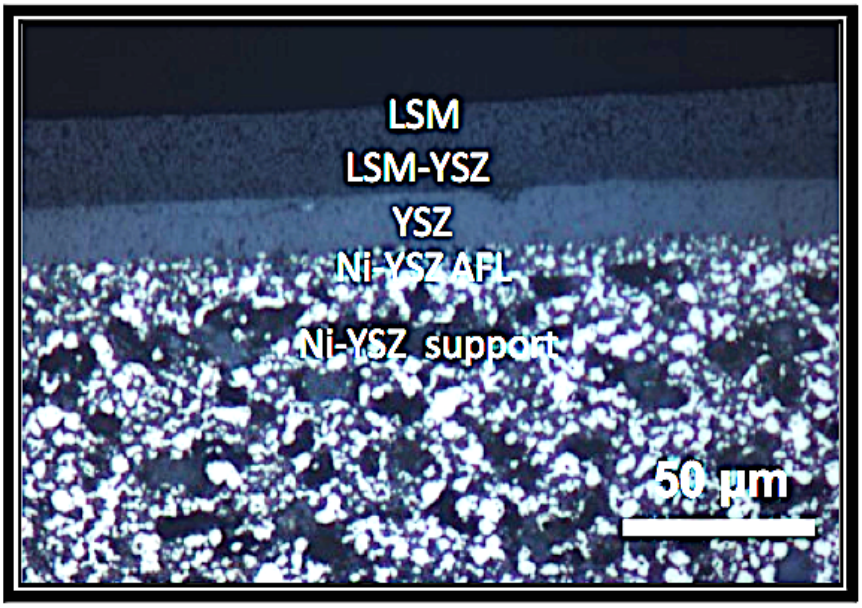

Figure 3-6: Cell fabrication steps and cross-section of a non-reduced Ni-YSZ/YSZ/LSM-YSZ/LSM cell

onto the Al_2O_3 testing tube. Obtaining a good seal between the cell and the testing tube is critical as a poor seal can lead to cell cracks and delamination resulting in fuel crossover at the site of the cracks. Fuel leakage adversely affects the OCV as the partial pressure difference between the electrodes is compromised which can lead to poor cell performance. Cells were sealed with either Ceramabond-552 VFG (Aremco) or Ag paste (DAD87) and tested under dry H_2 at 800^{o}C. The results of two sealing tests are shown below in Figure 3-7. The cell sealed with liberal amounts of Ceramabond - 552 VFG experienced cracks after testing as seen in Figure 3-7 (a). This cell had a very strong adhesion to the Al_2O_3 testing tube but the seal was porous as evidenced by the instability in the OCV measurements during testing. The cell sealed with a thin layer of Ag paste experienced delamination from the testing tube as seen in Figure 3-7 (b) and also experienced gas leakage at the delamination sites. The Ag paste however was dense and strongly bonded the cell to the Al_2O_3 testing tube. The results of this trial found that thick layers of Ag paste applied twice with an 8hrs oven dry at 120^{o}C in air after the first application and an overnight oven dry at 120^{o}C in air after the second application followed by curing at 800^{o}C for 1hr achieved the best seal between the two sealants. Despite several applications and an extensive curing schedule for the Ceramabond-552 VFG, cells mounted with this sealant cracked and resulted in gas leakage. This was due to the TEC difference between the Ni-ZrO_2 cells, the Ceramabond and the Al_2O_3

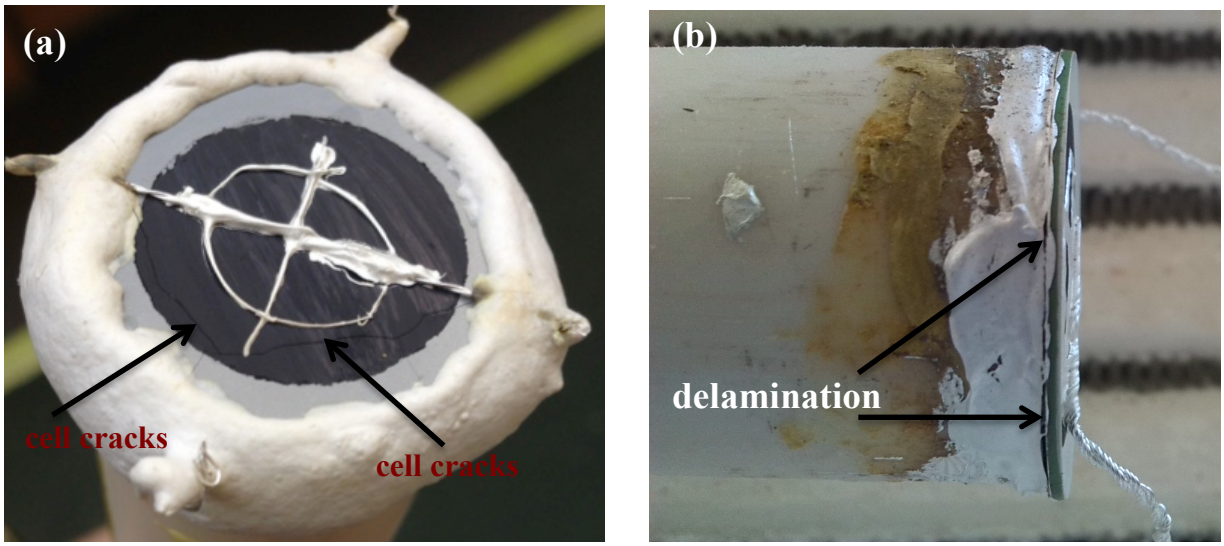

Figure 3-7: (a) Ni-YSZ cell sealed with Ceramabond-552 VFG and (b) Ni-YSZ sell sealed with DAD87 Ag paste

testing tube. These values are provided in Chapter 5, Section 5.7.2. Thus, the cells were mounted onto the Al_2O_3 testing tube, anode side down, using DAD87 Ag paste following the afore-mentioned drying schedule. A schematic of the Ni-YSZ cell to tube assembly is shown in Figure 3-8. Performance measurements for the lab grade and reference commercial grade cells were carried out. Full commercial grade cells were obtained from Ningbo Institute of Material Technology (Chinese Academy of Sciences, China) and served as reference cells to evaluate the reliability of our manufacturing and testing method.

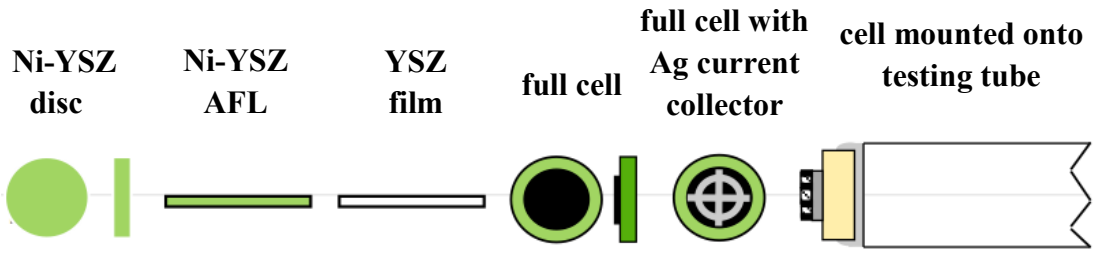

Figure 3-8: Cell to testing tube assembly

3.5.2 Cell Testing Rig and Test Station

The cells were tested using a horizontal tube furnace connected to hydrogen (H_2), methane (CH_4)

and nitrogen (N_2) fuel feeds each configured with separate mass flow controllers. Aalborg digital mass flow controllers controlled all fuel flows. This test rig design allowed multiple users to operate cells on a variety of different fuels. After Ag sealing and drying, the cell was placed into a horizontal tube furnace for testing with the cathode side open to ambient air. The cell was connected to an exhaust line that flowed through a water trap to carry all by-product gases away from the testing area and to prevent water condensation in the lines. A Solartron 1247 Potentiostat interfaced with Multistat software was used to take the measurements. A schematic of the cell test rig and single cell on tube assembly is shown in Figure 3-9.

3.5.3 SOFC Electrochemical Performance Measurement Procedure

The mounted cells on the Al_2O_3 testing tube were placed horizontally in a small tubular furnace with a homogeneous hot zone and heated slowly at 3°C/min up to 750°C where dry H_2 was introduced in small ml increments. The influence of the anode reduction condition has been studied by previous researchers [16], [120]–[123]. Li [120] reports that of cells reduced at 550, 650 and 750°C, the cells reduced at 650°C exhibit the best electrochemical performance when tested between 700-850°C because they possessed the most homogeneous microstructure. Wang [123] concluded that reducing Ni-YSZ anodes by introducing $5\%H_2$-$95\%N_2$ at the start of heating (25°C) up to 800°C enabled the reduction process to proceed faster leaving a non-homogenous anode microstructure with poor mechanical strength. When Ni-YSZ anodes were reduced by introducing $5\%H_2$-$95\%N_2$ at higher temperatures (800°C) however, the reduction process was delayed and the reduction rate was much slower compared to the samples in the first case. Wang also found an improvement in the mechanical strength of the samples reduced at 800°C though the fraction of reduced Ni was the same for both specimens tested under the different reducing conditions. Contrary to Li's findings, Grahl-Madsen [122] found a three-fold increase in the anode conductivity when the anode was reduced at 1000°C when compared to reduction at 800°C and a six-fold increase when compared to reduction at 650°C. Grahl-Madsen also states that heating the samples to a higher temperature does not further improve conductivity once the samples have been reduced at lower temperatures. The microstructures of the samples reduced at 1000°C had a continuous Ni phase which was likely formed by the redistribution of freshly formed Ni metal while the anode surface was still active, a process facilitated by the high temperature environment. According to Grahl-Madsen, this is unlikely to occur at lower temperatures due to slower reduction kinetics and even harder to achieve after heating to higher temperatures once reduction has occurred at lower temperatures due to the loss of surface activity of Ni. Results of the study by Fergus [16] are more exaggerated but support Grahl- Madsen's findings in that high Ni-YSZ anode conductivity was achieved

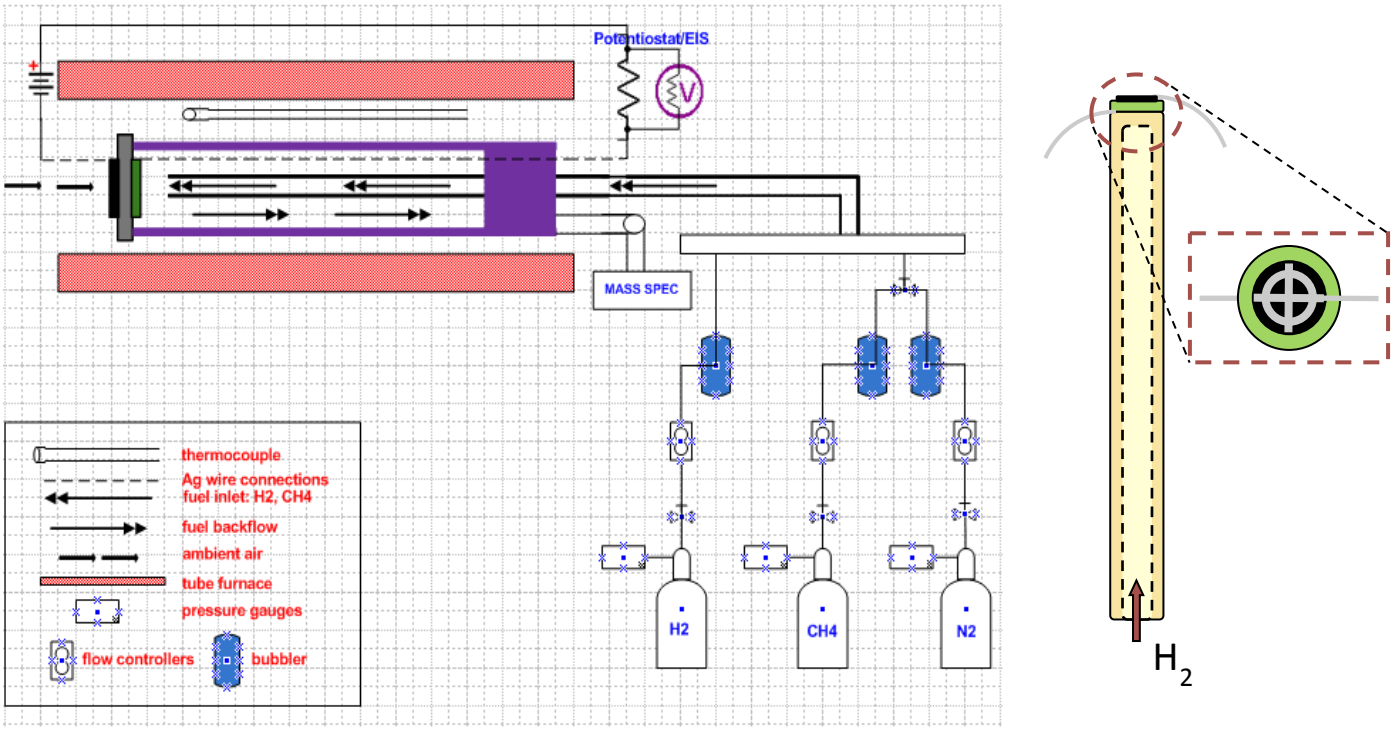

Figure 3-9: SOFC test rig schematic and single cell on tube assembly

when H_2 was introduced at 750°C but when H_2 was introduced at room temperature during the heat treatment up to 750°C, Ni-YSZ exhibited conductivities of 0.002 S cm^{-1}, properties similar to an insulator though all of the NiO had been fully reduced to Ni. Fergus also supports Grahl- Madsen's conclusion that once the anode microstructure is formed during reduction at lower temperatures, it does not improve at subsequent higher temperatures under reducing atmospheres. Fergus also found anode microstructures formed during lower temperature reduction contained isolated Ni particles disconnected from the YSZ. Monzon et al. [121] recently studied the influence of reduction temperature on sintered Ni-YSZ samples reduced between 400-800°C with maximum conductivity values observed for the samples reduced at 800°C under dry and humidified H_2 with the humidified H_2 sample exhibiting the largest degradation and a slightly greater loss of Ni connectivity. Isolated Ni particles containing internal porosity due to reduction occurring inside the particles was observed for the samples reduced at 400°C and 600°C with gaps existing in most Ni-YSZ interfaces. The findings of Monzon et al. support those of Grahl-Madsen and Fergus. Based on the results of the H_2 reduction studies mentioned herein, high temperature anode reduction at 750°C was chosen to finalise the cell testing procedure. The anode reduction temperature was kept similar to the operating temperature to further simplify the testing process. Such conditions could be advantageous for improving anode strength and conductivity for an overall better cell performance.

After slowly introducing H_2 at 750°C, the cells were heated at 3°C/min to the operating temperature of 800°C, where they dwelled in OCV mode for five hours. A five-hour dwell in OCV mode resulted in cell stabilisation with small voltage fluctuations between 0.01-0.10V deemed acceptable. If much larger fluctuations > 1.0V were observed, the test was aborted as this was indicative of cell cracks or lost electrode contacts during testing. After OCV stabilisation, potential stair ($i - V$), potentiostatic and impedance measurements were obtained. Figure 3-10 outlines the cell testing procedure. Performance data for cells tested at 750°C and 800°C on a simulated biogas mixture with CH_4:CO_2=2 was obtained similarly. The CH_4:CO_2 = 2 composition was chosen as this is the regime where carbon deposition is expected as seen in the C-H-O ternary (Figure 2.7) presented in Chapter 2, Section 2.3.2. In addition, biogas has a similar composition though the CH_4:CO_2 ratio varies depending on the source of the bio waste. YSZ and 10Sc1CeSZ performance on H_2 and biogas will be demonstrated.

3.5.4 Electrochemical Impedance Spectroscopy (EIS)

Fired bulk electrolyte pellets were prepared for examination of their electrical properties using Alternating Current (AC) Electrochemical Impedance Spectroscopy (EIS). EIS measures the resistance of flow of electric current through an ionic conductor by applying an AC signal over a broad frequency range to the cell and recording the cell response [124]. The signal amplitude is defined and the output voltage or current for an applied current or voltage is measured across the sample within a given temperature range. Measurements performed over a given frequency range are part of the EIS standard procedure as it enables the three different contributions to the total resistance - individual bulk, grain boundary and electrode resistance contributions – to be distinguished [124]. EIS is a commonly used analysis tool in SOFC research for investigating the influence of cell microstructure on conductivity and electrochemical reactions and how this impacts overall cell performance.

EIS measurements are fitted to an equivalent circuit model that serves as a physical representation of the test system and is used to analyse the data and better explain the electrochemical behaviour of the cell. Most EIS models typically consist of multiple electrical elements, namely, resistors, inductors and capacitors, combined in a unique way that resembles the test circuit and gives meaning to the impedance data. Researchers report that in an AC field, materials with very high resistance possess an inductance and/or capacitance and for the case of ionic conductors, resistors and capacitors can be used to model ionic conducting electrolytes and SOFCs [125]–[127]. The equivalent circuit model adopted for the bulk YSZ and 10Sc1CeSZ electrolyte conductivity study consisted of parallel resistor-capacitor elements in series as pictured in Figure 3-11. This R-C circuit is a commonly used equivalent circuit model for

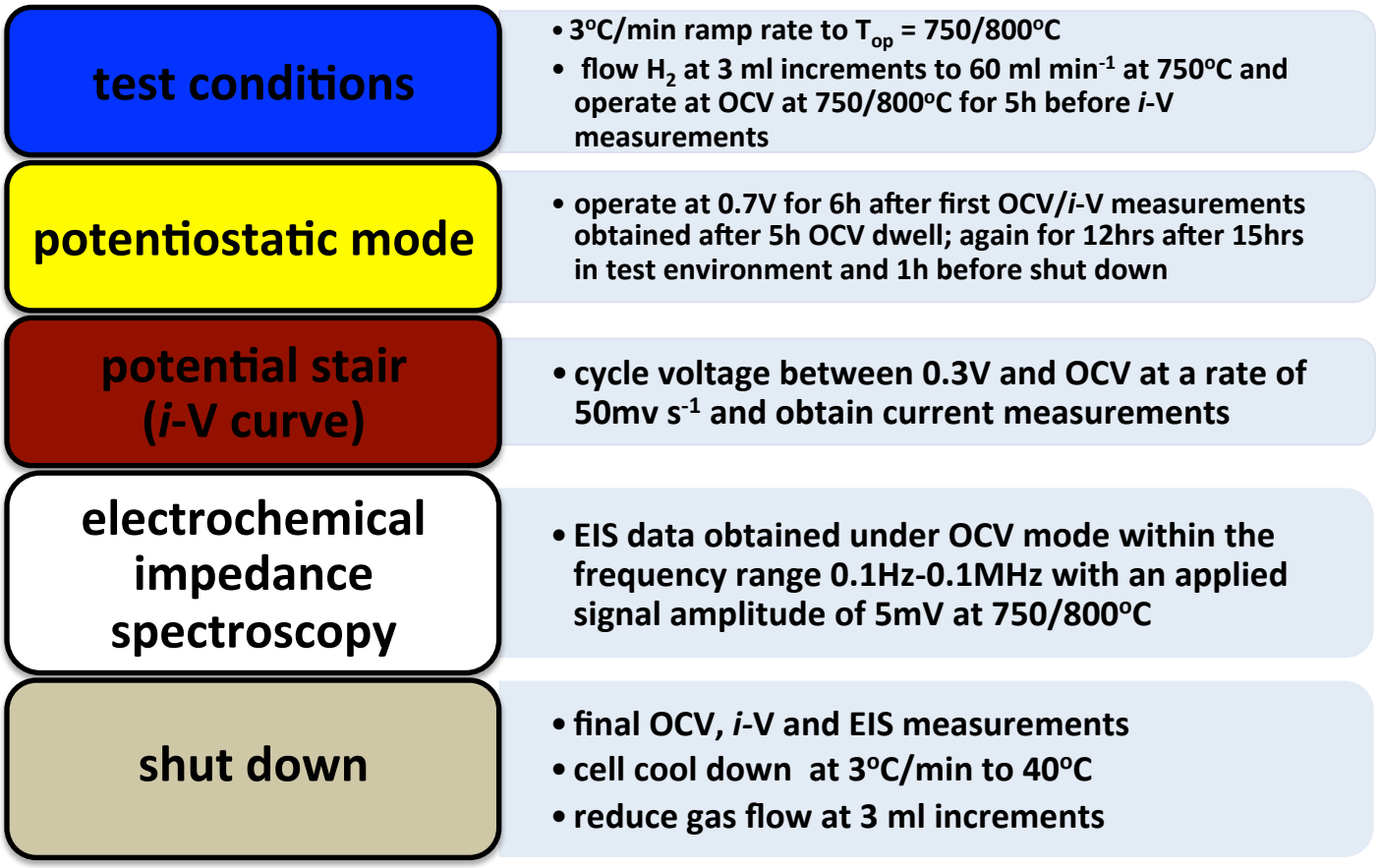

Figure 3-10: SOFC single cell testing procedure

measuring ZrO_2 electrolyte conductivity and lends itself to the graphical representation of EIS data contained in a typical Nyquist Plot as seen in Figure 3-12 (a) [125], [127], [128]. In a Nyquist plot the data appears as the imaginary part (-Im Z'') plotted against the real part (Real Z') where each semicircle represents an R-C parallel circuit in the model allowing the individual resistance contributions to be determined. The semi-circles shown relate to grain (R_g) and grain boundary (R_{gb}) resistance contributions while R_{ohm} is the ohmic resistance which is a sum total of the wire, contact and SOFC component resistances. The resistance values are obtained from the difference in the X-axis intercepts of each semicircle. The plots generated by the EIS plotting software produce semicircles with combined arcs so the R-values reflect the calculated X-axis intercept differences. The equivalent circuit model used to generate EIS measurements for the anode supported cells is shown in Figure 3-12 (b) where R1 is ohmic resistance, and the R2-C2 and R3-C3 circuits are related to the resistances of the electrodes and was adopted from previous researchers [129].

EIS measurements were carried out on bulk electrolyte pellets fired at 1500°C-6hrs using a

Solartron1260 potentiostat/galvanostat with frequency response analyser capabilities within the frequency range 0.1Hz – 0.1MHz between 300 – 730°C in air. Pt electrodes were applied onto the sample's surface and the samples were placed into the furnace and tested under the appropriate conditions. EIS measurements for the single cell SOFCs were obtained during dry H_2 operation at 800°C under open circuit voltage conditions using a Solartron 1242 potentiostat/galvanostat with frequency response analyser capabilities over the frequency range 0.1Hz – 0.1MHz with applied signal amplitude of 5mV at 800°C. The ohmic resistance (R_{ohm}) was determined by the intercept of the data at high frequency, the total resistance (R_{tot}) was determined by the intercept of the data at low frequency and the electrode resistance was determined by the difference between R_{ohm} and R_{tot} (R_{ohm}-R_{tot}).

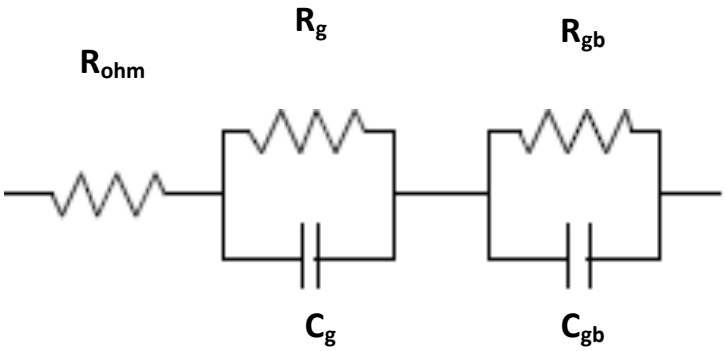

Figure 3-11: Equivalent circuit model for bulk ZrO_2 samples

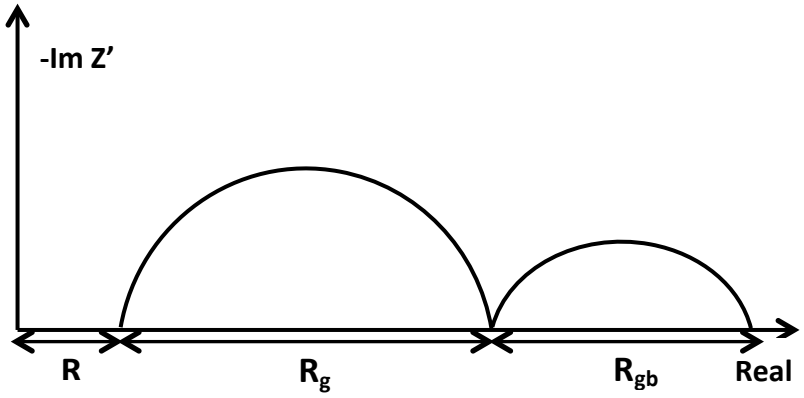

Figure 3-12 (a): Nyquist Plot of the cell processes related to the EQ circuit model in Figure 3-11

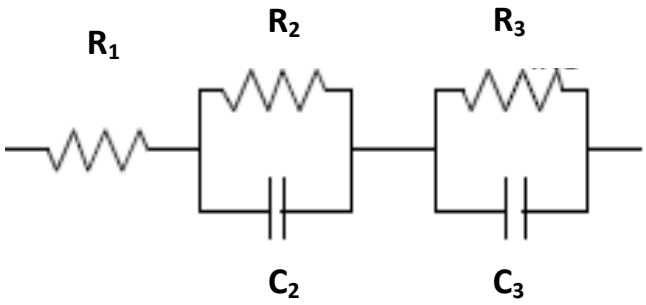

Figure 3-12 (b): EQ circuit model for Ni-ZrO_2 cells

3.5.5 Fuel Flow Rates and Fuel Utilisation

To isolate the fuel flow rate used during cell testing as part of the standardised cell manufacture and testing procedure, the lab grade and NIMTE (CAS) commercial grade Ni-YSZ cells were prepared and tested under various fuel flow rates ranging from 30 ml min^{-1} and 60 ml min^{-1} to 90 ml min^{-1} where they dwelled for one hour before performance data was obtained. The maximum flow rate of the flow controller was 100 ml min^{-1} which determined the range of flow rates that were used. High fuel flow rates are beneficial as more reactant is made available to the fuel cell increasing the amount of fuel that can be consumed and converted to produce current; insufficient fuel can lead to concentration polarisation effects. The increased pressure from higher flow rates may also improve performance by enhancing fuel transport but this is not always the case. Longer residence time under lower fuel rates may also improve cell performance. Waste fuel is a concern when using high fuel flow rates if the cell cannot efficiently convert the fuel into usable energy as well as the problem of anode oxidation at high fuel utilisation rates due to excess H_2O flooding the anode which can lead to anode degradation [130]. Fuel utilisation is defined as the fraction of reactants consumed relative to the total amount of reactants supplied and is expressed as:

$$U = \frac{I}{nFv} \qquad (3.4)\ [131]$$

where U is fuel utilisation, I is the cell output current, n is the number of electrons (for H_2, n = 2), F is Faraday's constant ($96,485\ C\ mol^{-1}$) and v is inlet fuel flow rate. For large SOFC stack systems good performance and high fuel utilisation rates that yield high efficiencies with minimal fuel waste are major balance of plant concerns but for purposes of this study which centres on lab scale single cells operating at relatively low fuel flow rates, this is less of an issue. Choosing a fuel flow rate that gives the best performance was the goal.

Polarisation curves for the lab grade YSZ and commercial grade YSZ cells (CAS) at varying fuel flow rates are plotted in Figure 3-13. To assess the influence of fuel flow rate on current output, the current density of all cells at a fixed voltage of 0.7V was compared and the values are listed in Table 3.4 along with the fuel utilisation rates at these varying flow rates. The lab grade YSZ cells achieved OCVs between 0.975 – 1.015V while the commercial grade cells achieved OCVs above 1.10V. The current density for the lab grade YSZ cells more than triples from 0.037 mA cm^{-2} to 0.133 mA cm^{-2} when the fuel flow rate doubles from 30 ml min^{-1} to 60 ml min^{-1} but then decreases to 0.073 mA cm^{-2} at the highest tested flow rate of 90 ml min^{-1}. The two commercial grade cells have current densities of 0.225 mA cm^{-2} (YSZ CAS-1) and 0.181 mA cm^{-2} (YSZ CAS-2) when tested under a fuel flow rate of 60 ml min^{-1} with fuel utilisation rates of 7.39% and 5.95% respectively. All cells exhibit low fuel utilisation as higher fuel utilisations nearer to 85% are considered ideal to obtain maximum current outputs [131]. And though the commercial cells have the highest fuel utilisation rates of all the tested cells, which correspond to the highest current densities, significant improvements in cell manufacture and testing are required to yield better performing cells. The higher current output of the commercial cell compared to the lab grade cell at the same fuel flow rate is largely influenced by anode microstructure since the fuel flow rate, fuel concentration, reduction temperature and residence time remained the same. The microstructures of the non-reduced commercial and lab grade NiO-YSZ samples are shown in Figure 3-14. The greater pore volume of the lab grade cell seen in Figure 3-14 (b) is apparent when compared to the commercial cell pictured in Figure 3-14 (a). Further examination of the microstructure of the lab grade cell suggests the coarser NiO powders used during cell manufacture resulted in larger NiO grains during sintering. More discussion regarding the characteristics of the starting powders is provided in Chapter 5, Section 5.1. And while the distribution of NiO for the lab grade sample appears to be homogenous, larger NiO grains upon reduction have been found to form isolated Ni grains that disrupt Ni phase continuity [80]. As a result, Ni-Ni particle contact is lowered and the effective current path is decreased, further reducing anode conductivity [80]. And due to the lower sintering rate of coarser particles, material densification and improved association between the metallic and ceramic phases can be compromised. Larger Ni grains have also been found to exhibit a greater degree of coarsening after extended exposure in reducing environments [132]. This growth and surface roughening of the Ni grains reduces the number of active TPB sites and further degrades cell performance. Researchers also report that highly porous anodes can reduce anode conductivity as the driving force for the reduction of NiO to Ni is the lowering of the surface energy of the NiO grain contacts [133]. *That is to say, NiO grain boundary sites are more*

energetically favoured for carrying out reduction processes [133]. While ideal porosities within the 20-40% better facilitate gas diffusion to the electrochemical reaction sites [7], [90], anodes with much larger

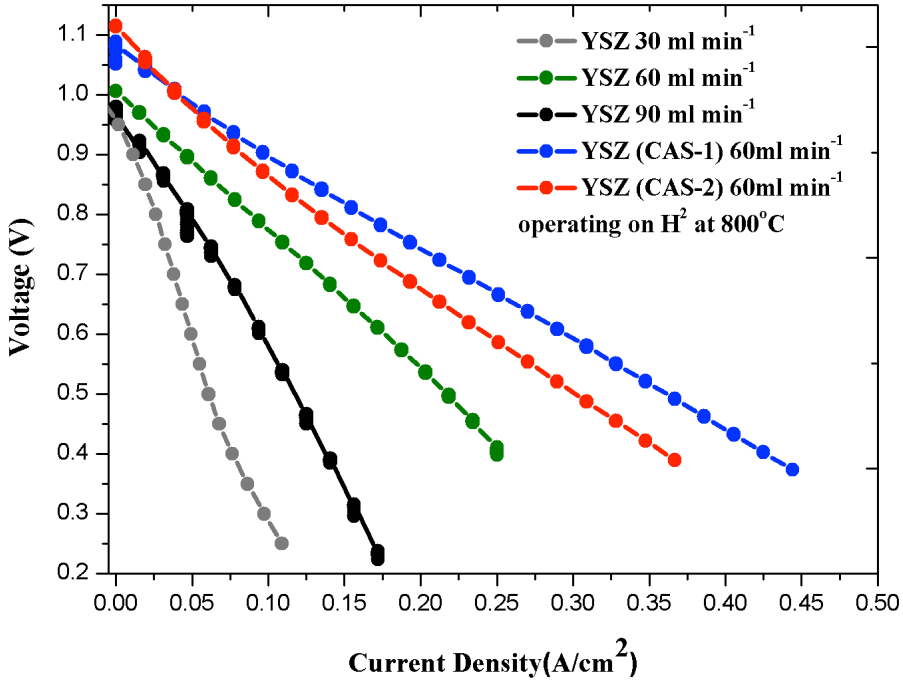

Figure 3-13: Polarisation curves for lab grade and commercial grade YSZ cells under varying H_2 fuel flow rates at 800°C

Table 3.4: Performance of Lab Grade and Commercial Grade YSZ Cells on H_2 at 800°C

SAMPLE	H_2 Flow Rate (ml min^{-1})	OCV (V)	CD at 0.7V (A cm^{-2})	U_f at 0.7V (%)
YSZ	30	0.975	0.0367	2.41
YSZ	60	1.015	0.1331	4.37
YSZ	90	0.983	0.0731	1.61
YSZ (CAS-1)	60	1.091	0.2253	7.39
YSZ (CAS-2)	60	1.121	0.1812	5.95

OCV = open circuit voltage *CD = current density* *U_f = fuel utilisation*

pore volumes reduce the number of NiO particle contacts further limiting the reduction process as NiO-NiO contact and NiO-Ni interfaces promote Ni reduction [133]. This can be used to explain the improved performance of the commercial YSZ cell as there is less porosity and an even distribution of much smaller NiO grains throughout the anode. The smaller NiO grains likely produced using finer NiO powders contributed to better NiO-NiO contacting for enhanced Ni reduction and improved connectivity

through the Ni phase. The lab grade cell results show the greatest performance losses for the cell operated at the highest fuel flow rate, which also exhibited the lowest fuel utilisation. So in this case even though more fuel was fed to the cell not all of the fuel was electrochemically oxidised and

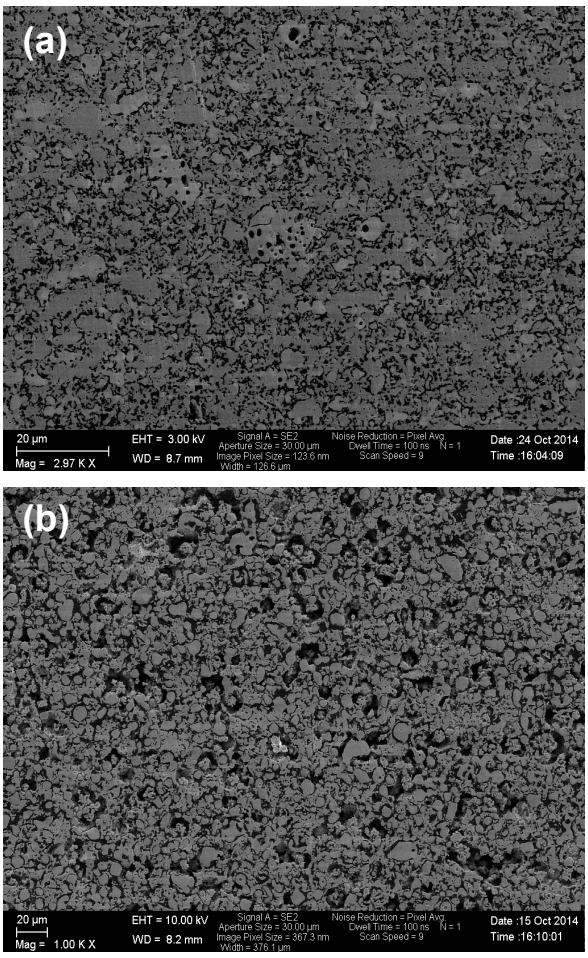

Figure 3-14: SEM micrographs of (a) commercial grade non-reduced NiO-YSZ anode (b) lab grade non-reduced NiO-YSZ in BSE imaging mode

converted into usable electrical energy. The results suggest the higher 90 ml min^{-1} flow rate would have yielded even more fuel waste while the lower 30 ml min^{-1} flow rate would have sacrificed performance as evidenced by the polarisation curves for the lab grade cells. Because the lab grade cells operating under the 60 ml min^{-1} flow rate had the highest current outputs, the 60 ml min^{-1} flow rate was chosen. H_2 was introduced at 750^{o}C in 3 ml increments until the target 60 ml min^{-1} flow rate was achieved. After a 15 min stabilisation at 60 ml min^{-1}, the temperature was increased at 3^{o}C/min to the target operating temperature.

Biogas fuelled SOFCs were tested under H_2 and CO_2:CH_4 using fuel flow rates of 28 ml min^{-1} and 70 ml min^{-1}. For cells fuelled by 28 ml min^{-1} and 70 ml min^{-1} H_2, the fuel feed mixtures were $21H_2$:7He and $63H_2$:7He respectively. For cells fuelled by 28 ml min^{-1} and 70 ml min^{-1} CO_2:CH_4 the fuel feed mixtures were $7CO_2$:$14CH_4$:7He and $21CO_2$:$42CH_4$:7He respectively. Helium (He) was added to the fuel feed as a carrier gas for mass spectroscopy analysis.

3.5.6 Variable Temperature Operation

Performance data for the lab grade YSZ cells was obtained at varying operating temperatures to determine the target operating temperature to be used throughout the study. Figure 3-15 shows cell performances at 600, 700 and 800°C under H_2 at the designated 60 ml min^{-1} fuel flow rate. The cell was left to equilibrate at each temperature for 5hrs after which $i-V$ data was obtained. After the 5hr dwell, cell stabilisation with minimal to no voltage fluctuations were achieved. Two sets of $i-V$ measurements were taken at 800°C – one after the initial 5hr dwell and then a second after 21hrs; a total residence time of 24hrs under H_2 operation at 800°C. The polarisation and power density curves pictured in Figure 3-15 show the influence of temperature on cell performance. Peak power densities of 0.115 W cm^{-2}, 0.169 W cm^{-2}, 0.203 W cm^{-2} and 0.213 W cm^{-2} were obtained at 600, 700, 800 and 800°C-24hrs respectively. Observed performance increases with increasing operating temperature were expected due to enhanced reaction kinetics at elevated temperatures. As seen in Figure 3-16, the sizes of the impedance arcs decrease with increasing temperature primarily due to decreases in activation overpotentials which contribute the most at low current densities which relates to the OCV conditions under which these impedance measurements were taken. And because the impedance values were obtained at OCV, the cell resistance is dominated mostly by these losses. Decreases in the ohmic resistance are also observed at increasing temperatures due to decreases in the electrolyte contribution to the ohmic resistance. This is attributed to the temperature dependent conductivity of the YSZ electrolyte, which increases at higher operating temperatures. And as the electrolyte thickness for each of the tested cells was maintained at 12 µm, ohmic losses through the use of a thin electrolyte film were minimised for all samples. A slight increase in current output is also observed for the extended dwell at 800°C-24hrs most likely due to improved activation processes at the electrodes. Additional time in the H_2 environment allows the reduction process to go to completion and contributes to the formation of a continuous anode microstructure with good Ni connectivity and improved electronic conducting pathways. Such changes in anode microstructure, increased porosity due to a more complete Ni reduction process for instance, are in favour of enhanced mass transport and improved fuel conversion further reducing polarisation losses.

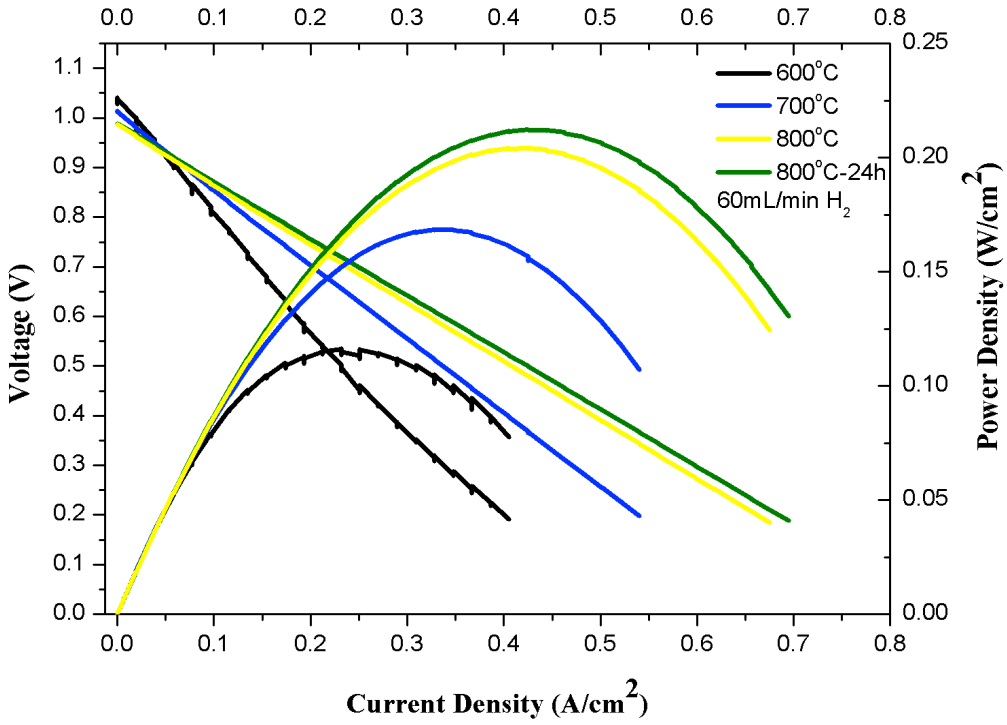

Figure 3-15: SOFC performance curves of the tested lab grade YSZ cells at 600, 700, 800 and 800°C-24hrs

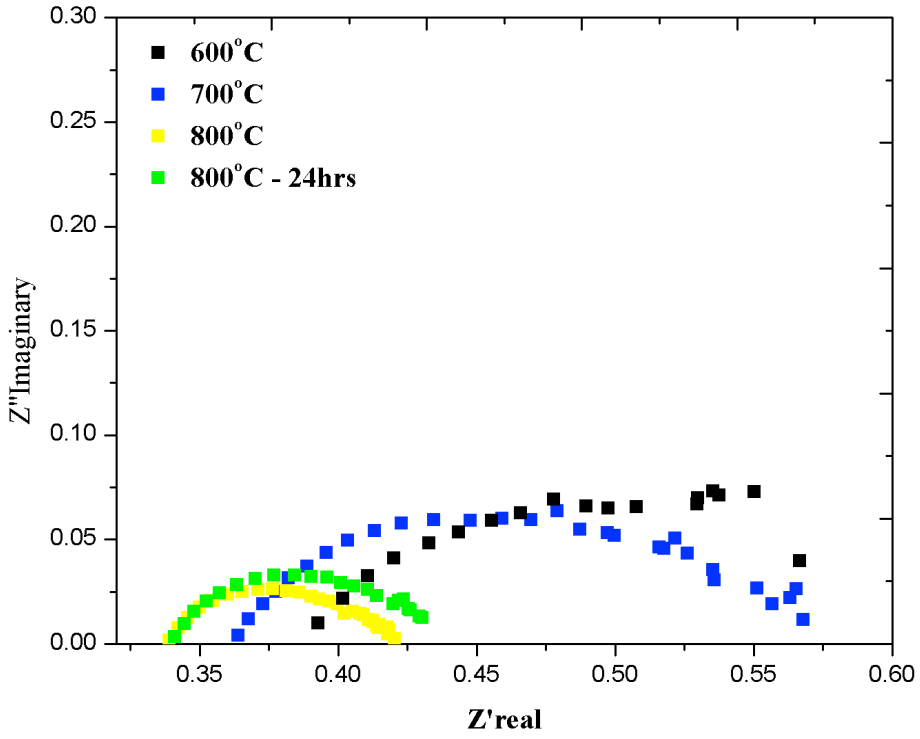

Figure 3-16: Nyquist plots of the tested lab grade YSZ cells at 600, 700, 800 and 800°C-24hrs

3.5.7 Eight-Strand Silver Leading Wire Bundle for Testing

Improvements in the power densities of lab grade Ni-YSZ cells are plotted in Figure 3-17 and are attributed to the use of a thicker Ag leading wire bundle for current collection during testing. The Ag wires supplied by Scientific Wire Company were 0.25 mm in diameter per strand and 300 mm in length with the resistivity of the Ag wire at 1.58 x 10^{-8} Ω m as reported by Scientific Wire Company. Separate performance tests of the lab grade Ni-YSZ cells using a two-strand leading wire bundle and an eight-strand leading wire bundle show an increase in peak power performance by a factor of two due to an increase in the current flow through the wires by a factor of six. Due to the increased current draw, the use of an eight-strand Ag leading wire bundle was implemented as part of the standardised testing procedure.

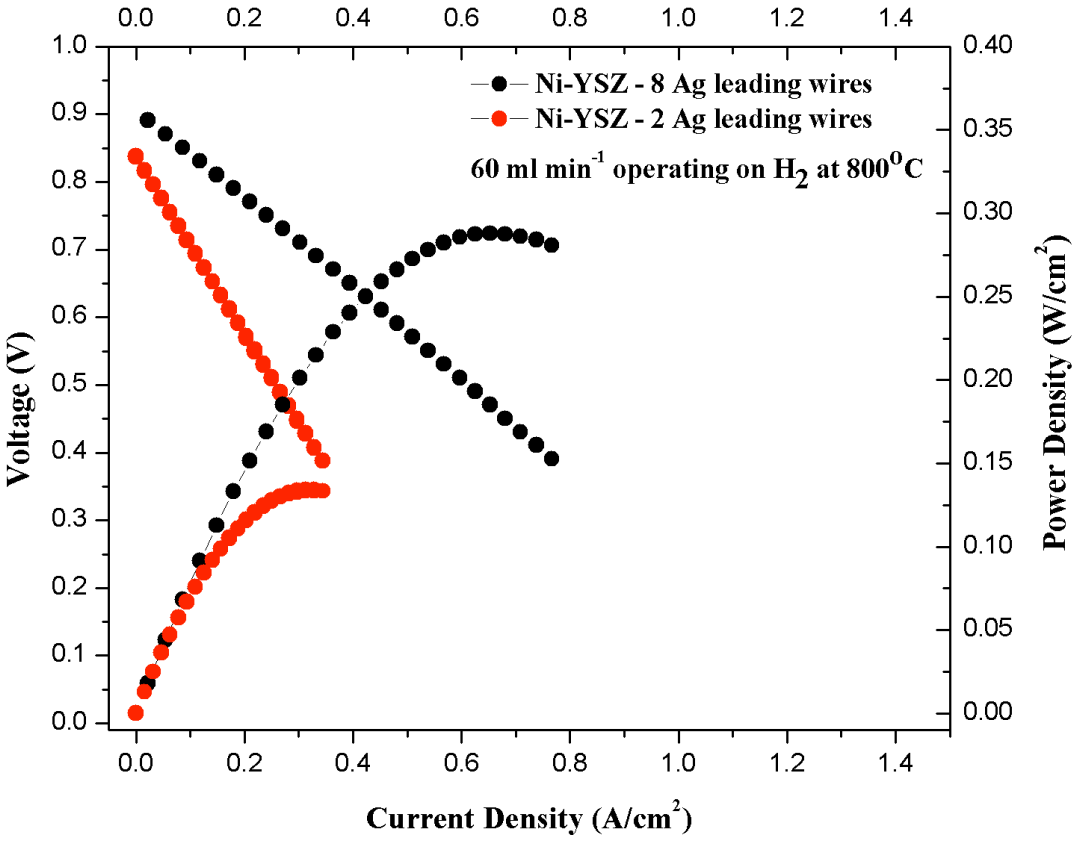

Figure 3-17: Performance comparison for a lab grade Ni-YSZ cell using a two-strand Ag leading wire bundle and an eight-strand Ag leading wire bundle

3.6 SUMMARY

After review of candidate SOFC electrolyte materials, ZrO_2 doped with 10 mol% Sc_2O_3 and 1 mol% CeO_2 was the material composition chosen for this research. 10Sc1CeSZ exhibited the best properties for the test conditions explored in this study. The anode is based on a Ni-10Sc1CeSZ structure to investigate the effectiveness of CeO_2 against coking in hydrocarbon testing environments. Constituent NiO and ZrO_2 powders were combined in 70:30 and 60:40 wt% ratios to prepare the Ni-YSZ and Ni-10Sc1CeSZ anode powders respectively. These powders were then milled, sieved and pressed to produce the Ni-YSZ and Ni-10Sc1CeSZ substrates, which were pre-fired and used as supporting structures for the IT-SOFCs. Ni-ZrO_2 AFLs in 50:50 wt% ratios and 8YSZ and 10Sc1CeSZ electrolyte thin films were deposited via screen-printing, GDC blocking layers were deposited for the 10Sc1CeSZ cells, and all were co-fired at 1400^{o}C-4hrs in a single step to produce the Ni-ZrO_2 half cells. LSM-YSZ cathodes for the YSZ cells and LSCF cathodes for the 10Sc1CeSZ cells were applied by paint brushing. Ag paste was used as a current collector to attach the eight-strand Ag leading wire bundles to the electrode surfaces. Ag paste was also used to attach the cells onto the Al_2O_3 testing tubes to achieve leak tight seals in preparation for testing.

The cells were heated to 750^{o}C at a ramp rate of 3^{o}C/min where H_2 was introduced at 3 ml increments to the target fuel flow rate of 60 ml min^{-1}. After a 10 min stabilisation at 60 ml min^{-1}, the cell was heated at a ramp rate of 3^{o}C/min to the target operating temperature of 800^{o}C. Peak power densities of 0.203 W cm^{-2} and 0.213 W cm^{-2} obtained for the YSZ cells tested at 800^{o}C and 800^{o}C-24hrs were the best performances of all cells tested between 600 – 800^{o}C with corresponding decreases in cell polarisation.

REFERENCES

[1] A. J. Jacobson, Materials for Solid Oxide Fuel Cells. *Chem. Mater.*, 2010. 22 (3): p. 660-674.

[2] K. Kendall and M. Kendall, *High-temperature Solid Oxide Fuel Cells for the 21st Century: Fundamentals, Design and Applications*, Elsevier Science, 2016.

[3] X. M. Ge, S. H. Chan, Q. L. Liu and Q. Sun, Solid Oxide Fuel Cell Anode Materials for Direct Hydrocarbon Utilization. *Adv. Energy Mater.*, 2012. 2 (10): p. 1156-1181.

[4] O. Yamamoto, Solid oxide fuel cells: fundamental aspects and prospects. *Electrochim. Acta.*, 2000. 45 (15–16): p. 2423-2435.

[5] N. Q. Minh, Ceramic Fuel Cells. *J. Am. Ceram. Soc.*, 1993. 76 (3): 563-588.

[6] R. M. Ormerod, Solid oxide fuel cells. *Chem. Soc. Rev.*, 2003. 32 (1): p. 17-28.

[7] J. Larminie and A. Dicks, *Fuel Cell Systems Explained*, John Wiley and Sons, 2003.

[8] P. Holtappels, U. Vogt and T. Graule, Ceramic Materials for Advanced Solid Oxide Fuel Cells. *Adv. Eng. Mater.*, 2005. 7 (5): p. 292-302.

[9] H. Wang, Z. Gao, and S. A. Barnett, Anode-Supported Solid Oxide Fuel Cells Fabricated by Single Step Reduced-Temperature Co-Firing. *J. Electrochem. Soc.*, 2016. 163 (3): p. F196-F201.

[10] E. D. Wachsman and K. T. Lee, Lowering the Temperature of Solid Oxide Fuel Cells. *Science*, 2011. 334 (6058): p. 935-939.

[11] A. Tarancón, Strategies for Lowering Solid Oxide Fuel Cells Operating Temperature. *Energies*, 2009. 2 (4): p. 1130-1150.

[12] O. Z. Sharaf and M. F. Orhan, An overview of fuel cell technology: Fundamentals and Applications. *Renew. Sustain. Energy Rev.*, 2014. 32 (1): p. 810-853.

[13] B. C. Steele and A. Heinzel, Materials for fuel-cell technologies. *Nature*, 2001. 414 (6861): p. 345-352.

[14] B.C.H. Steele, Appraisal of $Ce_{1-y}Gd_yO_{2-y/2}$ electrolytes for IT-SOFC operation at 500^{o}C. *Solid State Ionics*, 2000. 129 (1): p 95-110.

[15] J. W. Fergus, Electrolytes for solid oxide fuel cells. *J. Power Sources*, 2006. 162 (1): p. 30-40.

[16] J. Fergus, R. Hui, X. Li, D. P. Wilkinson and J. Zhang, *Solid Oxide Fuel Cells: Materials Properties and Performance*, CRC Press, 2008.

[17] M. Sahibzada, B. C. H. Steele, K. Zheng, R. A. Rudkin, and I. S. Metcalfe, Development of solid oxide fuel cells based on a $Ce(Gd)O_{2-x}$ electrolyte film for intermediate temperature operation. *Catal. Today.*, 1997. 38 (4): p. 459-466.

[18] H. Inaba, H., Tagawa, Ceria-based solid electrolytes - review. *Solid State Ionics*, 1996. 83 (1–2): p. 1-16.

[19] T. Ishihara, H. Matsuda and Y. Takita, Doped $LaGaO_3$ Perovskite Type Oxide as a New Oxide Ionic Conductor. *J. Am. Chem. Soc.*, 1994. 116 (9): p. 3801-3803.

[20] Z. Gao, E. C. Miller and S. A. Barnett, A high power density intermediate-temperature solid oxide fuel cell with thin $(La_{0.9}Sr_{0.1})_{0.98}(Ga_{0.8}Mg_{0.2})O_{3-\partial}$ electrolyte and nano-scale anode. *Adv. Funct. Mater.*, 2014. 98 (2014): p. 5703-5709.

[21] K. Huang, M. Feng, J. B. Goodenough and M. Schmerling, Characterization of Sr-Doped $LaMnO_3$ and $LaCoO_3$ as Cathode Materials for a Doped $LaGaO_3$ Ceramic Fuel Cell. *J. Electrochem. Soc.,* 1996. 143 (11): p. 3630-3636.

[22] A. L. Shaula, V. V. Kharton and F. M. B. Marques, Phase interaction and oxygen transport in $La_{0.8}Sr_{0.2}Fe_{0.8}Co_{0.2}O_3$–$(La_{0.9}Sr_{0.1})_{0.98}Ga_{0.8}Mg_{0.2}O_3$ composites. *J. Eur. Ceram. Soc.*, 2004. 24 (9): p. 2631-2639.

[23] H. Taroco, J. Santos, R. Domingues and T. Matencio, *Advances in Ceramics - Synthesis and Characterization, Processing and Specific Applications,* Intech, 2011.

[24] K. Huang, J.-H. Wan and J. B. Goodenough, Increasing Power Density of LSGM-Based Solid Oxide Fuel Cells Using New Anode Materials. *J. Electrochem. Soc.*, 2001. 148 (7): p. A788-A794.

[25] O. Yamamoto, Electrical conductivity of stabilized zirconia with ytterbia and scandia. *Solid State Ionics*, 1995. 79 (1): p. 137-142.

[26] S. Badwal, Zirconia-based solid electrolytes: microstructure, stability and ionic conductivity. *Solid State Ionics*, 1992. 52 (1–3): p. 23-32.

[27] N. H. Menzler, F. Tietz, S. Uhlenbruck, H. P. Buchkremer and D. Stöver, Materials and manufacturing technologies for solid oxide fuel cells. *J. Mater. Sci.*, 2010. 45 (12): p. 3109-3135.

[28] S. Badwal, Scandia–zirconia electrolytes for intermediate temperature solid oxide fuel cell operation. *Solid State Ionics*, 2000. 136–137 (1–2): p. 91-99.

[29] C. Haering, A. Roosen and H. Schichl, Degradation of the electrical conductivity in stabilised zirconia systems Part I: Yttria-stabilised zirconia. *Solid State Ionics*, 2005. 176 (3–4): p. 261-268.

[30] R. Ruh, H. J. Garrett, R. F. Domagala and V. A. Patel, The System Zirconia-Scandia. *J. Am. Ceram. Soc.*, 1977. 60 (9–10): p. 399-403.

[31] C. N. Shyam Kumar and R. Bauri, Enhancing the phase stability and ionic conductivity of scandia stabilized zirconia by rare earth co-doping. *J. Phys. Chem. Solids*, 2014. 75 (5): p. 642-650.

[32] H. A. Abbas, C. Argirusis, M. Kilo, H. D. Wiemhöfer, F. F. Hammad and Z. M. Hanafi, Preparation and conductivity of ternary scandia-stabilised zirconia. *Solid State Ionics*, 2011. 184 (1): p. 6-9.

[33] Y. Arachi, T. Asai, O. Yamamoto, Y. Takeda, N. Imanishi, K. Kawate and C. Tamakoshi, Electrical Conductivity of ZrO_2-Sc_2O_3 Doped with HfO_2, CeO_2, and Ga_2O_3. *J. Electrochem. Soc.*, 2001. 148 (5): p. A520-A523.

[34] T. Ishii, Structural phase transition and ionic conductivity in 0.88ZrO,-(0.12 -x) Sc,O,-xAl_2O_3. *Solid State Ionics*, 1995. 78 (3–4): p. 333-338.

[35] S.-W. Choi, K.-J. Kim, M.-Y. Kim, J. Lim, S.-H. Yang, Y. S. Kim and H.-S. Kim, Effect of Ceria Content of CeScSZ Powder on the Phase Stability and Electrical Conductivity of SOFC Electrolyte. *ECS Trans.,* 2015. 68 (1): p. 405-412.

[36] Z. Wang, M. Cheng, Z. Bi, Y. Dong, H. Zhang, J. Zhang, Z. Feng and C. Li, Structure and impedance of ZrO_2 doped with Sc_2O_3 and CeO_2. *Mater. Lett*., 2015. 59 (19–20): p. 2579-2582.

[37] D. Lee, W. Kim, S. Choi, J. Kim, H. Lee and J. Lee, Characterization of ZrO co-doped with ScO and CeO electrolyte for the application of intermediate temperature SOFCs. *Solid State Ionics*, 2005. 176 (1–2): p. 33-39.

[38] H. P. Dasari, J. S. Ahn, K. Ahn, S. Y. Park, J. Hong, H. Kim, K. J. Yoon, J. W. Son, H. W. Lee and J. H. Lee, Synthesis, sintering and conductivity behavior of ceria-doped Scandia-stabilized zirconia. *Solid State Ionics*, 2014. 263 (1): p. 103-109.

[39] X.-F. Ye, B. Huang, S. R. Wang, Z. R. Wang, L. Xiong and T. L. Wen, Preparation and performance of a Cu–CeO_2–ScSZ composite anode for SOFCs running on ethanol fuel. *J. Power Sources*, 2007. 164 (1): p. 203-209.

[40] C. J. Laycock, J. Z. Staniforth and R. M. Ormerod, Biogas as a fuel for solid oxide fuel cells and synthesis gas production: effects of ceria-doping and hydrogen sulfide on the performance of nickel-based anode materials. *Dalton Trans.*, 2011. 40 (20): p. 5494-5504.

[41] X.-F. Ye, S. R. Wang, Q. Hu, J. Y. Chen, T. L. Wen and Z. Y. Wen, Improvement of Cu–CeO_2 anodes for SOFCs running on ethanol fuels. *Solid State Ionics*, 2009. 180 (2–3): p. 276-281.

[42] C. N. Shyam Kumar and R. Bauri, Enhancing the phase stability and ionic conductivity of scandia stabilized zirconia by rare earth co-doping. *J. Phys. Chem. Solids*, 2014. 75 (5): p. 642-650.

[43] V. Vijaya Lakshmi, R. Bauri, A. S. Gandhi and S. Paul, Synthesis and characterization of nanocrystalline ScSZ electrolyte for SOFCs. *Int. J. Hydrogen Energy*, 2011. 36 (22): p. 1496-14942.

[44] S. Yarmolenko, J. Sankar, N. Bernier, M. Klimov, J. Kapat, and N. Orlovskaya, Phase Stability and Sintering Behavior of 10 mol % Sc_2O_3–1 mol % CeO_2–ZrO_2 Ceramics. *J. Fuel Cell Sci. Technol.*, 2009. 6 (2): p. 021007-9.

[45] M. Liu, C. R. He, W. G. Wang and J. X. Wang, Synthesis and characterization of 10Sc1CeSZ powders prepared by a solid-liquid method for electrolyte-supported solid oxide fuel cells. *Ceram. Int.*, 2014. 40 (4): p. 5441-5446

[46] C. D. Savaniu and J. T. S. Irvine, La-doped $SrTiO_3$ as anode material for IT-SOFC. *Solid State Ionics*, 2011. 192 (1): p. 491-493.

[47] M. J. Escudero, J. T. S. Irvine and L. Daza, Development of anode material based on La-substituted $SrTiO_3$ perovskites doped with manganese and/or gallium for SOFC. *J. Power Sources*, 2009. 192 (1): p. 43-50.

[48] S. Hui and A. Petric, Evaluation of yttrium-doped $SrTiO_3$ as an anode for solid oxide fuel cells. *J. Eur. Ceram. Soc.*, 2002. 22 (9-10): p. 1673-1681.

[49] X. Li, H. Zhao, W. Shen, F. Gao, X. Huang, Y. Li and Z. Zhu, Synthesis and properties of Y-doped $SrTiO_3$ as an anode material for SOFCs. *J. Power Sources*, 2007. 166 (1): p. 47-52.

[50] Q. Ma, F. Tietz and D. Stöver, Nonstoichiometric Y-substituted $SrTiO_3$ materials as anodes for solid oxide fuel cells. *Solid State Ionics*, 2011. 192 (1): p. 535-539.

[51] D. Neagu and J. T. S. Irvine, Structure and Properties of $La_{0.4}Sr_{0.4}TiO_3$ Ceramics for Use as Anode Materials in Solid Oxide Fuel Cells. *Chem. Mater.*, 2010. 22 (17): p. 5042-5053.

[52] G. Pudmich, B. A. Boukamp, W. Jungen, W. Zipprich and F. Tietz, Chromite / titanate based perovskites for application as anodes in solid oxide fuel cells. *Solid Sate Ionics*, 2000. 135 (1-4): p. 433-438.

[53] C.-D. Savaniu, D. N. Miller,and J. T. S. Irvine, Scale Up and Anode Development for La-Doped $SrTiO_3$ Anode-Supported SOFCs. *J. Am. Ceram. Soc.*, 2013. 96 (6): p. 1718-1723.

[54] O. A. Marina, N. L. Canfield and J. W. Stevenson, Thermal, electrical, and electrocatalytical properties of lanthanum-doped strontium titanate. *Solid State Ionics*, 2002. 149 (1–2): p. 21-28.

[55] A. Atkinson, S. Barnett, R. J. Gorte, J. T. S. Irvine, A. J. McEvoy, M. Mogensen, S. C. Singhal and J. Vohs, Advanced anodes for high-temperature fuel cells. *Nat. Mater.*, 2004. 3 (1): p. 17-27.

[56] S. Cho, D. E. Fowler, E. C. Miller, J. S. Cronin, K. R. Poeppelmeier and S. A. Barnett, Fe-substituted $SrTiO_{3-\delta}$–$Ce_{0.9}Gd_{0.1}O_2$ composite anodes for solid oxide fuel cells. *Energy Environ. Sci.*, 2013. 6 (1): p. 1850-1857.

[57] J. Karczewski, B. Riegel, M. Gazda, P. Jasinski and B. Kusz, Electrical and structural properties of Nb-doped $SrTiO_3$ ceramics. *J. Electroceram.*, 2009. 24 (4): p. 326-330.

[58] M. D. Gross, J. M. Vohs and R. J. Gorte, A Strategy for Achieving High Performance with SOFC Ceramic Anodes. *Electrochem. Solid-State Lett.*, 2007. 10 (4): p. B65-B69.

[59] R. J. Gorte and J. M. Vohs, Nanostructured anodes for solid oxide fuel cells. *Curr. Opin. Colloid Interface Sci.*, 2009. 14 (4): p. 236-244.

[60] S. Park, R. J. Gorte and J. M. Vohs, Tape Cast Solid-Oxide Fuel Cells for the Direct Oxidation of Hydrocarbons. *J. Electrochem. Soc.*, 2001. 148 (5): p. A443-A447.

[61] B. Huang, S. R. Wang, R. Z. Liu and T. L. Wen, Preparation and performance characterization of the Fe–Ni/ScSZ cermet anode for oxidation of ethanol fuel in SOFCs. *J. Power Sources*, 2007. 167 (2): p. 288-294.

[62] A. Hornés, P. Bera, M. Fernández-García, A. Guerrero-Ruiz, and A. Martínez-Arias, Catalytic and redox properties of bimetallic Cu–Ni systems combined with CeO_2 or Gd-doped CeO_2 for methane oxidation and decomposition. *Appl. Catal. B Environ.*, 2012. 111–112 (1): p. 96-105.

[63] A. Benyoucef, D. Klein, C. Coddet and B. Benyoucef, Development and characterisation of (Ni, Cu, Co)-YSZ and Cu-Co-YSZ cermets anode materials for SOFC application. *Surf. Coatings Technol.*, 2008. 202 (10): p. 2202-2207.

[64] H. Kim, C. Lu, W. L. Worrell, J. M. Vohs, and R. J. Gorte, Cu-Ni Cermet Anodes for Direct Oxidation of Methane in Solid-Oxide Fuel Cells. *J. Electrochem. Soc.*, 2002. 49 (3): p. A247-A250.

[65] H. Sumi, K. Ukai, Y. Mizutani, H. Mori, C. Wen, H. Takahashi and O. Yamamoto, Performance of nickel-scandia-stabilized zirconia cermet anodes for SOFCs in 3% H_2O-CH_4. *Solid State Ionics*, 2004. 174 (1–4): p. 151-156.

[66] S. An, C. Lu, W. L. Worrell, J. M. Vohs and R. J. Gorte, Scandia Stabilized Zirconia (ScSZ) SOFCs for the Direct Oxidation of Hydrocarbon Fuels. *(Solid-State Ionic Devices III) Proc. Int. Symp. Electrochem. Soc.*, 2003. 2002-26 (1): p. 66-69.

[67] Y. Shiratori, T. Oshima and K. Sasaki, Feasibility of direct-biogas SOFC. *Int. J. Hydrogen Energy*, 2008. 33 (21): p. 6316-6321.

[68] K. Ke, A. Gunji, H. Mori, S. Tsuchida, H. Takahashi, K. Ukai, Y. Mizutani, H. Sumi, M. Yokoyama and K. Waki, Effect of oxide on carbon deposition behavior of CH_4 fuel on Ni/ScSZ cermet anode in high temperature SOFCs. *Solid State Ionics*, 2006. 177 (5–6): p. 541-547.

[69] H. Kishimoto, K. Yamaji, T. Horita, Y. Xiong, N. Sakai, M. E. Brito and H. Yokokawa, Feasibility of liquid hydrocarbon fuels for SOFC with Ni–ScSZ anode. *J. Power Sources*, 2007. 172 (1): p. 67-71.

[70] Z. Cai, T. N. Lan, S. Wang and M. Dokiya, Supported $Zr(Sc)O_2$ SOFCs for reduced temperature prepared by slurry coating and co-firing. *Solid State Ionics*, 2002. 153 (1): p. 583-590.

[71] M. R. Somalu, V. Yufit, D. Cumming, E. Lorente and N. P. Brandon, Fabrication and characterization of Ni/ScSZ cermet anodes for IT-SOFCs. *Int. J. Hydrogen Energy*, 2011. 36 (9): p. 5557-5566.

[72] C. Sun, R. Hui, and J. Roller, Cathode materials for solid oxide fuel cells: A review. *J. Solid State Electrochem.*, 2009. 14 (7): p. 1125-1144.

[73] O. Yamamoto, Y. Takeda, R. Kanno and M. Noda, Perovskite-type oxides as oxygen electrodes for high temperature oxide fuel cells. *Sold State Ionics*, 1987. 22 (2–3): p. 241-246.

[74] H. Anderson, Review of p-type doped perovskite materials for SOFC and other applications. *Solid State Ionics*, 1992. 52 (1–3): p.33-41.

[75] T. Kawada, N. Sakai, H. Yokokawa, M. Dokiya and I. Anzai, Reaction between solid oxide fuel cell materials. *Solid State Ionics*, 1992. 50 (3–4): p. 189-196.

[76] G. Stochniol, E. Syskakis and A. Naoumidis, Chemical Compatibility between Strontium-Doped Lanthanum Manganite and Yttria-Stabilized Zirconia. *J. Am. Ceram. Soc.*, 1995. 78 (4): p. 929-932.

[77] R. Knibbe, J. Hjelm, M. Menon, N. Pryds, M. Søgaard, H. J. Wang and K. Neufeld, Cathode-Electrolyte Interfaces with CGO Barrier Layers in SOFC. *J. Am. Ceram. Soc.*, 2010. 93 (9): p. 2877-2883.

[78] A. Sarikaya, V. Petrovsky and F. Dogan, Development of the anode pore structure and its effects on the performance of solid oxide fuel cells. *Int. J. Hydrogen Energy*, 2013. 38 (24): p. 10081-10091.

[79] F. Zhao and A. V. Virkar, Dependence of polarization in anode-supported solid oxide fuel cells on various cell parameters. *J. Power Sources*, 2005. 141 (1): p. 79-95.

[80] J. H. Yu, G. W. Park, S. Lee and S. K. Woo, Microstructural effects on the electrical and mechanical properties of Ni–YSZ cermet for SOFC anode. *J. Power Sources*, 2007. 163 (2): p. 926-932.

[81] F. Tietz, F. J. Dias, D. Simwonis and D. Stöver, Evaluation of commercial nickel oxide powders for components in solid oxide fuel cells. *J. Eur. Ceram. Soc.*, 2000. 20 (8): p. 1023-1034.

[82] C. Jin, J. Liu, L. Li and Y. Bai, Electrochemical properties analysis of tubular NiO-YSZ anode-supported SOFCs fabricated by the phase-inversion method. *J. Memb. Sci.*, 2009. 341 (1–2): p. 233-237.

[83] A Sanson, P. Pinasco and E. Roncari, Influence of pore formers on slurry composition and microstructure of tape cast supporting anodes for SOFCs. *J. Eur. Ceram. Soc.*, 2008. 28 (6): p. 1221-1226.

[84] D. W. Dees, T. D. Claar and D. C. Fee, Conductivity of Porous Ni / ZrO_2-Y_20_3 Cermets. *J. Electrochem. Soc.*, 1987. 134 (9): p. 2141-2146.

[85] T. Kawada, N. Sakai, H. Yokokawa, M. Dokiya, M. Mori and T. Iwata, Characteristics of Slurry-Coated Nickel Zirconia Cermet Anodes for Solid Oxide Fuel Cells. *J. Electrochem. Soc.*, 1990. 137 (10): p. 3042-3047.

[86] M. Kishimoto, K. Miyawaki, H. Iwai, M. Saito and H. Yoshida, Effect of composition ratio of Ni-YSZ anode on distribution of effective three-phase boundary and power generation performance. *Fuel Cells*, 2013. 13 (4): p. 476-486.

[87] D. McLachlan, M. Blaszkiewicz, R. E. Newnham, Electrical Resistivity of Composites. *J. Am. Ceram. Soc.*, 1990. 73 (8): p. 2187-2203.

[88] T. Kawashima and M.Hishinuma, Analysis of Electrical Conduction Paths in Ni-YSZ Particulate Composites Using Percolation Theory. *Mater. Trans.*, 1996. 37 (7): p. 1397-1403.

[89] J. H. Lee, H. Moon, H. W. Lee, J. Kim, J. D. Kim and K. H. Yoon, Quantitative analysis of microstructure and its related electrical property of SOFC anode, Ni-YSZ cermet. *Solid State Ionics*, 2002. 148 (1–2): p. 15-26.

[90] W. Z. Zhu and S. C. Deevi, A review on the status of anode materials for solid oxide fuel cells. *Mater. Sci. Eng. A*, 2003. 362 (1–2): p. 228-239.

[91] S. K. Pratihar, R. N. Basu, S. Mazumder and H. S. Maiti, Electrical Conductivity and Microstructure of Ni-YSZ Anode Prepared by Liquid Dispersion Method. *(SOFC VI) Proc. Sixth Int. Symp. Electrochem. Soc.*, 1999. 99–19 (1): p. 513-517.

[92] I. Kagomiya, S. Kaneko, K. Kakimoto, K. Park and K. H. Cho, Fabrication and Power Densities of Anode-Supported Solid Oxide Fuel Cells with Different Ni-YSZ Anode Functional Layer Thicknesses. *Fuel Cells*, 2015. 15 (1): p. 90-97.

[93] S. Cho, Y. Kim, J. H. Kim, A. Manthiram and H. Wang, High power density thin film SOFCs with YSZ/GDC bilayer electrolyte. *Electrochim. Acta.*, 2011. 56 (16): p. 5472-5477.

[94] S. D. Kim, J. J. Lee, H. Moon, S. H. Hyun, J. Moon, J. Kim and H. W. Lee, Effects of anode and electrolyte microstructures on performance of solid oxide fuel cells. *J. Power Sources*, 2007. 169 (2): p. 265-270.

[95] S. P. Jiang and S. H. Chan, A review of anode materials development in solid oxide fuel cells. *J. Mater. Sci.*, 2004. 39 (14): p. 4405-4439.

[96] K. Chen, X. Chen, Z. Lü, N. Ai, X. Huang and W. Su, Performance of an anode-supported SOFC with anode functional layers. *Electrochim. Acta.*, 2008. 53 (27): p. 7825-7830.

[97] H. Moon, S. D. Kim, E. W. Park, S. H. Hyun and H. S. Kim, Characteristics of SOFC single cells with anode active layer via tape casting and co-firing. *Int. J. Hydrogen Energy*, 2008. 33 (11): p. 2826-2833.

[98] A. V. Virkar, J. Chen, C. W. Tanner and J. W. Kim, Role of electrode microstructure on activation and concentration polarizations in solid oxide fuel cells. *Solid State Ionics*, 2000. 131(1): p. 189–198.

[99] R. Gorte, Novel SOFC anodes for the direct electrochemical oxidation of hydrocarbons. *J. Catal.*, 2003. 216 (1–2): p. 477-486.

[100] R. E. Williford, L. A. Chick, G. D. Maupin, S. P. Simner and J. W. Stevenson, Diffusion Limitations in the Porous Anodes of SOFCs. *J. Electrochem. Soc.*, 2003. 150 (8): p. A1067-A1072.

[101] J. R. Wilson and S. A. Barnett, Solid Oxide Fuel Cell Ni–YSZ Anodes: Effect of Composition on Microstructure and Performance. *Electrochem. Solid-State Lett.*, 2008. 11 (10): p. B181-B185.

[102] N. Vivet, S. Chupin, E. Estrade, A. Richard, S. Bonnamy, D. Rochais and E. Bruneton, Effect of Ni content in SOFC Ni-YSZ cermets: A three-dimensional study by FIB-SEM tomography. *J. Power Sources*, 2011. 196 (23): p. 9989-9997.

[103] T. Yamaguchi, H. Sumi, K. Hamamoto, T. Suzuki, Y. Fujishiro, J. D. Carter and S. A. Barnett, Effect of nanostructured anode functional layer thickness on the solid-oxide fuel cell performance in the intermediate temperature. *Int. J. Hydrogen Energy*, 2014. 39 (34): p. 19731-19736.

[104] J. Kong, K. Sun, D. Zhou, N. Zhang, J. Mu and J. Qiao, Ni-YSZ gradient anodes for anode-supported SOFCs. *J. Power Sources*, 2007. 166 (2): p. 337-342.

[105] A. A. E. Hassan, N. H. Menzler, G. Blass, M. E. Ali, H. P. Buchkremer and D. Stöver, Development of an optimized anode functional layer for solid oxide fuel cell applications. *Adv. Eng. Mater.*, 2002. 4 (3): p. 125-129.

[106] A. C. Müller, D. Herbstritt and E. Ivers-Tiffée, Development of a multilayer anode for solid oxide fuel cells. *Solid State Ionics*, 2002. 152–153 (1): p. 537-542.

[107] W. Huebner, D. M. Reed and H. U. Anderson, Solid Oxide Fuel Cell Performance Studies: Anode Development. *(SOFC VI) Proc. Sixth Int. Symp. Electrochem. Soc.*, 1999. 99–19 (1): p. 503-512.

[108] S. de Souza, Thin-film solid oxide fuel cell with high performance at low-temperature. *Solid State Ionics*, 1997. 98 (1–2): p. 57-61.

[109] W. Bao, Q. Chang and G. Meng, Effect of NiO/YSZ compositions on the co-sintering process of anode-supported fuel cell. *J. Memb. Sci.*, 2005. 259 (1–2): p. 103-109.

[110] Y. Zhang, X. Huang, Z. Lu, X. Ge, J. Xu, X. Xin, X. Sha and W. Su, Effect of starting powder on screen-printed YSZ films used as electrolyte in SOFCs. *Solid State Ionics*, 2006. 177 (3–4): p. 281-287.

[111] Z. Wang, K. Sun, S. Shen, X. Zhou, J. Qiao and N. Zhang, Effect of co-sintering temperature on the performance of SOFC with YSZ electrolyte thin films fabricated by dip-coating method. *J. Solid State Electrochem.*, 2009. 14 (4): p. 637-642.

[112] S. P. Simner, J. P. Shelton, M. D. Anderson and J. W. Stevenson, Interaction between La(Sr)FeO_3 SOFC cathode and YSZ electrolyte. *Solid State Ionics*, 2003. 161 (1–2): p. 11-18.

[113] T. Tsai and S. A. Barnett, Increased solid-oxide fuel cell power density using interfacial ceria layers. *Solid State Ionics*, 1997. 98 (3–4): p. 191-196.

[114] T. Tsai and S. A. Barnett, Effect of Mixed-Conducting Interfacial Layers on Solid Oxide Fuel Cell Anode Performance. *J. Electrochem. Soc.,* 1998. 145 (5): p. 1696-1701.

[115] S. P. Simner, J. F. Bonnett, N. L. Canfield, K. D. Meinhardt, V. L. Sprenkle and J. W. Stevenson, Optimized Lanthanum Ferrite-Based Cathodes for Anode-Supported SOFCs. *Electrochem. Solid-State Lett..,* 2002. 5 (7): p. A173-A175.

[116] J. Scott Cronin, K. Muangnapoh, Z. Patterson, K. J. Yakal-Kremski, V. P. Dravid and S. A. Barnett, Effect of Firing Temperature on LSM-YSZ Composite Cathodes: A Combined Three-Dimensional Microstructure and Impedance Spectroscopy Study. *J. Electrochem. Soc.*, 2012. 159 (4): p. B385-B393.

[117] Y. Leng, S. H. Chan and Q. Liu, Development of LSCF-GDC composite cathodes for low-temperature solid oxide fuel cells with thin film GDC electrolyte. *Int. J. Hydrogen Energy*, 2008. 33 (14): p. 3808-3817.

[118] L. Sr, C. Cathode, Z. Electrolyte, H. Uchida, S. Arisaka and M. Watanabe, High Performance Electrode for Medium-Temperature Solid Oxide Fuel Cells. *Electrochem. Solid-State Lett.*, 1999. 2 (9): p. A13-A18.

[119] H. Abe, K. Murata, T. Fukui, W-J. Moon, K. Kaneko and M. Naito, Microstructural control of Ni – YSZ cermet anode for planar thin-film SOFCs. *Fuel Cells Bull*., 2006. 3 (1): p. 12-15.

[120] T. S. Li, W. G. Wang, H. Miao, T. Chen and C. Xu, Effect of reduction temperature on the electrochemical properties of a Ni/YSZ anode-supported solid oxide fuel cell. *J. Alloys Compd.*, 2010. 495 (1): p. 138-143.

[121] H. Monzon, M. A. Laguna-Bercero, The Influence of Reduction Conditions on a Ni-YSZ SOFC Anode Microstructure and Evolution. *ECS Trans.*, 2015. 68 (1): p. 1229-1235.

[122] L. Grahl-Madsen, P. H. Larsen, N. Bonanos, J. Engell and S. Linderoth, Mechanical strength and electrical conductivity of Ni-YSZ cermets fabricated by viscous processing. *J. Mater. Sci.*, 2006. 41 (4): p. 1097-1107.

[123] Y. Wang, M. E. Walter, K. Sabolsky and M. M. Seabaugh, Effects of powder sizes and reduction parameters on the strength of Ni-YSZ anodes. *Solid State Ionics*, 2006. 177 (17–18): p. 1517-1527.

[124] E. Barsoukov and J. R. Macdonald, *Impedance Spectroscopy: Theory, Experiment, and Applications*, Wiley, 2005.

[125] J.-M. Winand and J. Depireux, Measurement of Ionic Conductivity in Solid Electrolytes. *Europhys. Lett.*, 2007. 8 (5): p. 445-452.

[126] J. E. Bauerle, Study of solid electrolyte polarization by a complex admittance method. *J. Phys. Chem. Solids.*, 1969. 30 (1): p. 2657-2670. 1969.

[127] C. Zhang, C. Li, G. Zhang and X. Ning, Ionic conductivity and its temperature dependence of atmospheric plasma-sprayed yttria stabilized zirconia electrolyte. *Mater. Sci. and Eng B*., 2007. 137 (1): p. 24-30.

[128] J. T. S. Irvine, D. C. Sinclair and A. R. West, Electroceramics : Characterization by Impedance Spectroscopy. *Adv Mater*., 1990. 2 (3): p 132-138.

[129] P. Jasinksi, Impedance spectroscopy of single chamber SOFC. *Solid State Ionics*, 2004. 175 (1): p. 35-38.

[130] D. Sarantaridis and A. Atkinson, Redox Cycling of Ni-Based Solid Oxide Fuel Cell Anodes: A Review. *Fuel Cells*, 2007. 7 (3): p. 246-258.

[131] K. Huang, Fuel utilization and fuel sensitivity of solid oxide fuel cells. *J. Power Sources*, 2011. 196 (5): p. 2763-2767.

[132] D. Simwonis, F. Tietz and D. Stover, Nickel coarsening in annealed Ni / 8YSZ anode substrates for solid oxide fuel cells. *Solid State Ionics*, 2000. 132 (2000): p. 241-251.

[133] Y. Brodnikovskyi, B. Vasyliv, V. Podhurska, M. Andrzejczuk, N. McDonald, O. Kyrpa, O. Ostash, R. Steinberger-Wilckens and M. Lewandowska, Influence of reduction conditions of NiO on its mechanical and electrical properties. *J. Electrochem. Sci. Eng.*, 2016. 6 (1): p. 113-121.

CHAPTER 4
EXPERIMENTAL ANALYSIS

This chapter outlines the analysis methods used to characterise the raw materials chosen for the manufacture of anode supported SOFCs discussed in this study.

4.1 PARTICLE SIZE ANALYSIS

Analysis of powder properties is an integral step in the manufacture of SOFCs, which involves an evaluation of the starting powders to determine their physical properties and assess their suitability for achieving the desired product. When combining various powders, knowing certain characteristics beforehand such as surface area, surface energy, degree of agglomeration and particle size, shape and distribution is extremely important as these properties strongly influence compaction, powder flow properties and sintering behaviour and heavily impact the materials selection process. This process is

critical for developing and standardising production methods that meet quality criteria based on the specification for a given application. As mentioned in Chapter 3, the raw powders used to prepare the SOFCs used in this study were mixed via wet ball milling and then ground and screened. The primary purpose of ball milling the constituent powders was to ensure adequate mixing and homogeneous powder distribution. Grinding was performed to break up large powder chunks and screening was carried out to narrow the size distribution of the powders as determined by the open area of the mesh screen of the sieve. Whilst ball milling breaks up agglomerates and reduces powder particle size, oftentimes depending on milling time and grinding media, it produces a broader particle size distribution. Particle size analysis was carried out on the as-received sample powders in this study to determine mean particle size via laser scattering using a Malvern Instruments ZetaSizer HPPS.

4.2 SURFACE AREA DETERMINATION (BET)

Brunauer, Emmet and Teller are the scientists responsible for developing the most widely used method of determining the surface area of a material known as BET analysis [1] . The specific surface area of a powder is defined as the area of the surface of particles per unit mass or volume of material. Powder surface area is commonly measured by means of physical gas adsorption where the adsorbate, usually liquid N_2 at 77K, condenses onto the surface of a degassed powder sample with the measured amount of adsorbed gas for a given temperature at varying pressures being related to the powder surface area. A Qauntachrome Autosorb Dual Port Surface Area Analyser was used in this research with liquid N_2 as the adsorbate gas.

4.3 X-RAY DIFFRACTION

X-ray Diffraction (XRD) is a technique used to identify and analyse the chemical composition and structure of a material. Phase identification, crystal structure, grain size and grain orientation can all be determined by XRD. In 1912 W. H. Bragg found that crystalline materials reflect X-rays in a unique pattern specific to a given material. So during analysis, the pattern of an unknown sample is referenced against the pattern of a known standard thus, chemical identification is determined. The incident X-ray beam is generated by bombarding a target, usually Cu, with a beam of electrons that emit photons and by the process of de-excitation emit X-rays. The relationship between θ – the angle between the lattice planes and the X-rays, the wavelength of the incident beam λ and the spacing between the lattice planes d is known as Bragg's Law:

$$n\lambda = 2dsin\theta \qquad (4.1)$$

where the integer n is referred to as the order of diffraction [2]. The X-ray powder diffraction scans presented in this study were obtained using a Siemens D5005 X-ray Diffractometer. A Cu target was used with a Ni filter to absorb the CuK_{β} radiation so the source of radiation for this study was a weighted average of $CuK\alpha_1$ and $CuK\alpha_2$ = 1.5404Å at 40kV and 20 mA within the 20-70 ($2\theta^{o}$) range. XRD patterns for these samples were generated and referenced against known patterns of a specific material for phase identification. For purposes of this study, XRD analysis was used to differentiate among the various oxides and determines the phase purity of a given material.

4.4 X-RAY FLUORESCENCE

X-ray Fluorescence (XRF) is an analytical technique used to determine the elemental composition of a material. It describes the behaviour of atoms within a material after being exposed to radiation. Unlike XRD where the sample diffracts the incident X-ray beam, during XRF, the sample absorbs the X-rays and as a consequence emits X-rays due to electron energy transitions. The emitted X-rays which are unique to the elements in the sample through wavelength and atomic number can thus be used to identify the presence of such elements in that sample. In this study, the elemental composition of the anode supports was determined via XRF and was a characterisation method used to ascertain the appropriateness of our fabrication method for the bulk anode supports.

4.5 ARCHIMEDES METHOD

Archimedes' principle states the weight of a fluid displaced by a body fully or partially submerged in that fluid is equal to the upward force (buoyant force) exerted on the body. The apparent porosity of a material can be measured using this technique provided the dry weight, the soaked weight and the suspended weight of a material is known. The oxides studied in this work contain both open and closed pores where open pores serve as fuel transport mediums and closed pores remain impenetrable. As mentioned earlier, pore size, pore count, pore shape and pore connectivity are all important pore characteristics that can be manipulated to achieve the desired microstructure for enhanced performance. Each SOFC component allows for a different level of porosity based on the different component requirements. A balanced number of pores are needed in the bulk as too many pores compromise mechanical strength and too few pores restrict fuel transport. The electrolyte calls for near zero porosity as the presence of pores are sites for leakage though non-interconnected porosity, when minimal, is

allowed. For purposes of this work, Archimedes' method in water was used to measure the apparent porosity in the anode support with the bulk density and real porosity values later determined. In Equation 4.2, the apparent porosity is calculated and reported as a percentage where S_s is the saturated sample weight, S_d is the dry sample weight in air and S_w is the weight obtained while suspending the sample in water.

$$\text{Apparent Porosity (\%)} = \left(\frac{S_s - S_d}{S_s - S_w}\right) x\ 100 \qquad (4.2)$$

Apparent porosity does not include the volume of closed pores but real porosity takes into account both open and closed pores and is a better representation of the true porosity of the ceramic. Equation 4.3 was used to calculate the bulk density

$$\text{Bulk Density } (B_d) = \frac{S_d}{(S_s - S_w)} \qquad (4.3)$$

and the bulk density was used in Equation 4.4 to calculate the real porosity substituting the reported density values for ρ.

$$\text{Real Porosity (\%)} = \frac{(\rho - B_d)}{\rho}\ x\ 100 \qquad (4.4)$$

4.6 DILATOMETRY

Dilatometry is a technique used to measure the linear dimensional changes of a material as a function of time and/or temperature. During analysis, the sample is placed into a sample holder housed within a horizontal furnace. In this research, shrinkage behaviour was studied and TEC's were calculated to understand the thermal behaviour of the different starting materials and to tailor the sintering process to their properties to achieve a high-quality, multi-layered fired ceramic. A horizontal pushrod is moved until it just slightly touches the sample surface giving an initial sample length of L_o. As the sample undergoes the time/temperature program its length changes, according to the expansion properties of the material, along with the pushrod, and the sample holder as they too are exposed to the time/temperature program. The displacement recorded is a sum total of these three length changes. The data is corrected using measurements obtained from a reference standard tested under identical conditions so the

expansion behaviour of the test sample can be isolated. The coefficient of thermal expansion α is defined by the expression:

$$\alpha = \frac{\Delta L}{L_o}\left(\frac{1}{\Delta T}\right) \qquad (4.5)$$

where ΔL is the change in length, Lo is the initial sample length and ΔT is the change in temperature [3]. For green compacts, the dimensional changes measured are firing shrinkages which were a sum total of organic burnout shrinkages and sintering shrinkages. TECs were calculated on specimens that had been fabricated to the specifications they were used in the SOFC testing environment, either pre-fired to 1200°C-4hrs or fully fired to 1400°C-4hrs.

Figure 4-1 shows The Netzsch DIL 402 PC dilatometer used in this work, which contained an alumina tube sample holder with a thermocouple placed slightly above the sample to dictate the output temperature. The instrument was equipped with temperature program capabilities as well as enabled testing in different gas environments. Measurements were carried out in H_2 or in static air at 5°C/minute up to target temperatures of 800°C and 1400°C where they dwelled for 19hrs at 800°C. The measured sample dimensions were 20mm in height and 10mm in diameter.

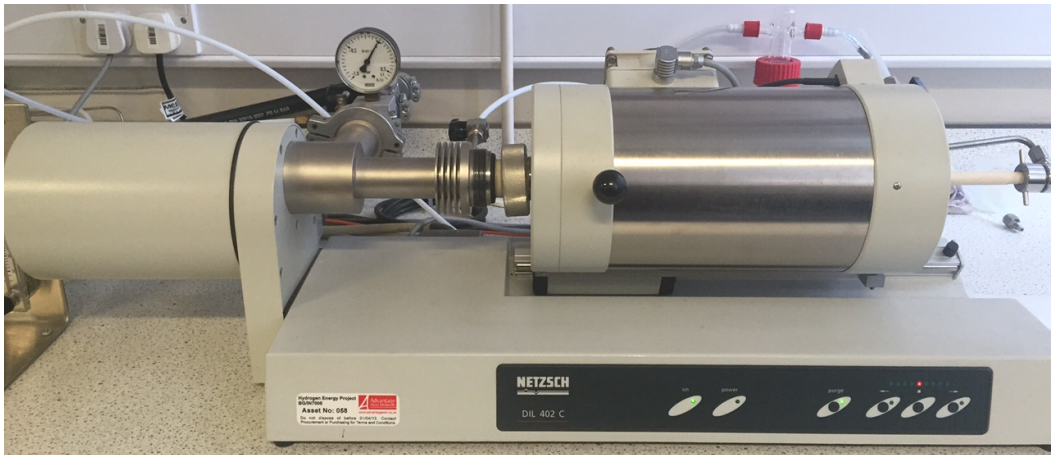

Figure 4-1: NETZSCH DIL 402 PC Dilatometer

4.7 THERMOGRAVIMETRIC ANALYSIS (TGA)

One means of assessing the thermal stability of a material is to perform thermogravimetric analysis (TGA) to monitor sample mass changes as a function of temperature. TGA is a technique that

measures the weight loss or weight gain of a specimen as it is heated or cooled. The loss of a variety of different substances can be quantified via TGA such as water, solvents, plasticizers and other carbon-containing additives. For the purposes of this work, standardising a ceramic processing procedure with minimal problems requires a controlled sintering schedule that allows for the complete decomposition and slow release of carbonaceous species from both the SOFC green compact and thin film. Trapped carbon or rapid de-binding of organic binders and fillers can lead to cracks, shape deformation, compromised mechanical strength and sample contamination. TGA identifies onset temperatures where carbon release begins and final temperatures where carbon has been completely removed. This makes selecting binder burnout temperatures easier and supports the selected firing program. TGA experiments were carried out in air within the 120 – 900^{o}C temperature range using a NETZSCH TG 209 F1 Thermogravimetric Analyser pictured in Figure 4-2.

Figure 4-2: NETZSCH TG209 F1 Libra Thermogravimetric Analyser

4.8 SCANNING ELECTRON MICROSCOPY

Scanning Electron microscopy (SEM) is a microscopy technique that uses electrons instead of light to create 2-D and 3-D images of a sample. The benefits to using electron microscopes are they can reach much higher magnifications than light microscopes and can achieve quality, high-resolution images allowing sample characteristics to be observed in finer detail. In this work all starting powders and cell microstructures were examined using either a Hitachi TM 3030 Plus Tabletop SEM or a Philips XL30 LaB6 SEM at an accelerating voltage of 20kV while elemental identification was obtained via energy dispersive X-ray analysis (EDX). The samples were gold coated to prevent charge build up during

analysis.

Examining cell microstructure – interfaces, pore evolution, grain characteristics and surface defects – using 3-D image analysis and reconstruction of Ni-10Sc1CeSZ anodes was carried out to gain a better understanding of the spatial relationships within the electrodes and how these relationships influence electrode microstructure and overall cell performance. The samples were first impregnated with a low-viscosity resin and polished with a BIB machine (IM4000, Hitachi) applying the same parameters used for 2D cross-sectional analysis. Focused ion beam (FIB)-SEM investigations, which involves alternating ion sectioning and SEM imaging were carried out with a Helios Nanolab 600i (FEI) with Ga liquid metal ion source. The serial sectioning was done with an ion beam current of 2.5 nA and an accelerating voltage of 20 kV while 0.69 nA beam current and 2.0 kV accelerating voltage were used for serial SEM imaging with the through-the-lens detector (TLD). The image stack obtained from FIB-tomography was pre-processed (*i.e.*, alignment, cropping, filtering, segmentation) and 3D reconstructed images as well as 3D surfaces were obtained using Fiji and Avizo software packages, respectively.

4.9 INTERFEROMETRY

Laser interferometry was used to measure the roughness of anode support surfaces using an optical interference profiler (KLA Tencor MicroXAM2). Each substrate was scanned in 1 mm vertical sweeps 6 times in separate regions with surface roughness values of the profiled area reported. Sample textures up to 20 μm below the pellet surface with trough depths up to 60 μm were examined. This investigation allowed the surface quality of the substrates to be assessed and the potential for achieving defect free screen-printed films evaluated. The basic principle of interferometry states a device integrated with a beam splitter splits a single light beam source into two separate beams, one directed at the test surface (sample), the other at the reference surface (mirror inside the instrument). These two reflected light beams are then recombined resulting in a recorded interference pattern. This interference pattern contains information regarding both the sample surface roughness and the reference mirror roughness using the assumption the reference mirror is smooth contributing minimally to the measured surface roughness. The sample is mounted onto the instrument stage as seen in Figure 4-3 with a 20X optical lens setting, the surface is then scanned and the root mean square roughness (S_q) and average roughness (S_a) values were obtained.

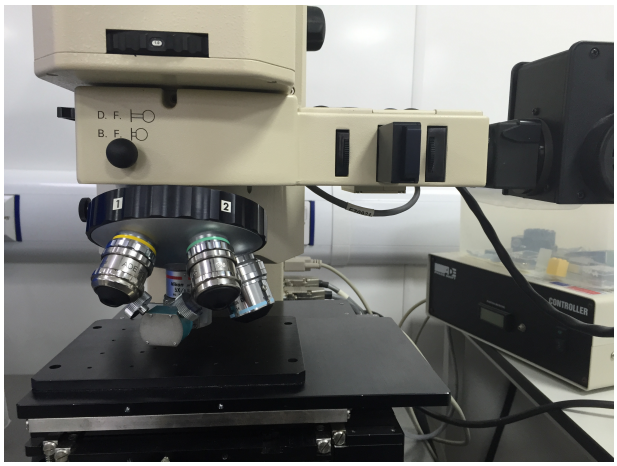

Figure 4-3: Interferometer sample stage and lenses

4.10 ELECTROCHEMICAL IMPEDANCE SPECTROSCOPY (EIS)

Electrochemical Impedance Spectroscopy (EIS) was used to measure the conductivity of dense YSZ and 10Sc1CeSZ electrolyte pellets as well as the resistances of the YSZ and 10Sc1CeSZ cells. More discussion regarding principles of EIS, its use for measuring resistances in both oxide conductors and SOFCs and the testing conditions used for the measurement of these samples is provided in Chapter 3, Section 3.4.3. As mentioned previously, EIS measures the resistance of flow of electric current through a sample by applying an AC signal to the sample and recording the sample's response. For the electrolyte pellets, sample resistance is related to electrical resistivity as shown in Equation 4.6 when sample thickness l and sample area A are known. Sample conductivity is simply the inverse of resistivity, which can be calculated from Equation 4.7 where σ is conductivity expressed in S m^{-1} and ρ is resistivity expressed in Ω m^{-1}.

$$\rho = \frac{AR}{l} \tag{4.6}$$

$$\sigma = \frac{1}{\rho} \tag{4.7}$$

Conductivity values for the YSZ and 10Sc1CeSZ electrolytes were plotted according to the Arrhenius expression shown in Equation 4.8 that examines the rate constants and activation energy of a reaction as a function of temperature. The change in conductivity with temperature is exponential so for

the relationship between temperature and conductivity to be shown more clearly, the Arrhenius plot is used to show data as a linear graph of $ln\sigma$ vs $\left(\frac{1}{T}\right)$:

$$\sigma = Aexp\left(\frac{-E_a}{K_bT}\right) \qquad (4.8)$$

where A is the pre-exponential factor, E_a is the activation energy, K_b is Boltzmann's constant (8.617×10^{-5} eV K^{-1}) and T is the temperature in Kelvin. Equation 4.8 can be re-written as

$$ln\sigma = lnA + \left(-\frac{E_a}{K_bT}\right) \qquad (4.9)$$

so the slope $\left(\frac{-E_a}{K_b}\right)$, of the the $ln\sigma$ vs $\left(\frac{1}{T}\right)$ graph is made obvious. E_a is the energy required to initiate a reaction and for purposes mentioned here relates to the energy needed to move ions through the lattice. First order curve fitting of the conductivity data contained in the Arrhenius plots was employed to more accurately calculate E_a. In some cases, best fits to the conductivity data came with second order curve fitting primarily observed at upper limit temperatures as point deviations from the trendline were minimal. This phenomena is not easily explained but will be explored further in later chapters. Where applicable, the Arrhenius plots were divided into segments and the best data fit, either the linear or polynomial trend, was used.

4.11 RHEOLOGY

Screen-printing is a reproducible, widely accepted manufacturing technique used for the deposition of thick films during SOFC fabrication, the primary reason it was the method of choice for this study. Factors such as print speed, snap-off distance, screen mesh count, print-dry sequence, the number of print passes and ink rheology all influence the properties of the printed layers. Several studies have shown the impact of ink rheology on film properties and have connected these findings to mechanical strength and microstructure.

Rheology is the study of a fluid's behaviour under an applied force. A variety of different rheological tests can be conducted to characterise a material and these are discussed in detail elsewhere [4]. The rheology study carried out in this work is limited in scope and only aims to correlate ink solids

loading with viscosity, screen-printability and layer density. Determining the proper amount of powder in the vehicle that led to facile printing while producing high-quality films with the desired thickness, porosity and microstructure was the goal.

A TA Instruments AK62 rheometer shown in Figure 4-4 with a 25 mm diameter plate was used to obtain viscosity data for the screen printing inks. Steady state viscosity flow vs. shear rate curves was generated with the shear rate varied within the range 0-100 s^{-1}. All experiments were performed at room temperature.

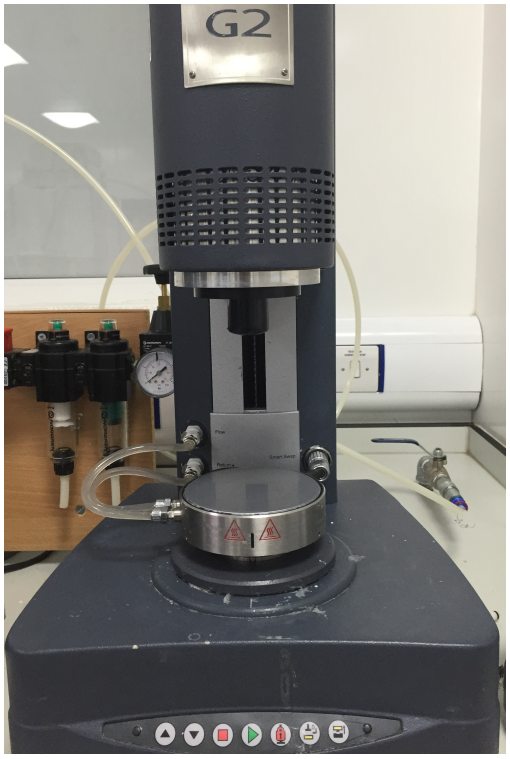

Figure 4-4: TA Instruments AK-62 Rheometer

4.12 MASS SPECTROSCOPY

A Quadropole Mass Spectrometer was used to monitor the change in fuel concentration during the electrochemical performance tests by examining the anode exhaust gases. This analysis was performed to garner insight into the nature of the reactions occurring at the anode. Helium was used as the carrier gas and fed to the cells at a flow rate of 7 ml min^{-1}. More information regarding the standardised procedure for the mass spectrometer measurements can be found elsewhere [5].

REFERENCES

[1] T. A. Ring, *Fundamentals of Ceramic Powder Processing and Synthesis*. Elsevier Science, 1996.

[2] B.D. Cullity and S. R. Stock, *Elements of X-ray Diffraction*. Prentice Hall, 2001.

[3] S. Stoupin and Y. V. Shvyd'Ko, Thermal Expansion of Diamond at Low Temperatures. *Phys. Rev. Lett.*, 2010. 104 (8): p. 9-16.

[4] M. R. Somalu, V. Yufit, I. P. Shapiro, P. Xiao, and N. P. Brandon, The impact of ink rheology on the properties of screen-printed solid oxide fuel cell anodes. *Int. J. Hydrogen Energy*, 2013. 38 (16): p. 6789-6801.

[5] A. Dhir, *Improved Microtubular Solid Oxide Fuel Cells,* PhD Thesis, University of Birmingham, 2008.

CHAPTER 5
YSZ SYSTEM CHARACTERISATION

This chapter reports the properties of the YSZ system. Results show successful anode supported Ni-YSZ cell development and manufacture. This fabrication method will be extended to the 10Sc1CeSZ system discussed in further detail in Chapters 6 and 7.

5.1 POWDER PROPERTIES

Technical specifications for all commercial powders used in this work are listed in Table 5-1. As this chapter outlines findings related to the YSZ system, discussion will centre on materials used during Ni-YSZ cell fabrication. Some powder properties were not provided by the supplier (not disclosed) or were unavailable (N/A). In the spaces reserved for the cathode powders, - - markers indicate missing data since analysis was not carried out on these materials as this research focused on anode-electrolyte half-cell development. All NiO powders were green in colour indicating they were most likely prepared

via thermal composition of $Ni(OH)_2$ compounds and heat treated at temperatures upwards of 1000°C for intergranular sintering to remove any pores. [1]

Table 5.1: Properties of SOFC Commercial Powders

Powder	Vendor	BET meas (m^2/g)	BET spec (m^2/g)	d_{50} meas (μm)	d_{50} spec (μm)	Powder Synthesis
TZ8YS	TOSOH	4.26	7±2	0.501±0.269	0.60	coprecipitation
NiO	Pi-KEM	2.80	3.2	0.907±0.072	0.75	not disclosed
NiO-A	NOVAMET	6.79	2.71	4.931± 1.658	9.20	oxidation
10Gd90Ce	FCM	6.789	8.5	0.200±0.171	0.37	precipitation
10Sc1CeSZ	IPMS	33.55	46.55	1.027±0.249	0.011- 0.013	coprecipitation
10Sc1CeSZ	DKKK	9.829	10.4	0.273±0.237	0.090	coprecipitation
Tapioca Starch	MARKET	3.376	N/A	5.719±2.274*	N/A	N/A
Wheat Flour	MARKET	1.33	N/A	0.137*	N/A	N/A
Carbon Black	VULCAN	253.7	not disclosed	0.011*	not disclosed	N/A
LSCF	PRAXAIR	--	11.8	--	0.9	combust spray
LSM	PRAXAIR	--	4.82	--	1.3	combust spray

Powder	Vendor	Color	Theoretical Density (g/cm^3)	Powder Morphology
TZ8YS	TOSOH	white	6.09	closely packed aggregate grains
NiO	Pi-KEM	dark green	6.67	tightly bound crystallites, defined grains
NiO-A	NOVAMET	olive	6.67	spherical, tightly bound agglomerates
10Gd90Ce	FCM	cream	7.20	loosely bound, irregular agglomerates
10Sc1CeSZ	IPMS	cream	5.82	agglomerates with fine nano scale grains
10Sc1CeSZ	DKKK	cream	5.82	arbitrarily shaped crystallites
TapiocaStarch	MARKET	white	N/A	uniform, sphere shaped particles
Wheat Flour	MARKET	beige	N/A	arbitrarily shaped particles that form blocks
Carbon Black	VULCAN	black	4.50	uniform, loosely packed agglomerates
LSCF	PRAXAIR	black	6.33	--
LSM	PRAXAIR	black	6.50	--

Particle size measurements generated independently (d_{50}meas) are comparable with manufacturer reported data (d_{50}spec) that support the powder morphologies all of which are reported in Table 5.1. The BET measured surface area of NiO-A (6.79 m^2 g^{-1}) differs from the manufacturer specified surface area (2.71 m^2 g^{-1}) and is inconsistent with the measured and specified particle size data. Higher surface areas tend to correlate to smaller particle sizes or materials containing a lot of pores, as the ratio of surface area to volume of material is high. NiO-A has a measured and specified d_{50} greater than NiO though the measured specific surface area values suggest the opposite. This may be due to the presence of agglomerates in the measured NiO-A sample batch. The d_{50} value means 50% of the particles in the analysed batch are of the measured size or smaller so its possible for the NiO-A powder to be comprised of both fine and coarse particles though the range and distribution of particles at the d_{10} and d_{90} points

was not measured independently. Manufacturer technical specifications for the NiO-A powder report d_{10} and d_{90} values of 4.4 μm and 19.1 μm respectively. The large particle size is most likely caused by the powder synthesis method where high temperature processing resulted in the formation of large sized grains.

Small particles tend to agglomerate due to their high surface energy and the smaller the particles, the more tightly bound they may become which can increase the average particle size as they become more difficult to separate. In the case of NiO-A, the measured BET value reflects the presence of tightly smaller sized micron particles forming even larger sized micron scale aggregates, driving the specific surface area up towards a higher value. Though the measured BET value of the NiO-A powder is higher than the NiO powder, both yield micron sized d_{50} values with that of NiO-A significantly larger than NiO. This suggests the synthesis of NiO powder produced finer, better-dispersed powder and the d_{50} of NiO is more indicative of primary particle size as the lower BET means less agglomeration. NiO (Novamet), NiO (Pi-KEM) and 8YSZ (Tosoh) have manufacturer specified grain sizes (d_{50}) of 9.20 μm, 0.75 μm and 0.60 μm with measured grain sizes of 4.93 μm ($\pm$1.66), 0.91 μm ($\pm$0.57) and 0.50 μm ($\pm$0.27) respectively, with a measured (d_{50}) of 0.03 μm for grocery grade tapioca starch. The YSZ powder had the highest surface area of all the aforementioned powders, which reflects its smallest particle size.

Figure 5-1 illustrates the morphology of the powders used in Ni-YSZ manufacture. The NiO-A powder (a) contains spherical, micron scale agglomerates ranging from 1 μm to over 15 μm as the NiO powder pictured in (b) also consists of agglomerates but exhibits smooth surfaced, well shaped crystallite structures with grain sizes in the sub-micron region. The powder characteristics seen in these micrographs confirm the theory above. The coarser, hard agglomerated NiO-A powder is more likely to have a lower sintering rate and produce a less sintered compact while the finer NiO powder is likely to yield a more dense compact with a finer microstructure due to the higher sintering rate of the finer particles and the improved particle packing brought about by good uniformity as evidenced from less agglomeration.

Researchers have reported on powder property-microstructure property relationships, providing a link between a controlled microstructure and SOFC performance [1], [2]. Tietz's results stated smooth NiO crystallites with an average grain size (d_{50}) of 0.8 μm formed microstructures with a homogenous distribution of NiO, YSZ and pores [1]. It was shown that even finer NiO particles were encapsulated within the YSZ but the distribution of all three phases was comparable. Compacts made from finer NiO

powders exhibited higher shrinkages at earlier temperatures and produced a more sintered microstructure than compacts made using coarser NiO powders. Microstructures comprised of the coarsest NiO particles lacked a homogeneous distribution of NiO, were the least dense and had higher pore content. This led to lower conductivity due to the low Ni-Ni particle contact and an overall poor performance.

Guo et al. [2] reported the best performance on an anode supported Ni-YSZ cell with a centrifugal cast YSZ electrolyte was obtained using the finest NiO powders examined in the study (0.5-2 μm) while the coarsest powder yielded the poorest microstructure and exhibited the lowest performance. It was found that the coarser particles had poorer dispersion creating agglomerates and a non-homogeneous distribution of the two-phase powders in addition to poor porosity, which limited fuel transport. Anode powder properties and the degree of agglomeration influence how Ni particles distribute themselves within the YSZ matrix which all influence anode microstructure and performance. Thus, selecting the appropriate powders to help achieve the desired anode microstructural properties is important.

Figure 5-1 (c) shows uniform, spherical shaped micron sized particles for starch while (d) shows the YSZ powders have aggregate particles that form larger crystallites with a defined shape that appear to be closely packed together. Micrograph (e) shows finer YSZ particles distributed about the surfaces of NiO (prepared with NiO-A powder) and the pore channels seem to create a tortuous pathway even though they are open and continuous. Wheat flour and carbon black were considered as alternate pore formers to the tapioca starch but due to the non-homogenous, randomly shaped particle characteristics of the wheat flour powders and a weaker NiO-YSZ support handling strength when using the carbon black powders, both were excluded. Tapioca starch was chosen due to the relationship between pore former particles and distinct pore structures and was assumed to increase mass transport and create a uniform and continuous pore distribution as was found in previous investigations [3], [4]. Images of wheat flour and carbon black are shown in Figure 5-1 (f) and (g) respectively.

5.2 SINTERING CHARACTERISTICS OF Ni-YSZ ANODE SUPPORTS

5.2.1 Ni-YSZ Porosity and Shrinkage Studies

Archimedes measurements were conducted on Ni-YSZ support discs prepared from NiO-A powder to obtain apparent porosity values for the samples fired under different pre-sintering conditions. The anode substrate serves as the mechanical support of the cell, transports fuel gas, removes reacted gas and carries electrons through the Ni phase to the reaction sites [5], [6]. Despite the agglomeration of the

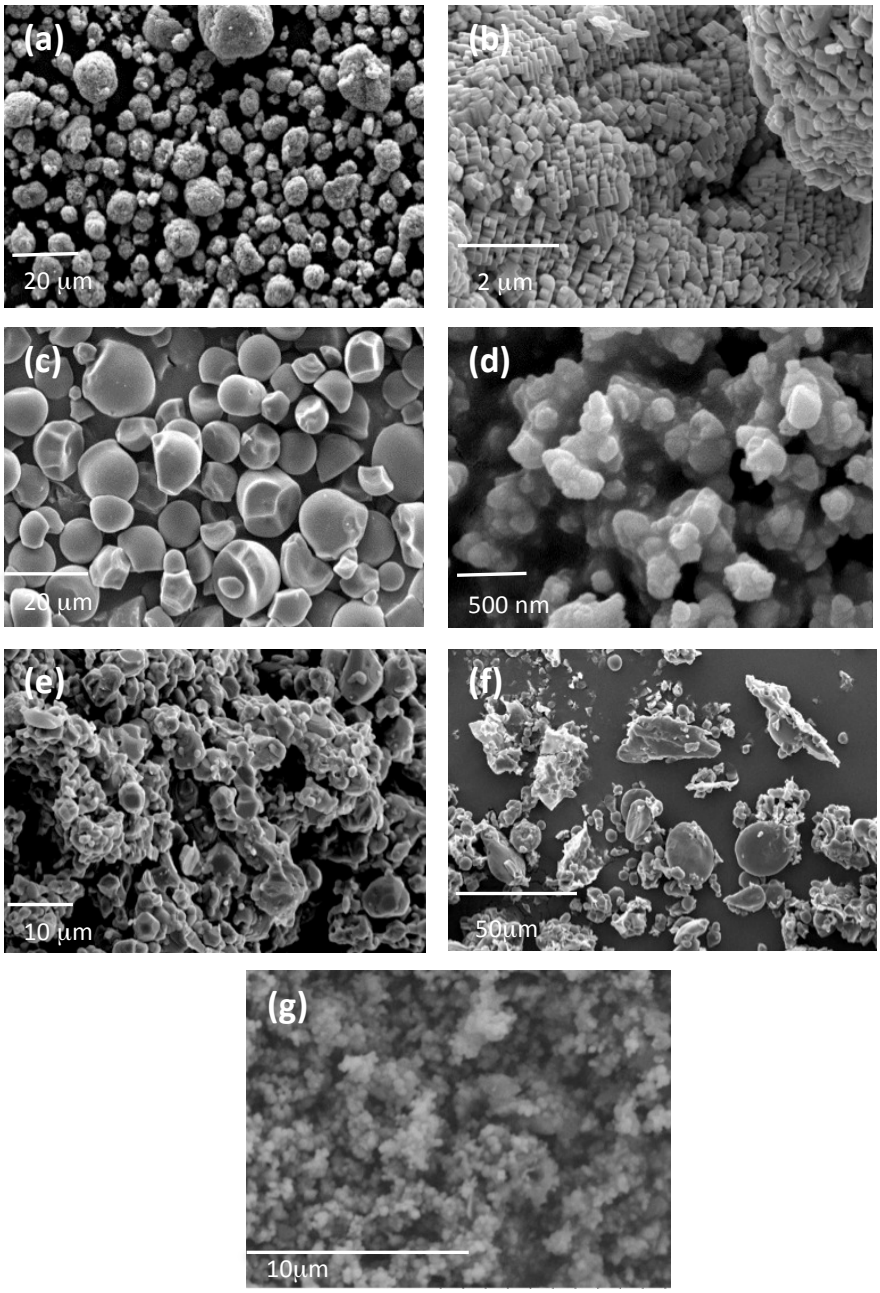

Figure 5-1: SEM images of as-received (a) NiO-A (Novamet), (b) NiO (Pi-KEM), (c) tapioca starch, (d) TZ8YS (TOSOH), (e) non-reduced NiO-YSZ, (f) wheat flour, (g) carbon black

as-received NiO-A powder, it was assumed this coarser powder would achieve porosities closer to the target porosity range providing good fuel permeability due to the lower sintering rate. Better particle packing could also be realised based on the wide particle distribution contributing to a high packing density in the green compact resulting in a more uniform microstructure. Poor electronic conductivity stemming from poor Ni-Ni contact caused by the agglomeration seemed possible to overcome by ball

milling the as-received powder to break up the agglomerates. In comparison, the finer NiO powder would give greater shrinkage with less porosity due to the higher sintering rate moving away from the target porosity range. While support strength would be improved, matching shrinkages in the SOFC component and having good pore count and pore distribution was priority and thought best achieved with the coarse NiO-A powder. All support pellets were thus prepared using the NiO-A powder.

1000-1200^{o}C was the chosen temperature range for pre-firing the anode supports even though NiO-YSZ starts to sinter at 900^{o}C with full density possible at 1600^{o}C [7], [8]. Temperatures above 900^{o}C were chosen to isolate the pre-sintering schedule that yielded support pellets with 40-45% target porosities and sufficient strength for handling. Larger target porosities were set for the pre-fired anode substrates to accommodate more densification during anode-electrolyte co-firing. This helps to better tailor the shrinkages of the half-cell multilayer and ensures the anode porosity falls within the 20-40% range, which is considered ideal for the mass transport of reactants, cell byproducts and fuel re-circulation [5], [9]. Because each component in the half-cell multilayer has different shrinkage properties, (anode support, anode functional layer, electrolyte layer) it is important to select anode support processing conditions that yield compacts with partial sintering so shrinkage mismatches between all components in the half-cell during the co-sintering stage are minimised.

Literature reports the required anode support strength be a minimum of 100MPa for continued SOFC manufacture [10]. Since mechanical strength data was not obtained for samples in this study, the support strength was assessed based on handling and pellets that could endure multiple print passes during screen-printing. Regarding the 1000^{o}C sample batch, only results for samples fired at 1000^{o}C for 4 and 8hrs were obtained though the pellets were fragile with the 1000^{o}C-2hrs and 1000^{o}C-6hrs pellets even more weak most likely due to too low firing temperatures and insufficient binding strength in the specimens after binder burnout. Because of this incomplete data, the 1000^{o}C results were omitted.

Table 5.2 lists the bulk density and apparent porosity values for the Ni-8YSZ supports fired at different pre-sintering conditions. Linear shrinkage values were calculated according to Equation (5.1) and based on the 1-D change in pellet diameter before and after firing with $\frac{\Delta L}{L_o}$ as the linear shrinkage at a given temperature T:

$$\frac{\Delta L}{L_o}, \text{ where } \Delta L = L_{final} - L_{initial} \qquad (5.1)$$

Table 5.2. Density, Porosity and Shrinkage of Ni-YSZ Supports

Sintering Temperature (°C)	Sintering Time (hours)	Bulk Volume (cm^3)	Bulk Density (g/cm^3)	Apparent Porosity (%)	Real Porosity (%)	Linear Shrinkage (%)
1050	2	0.875	2.880	52.92±0.22	54.78	8.60±0.58
1100		0.782	3.200	44.29±2.97	49.76	10.44±0.58
1150		0.700	3.491	39.61±2.52	45.19	11.09±0.34
1200		0.761	3.122	47.19±0.53	50.99	12.90±0.27
1050	4	0.952	2.627	54.27±1.18	58.77	2.11±0.00
1100		0.897	2.700	53.07±3.94	57.62	4.47±1.73
1150		0.938	2.592	51.92±1.81	59.31	5.26±0.00
1200		0.794	3.078	43.52±0.99	51.67	9.21±0.00
1050	6	0.892	2.956	51.65±0.24	59.30	5.35±0.58
1100		0.834	3.033	44.95±0.72	52.38	8.33±0.58
1150		0.853	2.889	47.67±1.76	54.64	11.14±0.58
1200		0.742	3.360	40.81±1.14	47.25	11.84±0.00
1050	8	0.878	2.925	50.94±1.53	54.09	8.33±0.40
1100		0.822	3.114	44.96±1.70	51.12	9.91±0.50
1150		0.651	3.230	46.99±0.16	49.29	11.93±0.58
1200		0.738	3.352	42.25±0.60	47.39	12.72±0.58

Standard deviation of the linear shrinkage and apparent porosity values was calculated as five Archimedes measurements were taken for each pellet at each firing condition. Standard error values fall within ±1.75% for linear shrinkage and within ± 4.00% for apparent porosity suggesting normal distribution for both data sets. For an easier examination of shrinkage as a function of temperature, the data for each sample set is plotted in Figure 5-2.

Upon initial observation, the onset sintering of each sample set varies. The highest shrinkage was 12.72% for the NiO-YSZ pellet sintered at 1200°C-8hrs. This confirms the prediction, as sintering is a time and highly temperature dependent process with increasing temperatures generally showing an increase in shrinkage leading to higher densification with greater pore removal. The lowest shrinkage was 2.11% for NiO-YSZ sintered at 1050°C-4hrs suggesting minimal changes in the linear shrinkage from room temperature to 1050°C. The trend of increasing pellet shrinkage with increasing temperature for a given dwell time is observed for all samples with the exception of the 2h dwell group not excluding possible errors in measurement for the 1150°C-2hrs and 1200°C-2hrs pellets which highlight a slight disruption of the trend. For this group, the greatest volume shrinkage takes place between 1050°C and 1100°C where it peaks and then shows little change beyond 1100°C.

The pellets fired under the 8hr schedule saw the greatest shrinkages overall with slightly lower shrinkages at 1100°C-8hrs when compared against the 1100°C-2hrs sample though the difference is less

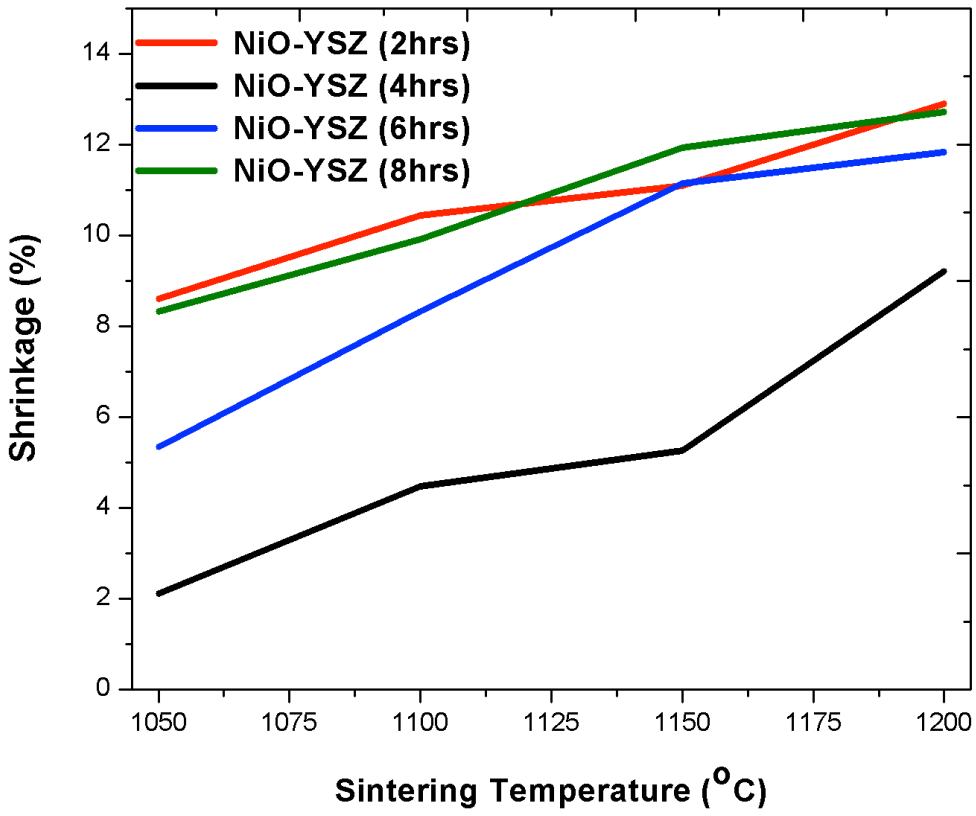

Figure 5-2: Linear shrinkage of NiO-YSZ anode supports as a function of pre-firing temperature and dwell time

than 0.05% and can be considered negligible. There was no linear relationship for shrinkage at a given temperature as a function of dwell time. This is due to shrinkage being controlled by pore removal via vacancy diffusion along grain boundaries, a process largely controlled by particle size and temperature.

Figure 5-3 isolates the Ni-YSZ anode support porosity data contained in table 5.2 for a better visual comparison. The porosity data corresponds well with the linear shrinkage data confirming the progress of sintering. Each batch had samples that yielded the target porosities except the 1150°C-2hrs batch, which falls just short of the minimum 40% porosity mark. A few samples in the 1100°C and 1150°C batch were too mechanically fragile to manufacture to completion. All samples in the 1050°C batch broke during handling. Only samples in the 1150°C-8hrs and 1200°C-4hrs, 6hrs and 8hrs batch gave consistently strong pellets. Samples in the 1200°C-4hrs were chosen as they achieved the required mechanical strength and target porosities at the most energetically favourable processing condition. SOFC single cells were manufactured using these supports.

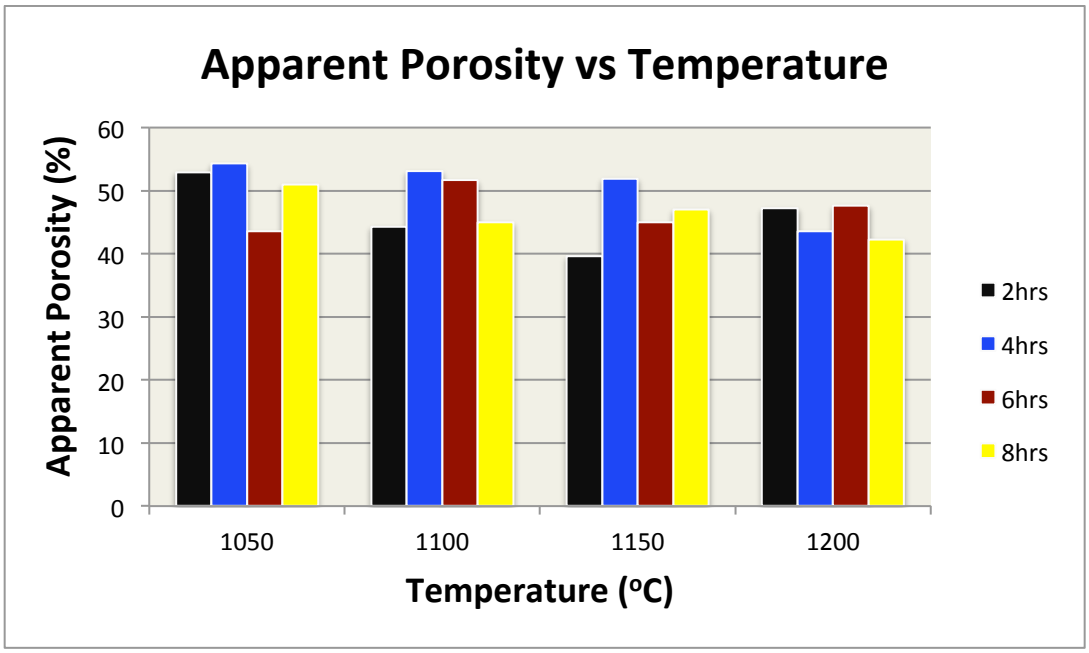

Figure 5-3: Porosity versus temperature for NiO-YSZ substrates as a function of time.

5.3 STRUCTURAL CHARACTERISATION

5.3.1 Phase Identification (XRD)

X-ray diffraction patterns of powder NiO-YSZ samples sintered at 1200°C-4hrs before and after reduction are presented in Figure 5-4. The phases present in these samples were identified by a search and match procedure. Analysis of these peaks according to the JCPDS database shows the peaks for the non-reduced NiO-YSZ samples (red pattern), corresponded to the expected reflections for cubic YSZ phase and cubic NiO phase. A scan of the as-received NiO-A powder (blue pattern) was generated to serve as a reference and to make NiO peak identification easier.

The high intensity of the NiO phase peaks in the non-reduced NiO-YSZ sample is due to the higher vol% of NiO relative to ZrO_2. Comparing the post reduced Ni-YSZ sample scan (black pattern) against the JCPDS database shows NiO is reduced to metallic Ni phase after reduction in H_2 at 800°C for 20hrs with the cubic YSZ profile unchanged. A low intensity peak in the reduced Ni-YSZ sample at 63.16° belongs to the cubic YSZ phase, corresponding to the (222) reflection. This peak was not readily observed in either of the red or blue NiO-YSZ patterns due an overlap of the high intensity peak at 62.9°, which corresponds to the (220) reflection for the NiO cubic phase. A slower scan rate was used for the reduced Ni-YSZ sample (step size of 0.01° and a scan rate of 0.2 s step^{-1}) so the 2θ regions where strong

NiO peaks were expected could be closely examined to exclude the presence of NiO. This allowed the low intensity peak at 63.16° belonging to the cubic YSZ to become more visible as no NiO peaks were identified. These results suggest the preparation method for producing phase pure composite powders is satisfactory and the reduction conditions for single cell testing are sufficient.

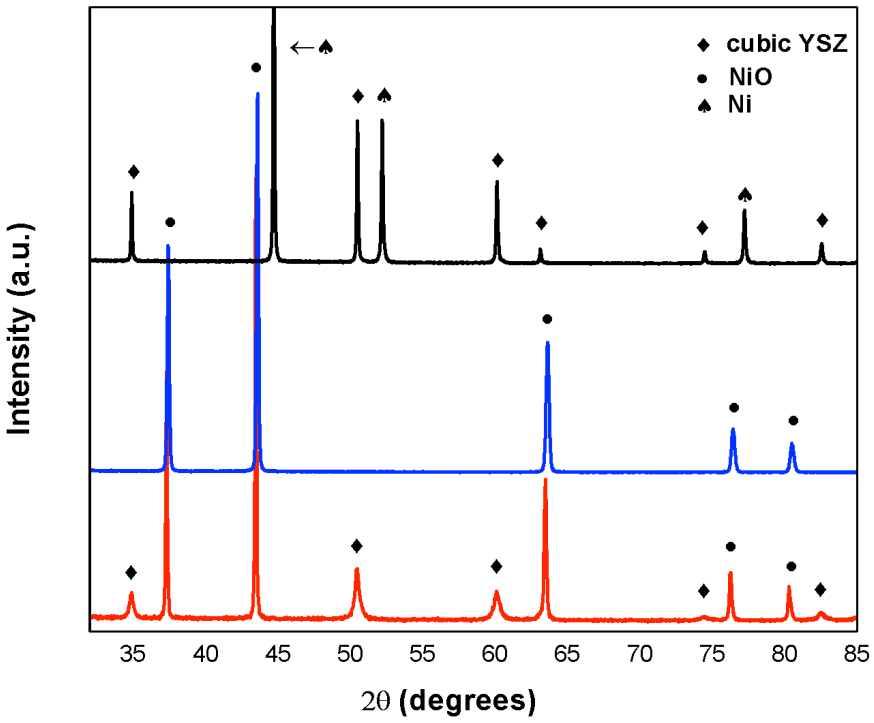

Figure 5-4: X-Ray Diffraction scans of non-reduced NiO-YSZ (red), as received NiO (blue) and reduced Ni-YSZ (black)

5.4 TOPOGRAPHY AND ANODE FUNCTIONAL LAYERS (AFLs)

5.4.1 Surface Roughness

*S*urface roughness measurements for the pre-fired Ni-YSZ discs with and without Ni-YSZ anode functional layer (AFL) films were generated. NiO-YSZ AFLs prepared with fine NiO powder (0.75 μm) in a 1:1 NiO-YSZ ratio was deposited onto the Ni-YSZ substrate surfaces. Clockwise in Figure 5-5 are the topography images for the 1050, 1100, 1150 and 1200°C-4hrs fired samples respectively without AFL. The accompanying table lists the values for the average sample roughness (S_a) and root mean square of the roughness (S_q) along with the standard deviation for each set.

Several roughness values are generated during the measurement though the (S_a) parameter is most commonly used for identifying surface roughness [11]. In Figure 5-5, the microstructural evolution of the samples is evident from the images. The decrease in surface roughness with increasing temperature is due to greater pore removal with smaller, finer pores remaining in the 1200°C-4hrs sintered compact

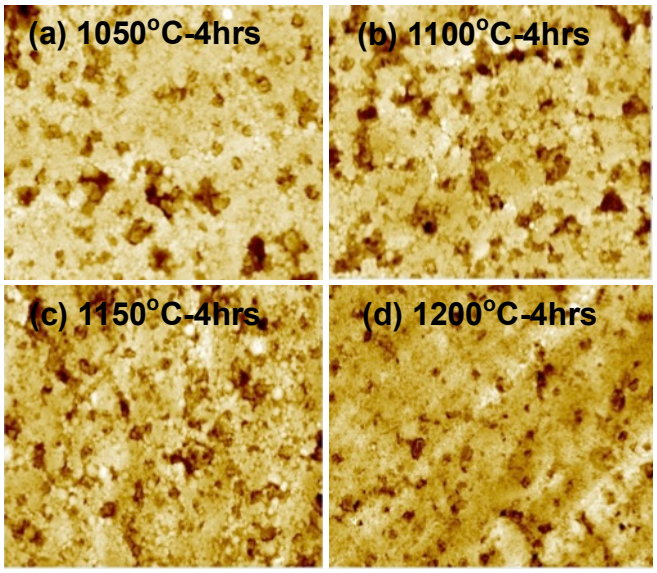

ID	(a) μm	(b) μm	(c) μm	(d) μm
S_a	2.0933	2.2567	1.9891	1.0652
SD	0.2197	0.1466	0.0532	0.0912
S_q	2.9283	2.6383	2.0423	1.6083
SD	0.8211	0.4233	0.3206	0.1196

Figure 5-5: Topography images and surface roughness values for the NiO-YSZ substrates sintered at (a) 1050°C (b) 1100°C (c) 1150°C and (d) 1200°C for 4hrs

that exhibited the lowest surface roughness. The reason for the slight increase in the (S_a) value for the 1100°C-4hrs sample is unknown. A more comprehensive plot showing the variation in the surface roughness (S_a) for samples with varying AFL thickness is presented in Figure 5-6.

5.4.2 Anode Functional Layers

Figure 5-6 shows the decrease in (S_a) for samples with varying AFL prints is more than 5 times lower than the (S_a) values of the non AFL group; the (S_a) values shown here fall between 0.5 – 0.28 μm with a 1-3% margin of error. Pellets within the 1000°C-4hrs and 1050°C-4hrs group were not examined as all broke during screen-printing. These results confirm that AFLs create a smoother surface due to the finer powders used to fabricate these layers, which resulted in lower pore content, smaller pores and an overall much finer microstructure. The cross-sectional morphology of a non-reduced sintered AFL layer is given in Section 5.7.4. As mentioned previously, a coarser microstructure for the cell support is

allowed as it better facilitates fuel transport to the reactant sites while removing reactant gases. The drawbacks to the use of an anode with a coarse microstructure for the electrochemical reactions are the reduced number of available active sites due to the lower surface area of coarser particles. Coarser particles are typically poorly dispersed and tend to be isolated from neighbouring grains during sintering. This adversely impacts densification as sintering progresses through particle contact, grain growth and pore removal. This partial sintering results in a disruption in the Ni conduction path and poor linkage between the metal and ceramic phases.

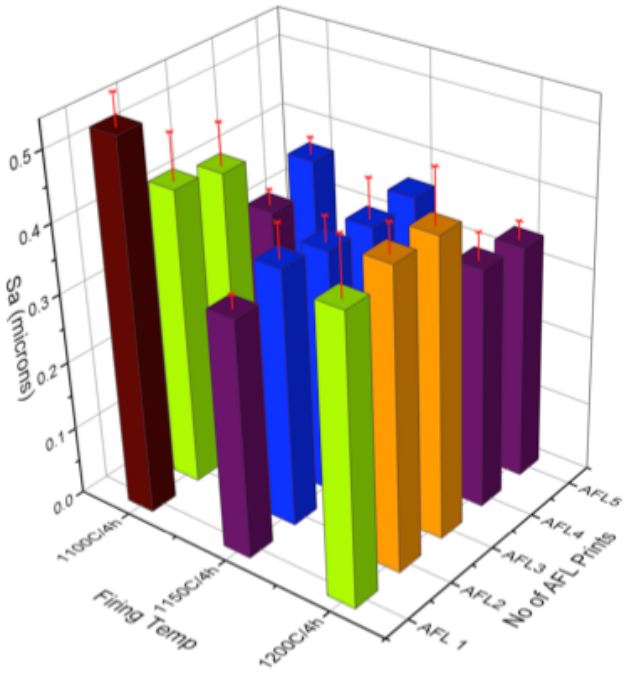

Figure 5-6: Surface roughness values for NiO-YSZ substrates with varying AFLs

As part of the AFL study, multiple layer AFL prints were deposited onto anode substrates to determine the influence of AFL layer thickness on substrate roughness. The presumption that thicker layers could mask even larger pores and surface defects on the bulk anode surface, prepping it for better electrolyte deposition was the motivation for this study. AFL1 – AFL5 denotes the number of AFL films printed onto the anode supports; AFL1 represents 1 print, AFL2 is 2 prints up to 5 prints (AFL5) with a 15 min ambient air dry and a 15 min oven dry in air at 120^{o}C between each print. Upon close examination however, there is no connection between AFL thickness and surface roughness. There is no trend within or between the sintered groups, as there appears to be more of a random distribution of the (S_a) values. These results confirm the use of AFLs create a smoother anode surface and since there is no

observed difference in (S_a) between AFL2 and AFL3 for the 1200°C group, bulk supports from this group were prepared using 2 AFL prints. Researchers have found increases in cell OCV with an increase in AFL thickness *as the effect of increasing AFL thickness is similar to the effect of increasing YSZ thickness* though ohmic and mass transport losses are observed if the AFL thickness becomes too large [12]. Thicker AFL layers limit gas diffusion across the anode and can compromise adhesion between the cell component layers due to differences in sintering shrinkages which are further exaggerated when functional layer thicknesses increase. Thus, an optimised AFL thickness that enhances performance without limitations due to restricted gas diffusion to the reactant sites must be reached.

The overall lower surface roughness values for the AFL printed samples compared to the non-AFL samples demonstrate the AFL films effectiveness in masking large pores and defects on the surface of the bare anode substrate. This increases the likelihood of fabricating gas impenetrable electrolyte films. And this is critical as attempting to manufacture a dense YSZ film onto a compromised anode surface lowers the probability of obtaining gas tight layers. The high anode substrate surface roughness is the result of the use of coarser powders and pore former additions that leave behind a rough and porous anode surface as seen in Figure 5-7 (a). And any defects on the support surface will be transferred to the printed layers as seen in Figure 5-7 (b) where a NiO AFL layer film has been deposited on a compromised pre-fired NiO anode substrate unless the thickness of the film is larger than the size of the defect. During heat treatment, the surface tension of the AFL film is reduced causing the film to "sink" into the pores, which creates pores or cracks in the film. Figure 5-7 (c) shows the presence of cracks in a fired YSZ film deposited onto an anode-AFL structure as the YSZ layer thickness was not large enough to minimise the substrate defects. These defects are sources of fuel leakage during testing and contribute to reduced oxygen partial pressures between the two cell electrodes. Combustion also occurs at the fuel leakage sites which causes a rise in the local temperature which can also lower OCV [12]. This drop in OCV results in an overall lowering of the cell performance. More discussion on the use of AFLs was provided in Chapter 3, Section 3.4.2.2. Based on these results, the use of AFLs were integrated into the cell fabrication procedure.

5.5 ELEMENTAL ANALYSIS

5.5.1 X-Ray Fluorescence (XRF)

Table 5.3 gives the chemical analysis of the NiO-YSZ substrates and NiO-YSZ AFLs obtained via XRF. The data shows there are no new impurities introduced into the starting powder during mixing

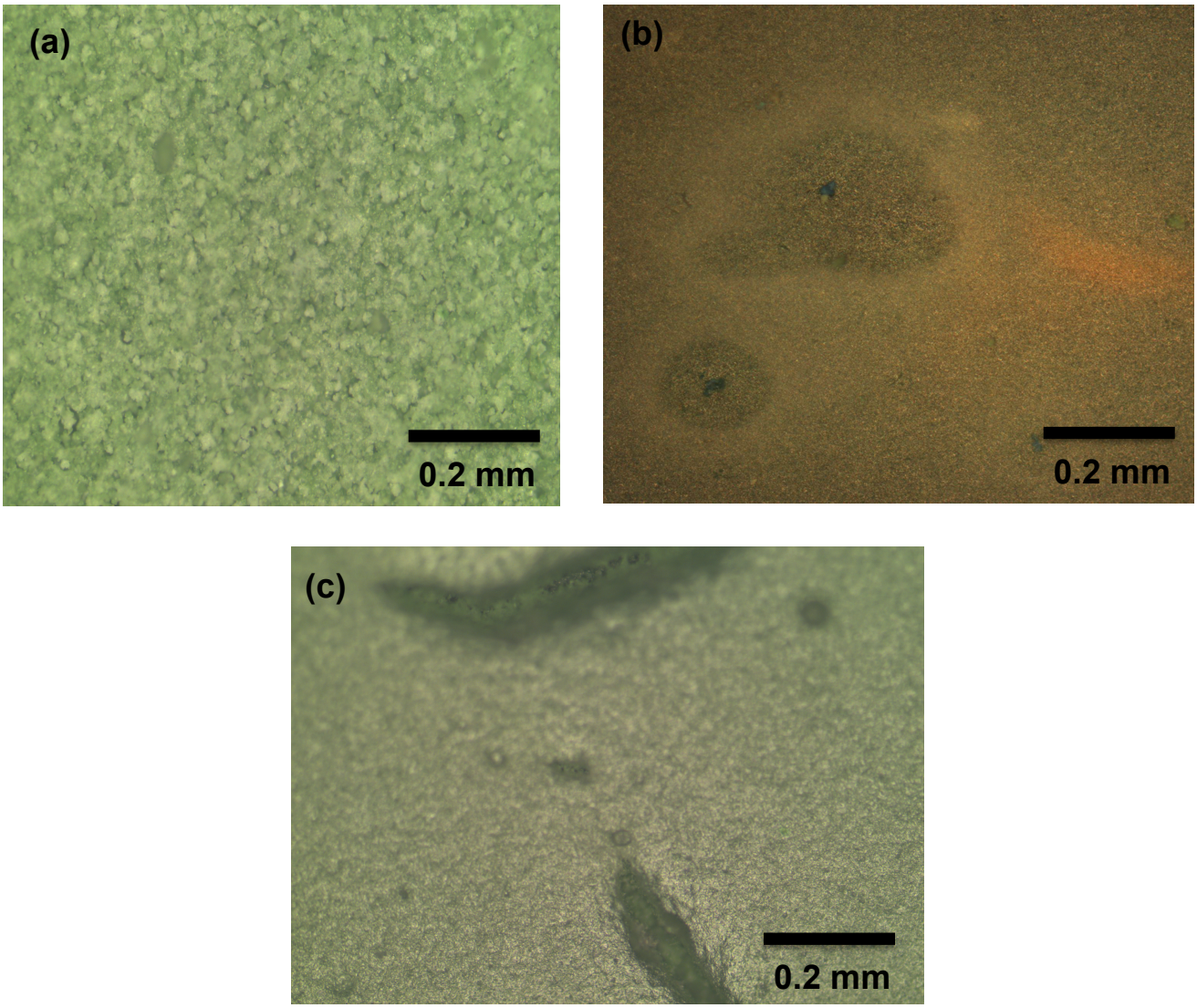

Figure 5-7: (a) pre-fired NiO-YSZ substrate surface (b) NiO AFL (c) fired YSZ layer

and no impurities introduced into the support pellets during the pre-firing stage. The precise analysis of oxide content in these materials is difficult to measure using traditional XRF methods due to the limitations of the instrument and low excitation X-rays emitted for lighter elements [13]. Thus, the data obtained here is provided in wt% per element though the relative amount of each element should be the same. The difference in the elemental composition of the bulk anode powders and the (AFL) powders is related to the difference in impurities present in the as-received NiO powders as these powders were obtained from different manufacturers. Changes in the mass between the green disc powder and the pre-fired disc powder are most likely due to water adsorption removed during heating.

Table 5.3: Elemental Composition of NiO-YSZ Anode Powders

70NiO:30YSZ pre-fired disc	Analysis (wt %)	70NiO:30YSZ green disc	Analysis (wt %)	50NiO:50YSZ AFL	Analysis (wt %)
Ni	67.59	Ni	69.75	Ni	46.65
Zr	26.92	Zr	25.81	Zr	46.39
Y	3.95	Y	3.86	Y	6.04
S	0.49	S	--	S	0.07
Na	0.46	Na	--	Hf	0.03
Nb	0.41	Nb	0.45	Nb	0.76
Cl	0.11	Cl	--	Zn	0.03
Fe	0.04	Fe	--	Fe	0.03
V	0.03	V	--	C	--
Cu	--	Cu	0.11	Cu	--
As	--	As	0.02	As	--

5.6 THERMOGRAVIMETRIC ANALYSIS (TGA) CURVES

A typical TGA curve pictured in Figure 5-8 shows the mass loss during heating of the organic additives present in the ink vehicle and added to component powders used during cell manufacture. The analysis starts at 120°C which explains why the graphs do not all start at the 100 wt% mark as expected when the analysis starts at 25°C as it was assumed any mass loss below 120°C for all samples was either the evaporation of water or solvents. The samples were analysed up to 900°C using a heating rate of 5°C/min but by 600°C all organics appear to be removed so the maximum temperature on the data plot is 700°C.

The weight loss for each material occurs in stages and can be identified by the temperature range in which the weight loss occurs. For Heraeus V-737, the vehicle used to prepare the screen printing inks, the initial loss below 200°C is the loss of water, solvents or plasticisers from the mixture. From 200 – 320°C the organic burnout process begins with final mass losses occurring between 320 – 410°C; organic removal is complete by 450°C. For Oxalic Acid, the mass loss region below 160°C corresponds to the loss of adsorbed water and the final loss of Oxalic Acid occurs between 160 – 200°C; beyond 200°C no Oxalic Acid remained. For PVB, weight loss starts at 200°C with thermal decomposition of PVB starting at 300°C and continuing until 420°C with the final removal of residual organics at 420-520°C. Tapioca Starch starts the burnout process at 250°C and continues until 380°C with final mass losses occurring between 400-490°C. The graphs of Heraeus, PVB and Tapioca Starch all overlap

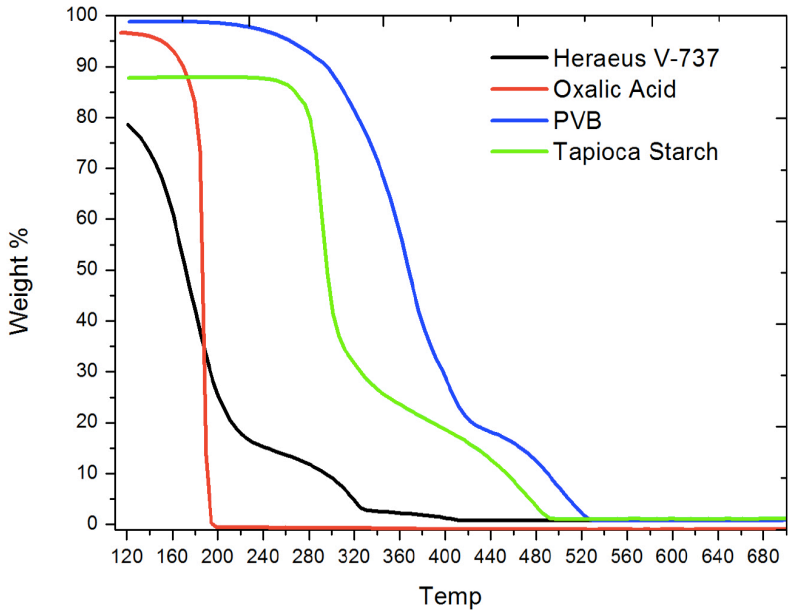

Figure 5-8: Thermogravimetric Analysis of organic additives used in SOFC manufacture during thermal treatment in air at a heating rate of 5°C/min

beyond 550°C due to axis scaling but values indicate <1.0 wt % organic compounds. The red plot for Oxalic Acid is visible as only <0.1 wt% organics remain so this graph sits slightly lower than the aforementioned plots. These results confirm the designated binder burnout schedule is suitable for removing organics from the ceramics prior to sintering.

5.7 SINTERING CHARACTERISTICS OF THE NiO-YSZ HALF CELL

5.7.1 Dilatometry and Shrinkage

Dilatometry curves for powders used to fabricate the NiO-YSZ/YSZ half-cells are pictured in Figure 5-9. The tests began at 25°C but as seen from TGA, only mass loss related to water, solvents and organics occur below 700°C so only the temperature range 800°C up to 1400°C, the co-firing temperature used during cell manufacture, is reported.

Figure 5-9, shows the maximum shrinkage for all powders occurred at the maximum temperature of 1400°C with the largest shrinkage observed for the 16hr milled YSZ powders. Researchers reported ball milling Tosoh YSZ powders for 13hrs broke up agglomerates, narrowed particle size distribution and improved powder dispersion within the ink-making vehicle making for a more homogenous printing ink and a better-sintered YSZ film [14], [15]. So in this work, as-received Tosoh YSZ powders were ball

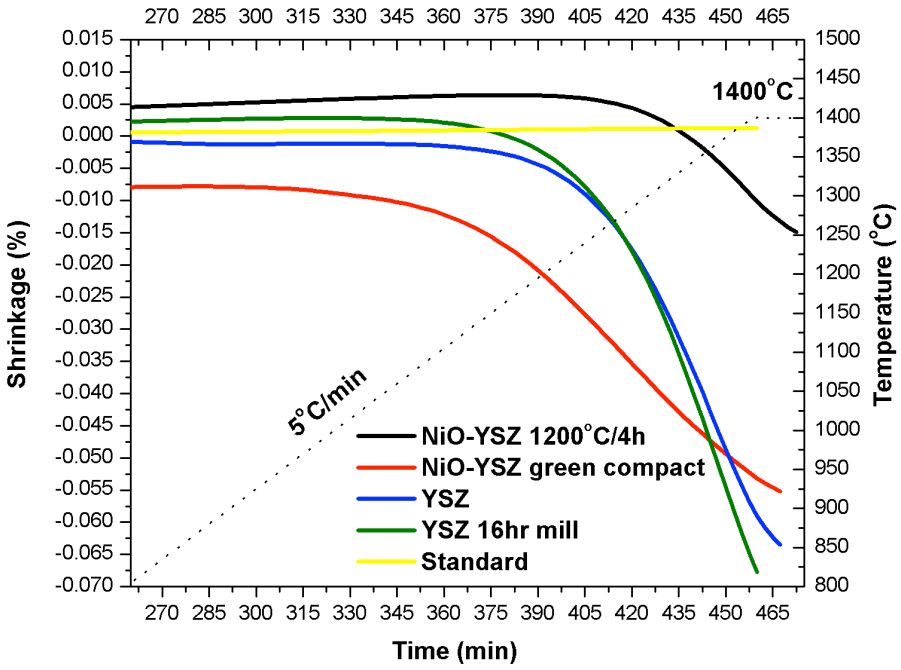

Figure 5-9: Sintering behaviour of SOFC component powders

milled for 8, 16, 24 and 32hrs but virtually no change in the specific surface area or powder morphology was observed. The 16hr milled YSZ powder was still used in the dilatometry study as the milling time closely matched that of previous researchers and comparing the shrinkage behaviour of the milled and unmilled YSZ powders was of interest for this work.

The NiO-YSZ 1200°C-4h sample exhibited the lowest shrinkage rate of all samples as was expected since it was partially sintered prior to the measurement. The sample was pre-fired to the condition of the anode supports and analysed to examine the sintering behaviour of the anode support during co-firing. Expansion occurs until 1275°C where shrinkage begins and continues until 1400°C. Authors report it is not uncommon for such thermal dilatation to occur prior to binder burnout and is related to the higher TECs of organic additives compared to the TECs of the ceramic [16], [17].

After binder burnout is complete, sintering begins and the sample begins to shrink. The dilatation observed here and for the 16hr milled YSZ sample until ~1125 °C, occurs after binder burnout (800°C) and may reflect the presence of organic residues in the samples or localised "bloating" caused by pressure build up due to the rapid evolution of CO_2 gases [16]. The samples measured during dilatometry did not closely follow the sintering schedule which called for slower ramp rates and increased dwell time

at early and late stage binder temperatures of 350°C and 500°C respectively due to time constraints related to instrument booking and availability, so its possible organics remained in these samples.

The green NiO-YSZ compact, prepared to analyse the sintering behaviour of the Ni-YSZ AFL film, had the highest shrinkage of all samples until 1325°C. Shrinkage had already started at 800°C which supports previous researchers findings [7], [8]. This sample shares the greatest mismatch with the NiO-YSZ 1200°C-4hrs sample with narrowing mismatches with both YSZ samples between 1250°C – 1375°C. The green NiO-YSZ shrinkage appears gradual over the measured temperature range and has less overall shrinkage than both YSZ samples. The 5.65% shrinkage from dilatometry does not agree well with the linear shrinkage value of 9.21% (Table 5.2). There is no clear explanation for this discrepancy in measurement.

The onset sintering of both the as-received and 16hr milled YSZ samples occurred at ~1135°C with the milling step slightly altering the sintering curve where an overall higher shrinkage for the milled powder is observed. This is not surprising as finer powders typically start to sinter at lower temperatures and exhibit a higher shrinkage. These results support the assumption that the milling step successfully broke up the agglomerates creating a slightly finer powder than the as-received YSZ powder. The smallest shrinkage mismatch is observed between the 16hr milled YSZ and the Ni-YSZ pre-fired support until 1200°C where the mismatch starts to widen. Electrolyte layers were printed with inks prepared with the milled YSZ powders due to the higher shrinkage and presumed enhanced densification.

5.7.2 Dilatometry and Thermal Expansion Coefficients

TEC's were calculated from dilatometry measurements obtained for the Ni-YSZ and YSZ samples. The specimens were manufactured and fired according to the processing conditions used to prepare them for SOFC testing to get some idea about how these materials interact with each other as a multilayered SOFC during operation. They were tested between 25 - 800°C where they dwelled for 19hrs. The YSZ was tested in both static air and in H_2 at 800°C since it is exposed to both oxidising and reducing environments during testing while Ni-YSZ was tested in H_2 only.

In the middle column of Table 5.4 the measured TECs are listed within the 120 – 800°C range and though not shown here, all materials showed minimal deviations in their TEC during the 19hr dwell at 800°C. There was also a trend of increasing TEC with increasing temperature for all measured samples. Literature values for YSZ at 600°C are in close agreement with the TEC for the measured YSZ

in air at the same temperature ($9.01x10^{-6}$) with the similar trend of increasing TEC with increasing temperature also observed [18].

A larger difference exists for the measured and reported TEC values of Ni-YSZ and this is likely due to the difference in NiO-YSZ composition as well as the testing environment – the measured NiO-YSZ was measured in H_2 while literature reports NiO-YSZ testing in air [19]. All materials have relatively low TECs with the green NiO-YSZ responsible for the greatest mismatch between the layers. The green NiO-YSZ mimics the AFL that sits between the substrate and the YSZ film and further contributes to the probability of curvature due to poor TEC matching. Al_2O_3, which comprises the cell housing material and Ag paste used to seal the cell onto the Al_2O_3 tube, are also provided. A large difference between the NiO-YSZ support and Al_2O_3 tube is also observed. This data coupled with the shrinkage data in Figure 5-9 supports the expectation of curvature and the consideration of additional steps that should be taken to minimise warpage and obtain a flat cell structure.

Table 5.4: Table of TECs for SOFC Component Materials

SYSTEM	TEC (α), K^{-1} (120°C-800°C)	REPORTED TECs
70NiO-30YSZ (1200°C-4hrs)	2.31E-5 after 19hr at 800°C	
70NiO-30YSZ (green)	3.62E-5 after 19hr at 800°C	75NiO-25YSZ - Air 1.29E-5 (800°C) [19]
YSZ (1400°C-4hrs) - air	2.57E-5 after 19hr at 800°C	1.05E-5 (600°C) [18]
YSZ (1400°C-4hrs) – H_2	2.34E-5 after 19hr at 800°C	
Al_2O_3	N/A	8.10E-6 - Air (1000°C, Almath)
Pure Silver	N/A	19.0E-6 [20]

5.7.3 Co-firing Characteristics of the Ni-YSZ/YSZ Half Cell

Different shrinkage rates between the multilayers in a SOFC often lead to sintering induced stresses during co-firing [21], [22]. These stresses act on the film and can produce cracks as seen in Figure 5-10 (a) or cell curvature as seen in Figure 5-10 (b)-1. Both introduce sealing and testing challenges that lead to compromised performance or even failure. YSZ films were screen-printed onto the NiO-YSZ/NiO-YSZ (AFL) structure and half-cells were co-fired to 1400^{o}C-4hrs. For more discussion regarding sintering schedule and target co-firing temperature selection refer to Chapter 3, Section 3.4.2.3. YSZ inks of different loadings were prepared and viscosity data at different shear rates as a function of solids loading can be found in Figure 5-11. Using ink viscosity values as a general indicator for ink printability is not reliable as ink viscosity is strongly determined by solids loading and starting powder properties. So acceptable viscosity ranges for printing inks prepared with coarse, micron sized powders would not be a useful guide for determining printability for inks prepared with nanoscale powder.

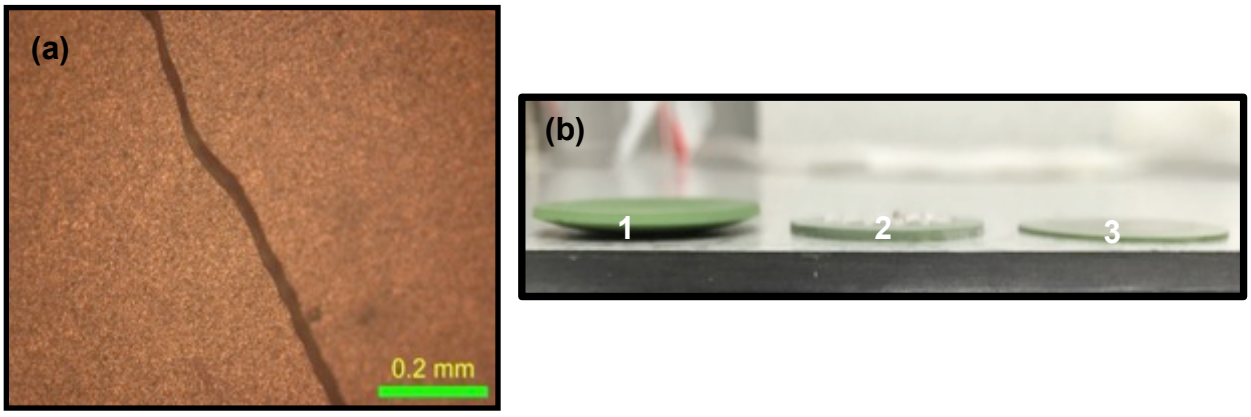

Figure 5-10: (a) YSZ layer crack and (b) NiO-YSZ/YSZ curvature to flatness

The viscosity data in Figure 5-11 illustrates the trend of increasing viscosity with increasing solids loading due to improved particle association brought about by higher powder content. This improved particle association helps to create better particle contact and higher powder packing, which can promote higher layer densification. The goal was to obtain ink with the highest solids loading that was still printable. An increase in ink tackiness with increasing viscosity was also observed so the only printable YSZ inks with the highest solids loading was vol 40% and vol 45%. Screen mesh imprints

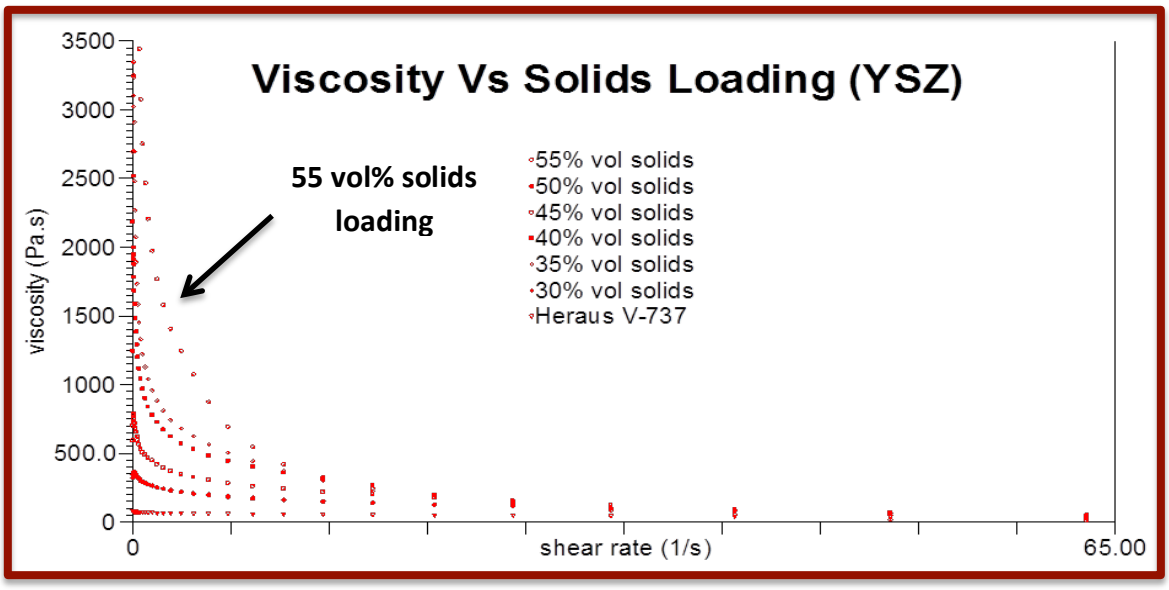

Figure 5-11: Ink loading vs viscosity for YSZ inks. The arrow identifies the curve for the 55% vol solids ink with the remaining plots appearing in the top down direction as denoted by the legend

were observed in films printed with the vol 45% inks so YSZ layers were printed using vol 40% inks.

Because the YSZ layer shrinks more than the NiO-YSZ, curvature towards the YSZ layer during co-firing was observed as shown in Figure 5-10 (b)-1; similar observations were also reported by other researchers [23]–[25]. When the shrinkage rate of the anode is larger than the electrolyte (this can be manipulated via powder processing and increased layer thickness), curvature towards the anode will occur. Figure 5-12 illustrates the relationship between curvature and differences in sintering kinetics between the layers. Cell curvature toward the electrolyte can be suppressed by applying weight or adding "compensation layers" between the electrolyte and anode which have shrinkage characteristics similar to the electrolyte [22]. Our research trials have repeatedly shown that half-cell concave up curvature can be constrained when samples are weighed down by force as seen in Figure 5-10 (b)-2; a commercial tape cast Ni-YSZ half-cell is pictured in Figure 5-10 (b)-3 for comparison. Thus, the cells were placed between two 5 cm x 5 cm Al_2O_3 squares that exerted a force of 0.1 N, which proved successful for producing flat cells. The manufacturing sequence up to the co-firing stage is pictured in Figure 5-13. Stage (a) is the pre-fired NiO-YSZ substrate, (b) and (c) show the printed NiO-YSZ AFL and YSZ electrolyte layer respectively and (d) is the fired anode-electrolyte bi-layer.

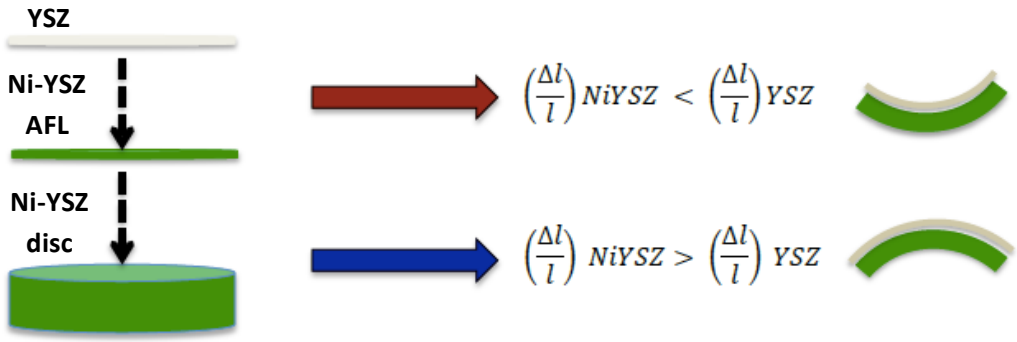

Figure 5-12: Illustration relating cell curvature to sintering kinetic mismatches [26]

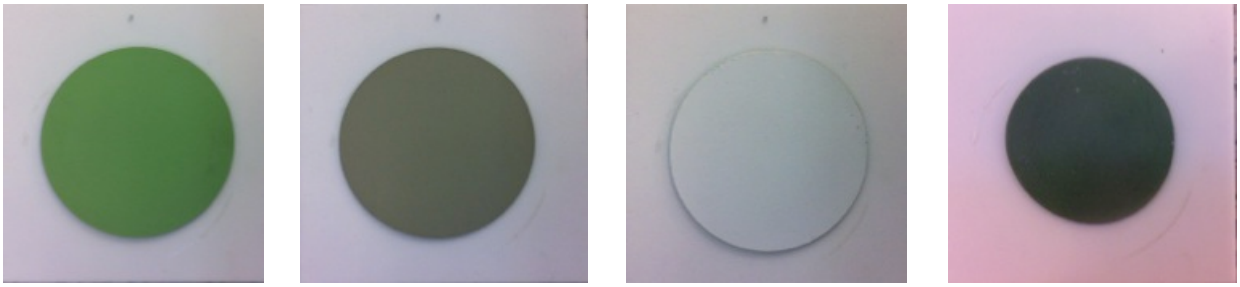

Figure 5-13: Stages of NiO-YSZ/YSZ half-cell manufacture

5.7.4 Ni-YSZ Cell Microstructure

Cross-sectional SEM images of the Ni-YSZ lab grade cells were generated to examine cell component microstructure with a primary focus on evaluating YSZ electrolyte layer densification. Figure 5-14 shows a complete Ni-YSZ/YSZ/LSM-YSZ/LSM cell with excellent adhesion between all cell component layers. This suggests that the weight used to obtain cell flatness during half-cell co-fire was also sufficient enough to achieve complete contact between the anode and electrolyte, which provided a satisfactory foundation for cathode deposition. The anode support microstructure shows well-distributed large NiO particles and fine YSZ particles that create a network of NiO and YSZ phases with good NiO-YSZ contact. The Ni-YSZ AFL layer has a finer microstructure with finer pores. The total cathode consisting of the LSM-YSZ composite and LSM pure layers showed a thickness of ~35 μm with

a continuous microstructure and good particle distribution observed for the LSM-YSZ layer while the LSM layer appeared to have a more coarser microstructure evident of poorly dispersed powders along with some interconnected porosity. These findings show screen-printing has been successfully implemented for the manufacture of anode supported single cells. The relationship between cell microstructure and electrical performance will be discussed further in Chapter 7.

The 12 μm YSZ layer is uniform and quite dense though it contains fine, closed pores that at low levels is acceptable and should not have a significant impact on the OCV. Electrolyte porosity was calculated using Image J image-editing software. A portion of the electrolyte region for the sample pictured in Figure 5-14 was analysed and the pore count and pore size distribution was determined. Figure 5-15 shows the analysed electrolyte portion along with the histogram that displays these findings. The calculated YSZ electrolyte porosity was 3.81% with a narrow pore size distribution range of average pore sizes falling between 0.12 μm and 0.18 μm. These results quantitatively support the microstructure information obtained from SEM images.

For comparison, an image of a commercial anode supported Ni-YSZ cell from Ningbo Institute of Material Technology (China) is pictured in Figure 5-16. The cell was manufactured via tape casting with a screen-printed cathode, which yielded good phase distribution in the electrodes and a dense 10 μm YSZ electrolyte layer with small closed porosity. The difference in microstructures between each of the cell components is easily distinguishable and good layer adhesion between the components is observed.

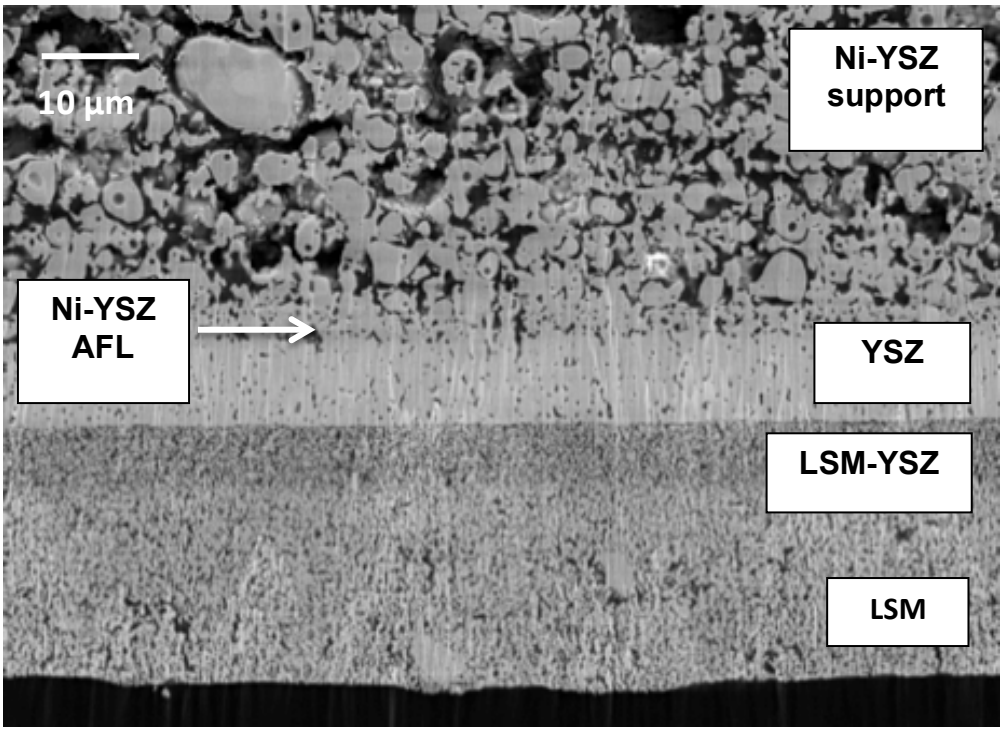

Figure 5-14: SEM secondary imaging of a Ni-YSZ/YSZ/LSM-YSZ cell

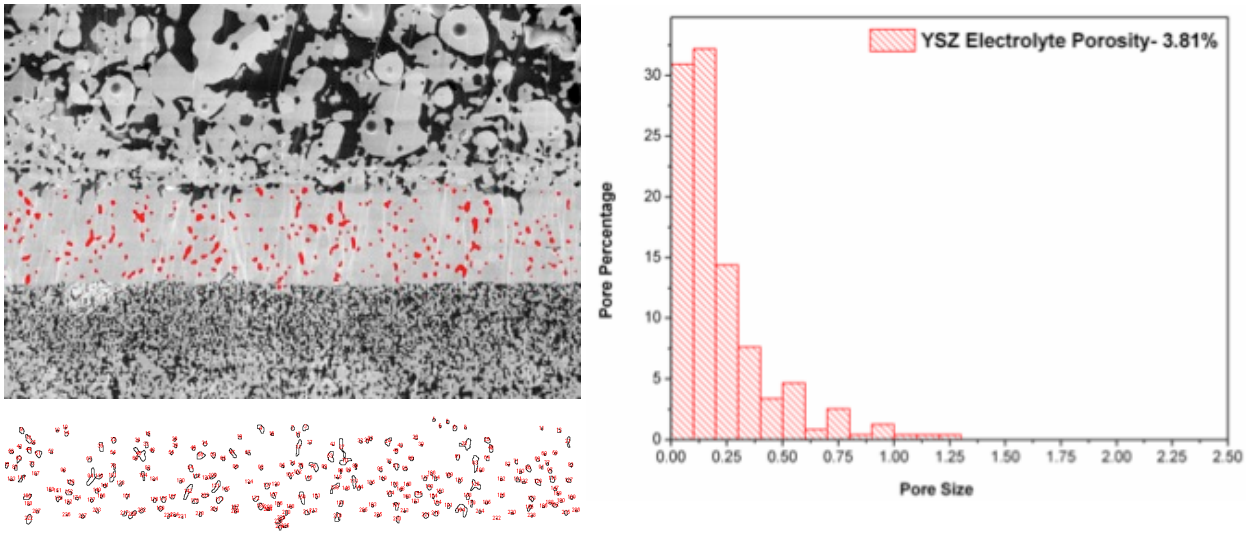

Figure 5-15: YSZ pore size distribution

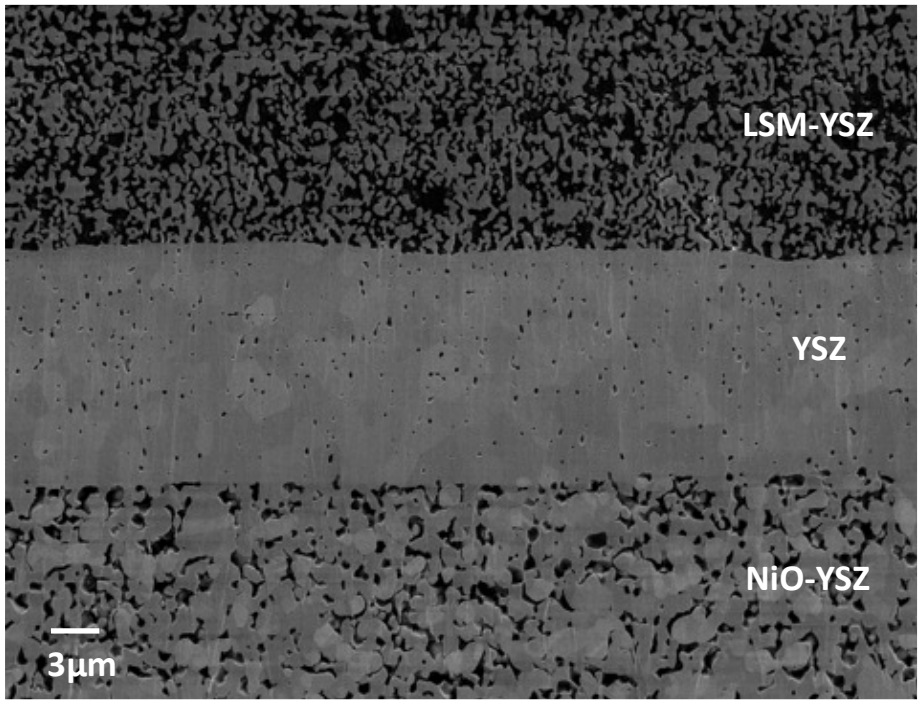

Figure 5-16: Cross-sectional SEM of a commercial YSZ anode supported cell

5.8 SUMMARY

Anode supported YSZ single cells have been successfully manufactured via uniaxial die-pressing, screen-printing and co-sintering. The standardised ceramic-processing route produced phase pure component powders without any contaminants introduced during the process. Coarse NiO powders were used to prepare the Ni-YSZ substrates while finer NiO powders were used to prepare the Ni-YSZ AFLs. The difference in microstructure between the two anodes are evident with smaller pores and a lower pore count observed for the AFLs compared to a greater quantity of larger sized pores seen for the anode substrate. The porous anode surfaces were modified through the use of a fine AFL structure that reduced anode surface roughness, which aided in the densification of the electrolyte films. The Ni-YSZ anode substrates were pre-fired at 1200^{o}C-4hrs and exhibited sufficient strength for handling allowing the completion of the manufacturing sequence through to the anode-electrolyte co-firing stage. Shrinkage mismatches between the anode substrate, AFL and electrolyte films caused concave up curvature in the multilayer during co-firing but an applied load to the half-cells during co-firing proved successful for avoiding warpage. The proposed sintering schedule allowed for the complete burnout of organics and yielded highly dense YSZ films containing 3.81% porosity.

REFERENCES

[1] F. Tietz, F. J. Dias, D. Simwonis and D. Stöver, Evaluation of commercial nickel oxide powders for components in solid oxide fuel cells. *J. Eur. Ceram. Soc.*, 2000. 20 (8): p. 1023-1034.

[2] W. Guo and J. Liu, The effect of nickel oxide microstructure on the performance of Ni–YSZ anode-supported SOFCs. *Solid State Ionics*, 2008. 179 (27–32): p. 1516-1520.

[3] A. Sarikaya, V. Petrovsky and F. Dogan, Development of the anode pore structure and its effects on the performance of solid oxide fuel cells. *Int. J. Hydrogen Energy*, 2013. 38 (24): p. 10081-10091.

[4] A. Sanson, P. Pinasco and E. Roncari, Influence of pore formers on slurry composition and microstructure of tape cast supporting anodes for SOFCs. *J. Eur. Ceram. Soc.*, 2008. 28 (6): p. 1221-1226.

[5] W. Z. Zhu and S. C. Deevi, A review on the status of anode materials for solid oxide fuel cells. *Mater. Sci. Eng. A*., 2003. 362 (1–2): p. 228-239.

[6] F. Zhao and A. V. Virkar, Dependence of polarization in anode-supported solid oxide fuel cells on various cell parameters. *J. Power Sources*, 2005. 14 (1): p. 79-95.

[7] W. Bao, Q. Chang and G. Meng, Effect of NiO/YSZ compositions on the co-sintering process of anode-supported fuel cell. *J. Memb. Sci.*, 2005. 259 (1–2): p. 103-109.

[8] N. H. Menzler, F. Tietz, S. Uhlenbruck, H. P. Buchkremer and D. Stöver, Materials and manufacturing technologies for solid oxide fuel cells. *J. Mater. Sci.*, 2010. 45 (12): p. 3109-3135.

[9] J. Larminie and A. Dicks, *Fuel Cell Systems Explained*, John Wiley and Sons 2003.

[10] O. Vasylyev, I. Brodnikovskyi, M. Brychevskyi and I. Pryshchepa, NiO-10Sc1CeSZ Anode: Structure and Mechanical Behavior. Advances in Solid Oxide Fuel Cells III: *Ceram. Eng. Sci. Proc*., 2007. 28 (4): p. 361-376.

[11] J. C. Stover, *Optical Scattering: Measurement and Analysis*, SPIE Optical Engineering Press, 1995.

[12] K. Chen, X. Chen, Z. Lü, N. Ai, X. Huang and W. Su, Performance of an anode-supported SOFC with anode functional layers. *Electrochim. Acta*., 2008. 53 (27): p. 7825-7830.

[13] B. D. Cullity and S. R. Stock, *Elements of X-ray Diffraction*, Prentice Hall, 2001.

[14] Y. Zhang, X. Huang, Z. Lu, Z. Liu, X. Ge, J. Xu, X. Xin, X. Sha and W. Su, A study of the process parameters for yttria-stabilized zirconia electrolyte films prepared by screen-printing. *J. Power Sources*, 2006. 160 (2): p. 1065-1073.

[15] Y. Zhang, X. Huang, Z. Lu, X. Ge, J. Xu, X. Xin, X. Sha and W. Su, Effect of starting powder on screen-printed YSZ films used as electrolyte in SOFCs. *Solid State Ionics*, 2006. 177 (3–4): p. 281-287.

[16] J. B. Wachtman, Fabrication of Ceramics. *Ceram. Eng. Sci. Proc*., 2009. 14 (11–12): p. 20-32.

[17] K. Maca, V. Pouchly and A. R. Boccaccini, Sintering densification curve: A practical approach for its construction from dilatometric shrinkage data. *Sci. Sinter.*, 2008. 40 (2): p. 117-122.

[18] H. Hayashi, T. Saitou, N. Maruyama, H. Inaba, K. Kawamura and M. Mori, Thermal expansion coefficient of yttria stabilized zirconia for various yttria contents. *Solid State Ionics*, 2005. 176 (5–6): p. 613-619.

[19] J. Johnson and J. Qu, Effective modulus and coefficient of thermal expansion of Ni–YSZ porous cermets. *J. Power Sources*, 2008. 181 (1): p. 85-92.

[20] S. Stoupin and Y. V. Shvyd'Ko, Thermal expansion of diamond at low temperatures. *Phys. Rev. Lett.*, 2012. 104 (8): p. 9-16.

[21] W. Li, K. Hasinska, M. Seabaugh, S. Swartz and J. Lannutti, Curvature in solid oxide fuel cells. *J. Power Sources*, 2004. 138 (1–2): p. 145-155.

[22] J. Malzbender, T. Wakui and R. W. Steinbrech, Curvature of planar solid oxide fuel cells during sealing and cooling of stacks. *Fuel Cells*, 2006. 6 (2): p. 123-129.

[23] S. H. Lee, G. L. Messing and D. J. Green, Warpage Evolution of Screen Printed Multilayer Ceramics during Co-Firing. *Key Eng. Mater.*, 2004. 264–268 (1): p. 321-330.

[24] P. Von Dollen and S. Barnett, A Study of Screen Printed Yttria-Stabilized Zirconia Layers for Solid Oxide Fuel Cells. *J. Am. Ceram. Soc.*, 2005. 88 (12): p. 3361-3368.

[25] M. Cologna, V. M. Sglavo and M. Bertoldi, Sintering and Deformation of Solid Oxide Fuel Cells Produced by Sequential Tape Casting. *Int. J. Appl. Ceram. Technol.*, 2010. 7 (6): p. 803-813.

[26] M. K. Lankin and K. Karan, Effect of Processing Conditions on Curvature of Anode/Electrolyte SOFC Half-Cells Fabricated by Electrophoretic Deposition. *J. Fuel Cell Sci. Technol.*, 2009. 6 (2): p. 021001: 1-8.

CHAPTER 6
10Sc1CeSZ SYSTEM CHARACTERISATION

This chapter reports the properties of the 10Sc1CeSZ system. Initial results show successful manufacture of anode supported Ni-10Sc1CeSZ cells with poor quality screen-printed 10Sc1CeSZ electrolyte layers. After several experimental trials, satisfactory screen-printed 10Sc1CeSZ layers were obtained. Comparisons of the electrical performance between the YSZ and 10Sc1CeSZ systems are discussed in further detail in Chapter 7.

6.1 10Sc1CeSZ POWDER PROPERTIES

Technical data for all commercial powders used in this study can be found in Chapter 5, Table 5.1. This chapter focuses on the development of the 10Sc1CeSZ system so a more detailed discussion regarding the powders used in the fabrication of Ni-10Sc1CeSZ cells and their properties will be provided. A detailed analysis of the cathode powders is not given as the focus of this study is on anode-electrolyte half-cell development. The two 10Sc1CeSZ electrolyte powders supplied by IPMS and DKKK had manufacturer specified BET surface areas of 33.55 $m^2 g^{-1}$ and 9.829 $m^2 g^{-1}$ respectively.

The measured surface area values for these powders were 39.47 m^2 g^{-1} and 10.4 m^2 g^{-1} respectively. The difference between the specified and measured BET values for the IPMS powder is slightly greater than for the DKKK powder resulting in value differentials of 14.9%. For the DKKK powder, although there is a small 5% differential in the absolute specified and measured BET values, the values are moderately large and in the same range and correlate to smaller particle sizes of 0.090 μm and 0.273 μm for the specified and measured d_{50} values respectively. Higher surface areas tend to relate to smaller particle sizes, a correlation commonly seen, as the ratio of surface area to material volume is high. This is not always the case as some surface area values do not reflect the interparticle pore volume contained within a given test sample. As mentioned in Chapter 4, Section 4.2, the surface area technique applied to measure the external surface area of the powder samples in this work was the BET method, the same manufacturer specified method employed for both the DKKK and IPMS powders which allows for a direct comparison of these values.

For the IPMS powder, the specified and measured d_{50} values were 0.011 μm and 1.027 μm respectively. The results of the manufacturer specified d_{50} approximation for the IPMS powder relates to the higher specified surface area values, values much larger than the DKKK surface area estimations, yielding noticeably smaller d_{50} sizes when compared against the DKKK powder. Laser scattering was used to obtain the measured values while the manufacturer specified measurement technique was not disclosed. During laser scattering the powder must be well dispersed in solution for an accurate measurement. If there were any sedimentation or poorly dispersed powder the collected data would give a false reading. This could explain the discrepancy. The Gadolinia doped Ceria (GDC) powder obtained from Fuel Cell Materials (FCM) has specified and measured d_{50} sizes in the micron scale range with values of 0.37 μm and 0.200 μm ($\pm$0.171) respectively. The specified and measured BET surface area values of 6.79 m^2 g^{-1} and 8.50 m^2 g^{-1} respectively reflect a 20% difference between the values which correlate with the specified and measured particle sizes.

The microstructural characterisation of the powders obtained via SEM and TEM is shown in Figure 6-1. SEM images were initially obtained to report the average particle size but later investigations via TEM determined whether particles were composed of many crystals with the average size of each crystallite assessed. The SEM image of the IPMS 10Sc1CeSZ powder (a) shows tightly bound spheroidal shaped particles ranging in size from ≈ 0.05 μm – 0.25 μm with the TEM image of this powder (b) showing fine nanoscale crystallites having average sizes between 11-13 nm. An SEM of the DKKK 10Sc1CeSZ powder (c) shows smooth surfaced particles with the largest agglomerate size ≈ 1.5

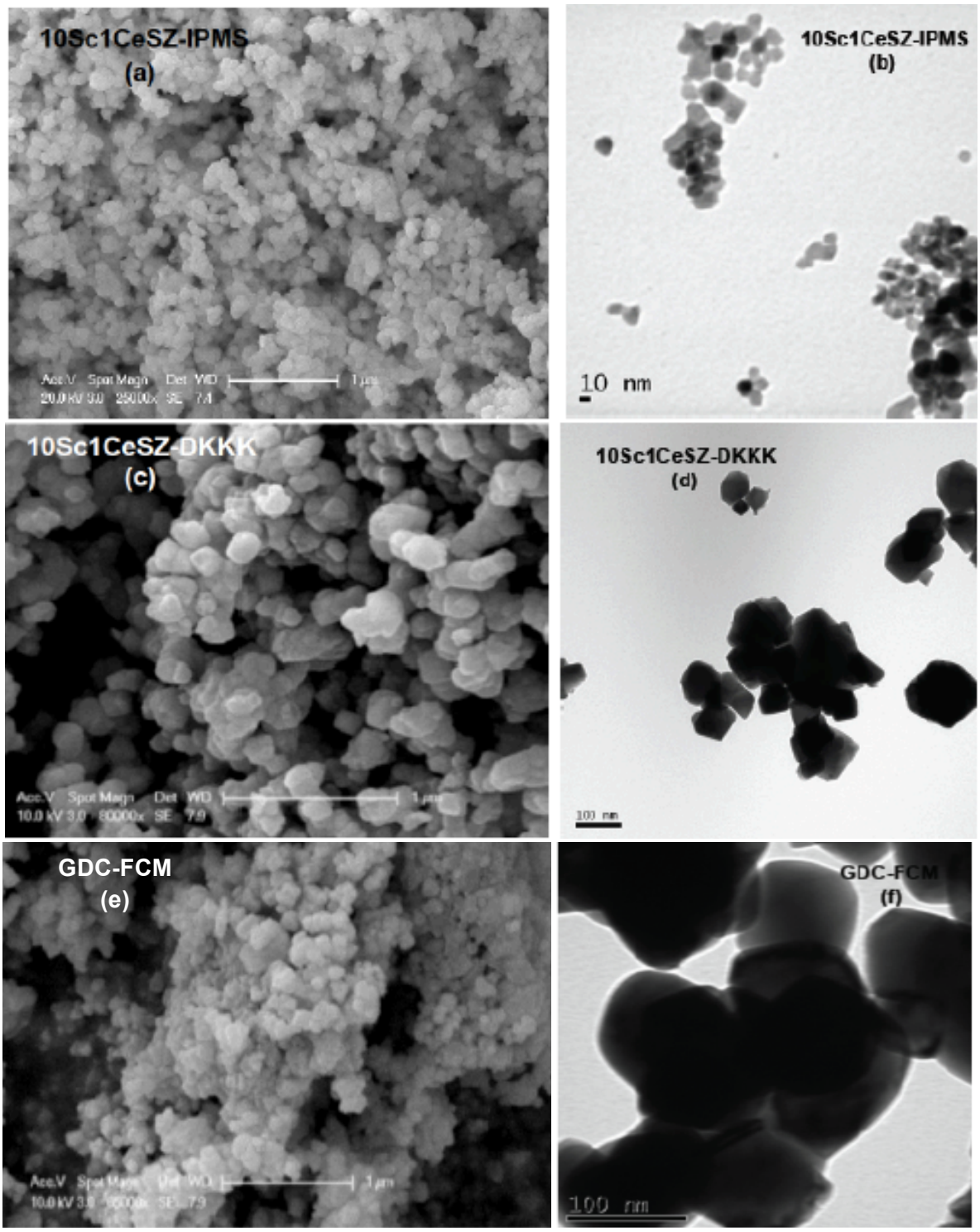

Figure 6-1: SEM/TEM micrographs of as received powders: (a) SEM-IPMS 10Sc1CeSZ, (b) TEM-IPMS 10Sc1CeSZ, (c) SEM-DKKK 10Sc1CeSZ, (d) TEM-DKKK 10Sc1CeSZ (e) SEM-FCM GDC, (f) TEM-FCM GDC

μm and the average crystallite size ≈ 0.1 μm as seen in the TEM image in (d) which are in agreement with the measured and specified d_{50} values. The SEM micrograph of the FCM GDC powder (e) shows loosely bound irregular shaped agglomerates with sizes greater ≈ 2.0 μm with the TEM image of this powder (f) showing crystallites with average sizes ≈ 0.1 μm. The properties of the starting powder determine how powder characteristics influence powder dispersion in polymer-based inks and ultimately affect the quality of the screen-printed films. Previous researchers investigated the influence of the properties of as-received Tosoh YSZ powders and ball milled Tosoh YSZ powders on screen-printed YSZ films and found the ball milled Tosoh YSZ powders produced better quality films yielding better performing cells [1]. The ball milled Tosoh YSZ powder was confirmed to have less agglomerates and a smaller particle size. Researchers report a narrower particle size distribution and greater uniformity for the ball milled powder when compared against the as-received powder [1]. The sintered film prepared with the ball milled Tosoh YSZ (B) powder was dense without pinholes while the sintered film prepared with the as-received Tosoh YSZ (A) powder contained many pores. The OCV of Cell-B was 1.04V while the OCV of the Cell-A was 0.82V. The idea that finer, well-distributed 10Sc1CeSZ powders could improve particle packing with the higher sintering activity resulting in higher shrinkages and densely sintered films was the motivation behind choosing the IPMS nanoscale 10Sc1CeSZ electrolyte powders instead of the micron scale DKKK powders. Thus, initial cells were prepared using IPMS 10Sc1CeSZ powders for the electrolyte in the Ni-10Sc1CeSZ cermet anode and for the 10Sc1CeSZ electrolyte layers.

6.2 SINTERING CHARACTERISTICS OF THE Ni-10Sc1CeSZ ANODE SUPPORTS

6.2.1 Ni-10Sc1CeSZ Porosity and Shrinkage Studies

Initial Ni-10Sc1CeSZ anode supports were prepared using the 70:30 wt% composition determined from the NiO-YSZ study. The cell preparation method for the Ni-YSZ supports is outlined in Chapter 3, Section 3.4. In the interest of achieving the research goals within the allotted time frame, the ceramic processing route established for the YSZ system was extended to the 10Sc1CeSZ system. Results of preparing Ni-10Sc1CeSZ supports using the Ni-YSZ fabrication method yielded substrates with poor strength during handling. Samples prepared and sintered to the firing conditions chosen for the Ni-YSZ pellets broke during screen-printing and showed powdery surfaces that would crumble during handling and printing. This was likely due to the insufficient amount of 10Sc1CeSZ, the ceramic component of the cermet-anode added to increase the mechanical strength of the anode support. It became obvious early on that the standardised processing method developed for the Ni-YSZ system was

not directly transferable to the Ni-10Sc1CeSZ system due to the difference in the properties between the as-received 8YSZ (TOSOH) and 10Sc1CeSZ (IPMS) powders.

Though the d_{50} for the IPMS 10Sc1CeSZ powder (11 nm) is smaller than the d_{50} for the 8YSZ (TOSOH) powder (0.50 μm, ±0.27), which is expected to have a higher sintering activity yielding a denser compact with higher mechanical strength, these powders were mixed with the coarser NiO-Novamet powder ($d_{50} \approx 9.20$ μm) which influenced powder mixing and densifications within the compact. The difference between the Ni-YSZ and Ni-10Sc1CeSZ fired compacts for the 70:30 wt% composition can be explained by a better mixing and a better powder distribution between the NiO-Novamet powder and the 8YSZ (Tosoh) powder. The finer particle characteristics of the 10Sc1CeSZ powder may have contributed to poorly dispersed agglomerates and a non-homogeneous distribution of the 10Sc1CeSZ particles. It could be assumed that the binding strength between the agglomerates was relatively strong though this has not been confirmed. These substrates also contained 10% pore former so in the case of the 10Sc1CeSZ system, this resulted in poor interlinkage between the 10Sc1CeSZ particles further weakening the compact. Thus, Ni-10Sc1CeSZ anode supports were fabricated without pore former and with a higher 10Sc1CeSZ content. The Ni-10Sc1CeSZ anode supports were prepared in a 60:40 (57:38 vol% Ni-10Sc1CeSZ) composition.

Table 6.1 lists the bulk density and porosity values for the 60:40 Ni-10Sc1CeSZ anode supports fired at different pre-sintering conditions. This is a repeat of the 70:30 Ni-YSZ porosity study outlined in Chapter 5, Section 5.2.1 with the measurements obtained in a similar fashion. It was best practice to obtain the porosity data for this sample batch, as the substrate composition was different. The results show an overall trend of a decrease in porosity with an increase in temperature for the 60:40 wt% Ni-10Sc1CeSZ samples. The apparent porosity only considers open porosity while real porosity takes into account both open and closed pores but for purposes of relative comparisons, the data remains useful. When compared with the 70:30 wt% Ni-YSZ porosity data outlined in Chapter 5, all of the samples in the 60:40 wt% Ni-10Sc1CeSZ batch were strong enough for porosity testing while the 70:30 wt% Ni-YSZ samples in the 1000°C batch were excluded due to poor mechanical strength during handling. This is due primarily to the removal of the pore former and the increase in 10Sc1CeSZ content for the 60:40 wt% Ni-10Sc1CeSZ samples. Within a given temperature group for the 60:40 wt% Ni10Sc1CeSZ samples, as was seen for the Ni-YSZ samples, there was practically no correlation between porosity and dwell time as seen in Figure 6-2, except for the 1100°C group where the trend of decreasing porosity with increased dwell time is observed, as the sintering process is largely controlled

Table 6.1. Density and Porosity of NiO-10Sc1CeSZ Supports					
Sintering Temperature (°C)	**Sintering Time (hours)**	**Bulk Volume (cm^3)**	**Bulk Density (g/cm^3)**	**Apparent Porosity (%)**	**Real Porosity (%)**
1000	2	0.545	3.562	41.62 ± 0.84	44.08
1050		0.139	3.791	39.56 ± 0.54	40.49
1100		0.361	3.969	36.81 ± 0.67	37.69
1150		0.230	4.189	31.00 ± 0.32	34.24
1200		0.661	4.442	29.18 ± 0.38	30.30
1000	4	0.289	3.760	40.10 ± 0.79	40.97
1050		0.270	3.944	37.66 ± 0.69	38.08
1100		0.172	3.959	35.97 ± 0.67	37.85
1150		0.318	4.024	33.59 ± 0.21	36.83
1200		0.679	4.335	30.65 ± 0.29	31.95
1000	6	0.232	3.568	42.33 ± 0.57	43.99
1050		0.345	3.883	38.08 ± 0.29	39.04
1100		0.167	4.178	34.94 ± 1.91	34.42
1150		0.203	4.364	28.77 ± 0.33	31.49
1200		0.676	4.366	29.45 ± 0.40	31.46
1000	8	0.179	3.731	40.61 ± 0.50	41.43
1050		0.206	3.845	38.53 ± 0.36	39.64
1100		0.289	3.963	34.46 ± 0.40	37.79
1150		0.703	4.190	32.05 ± 0.13	34.22
1200		0.663	4.404	29.18 ± 0.19	30.86

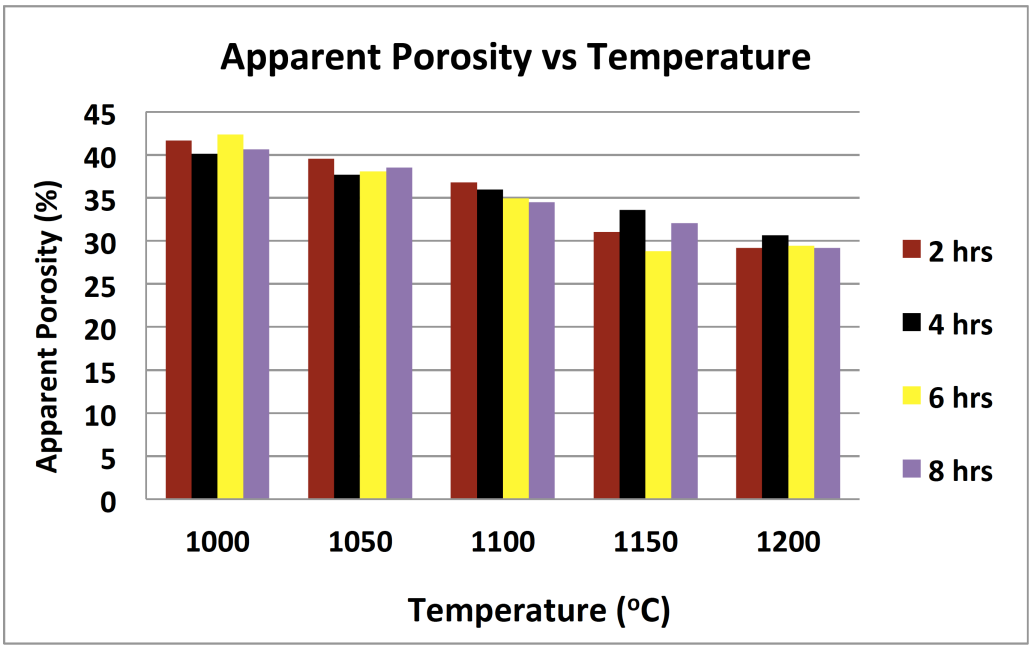

Figure 6-2: Apparent porosity versus sintering temperature for 60:40 wt% NiO-10Sc1CeSZ anode substrates as a function of time and temperature

by sintering temperature. The samples in the 1200°C temperature group saw the greatest shrinkages with minimal differences between the porosity values for the varying dwell times. Overall absolute porosity values for the 60:40 Ni-10Sc1CeSZ samples are smaller than those obtained for the Ni-YSZ samples. This is largely due to the absence of pore former.

6.3 STRUCTURAL CHARACTERISATION

6.3.1 Phase Identification (XRD)

X-ray powder diffraction scans for the NiO-10Sc1CeSZ samples fired at 1200°C-4hrs were obtained and are pictured in Figure 6-3. Although IPMS 10Sc1CeSZ powder was used for SOFC fabrication, structural characterisation was also carried out for DKKK powders. The phases present in these samples were identified by a search and match procedure. The scan revealed cubic phase for all of the powders, which is in agreement with the X-ray diffraction pattern shown in Chapter 5, Figure 5-6 for the NiO-YSZ samples fired at 1200°C-4hrs. Cubic phase ZrO_2 and cubic phase NiO were identified for

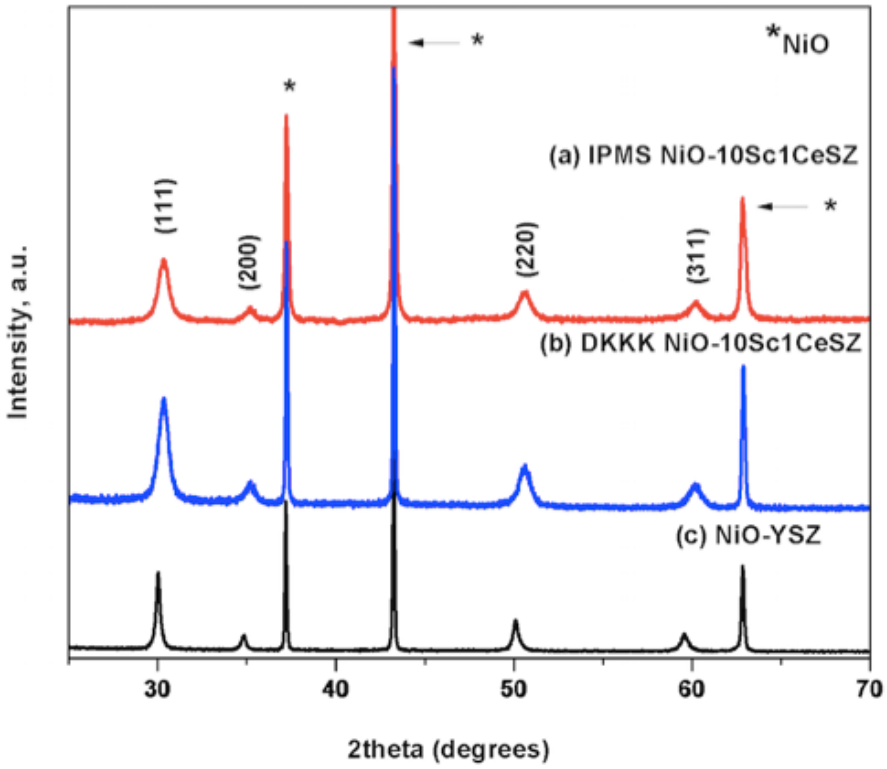

Figure 6-3: X-ray diffraction scans of (a) 60:40 NiO IPMS non-reduced NiO-10Sc1CeSZ, (b) DKKK non-reduced 60:40 NiO-10Sc1CeSZ and (c) 70:30 non-reduced NiO-YSZ

both 70:30 YSZ (1200°C-4hrs) and 60:40 10Sc1CeSZ (1200°C-4hrs) samples. The high intensity of the NiO phase peaks for all scans is due to the higher NiO content relative to YSZ and 10Sc1CeSZ while the narrow peaks indicate larger crystallites and the wider peaks indicate smaller crystallites [2]. The NiO-YSZ pattern was included to serve as a reference illustrating the ceramic processing method for the YSZ substrates was directly transferable to the 10Sc1CeSZ samples as it related to preparing phase pure anode substrates. No new peaks outside of the expected reflections for the 10Sc1CeSZ samples were seen.

6.4 ELEMENTAL ANALYSIS

6.4.1 X-ray Fluorescence (XRF)

Figure 6-4 is a plot providing the chemical analysis of the NiO-10Sc1CeSZ substrates and the powders used to prepare the NiO-10Sc1CeSZ anode functional layer (AFL) films obtained via XRF. The precise analysis of oxide content in these samples was difficult to measure due to the limitations of the instrument so the data provided in wt% per element serves as a comparison of the relative amount of each element. The difference in the elemental composition of the bulk is related to the difference in the 60:40 wt% NiO-10Sc1CeSZ composition for the bulk compared to the 50:50 wt% NiO-10Sc1CeSZ composition for the AFL films. There were impurities present in the powders but the sum of all

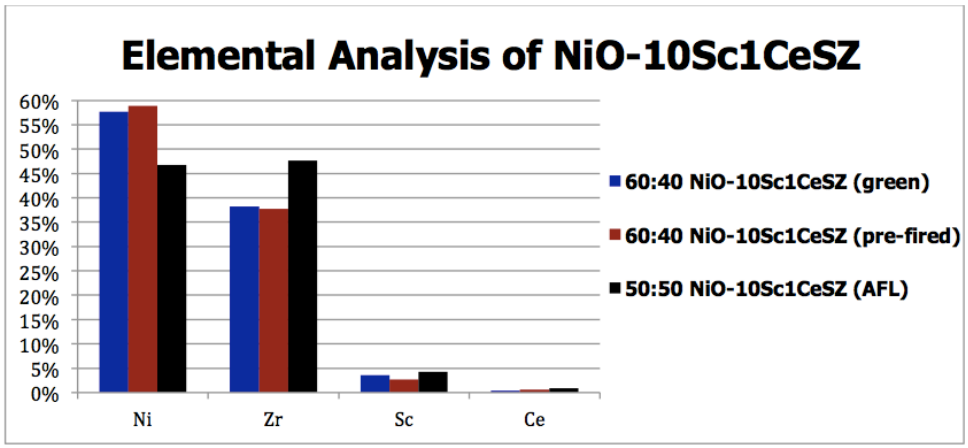

Figure 6-4: Elemental composition of NiO-10Sc1CeSZ anode powders

impurities were ≤1%. Identifying the relative amount of each impurity oxide by relating the impurity content to the height of the bars was impossible as the taller bars that correlated to higher NiO, ZrO_2 and Sc contents dominated the graph making the smaller bars, which correlated to the impurity contents invisible. Thus, to maintain the clarity of the column graph, the impurity contents were excluded. The data shows there are no new impurities introduced into the starting powder during mixing and no impurities introduced into the support pellets during the pre-firing stage.

6.5 CHARACTERISTICS OF THE NiO-10Sc1CeSZ HALF CELL

6.5.1 10Sc1CeSZ Ink Characteristics

10Sc1CeSZ electrolyte films were screen-printed onto Ni-10Sc1CeSZ substrates covered with 50:50 wt% Ni-10Sc1CeSZ AFL layers and fired at 1400^{o}C-4hrs as was the standardised fabrication procedure outlined in Chapter 3, Section 3.4.2.3 All anode substrates were reproducible with minimal changes in thickness or weight after pre-firing. The loading of the 10Sc1CeSZ electrolyte ink was 40 vol% solids, the same used for the YSZ inks, though the rheology of the10Sc1CeSZ ink was markedly different from the YSZ ink. The ink vehicle remained unchanged for all inks prepared in this study so the difference in the flow properties of the 10Sc1CeSZ ink compared to the YSZ ink was due to be related to the properties of the 10Sc1CeSZ powder. Powder particle size and powder loading greatly influence ink rheology and ultimately the microstructure of the fired film. The 10Sc1CeSZ ink prepared with as-received nanoscale IPMS 10Sc1CeSZ powder was "tacky" which didn't make for the best printing ink as the ink adopted a more solid like behaviour. Despite this visible viscosity difference, the wet film coverage over the anode support surface was still uniform and complete. During ink preparation, oftentimes ink loading has to be adjusted for the use of finer or coarse powder to maintain a printable paste [3]. A higher ink vehicle to solids ratio is usually required for finer powders with higher surface areas to ensure there is enough vehicle to coat the particle surfaces and homogenously mix the powder throughout the organic medium. A lower loading 10Sc1CeSZ ink may have yielded flow properties similar to the YSZ ink but a printable ink with maximum solids loading can help produce a dense film with less pores remaining after organic burnout which is desired. Higher solids loading inks have also been found to strengthen the particle network and improve density [4]. Thus, the 40 vol% solids 10Sc1CeSZ ink was used to prepare the first batch of cells.

6.5.2 Ni-10Sc1CeSZ Cell Microstructure

The 10Sc1CeSZ cells exhibited curvature towards the 10Sc1CeSZ electrolyte layer, the same as was observed for the YSZ cells, so they, too, were weighed down using Al_2O_3 plates which proved successful for flattening the cells. Micrographs of cross-sectional cuts of separate 10Sc1CeSZ cells prepared using the standardised fabrication method developed for the YSZ system are shown in Figure 6-5. The image in Figure 6-5 (a) obtained via SEM is of an anode supported reduced cell and the image in Figure 6-5 (b) obtained via optical microscopy is of another anode supported non-reduced cell. The cell in figure 6-5 (b) does not have an LSCF layer as this cell was not prepared for testing but strictly to examine the sintering of the 10Sc1CeSZ layer. In Figure 6-5 (a) the crack at the interface of the

10ScCeSZ electrolyte and GDC blocking layer can be easily seen. Large voids in the 35 μm thick 10ScCeSZ electrolyte layer are also observed which explains the low OCV measurement and poor performance to be further discussed in Chapter 7. The electrolyte layer thickness is higher than the 10-12 μm thickness typically seen for 3 printed layers and this is due to two additional print layers required because of ink clogging in a worn screen. New screens were ordered and the screen-printing resumed following the three-print layer procedure. There appears to be satisfactory adhesion between the 10Sc1CeSZ electrolyte and Ni-10Sc1CeSZ anode functional layer with good NiO-NiO particle contact and good Ni and 10Sc1CeSZ particle dispersion throughout the anode support microstructure. The composite LSCF-GDC and pure LSCF cathode also have good adhesion though poorly dispersed particles and large agglomerates are observed in the pure LSCF layer. Figure 6-7 (b) displays similar findings with large isolated pores in the 10ScCeSZ layer and complete GDC layer delamination from the 10ScCeSZ film.

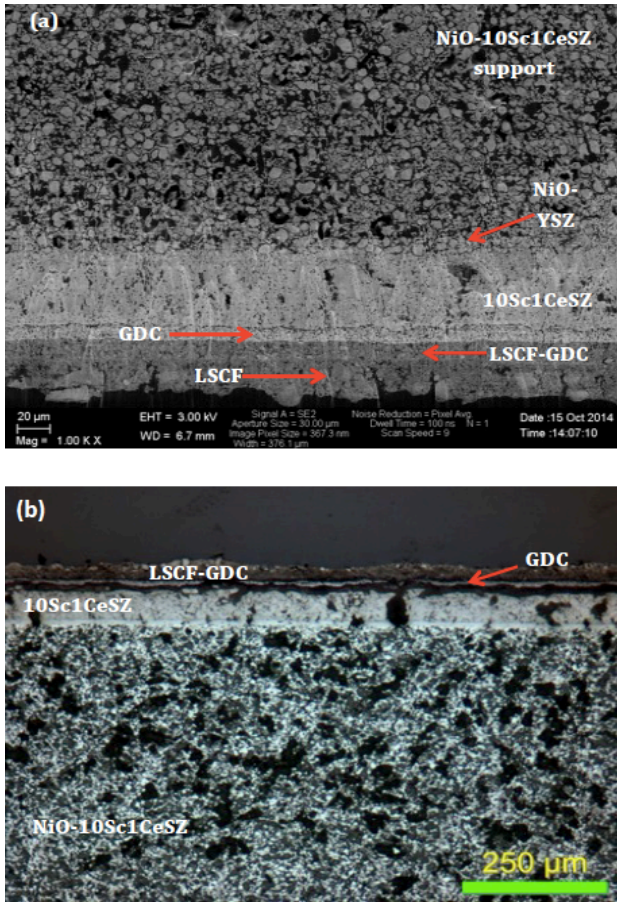

Figure 6-5: (a) Cross-sectional SEM image of a reduced Ni-10Sc1CeSZ cell (b) cross-sectional optical image of a non-reduced NiO-10Sc1CeSZ cell

The GDC delamination issue is largely related to shrinkage mismatches with the 10Sc1CeSZ layer and Ni-10Sc1CeSZ substrate. One way to address this problem is to relax the tensile stresses that cause such defects by matching the sintering rates of the substrate and bi-layers. Bordia et al. [5] provides another approach which considers a material's shear properties when examining the sintering kinetics of constrained films suggesting that a high rate of shear can reduce the magnitude of the tensile stress as shear deformation effects relax the incompatible stresses in the film allowing densification to proceed preventing any defects from developing. And while the shear properties of the materials used in this work have not been investigated, this theory has been introduced as a possible explanation for the observed retarded densification and delamination of the GDC film. The addition of the GDC blocking layer is to prevent interactions between the 10Sc1CeSZ electrolyte and LSCF cathode, though reactions between GDC and YSZ creating insulating phases at the electrolyte/blocking layer interface have been previously reported [6]–[9]. The formation of these resistive phases have deleterious effects on conductivity and cell stability which adversely influence SOFC performance [8], [9]. Zhou [8] reported the formation of solid solutions at 1000^{o}C dominated by YSZ diffusion into GDC for YSZ substrate samples spin coated with GDC films. These samples exhibited lower conductivity as well as dimensional changes due to TEC decreases for GDC due to the presence of YSZ. Tsoga reported inter-diffusion at the GDC-YSZ interface with Y and Zr ion penetration depths into GDC between 1-3 μm and Ce and Gd ion penetration depth into YSZ between 3-5 μm at 1200^{o}C [6]. Knibbe [9] reported diffusion between GDC and YSZ with the presence of a $SrZrO_3$ insulating layer at the interface between GDC and YSZ. Though the GDC prevents extensive Sr diffusion, the adjoining GDC-YSZ grains provide pathways for Sr diffusion via the GDC grain boundaries creating these insulating phases. BSE SEM images show a break in the adhesion of the GDC layer to the YSZ layer similar to what is observed for the 10Sc1CeSZ cell prepared in this work pictured in Figure 6-5 (a).

Pictured in Figure 6-6 (a) is a portion of the Ni-10Sc1CeSZ cell shown in Figure 6-5 presented at a higher magnification so a quantitative analysis of the 10Sc1CeSZ electrolyte layer porosity could be obtained. The accompanying histogram in Figure 6-6 (b) displays the pore size distribution. The electrolyte porosity was determined using image editing software and the calculated 10Sc1CeSZ porosity was 14.83%, 4 times higher than the calculated porosity of 3.81% for YSZ mentioned in Chapter 5, Section 5.7.4. The inset in Figure 6-6 (b) displays the histogram of the pore size distribution for the YSZ electrolyte layer. There was a larger pore count distribution for the 10Sc1CeSZ layer with the average pore size ≈ 0.1 μm compared to a lower pore count and a narrower pore size distribution for the YSZ layer with average pore sizes falling between 0.12 μm and 0.18 μm. For relative comparison, the sample

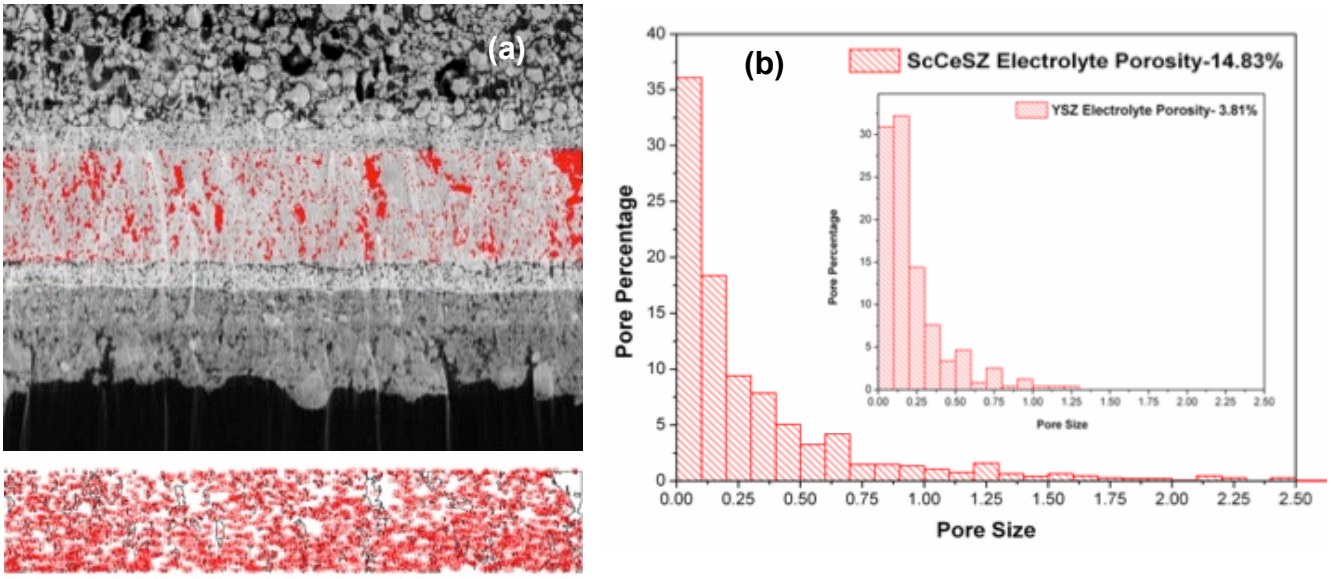

Figure 6-6: (a) excerpt from Figure 6-5 (a), (b) 10Sc1CeSZ pore size distribution

in Figure 6-7 is a commercial cell supplied by Ningbo Institute of Material Technology (China) showing a 0.1 mm thick dense 10Sc1CeSZ electrolyte with distinguishable component microstructures and good adhesion between the electrolyte and anode component of the cell.

The poor quality of the screen-printed 10Sc1CeSZ electrolyte layers compared against the screen-printed YSZ electrolyte layers and both commercial YSZ and 10Sc1CeSZ cells demonstrates the need for additional work to improve the sintering activity of the 10Sc1CeSZ films. These initial findings formed the basis of a series of experiments carried out to attempt to solve the GDC adhesion and 10Sc1CeSZ electrolyte densification issue.

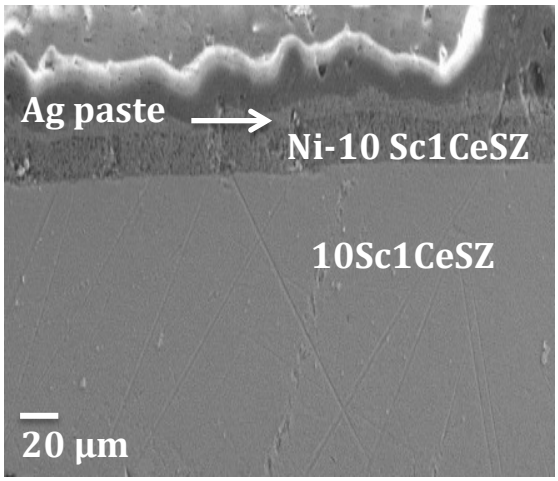

Figure 6-7: Cross-sectional SEM of a commercial 10Sc1CeSZ electrolyte supported cell

6.6 GDC ADHESION AND DESIGN OF EXPERIMENTS APPROACH

Several sample batches were prepared to address the GDC adhesion issue with the intention of simultaneously improving the 10Sc1CeSZ electrolyte layer densification. Previous researchers have achieved dense GDC interlayers deposited onto YSZ films after co-firing at 1400 – 1500^{o}C [10]. The fabrication approach for Cell GA, listed in the table in Figure 6-8, was prepared incorporating a composite 10Sc1CeSZ-GDC compatibility layer between the 10Sc1CeSZ electrolyte and GDC barrier layer with all printed layers fired during a single step at 1400^{o}C-4hrs. This was done to better match the shrinkages of GDC and 10Sc1CeSZ during co-firing and to minimise inter-diffusion between these layers. If the inter-diffusion could be minimised then any deleterious effects on sintering and electrical conductivity could also be avoided. The previous use of a three layer composite electrolyte cell YSZ/YSZ-GDC/GDC has been reported, though the focus of the investigation centred around YSZ and GDC transport properties and system conductivity at various temperatures and oxygen partial pressures [11]. The focus was less on the sintering characteristics and structural stability of the cell and more on how this system would behave in a testing environment. Despite these findings, a 10Sc1CeSZ cell following a similar configuration was prepared and the relationship between the manufacturing method and cell microstructure was examined.

As shown in Figure 6-8 (a), The LSCF-GDC and LSCF composite cathodes show agglomeration and poor powder distribution but good adhesion with one another and good contact with the GDC blocking layer. The 10Sc1CeSZ-GDC composite layer adheres well to both the GDC barrier layer and the 10Sc1CeSZ electrolyte layer though there is a crack that extends the length of the 10Sc1CeSZ layer as seen in the higher magnification SEM image pictured in Figure 6-9. This crack is likely due to the in-plane stress on the 10Sc1CeSZ electrolyte layer generated by the constraint of the semi-rigid, pre-fired anode support. Because there exists some common shrinkage between the substrate and the bi-layers, this results in only partial constraint with some compression on the bi-layer films by the support. This partial constraint however, still produces a tensile stress that limits the natural tendency of the 10Sc1CeSZ film to shrink in-plane relegating a large portion of the shrinkage in the direction perpendicular to the plane of the layer which reduces the driving force for sintering and can create cracks in the constrained film [12]. For the case of a fully constrained film that adheres to a non-shrinking substrate and does not crack, the tensile stress balances the sintering stress for in-plane shrinkage [13]. These incompatibility stresses for Cell GA were most likely magnified by the addition of the 10Sc1CeSZ-GDC composite layer. The 10Sc1CeSZ layer appears denser than both the GDC and the 10Sc1CeSZ-GDC layer with the most pores observed in the GDC layer and closed, isolated pores in the

10Sc1CeSZ layer. The X-ray map in Figure 6-8 (b) shows the elemental distribution throughout the cell making layer identification easier.

Cell GA (SA71B)	Single Step Multi-Layer Co-Fire – 1400°C-4hrs
Barrier Layer	GDC
Compatibility Layer	10Sc1CeSZ-GDC
Electrolyte	10Sc1CeSZ (as –received)
AFL	Ni – 10Sc1CeSZ

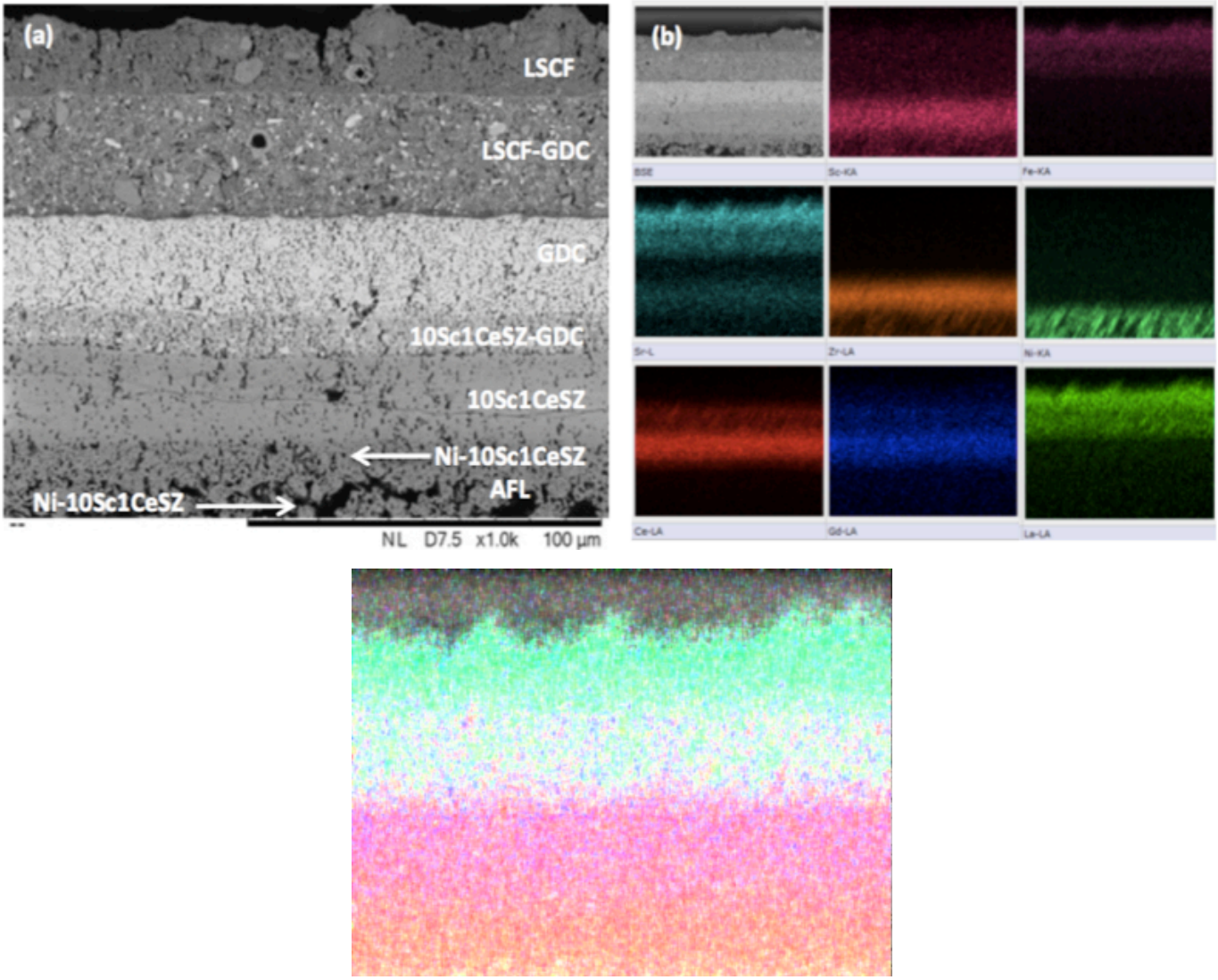

Figure 6-8: (a) Cross-sectional SEM of Cell GA obtained in BSE mode and (b) elemental X-ray mapping of Cell GA (c) X-ray combination map of Cell GA

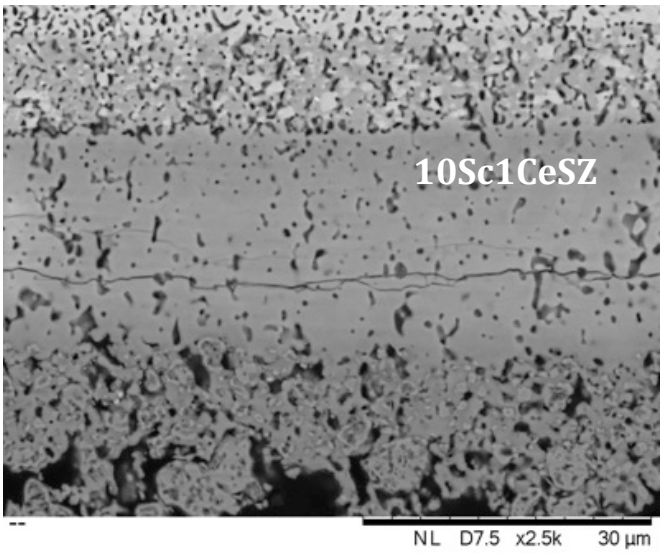

Figure 6-9: Portion of cell GA picture in Figure 6-8 (a) showing 10Sc1CeSZ electrolyte layer at a higher magnification

The combination X-ray map pictured in Figure 6-8 (c) blurs the demarcation of the 10Sc1CeSZ/10Sc1CeSZ-GDC and 10Sc1CeSZ-GDC/GDC interfaces due to the 10Sc1CeSZ-GDC layer showing pink (Sc), blue (Gd) and orange (Zr) colours. It is difficult to determine whether there is any inter-diffusion between the 10Sc1CeSZ electrolyte layer and GDC blocking layer possibly passing through the 10Sc1CeSZ-GDC composite layer as the composite layer contains both 10Sc1CeSZ and GDC. There is no Sr diffusion observed between the composite LSCF-GDC cathode and the GDC barrier layer however. While these preliminary results show promise for improving GDC adhesion, the density of the GDC and 10Sc1CeSZ films remains poor. To further improve upon the sintering behavior of the GDC and 10Sc1CeSZ layers, another cell without the composite layer was prepared as minimal information regarding the effectiveness of the 10Sc1CeSZ-GDC was obtained.

As seen in the table pictured in Figure 6-10, cell GB contained a screen-printed 10Sc1CeSZ-GDC bi-layer with the 10Sc1CeSZ and GDC layers fired under the same sintering conditions but fired separately; the Ni-10Sc1CeSZ/10Sc1CeSZ layer was co-fired at 1400^{o}C-4hrs followed by the sintering of the GDC layer at 1400^{o}C-4hrs. The separate co-firing of the GDC layer improved GDC adhesion to 10Sc1CeSZ though there is a crack in the GDC layer near to the 10Sc1CeSZ-GDC interface. This crack appears similarly to the crack in the 10Sc1CeSZ layer in cell GA. Because the anode-electrolyte layer was co-sintered at an earlier stage, this created an even greater shrinkage mismatch between the anode-electrolyte and GDC barrier layer during the two-step firing. This separate firing resulted in a non-

shrinking substrate that left the GDC film fully constrained. This mismatch, imposed stresses on the layers that were compounded by pressure applied to the sample to suppress the natural curvature during firing to maintain flatness. The 12 μm 10Sc1CeSZ layer appears reasonably dense though no improvement in the densification of the GDC layer is observed. The GDC layer is 25 μm thick with interconnected porosity and large isolated pores. A combination X-ray mapping of this cell is shown in Figure 6-10 (b) with the colour coded elemental distribution pictured separately. Elemental distribution of the pure and composite cathode was not provided as the focus was on the densification of the electrolyte and blocking layer.

Cell GB (SA71L)	**Separate GDC Co-Fire – 1400°C-4hrs Anode/Electrolyte Co-fire – 1400°C-4hrs**	
	Barrier Layer	GDC
	Electrolyte	10Sc1CeSZ (as received)
	AFL	Ni – 10Sc1CeSZ

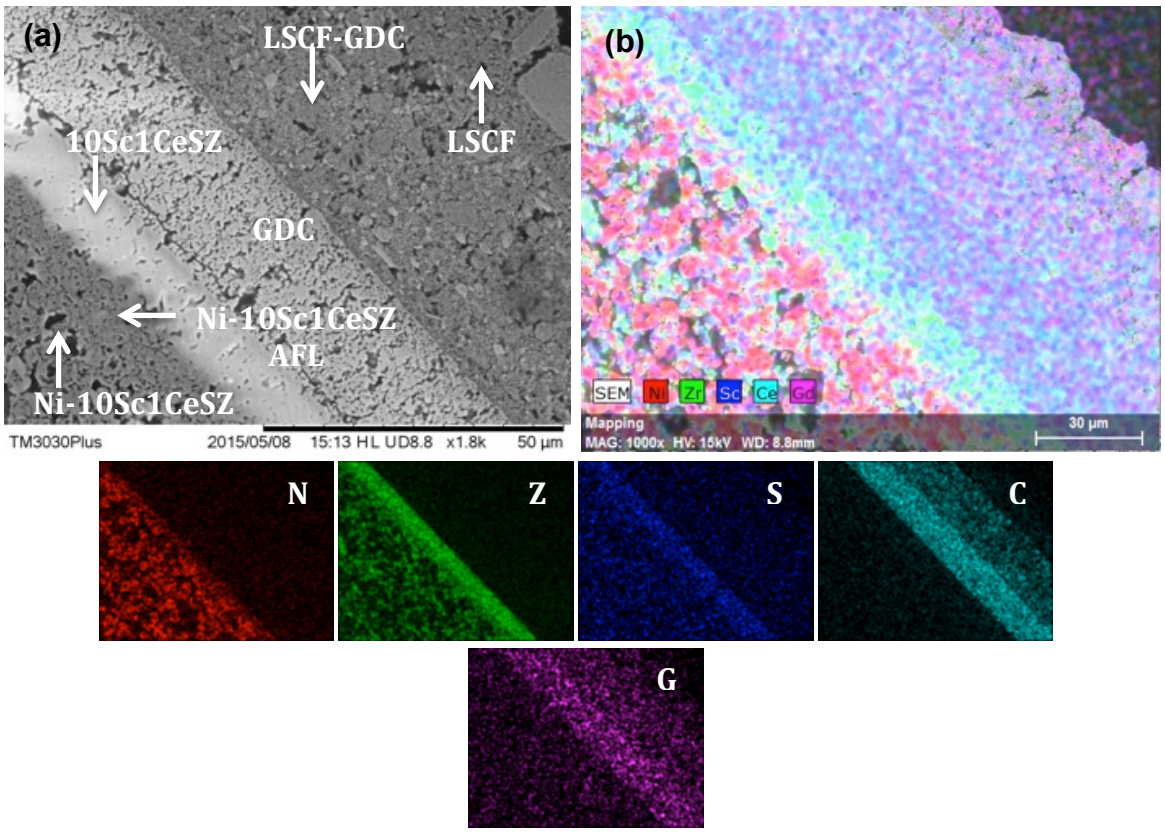

Figure 6-10: (a) Cross-sectional SEM of Cell GB obtained in BSE mode and (b) combination X-ray map of cell GB with colour coded elemental distribution

The separate co-firing step was effective for improving the sintering of the 10Sc1CeSZ electrolyte film but was ineffective for promoting GDC densification with the formation of a transverse crack defect observed at the GDC-10Sc1CeSZ interface. A reasonable explanation for the enhanced densification of the 10Sc1CeSZ layer is the 10Sc1CeSZ electrolyte component dominated the sintering activity of the half-cell during the anode-electrolyte firing stage due to the higher sintering rate of the nanoscale 10Sc1CeSZ powders, thus yielding greater shrinkage with less porosity. It is also possible that the 10Sc1CeSZ component of the Ni-10Sc1CeSZ anode dominated the sintering rate at elevated temperatures as was observed by Mucke et al. [14] above 1200^{o}C for Ni-YSZ/YSZ half cells, reducing the sintering mismatch between the anode and electrolyte resulting in a more dense electrolyte film. And because the anode-electrolyte co-sintering occurred prior to the sintering of the GDC layer, GDC densification was inhibited by the constraint of the substrate where the in-plane sintering stresses needed to shrink the film and produce a dense layer were absent. The delamination of GDC from the 10Sc1CeSZ film was a consequence of this sintering constraint. Yamaguchi found that substrates that undergo lateral shrinkage during co-firing have been found to produce films >98% theoretical densities compared to rigid substrates that do not shrink where films with only ~ 55% theoretical density were achieved [15]. The compressive force of a shrinking substrate assists in facilitating dense films with the shrinkage characteristics of the substrate heavily influencing the microstructural characteristics of the films deposited onto them. So while a denser 10Sc1CeSZ electrolyte layer was achieved the densification of the GDC barrier layer remained unchanged. Thus the last sample in the GDC adhesion sample series, Cell GC, was prepared to try and achieve a dense GDC layer without compromising the density of the 10Sc1CeSZ layer already obtained.

At this stage of the experimental process, the manufacturers of the IPMS 10Sc1CeSZ powders used in this study were consulted regarding suggested processing routes for the best use of their powder. Because the IPMS 10Sc1CeSZ powders are nanoscale and heavily agglomerated, it was suggested to ball mill the as-received powder overnight to break up the agglomerates before use. So Cell GC was prepared using as-received ball milled 10Sc1CeSZ powders that were used to make 40% vol solids loading ink, the standard ink loading for the electrolyte inks.

For Cell GC, considerable improvements in the density of the GDC film are evident as shown in Figure 6-11 (a), which is likely due to better shrinkage matching with the anode-electrolyte half-cell, however, there appears to be non-homogeneous distribution of the ball milled electrolyte powders based on the examination of the fired 10Sc1CeSZ film; Figure 6-11 (b) shows the X-ray combination map and

Cell GC (SA77)	Single Step Layer Co-Fire – 1400°C-4hrs	
	Barrier Layer	GDC
	Electrolyte	10Sc1CeSZ (ball milled)
	AFL	Ni – 10Sc1CeSZ

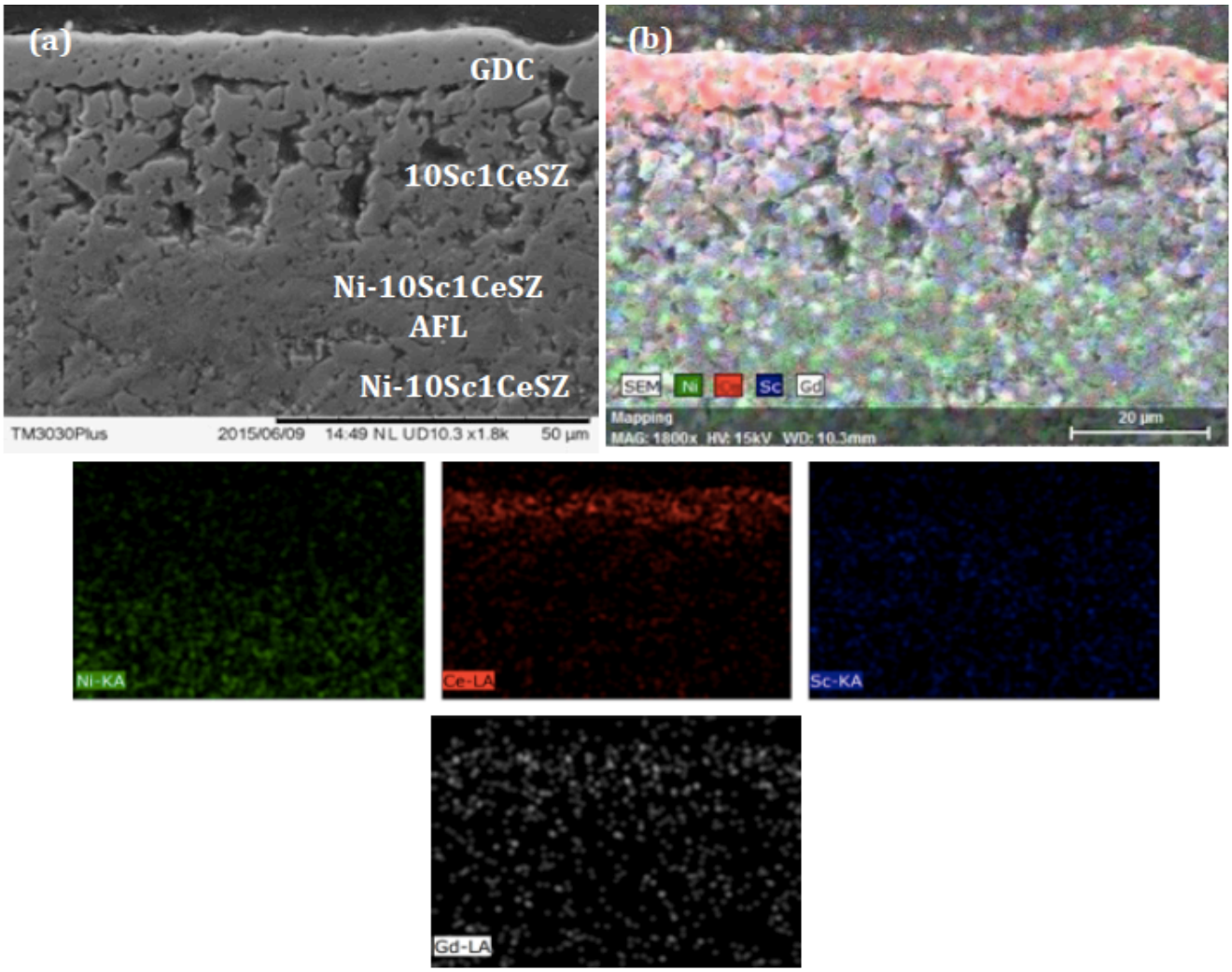

Figure 6-11: (a) Cross-sectional SEM of Cell GC obtained in SE mode and (b) elemental distribution of Cell GC determined via X-ray mapping

elemental distribution throughout the cell. It seems as though the ball milling was not effective in breaking up the agglomerates in the IPMS 10Sc1CeSZ as-received powders and this could simply be because the powders were not ball milled long enough. This 10Sc1CeSZ electrolyte layer looks worse than the sintered non ball milled 10Sc1CeSZ layers of cells GA and GB with cell GB exhibiting the most

enhanced densification of all 10Sc1CeSZ layers in this sample set. It is not completely understood why the ball milled 10Sc1CeSZ layer in cell GC looks worse than the two non-ball milled layers in cells GA and GB given the idea that fine, non agglomerated powders have better particle packing due to good uniformity unless, as stated previously, the overnight milling time was insufficient. It has been reported by Tekeli et al. [16] and Wang et al. [12] that cubic ZrO_2 exhibits enhanced grain growth during high-temperature sintering and this can inhibit densification as rapid grain growth forces grain boundaries to move faster than the pores which separates the pores from the grain boundary and can leave them isolated inside the grain. And because sintering involves pore removal via grain boundary diffusion, grain growth must be controlled and excessive grain boundary mobility suppressed so stability during sintering and full densification can be achieved. This could explain why the densification of the 10Sc1CeSZ film remained unchanged.

For each of these samples, the different manufacturing approaches yielded different outcomes but none were to the satisfaction of the project targets. The results of the GDC adhesion study prompted the preparation of another sample batch focused solely on 10Sc1CeSZ layer densification. Once a manufacturing route for obtaining dense 10Sc1CeSZ films is standardised, then a thorough investigation on the use of a GDC barrier layer can be explored, tailoring the properties of the GDC powder and screen-printed film to match the sintering characteristics of the anode-electrolyte half-cell. The samples presented in the ***10Sc1CeSZ Layer Densification I. – Manufacturing Modifications*** section below focus on cells prepared solely for the purpose of addressing the complications associated with 10Sc1CeSZ layer densification.

6.7 10Sc1CeSZ LAYER DENSIFICATION I. – MANUFACTURING MODIFICATIONS

The cells in this experimental group were manufactured to try and solve the 10Sc1CeSZ layer densification issue. Based on the improved sintering of the GDC layer in cell GC, GDC barrier layers were still deposited for Cells SA and SC to examine how their sintering activity and microstructure would be influenced by changes to the manufacturing route of the10Sc1CeSZ electrolyte, though the focus was strictly on densifying the 10Sc1CeSZ film. Changes to the starting powder properties, which were assumed to greatly influence ink rheology, ink loading, co-sintering temperature and the number of printed layers were all modified during the fabrication of this sample set.

For cell SA, ball milled 10Sc1CeSZ powders were used to prepare a higher loading 10Sc1CeSZ ink of 45 vol% solids compared to the standardised 40 vol% solids loading 10Sc1CeSZ inks used up to this stage in the research. The rationale for using a higher solids loading ink was to increase particle

packing. A higher solids loading also means less organics resulting in fewer pores after binder burnout during sintering. Cell SB electrolyte layers were screen-printed using the same 45 vol% solids loading ink but with an increase in the number of printed layers and an increase in the half-cell co-firing temperature from 1400 to 1450°C. Cell SC was fabricated using calcined DKKK powders, based on the unsatisfactory results of cells SA and SB, with the co-firing temperature unchanged at 1400°C.

The DKKK 10Sc1CeSZ powder with a higher as-received particle size (d_{50} = 90 nm) than the IPMS powder (d_{50} = 12 nm) was calcined at low temperatures (to not change the phase or start the sintering process) to slightly reduce the surface area and suppress the closed porosity [17] then ball milled to break up any agglomerates and improve powder mixing. As mentioned previously, the DKKK powder was not initially used due to the higher sintering activity of the finer IPMS powder. But after multiple unsuccessful trials to densify the 10Sc1CeSZ film using the IPMS powder, the use of calcined DKKK powders was driven by the idea to achieve a d_{50} similar to TOSOH 8YSZ powders (d_{50} = 0.5 μm) since the sintering of the screen-printed TOSOH 8YSZ layer achieved satisfactory density as reported in Chapter 5, Section 5.7.4. And since the agglomeration of the higher surface area IPMS powders created manufacturing difficulties, sacrificing shrinkage, sintering activity and packing density using the coarser DKKK powder seemed worthwhile if a reasonably dense, uniform film could be obtained. Thus, the use of the DKKK powder was explored.

Figure 6-12 shows the ceramic processing and manufacturing route for Cells SA, SB and SC. For cell SB, a five-print layer sample was prepared. The case for the use of thicker layers is similar to the case for the use of a higher solids loading ink without the limitations that are placed on ink formulations, which restrict the maximum solids loading achievable to that which yields a printable paste. Researchers obtained OCVs higher than 1.0V for screen-printed YSZ films when the number of prints were at least five layers or more [18]. The table in Figure 6-12 shows the surface area and calculated d_{50} values for the calcined DKKK powder. Based on the surface area and calculated d_{50} values, the 1050°C-3hrs powder was used to prepare the 10Sc1CeSZ electrolyte ink for Cell SC as this powder exhibited the lowest surface area after the various calcination treatments.

The microstructures of cells SA, SB and SC are shown in Figure 6-13. The 10Sc1CeSZ microstructure of cell SA seen in Figure 6-13 (a) and 6-13 (b) appears similar to the 10Sc1CeSZ microstructure of cell GC in Figure 6-11 (a) where the ball milled powders used in the printing of the 10Sc1CeSZ layers are still clustered and non-homogenously distributed after firing. The 10Sc1CeSZ electrolyte layer in cell SA was printed with a higher solids loading ink, which shows a slightly greater

particle connection when compared with cell GC, though overall, the film remained porous. Neither the ball milling nor the higher ink loading was effective in promoting 10Sc1CeSZ layer densification which can only be explained by the strong attractive Van der Waals forces between the particles forming tightly bound powder agglomerates which could not be broken even after milling, resulting in poor powder dispersion throughout the ink vehicle. This poor powder dispersion coupled with inadequate vehicle coverage on the particle surface caused by weak or repulsive interactions between the powder and vehicle left behind regions of localised pores in the microstructure after organic burnout where there was a void of material. The GDC layer sintering remains unchanged and somewhat dense, similar to what was observed for Cell GC.

Cell SA	Ball Milled, Higher Solids Loading 10Sc1CeSZ Bilayer Co-Fire 1400°C-4hrs
Barrier Layer	GDC
Electrolyte	10Sc1CeSZ (45 vol%)-IPMS
AFL	Ni – 10Sc1CeSZ

(a)

Cell SB	Ball Milled, Higher Solids Loading 10Sc1CeSZ Bilayer Co-Fire 1450°C-4hrs
Barrier Layer	GDC
Electrolyte	10Sc1CeSZ (45 vol%) - IPMS
AFL	Ni – 10Sc1CeSZ

(b)

Cell SC	Calcined ScSZ (1050°C-3hrs), Reg Loading Bilayer Co-Fire 1400°C-4hrs
Barrier Layer	GDC
Electrolyte	10Sc1CeSZ (40 vol%) - DKKK
AFL	Ni – 10Sc1CeSZ

(c)

ScSZ (DKKK)	BET (meas) m^2/g	d_{50} (meas) µm
as-received	9.829	.1305
calcined 750°C/3h	9.581	.1061
calcined 850°C/3h	2.903	.3503
calcined 950°C/3h	8.370	.1215
calcined 1050°C/3h	2.870	.3543

(d)

Figure 6-12: Ceramic processing route for cells (a) SA (b) SB (c) SC and (d) surface area and d_{50} values for DKKK powder calcined at various temperatures

Cell SB seen in Figure 6-13 (c) is similar to Cell GC and Cell SA as it relates to non-uniformity in the layer though the microstructure is more close-packed with fewer voids when compared with GC, SA and SC indicative of greater shrinkage due to the higher sintering temperature. A small increase in layer thickness due to the additional two wet prints is also observed. The microstructure of Cell SC seen in Figure 6-13 (d), prepared with the DKKK calcined 10Sc1CeSZ powder at the standardised 40 vol% solids is noticeably similar to that observed for the first fabricated 10Sc1CeSZ cell presented in Section 6.5.2. Complete GDC delamination and large voids in the 10Sc1CeSZ layer reveal the effect of bi-layer substrate shrinkage mismatches and poor powder-ink mixing. The calcined powder was assumed to increase the particle packing efficiency and improve the green density due to better particle distribution

brought about by the calcination and milling steps, aiding in the creation of a more uniform and dense structure [19]. It is possible that the calcination and milling steps produced rougher surfaced particles that were not so easily rearranged for a higher packing density. The poor powder dispersion of the 10Sc1CeSZ ink may not only be related to the intrinsic properties of both IPMS and DKKK powders but also to the components of the vehicle which require additional dispersing agents to assist in the homogeneous mixing of the powder in the organic suspension. Due to the less than satisfactory results obtained with this sample set, the final design of experiments will be presented in the next section, ***10Sc1CeSZ Layer Densification II. – The Use of Dispersants and Al_2O_3,*** where the fabrication of a dense 10Sc1CeSZ layer will be attempted through the use of dispersants and sintering aids.

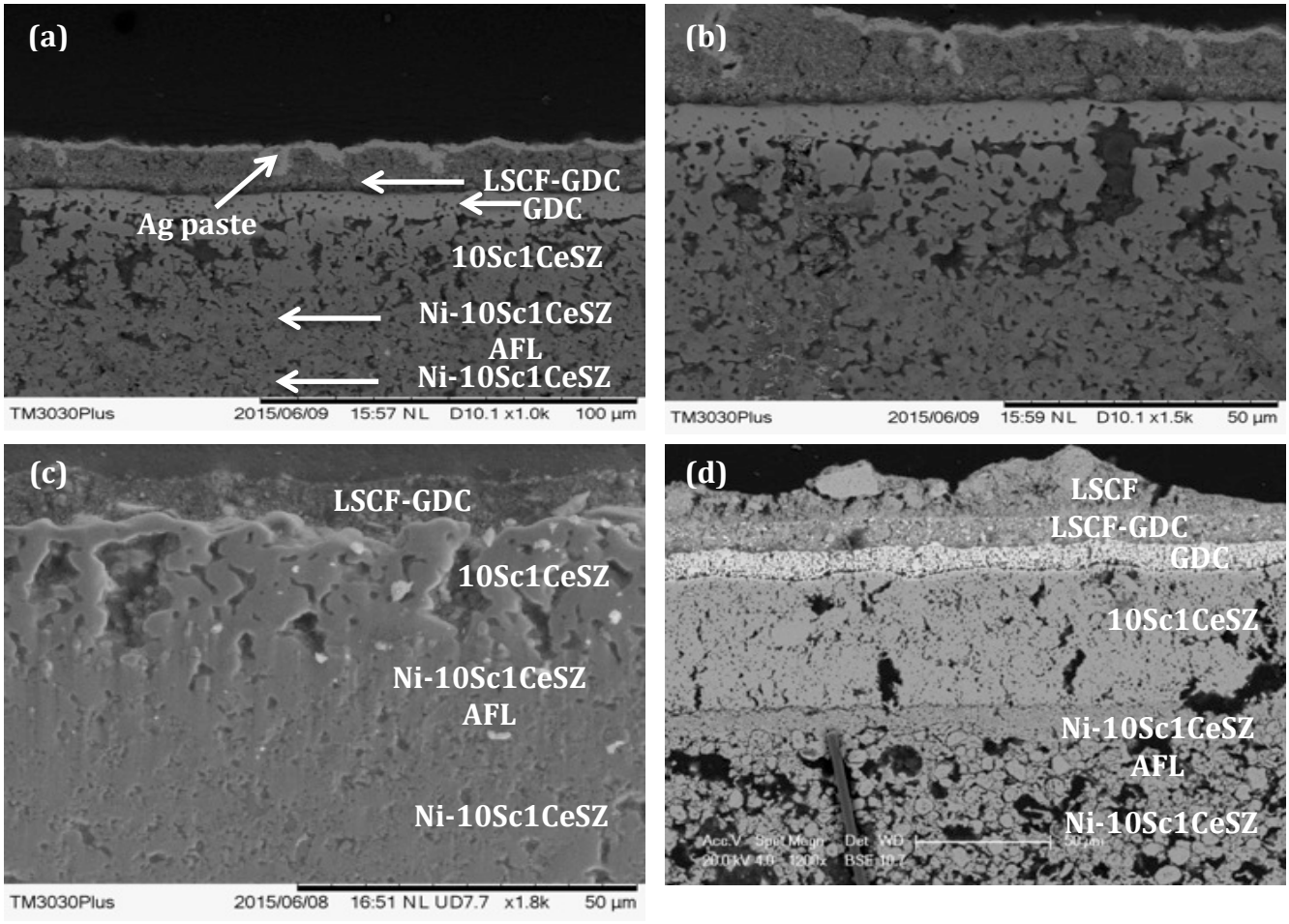

Figure 6-13: (a) SEM image of Cell SA in BSE mode (b) higher magnification of Cell SA in BSE mode (c) SEM image of Cell SB in SE mode (d) SEM micrograph of Cell SC in BSE mode

6.8 OPEN CIRCUIT VOLTAGE AND CELL MICROSTRUCTURE

Open circuit voltage (OCV) measurements for the YSZ and 10Sc1CeSZ cells were obtained to link the properties of the electrolyte to the cell potential, which could be used to predict performance. Figure 6-14 shows the initial OCV of cells after reduction for one hour under flowing H_2 at 800°C. More details regarding the electrochemical test sequence are outlined in Chapter 3, Section 3.5.3. As seen in Figure 6-14, cell 10Sc1CeSZ SC, which contained a printed electrolyte film from calcined 10Sc1CeSZ powders, had the lowest OCV of all cells as well as some instability as evidenced by the data fluctuations seen in the plot throughout the entire test run. The corresponding electrolyte microstructure can be seen in Figure 6-13 (d). The bottom up increase of cell OCVs when linked to the specific cell's microstructure, shows how the microstructural evolution and densification of the electrolyte layers is directly responsible for the improvement in cell OCV. Cell 10Sc1CeSZ (1) seen in Figure 6-5 (a) was the first cell prepared using the processing method developed for the YSZ system and shows the connection between the microstructural characteristics and OCV of this cell relative to the lab grade Ni-YSZ, commercial Ni-YSZ and 10Sc1CeSZ cells seen in Figures 5-14 (Chapter 5, Section 5.7.4), Figures 5-16 (Chapter 5, Section 5.7.4) and Figure 6-7 (Chapter 6, Section 6.5.2) respectively.

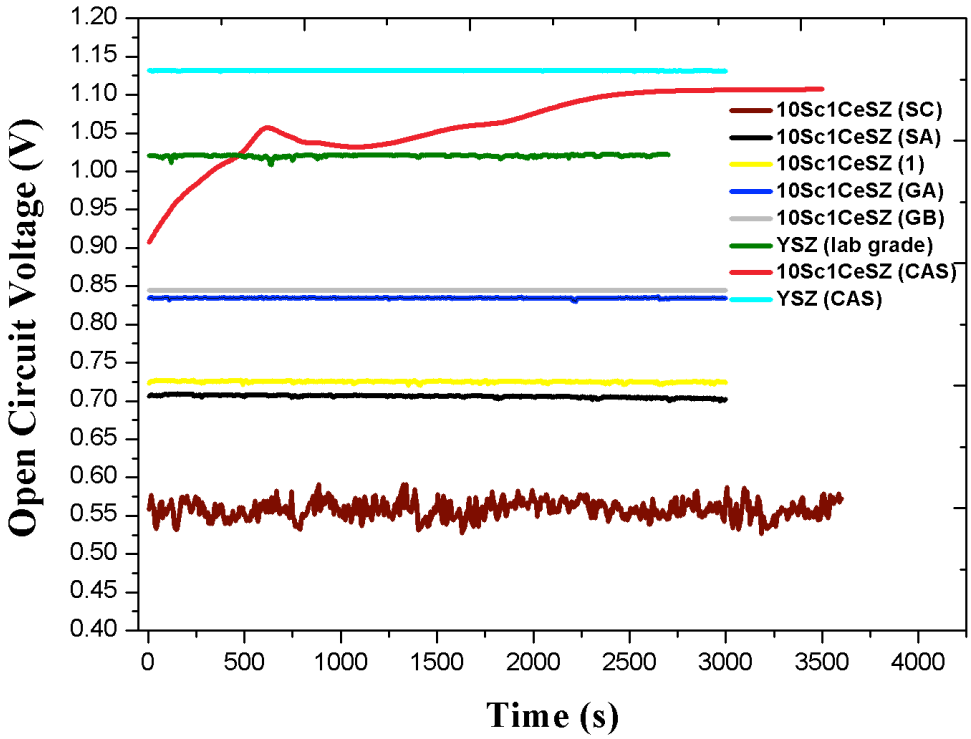

Figure 6-14: Open circuit voltages of various YSZ and 10Sc1CeSZ cells after reduction for one hour under flowing H_2 at 800°C

The degree of improvement in electrolyte densification required to obtain a satisfactory working cell is obvious with the microstructures of the commercial YSZ (CAS) and 10Sc1CeSZ (CAS) cells yielding OCVs of 1.143V and 1.121V respectively, the highest OCVs consistently achieved for all tested cells. The microstructures of these cells also exhibit the most enhanced electrolyte densification. Table 6.2 summarises the OCV values for the cells plotted in Figure 6-14. The large holes, cracks and agglomeration in the electrolyte layers of the 10Sc1CeSZ cells, contributed greatly to the consistently poor OCV results and supported the need for the extended Al_2O_3 dopant densification study carried out for the 10Sc1CeSZ system.

Table 6.2: Summarised List of OCVs for YSZ and 10Sc1CeSZ Cells Plotted in Figure 6-14

Sample ID	OCV (V)	Microstructure Reference
YSZ (CAS)	**1.143**	**Figure 5-16**
10Sc1CeSZ (CAS)	**1.121**	**Figure 6-7**
YSZ (lab grade)	**1.022**	**Figure 5-14**
10Sc1CeSZ (GB)	**0.845**	**Figure 6-10**
10Sc1CeSZ (GA)	**0.834**	**Figure 6-8, 6-9**
10Sc1CeSZ (1)	**0.725**	**Figure 6-5 (a)**
10Sc1CeSZ (SA)	**0.706**	**Figure 6-13 (a), (b)**
10Sc1CeSZ (SC)	**0.592**	**Figure 6-13 (d)**

6.9 10Sc1CeSZ LAYER DENSIFICATION II. – THE USE OF DISPERSANTS AND Al_2O_3

6.9.1 The Use of Dispersants

The fired 10Sc1CeSZ layers shown in part I of the 10Sc1CeSZ layer densification study show strongly bonded particle clusters that were not easily separated during ball milling or ink mixing. The composition of the V-737 vehicle (Heraeus, USA) used to prepare the printing inks in this study was not disclosed because of proprietary standards but in the case of the 10Sc1CeSZ system it was obvious the addition of processing additives to both the powder and ink slurries would be necessary to achieve a more homogeneous, uniformly packed and dense microstructure. The rheology behaviour of the printed

inks is sensitive to the properties of the powder as well as the organic additives that comprise the components of the vehicle. Previous researchers have reported stabilised, well dispersed YSZ suspensions with the use of dispersants [20], [21]. Stable systems are obtained when the particles in suspension can remain separated which, through the use of dispersants, is achieved when the dispersant adsorbs onto the particle surface and disassociates, modifying particle surface properties and then goes into solution further weakening and controlling Van der Waals particle-particle interactions [20]. The dispersants in literature that have been used to successfully disperse ZrO_2 suspensions are polyethyleneimine [17], [22] and Triton-X [23], [24] . These dispersants were readily available in our lab so these were used. The effect of the dispersions on the ceramic suspensions was determined by evaluation of the printed layers via SEM analysis.

Different 10Sc1CeSZ powder batches were prepared so the influence of starting powder properties on the degree of dispersion in the systems could be evaluated. Menzler reported better dispersion of calcined YSZ powders of a larger particle size compared to as-received YSZ powders of a lower particle size due to the lower surface energy of the calcined powders [17]. Less agglomeration was also reported. The films of the calcined powders were smooth, homogeneous and crack free while the films prepared using the as-received YSZ powders were rough with large cracks. For this study, the particle size (d_{50} = 90 nm) of the DKKK powders was slightly larger than that of the IPMS powders (d_{50} = 11 nm) so the influence of this difference on the fabrication of screen-printed 10Sc1CeSZ layers and ultimately the densification of the 10Sc1CeSZ electrolyte films was studied.

A table of the different samples A1, B1 and C1 prepared using different powder batches, 50:50 wt% as-received/calcined 10Sc1CeSZ powder, calcined 10Sc1CeSZ powder and as-received 10Sc1CeSZ, respectively, is shown in Figure 6-15. The powders were calcined at 1240^{o}C-3hrs – the sample sintering schedule used by Menzler [17]. The as-received/calcined powder combination was used as it was thought to widen the particle size distribution and yield a mix of moderate shrinkage-moderate compaction and high shrinkage-high compaction, balancing the shrinkage matches during half-cell co-firing. Matching the free sintering kinetics of the cell component layers reduces the stresses generated by the shrinkage mismatches preventing the formation of defects and interconnected porosity resulting in a dense microstructure. The powders were ball milled so a homogeneous mixing between the powders could be obtained. The layers were screen-printed using the standardised 40% vol solids loading inks prepared from these powders and fired at 1400^{o}C-4hrs. Samples A1-T1 and B1-T1 contained 0.6 wt% of polyethyleneimine dispersant with 0.6 wt% Triton X-100 dispersant added to sample C1-T1.

A1-T1	50:50 as-received/calcined 1240°C-3hrs DKKK powder, ball milled 8hrs
B1-T1	calcined 1240°C-3hrs DKKK powder
C1-T1	as received DKKK powder

Dispersants	*Sample A1-T1*	*Sample B1-T1*	*Sample C1-T1*
Polyethyleneimine	*X*	*X*	
Triton X-100			*X*

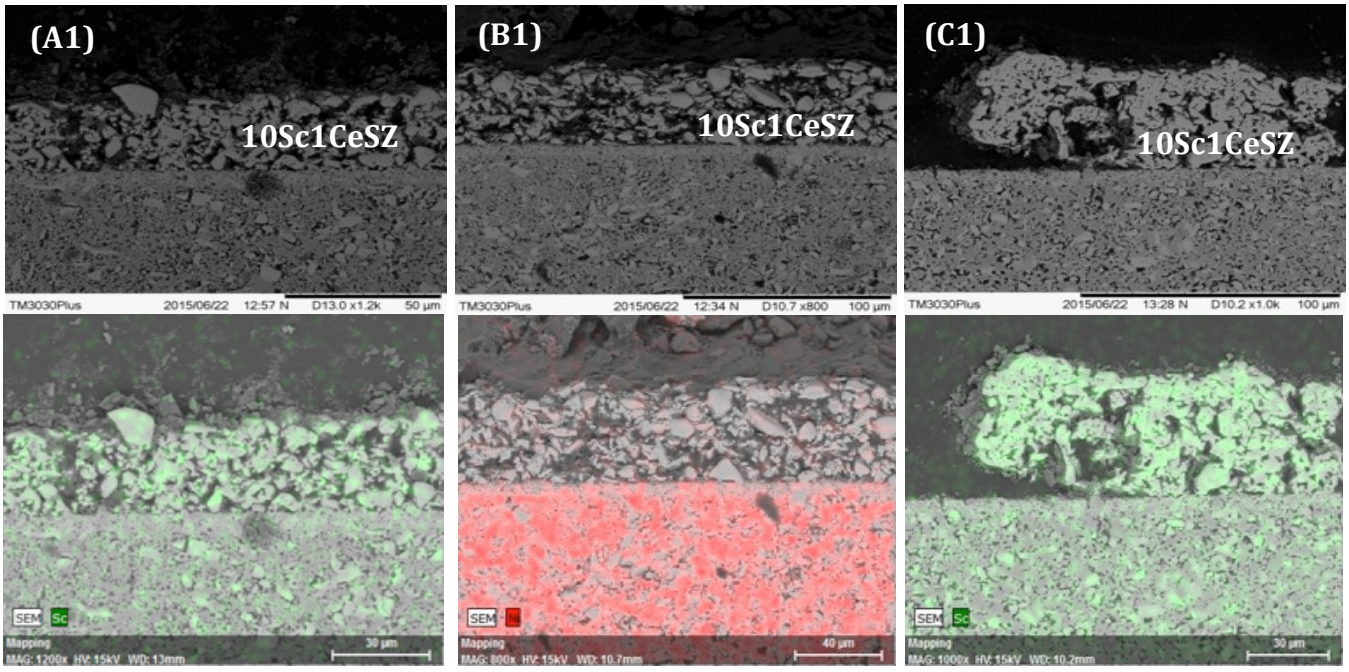

Figure 6-15: Cross-sectional SEM images of (A1), (B1) and (C1) obtained in BSE mode. EDX mapping of Sc (green-A1, C1) and Ni (red-B1) elemental distribution distinguishing the Ni-10Sc1CeSZ anode layers from the 10Sc1CeSZ electrolyte layers

None of the electrolyte films seen in Figure 6-15 have improved microstructures, with the electrolyte layer in sample C1 peeling away from the substrate surface. This is largely due to the rheological behaviour of the "tacky" ink being more viscous lacking flowability and insufficient bonding strength to adhere the green film to the substrate surface and/or a rough substrate surface compromising the adhesion property of the printed film. The high porosity content of all the samples is readily obvious which is attributed to the particle aggregates present in the poorly dispersed suspensions. For all of the samples analysed in parts I and II of the 10Sc1CeSZ layer densification study, IPMS and DKKK powders were used interchangeably with no significant difference or improvement in the microstructural evolution of the printed layers. The agglomeration seen in samples pictured in Figure 6-15 is extremely exaggerated unlike what has been observed previously which begs to reason it is the ceramic processing

route of the powders and the printing inks not necessarily the intrinsic properties of the starting powder. If IPMS powder was used it is suggested that similar results would be obtained. The manufacturing and testing of 10Sc1CeSZ cells cannot proceed unless a reasonably dense electrolyte film can be manufactured which is the motivation for these series of experiments. The final attempt to promote the densification of the 10Sc1CeSZ electrolyte film was explored through the use of Al_2O_3 as a sintering aid.

6.9.2 The Use of Al_2O_3

The use of transition metal oxide dopants has been found to enhance the sintering behaviour of Zirconia and Ceria systems [25]–[28]. The use of Al_2O_3 in YSZ has also been shown to improve the sinterability of YSZ promoting the formation of dense microstructures at lower temperatures [29]–[34]. Tekeli [31] found the solubility limit of Al_2O_3 in YSZ was 0.3 wt% (0.39 mol%) at 1300°C with densities greater than 95% theoretical densities achieved at this temperature. Hassan [30] found the solubility limit of Al_2O_3 in YSZ to be 0.1 mol% (0.08 wt%) at 1300°C and 0.5 mol% (0.39 wt%) at 1700°C with dense microstructures that lowered leak rates during helium leakage tests with Al_2O_3 additions below 1 wt% (1.29 mol%). Hotza investigated the addition of nanosized Al_2O_3 on the density of YSZ and reported 95% theoretical densities at 1300°C for samples containing 0.5 mol% (0.39 wt%) Al_2O_3 while samples fired at 1500°C achieved similar densities with 0.2 mol% (0.16 wt%) Al_2O_3 content. The solubility limit in their work was reported at 1 mol%. The enhanced densification of the Al_2O_3 doped YSZ systems has been ascribed to a liquid phase sintering mechanism [34].

During conventional liquid phase sintering, the binary eutectic temperature at which the solid and liquid phases coexist is well below the sintering temperature of the host material so the liquid phase coats the surfaces of the grains and reduces surface tension by smoothing the coarse grain surfaces. This allows for stronger particle contact and better particle arrangement producing a more dense structure. As the Al_2O_3 –YSZ phase diagram does not show the presence of a liquid phase below 1710°C, this theory has since been refuted with the possibility of a reaction between Al_2O_3 and YSZ resulting in the formation of a liquid phase [34]. Others suggest the improved sintering behaviour of Al_2O_3 -YSZ is due to Al^{3+} ions predominantly segregating at the grain boundaries creating a second impurity phase due to strain energy relaxation and electrostatic charge compensation brought about by the size mismatch of the host and solute ions [16], [31], [35], [36]. Work by Tekeli et al. [16], [31] showed the presence of an Al_2O phase at the grain boundaries limited fast grain growth, which is typically observed for cubic-ZrO_2 under normal sintering conditions, and lowered grain boundary mobility promoting enhanced densification by increasing grain boundary diffusivity [31]. Suarez et al. [35] showed that lower

activation energies for low levels of Al_2O_3 (<3 wt%) in 8YSZ was due to the presence of Al^{3+} in the grain boundary regions where a change in the sintering mechanism from grain boundary diffusion (GBD) for undoped 8YSZ to volumetric diffusion (VD) up to 3 wt% Al_2O in 8YSZ was observed with another mechanism change again from VD back to GBD for higher Al_2O_3 levels ≈ 10 wt%. Matsui et al. [36] also reported a reduction in activation energy during initial stage sintering for specimens containing 0.25 wt% Al_2O_3 in 7.8 mol% cubic - Y_2O_3-ZrO_2 brought about by the reduction of the surface energy of the YSZ powders due to the presence of Al^{3+} at the grain boundaries. This increased the densification rate of 7.8 mol% cubic - Y_2O_3-ZrO_2 significantly at temperatures <1290°C. The results of Matsui et al. and Suarez et al. are in agreement with work published by Harmer et al. [37] which states that dopant additions near to the solubility limit of the dopant in the host limits grain growth during initial stage sintering by forcing dopant segregation to the grain boundaries with grain boundary pinning occurring during final stage sintering due to increased volume fractions of the solute cations in the grain boundary. The promising results achieved with Al_2O_3 additions to YSZ motivated the use of Al_2O_3 as a sintering aid for the densification of the 10Sc1CeSZ electrolyte films despite the results being achieved for bulk YSZ pellets. It should be noted the free sintering activity observed in a bulk sample could be markedly different than that of a thin film co-fired with a supporting structure though the information obtained can be used to predict trends in the sintering behaviour of a material.

The microstructures of the half-cells prepared for this sample batch are presented in Figure 6-16. Sample A1-T2 was prepared using DKKK 10Sc1CeSZ powders calcined at 1240°C-3hrs while B1-T2 was prepared using as-received DKKK 10Sc1CeSZ powder. 1.29 mol% (1 wt%) nanoscale α-Al_2O_3 powder (Sigma, d_{50} = 5 nm) was added to the 10Sc1CeSZ powders at the ball milling stage. Inks were then prepared from the milled Al_2O_3-10Sc1CeSZ powders. Both samples were fired at 1550°C-4hrs. No dispersants were added to the powders. A TEM image of the α-Al_2O_3 powder is provided in Figure 6-17. The powder displays a skeletal bonding arrangement with agglomerate sizes ranging from 50 – 100 nm and observed crystallite sizes of 5 nm which support manufactured specified d_{50} values. The improved densification for both samples is obvious with no noticeable difference between the calcined sample shown in Figure 6-16 (a) and the as-received sample shown in Figure 6-16 (b). The uniformity of the layers is still poor with open and closed porosity clearly visible. The anode is completely dense because of the high sintering temperature. These results gave promise for the use of Al_2O_3 though it was not clear which had the greatest effect on the improved densification of the 10Sc1CeSZ layer – the higher sintering temperature or the Al_2O_3 addition. Thus a more detailed design of experiments using Al_2O_3 as a sintering aid was planned to close out this last phase of the densification

study and will be discussed in the section below.

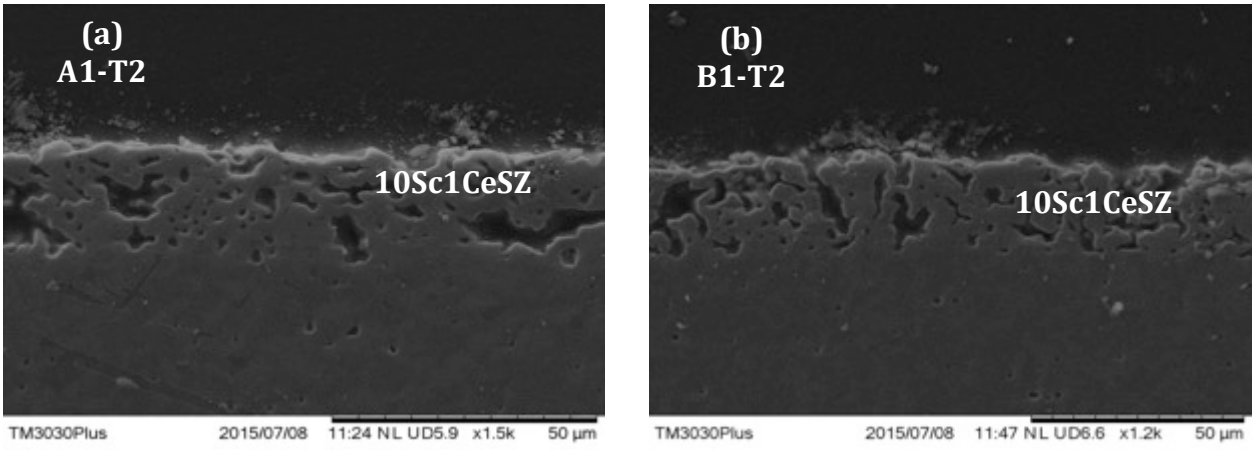

Figure 6-16: Cross-sectional SEM samples of (a) A1-T2 and (b) B1-T2 fired at 1550°C-4hrs

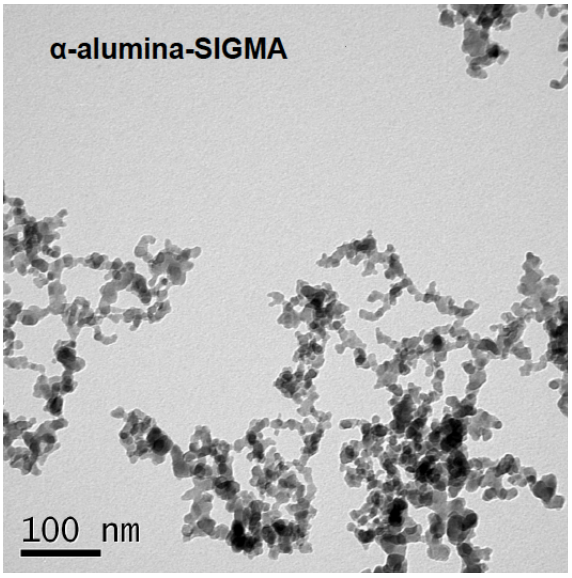

Figure 6-17: TEM micrograph of as-received α-Al_2O_3 (Sigma) powder

6.9.3 Isolating Al_2O_3 Concentration

The influence of Al_2O_3 additions on the sintered density of 10Sc1CeSZ films was further explored at varying Al_2O_3 dopant levels at a fixed firing temperature to isolate a dopant concentration that could be further explored at varying firing temperatures. Table 6.3 shows the samples categorized as low-level,

med-level and high-level according to the Al_2O_3 content. Low level refers to the 0.2 mol% (1a, 2) and 0.55 mol% (1b, 2) samples, mid-level refers to the 0.84 mol% (2c, 2) and 1.29 mol% samples and high level refers to the 1.55 mol% (3e, 2) samples. The number 2 refers to the fixed sintering temperature of 1325°C. The temperature designations range from 1-8 and represent firing temperatures of 1300, 1325, 1350, 1375, 1400, 1425, 1450 and 1550°C respectively. The selected Al_2O_3 levels were chosen based on the solubility limits of Al_2O_3 in 10Sc1CeSZ reported in literature [29], [30], [34]. The Al_2O_3 powders were combined and ball milled with the as-received DKKK 10Sc1CeSZ powders for efficient mixing. The Al_2O_3 –10Sc1CeSZ electrolyte layers were screen-printed using 40 vol% solids inks prepared with these powders.

Table 6.3: Experimental Matrix for Al_2O_3-10Sc1CeSZ Samples Listing Factors and Levels

Parameter	Low: a	Low: b	Med: c	Med: d	High: e	Med: f	Med: g	High: h
Al_2O_3-mol%	0.2	0.55	0.84	1.29	1.55	0.55	0.55	1.29
Temp (C°)-4h	1300	1325	1350	1375	1400	1425	1450	1550

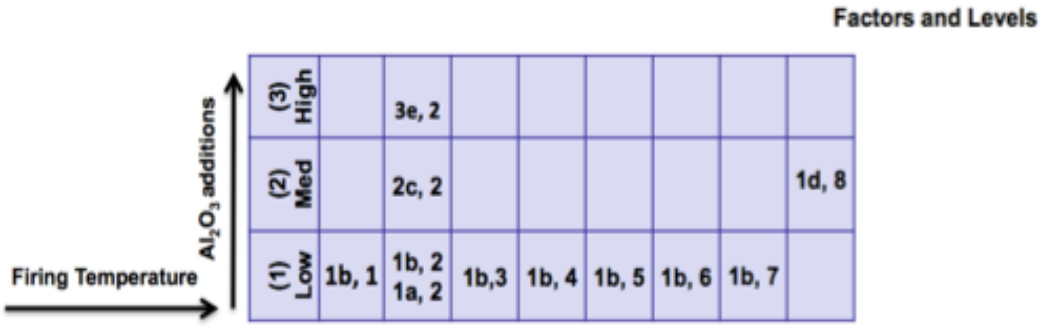

Printed 10Sc1CeSZ films containing varying levels of Al_2O_3 additions - 0.20 mol% (0.16 wt%), 0.55 mol% (0.45 wt%), 0.84 mol% (0.69 wt%), 1.29 mol% (1.05 wt%) and 1.55 mol% (1.27 wt%) were prepared. The 1d, 8 sample is the 1.29 mol% fired at 1550°C-4hrs discussed in the previous section. The results of this sample were provided in Figure 6-16. Figure 6-18 shows the microstructures of the 10Sc1CeSZ samples with varying Al_2O_3 content sintered at 1325°C-4hrs. Relatively dense structures are seen for all of the half-cells with the best microstructures of this sample set observed for the 0.20 mol% and 0.55 mol% samples as determined by electrolyte porosity calculations using image editing as described in Chapter 5, Section 5.74. The analysed regions are seen in Figure 6-19 with the porosity percentages and mean pore sizes provided in Table 6.4. The coating thickness of ~15 um for all samples reveals the reproducibility of the screen-printing method when the printing parameters and ink characteristics are fixed. No agglomeration is seen in any of the layers and the layers appear more

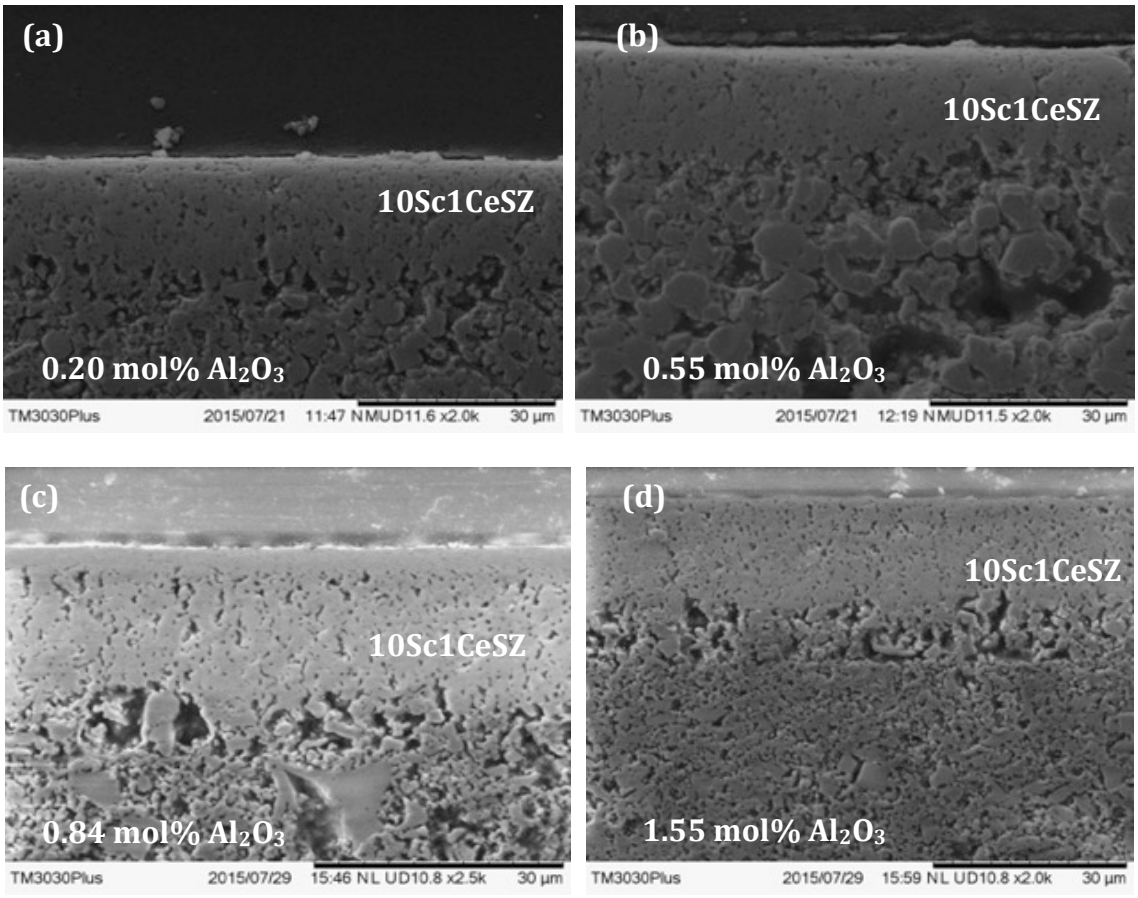

Figure 6-18: Cross-sectional images of doped Al_2O_3-10Sc1CeSZ half-cells fired at 1325°C-4hrs

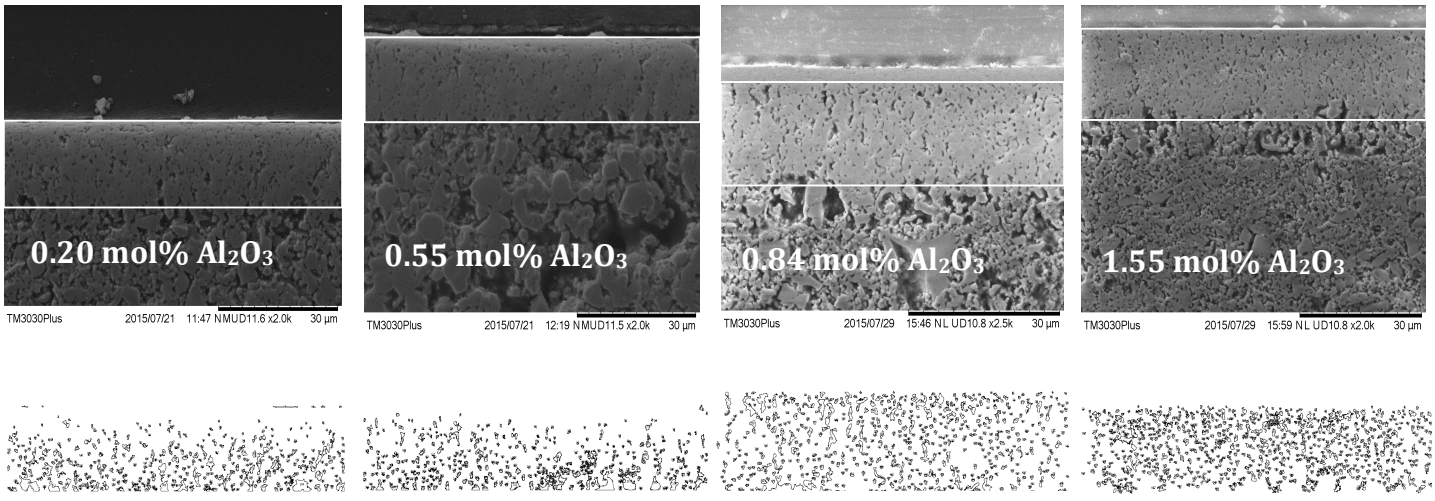

Figure 6-19: Analysed 10Sc1CeSZ electrolyte regions

Table 6.4: Porosities and Mean Pore Sizes for Al_2O_3-10Sc1CeSZ Samples Fired at 1325°C-4hrs

Sample (mol %)	Porosity (%)	Mean pore size (μm)
0.20 Al_2O_3	9.94	0.425
0.55 Al_2O_3	8.72	0.344
0.84 Al_2O_3	12.61	0.284
1.55 Al_2O_3	12.85	0.286

closely packed. The higher Al_2O_3 dopant concentrations seem to not be as effective in promoting densification as the lower concentrations suggesting the possibility that the solubility limit of Al_2O_3 in 10Sc1CeSZ may have been exceeded. Higher Al_2O_3 concentrations (>0.3 wt% Al_2O_3) were found to retard YSZ densification as excess Al_2O_3 may segregate at the grain boundaries hindering grain boundary diffusion through extreme grain boundary pinning [31]. Non-homogeneous distribution of Al_2O_3 in the YSZ lattice could also adversely affect the sintering rate due to a build up of Al_2O_3 around the perimeter of the YSZ grains hindering YSZ particle rearrangement and particle-particle contact [31]. The 0.55 mol% Al_2O_3 doped sample exhibits the most enhanced densification, slightly better than that of the 0.20 mol% sample, so it was chosen and formed the basis for the sintering temperature study. Half-cells containing electrolyte films with 0.55 mol% Al_2O_3 in 10Sc1CeSZ were prepared and fired at varying sintering temperatures where they dwelled for 4hrs. The phase purity of the 0.55 mol% Al_2O_3 - 10Sc1CeSZ sample under the chosen sintering schedule was determined via XRD.

6.9.4 0.55 mol% Al_2O_3 - 10Sc1CeSZ Sintering Condition

Results of the Al_2O_3-10Sc1CeSZ concentration study showed the 0.55 mol% Al_2O_3 doped sample exhibited the best electrolyte densification, thus 0.55 mol% Al_2O_3-10Sc1CeSZ samples sintered within the 1300-1450°C-4hrs range were prepared and the electrolyte layer density examined. Microstructural evolutions with increasing temperature were seen as evidenced by the calculated Al_2O_3-10Sc1CeSZ electrolyte porosities and mean pore values listed in Table 6.5 supported by the electrolyte morphologies seen in Figure 6-20. The crack seen in sample Figure 6-20 (d) fired at 1400°C-4hrs was caused during cross-sectional cutting and mounting. Highly dense electrolyte layers were observed for the samples fired at 1425°C-4hrs and 1450°C-4hrs though significant pore removal starts with the 1375°C-4hrs sample. The 1450°C-4hrs sample is the most dense with the smallest mean pore size but to avoid mass transport limitations in the anode, as a highly dense anode microstructure was beginning to form,

Table 6.5: Porosities and Mean Pore Sizes for 0.55 mol% Al_2O_3-10Sc1CeSZ Samples at Varying Sintering Temperatures

Temperature (^oC- 4hrs)	Porosity (%)	Mean pore size (μm)
1300	8.76	0.288
1350	8.62	0.344
1375	8.46	0.225
1400	8.35	0.547
1425	5.46	0.311
1450	2.122	0.188

Ni-10Sc1CeSZ anode supported cells with 0.55 mol% Al_2O_3-10Sc1CeSZ electrolyte layers fired at 1425^{o}C-4hrs were prepared and fabricated for testing. The analysed regions of the 0.55 mol% Al_2O_3-10Sc1CeSZ electrolyte films used to calculate the electrolyte porosities are pictured in Figure 6-21. The 0.55 mol% Al_2O_3-10Sc1CeSZ samples exhibited high packing densities and the overall porosity is the lowest it has ever been for any of the screen-printed 10Sc1CeSZ layers. These results demonstrate the effectiveness of Al_2O_3 as a sintering aid. And though Al_2O_3 did not enhance the sintering of 10Sc1CeSZ by producing dense microstructures at temperatures lower than what is required to densify YSZ electrolytes (~1400^{o}C), it did promote the densification of 10Sc1CeSZ. GDC interlayers were not deposited on these cells due to project constraints, as additional time for more detailed investigations regarding the compatibility of GDC with 10Sc1CeSZ would be required.

6.9.5 Phase Stability of 0.55 mol% Al_2O_3 – 10Sc1CeSZ

Figure 6-22 shows the XRD scan of the Al_2O_3 – 10Sc1CeSZ system with a magnified scan of the 1.55 mol% sample presented in Figure 6-23 for a clearer view. Single phase cubic ZrO_2 is seen for all of the samples meaning Al_2O_3 additions do not modify the crystal structure of the 10Sc1CeSZ system. Similar results are reported by Hotza [32] who used nanoscale Al_2O_3 powder with no Al_2O_3 peaks detected even for dopant levels up to 1 mol%. It was suggested that the Al_2O_3 diffused well into the cubic ZrO_2 lattice. Unit cell contraction was observed for this system as lattice parameter values decreased with increasing Al_2O_3 content as seen in Figure 6-24. The lattice parameter of 10Sc1CeSZ was estimated to be 5.091 and as the ionic radius of Al^{3+} is smaller (0.54Å) compared to the ionic radius

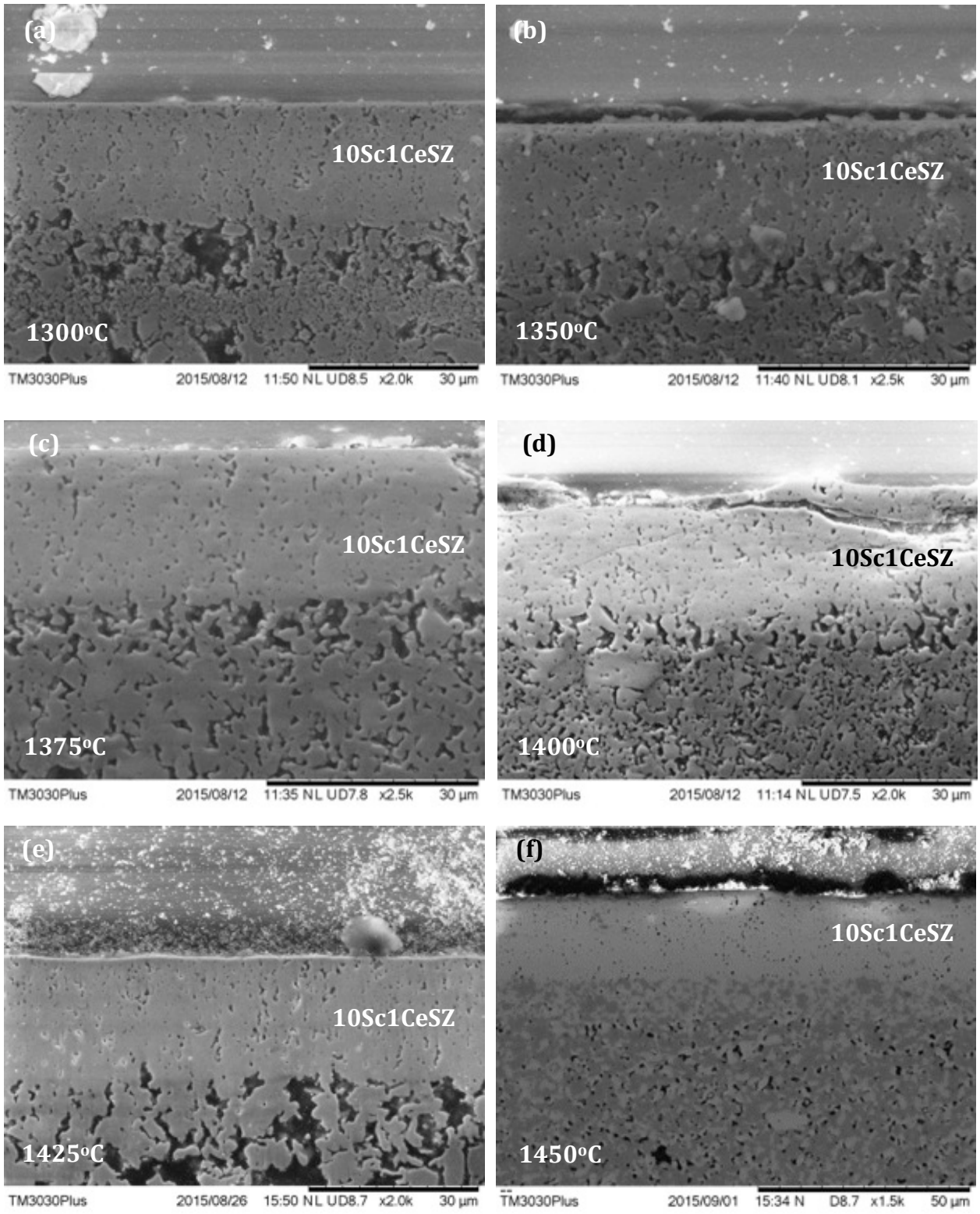

Figure 6-20: SEM images of 0.55 mol% Al_2O_3 doped 10Sc1CeSZ fired at varying temperatures (a) 1300°C-4hrs (b) 1350°C-4hrs (c) 1375°C-4hrs (d) 1400°C-4hrs (e) 1425°C-4hrs (f) 1450°C-4hrs

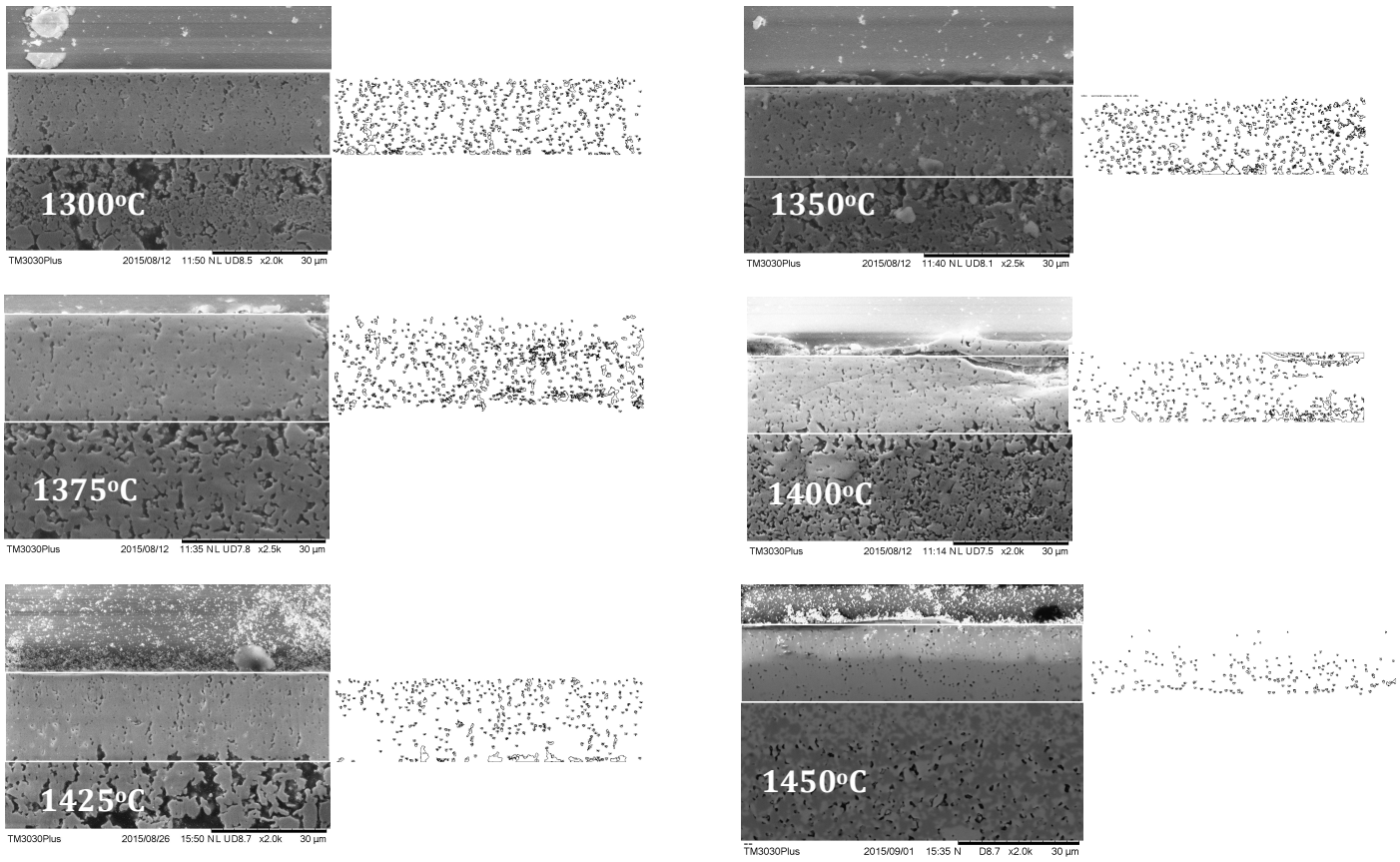

Figure 6-21: Analysed electrolyte regions of the 0.55 mol% Al_2O_3-10Sc1CeSZ samples

of Sc^{3+} (0.87Å) and Zr^{4+} (0.84Å) [16] this assumption is reasonable. The decrease in the lattice parameter is not linear as there exists some disruption in the trend for the absolute values but after a 2nd order curve fit to the data, a decreasing trend in the lattice parameter with increasing Al_2O_3 concentration is observed.

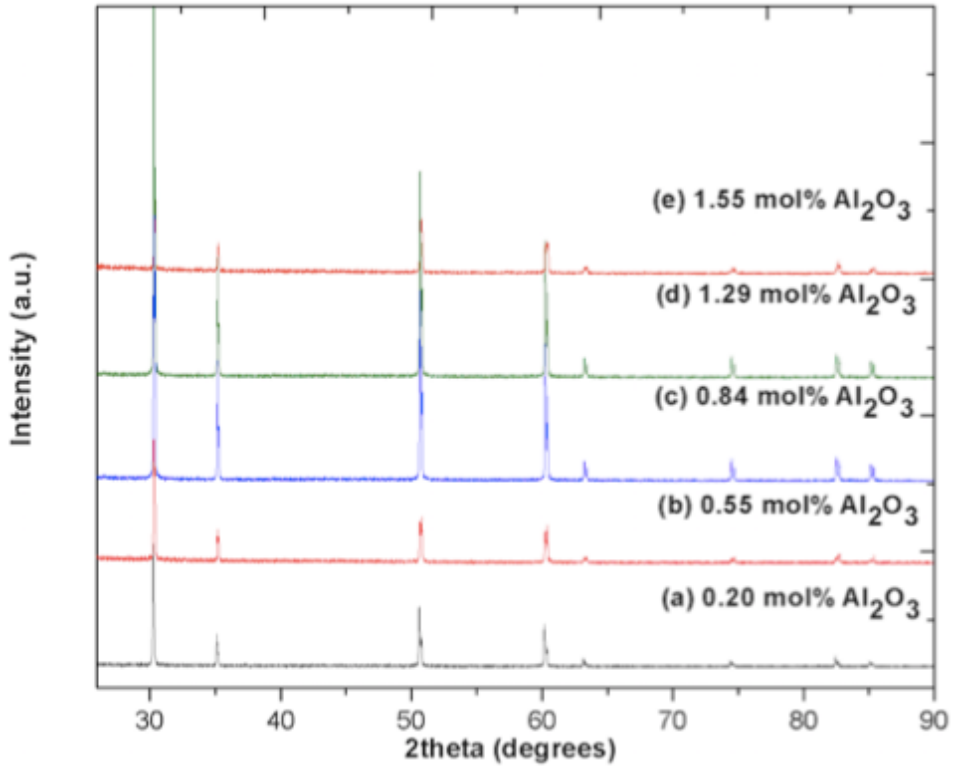

Figure 6-22: XRD scans of Al_2O_3 doped 10Sc1CeSZ at varying Al_2O_3 concentrations

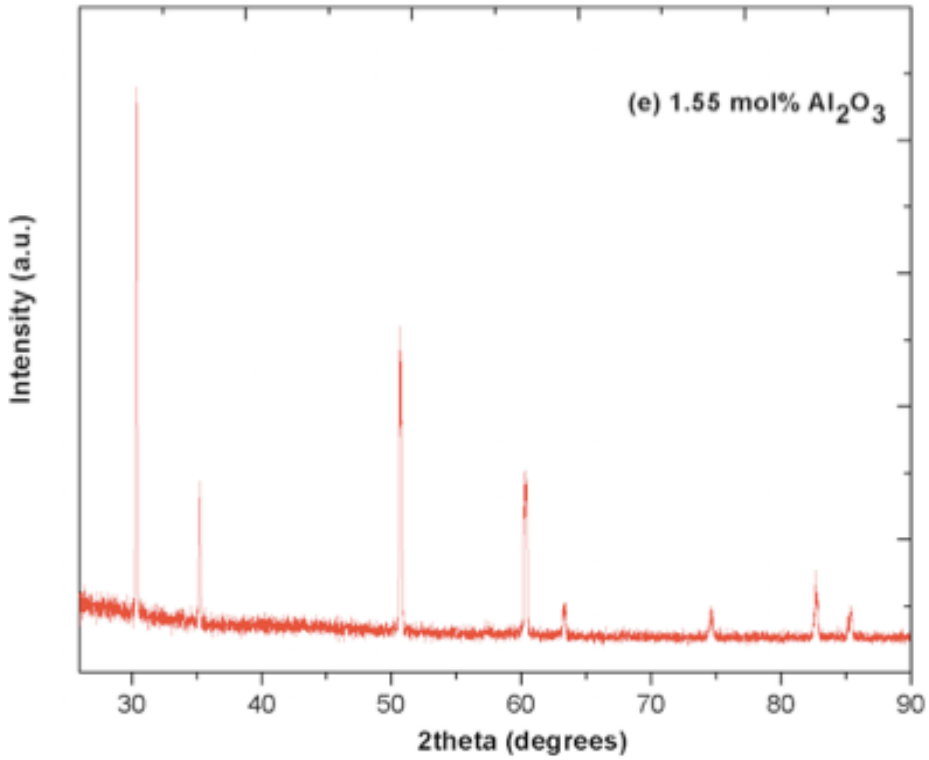

Figure 6-23: XRD scans of 1.55 mol% Al_2O_3 doped 10Sc1CeSZ

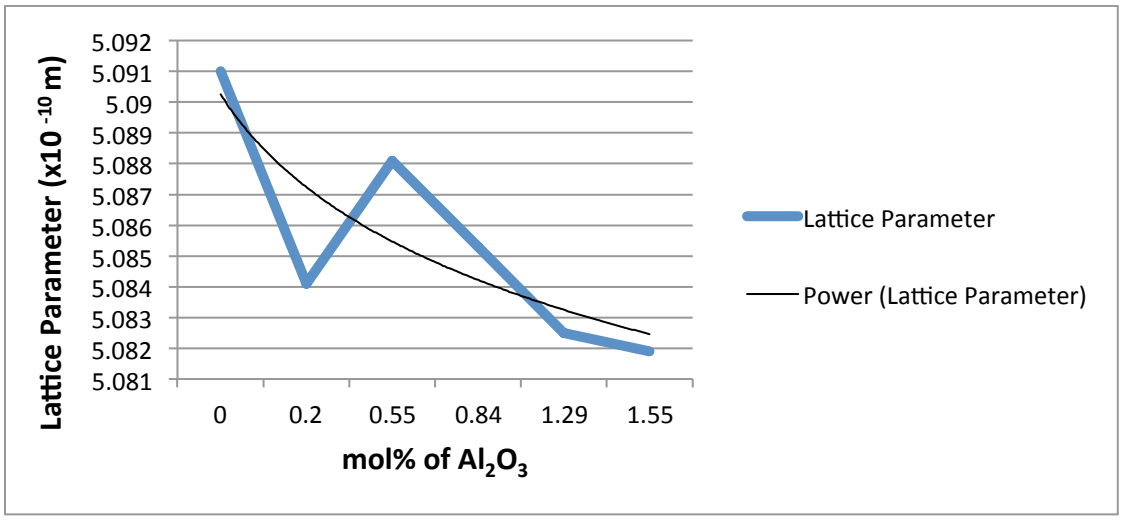

Figure 6-24: Lattice parameter change in 10Sc1CeSZ with increasing Al_2O_3 concentration

6.10 SUMMARY

The manufacturing route for the YSZ system was not directly transferable to the 10c1CeSZ system as changes were made to the anode substrate volume ratios such that the final 10Sc1CeSZ anode composition of 60:40 wt% reflected sufficient substrate strength for handling. The 1400°C-4hrs co-firing schedule did not produce dense 10Sc1CeSZ layers as OCV values of only 0.725V were achieved, so several manufacturing approaches were employed to try and achieve a dense 10Sc1CeSZ film. An increase in OCV to 0.834V was achieved with the use of a 10Sc1CeSZ-GDC compatibility layer between the 10Sc1CeSZ and GDC films. A slightly higher OCV of 0.845V was achieved when the GDC barrier layer was sintered in a separate firing step from the Ni-10Sc1CeSZ/10Sc1CeSZ anode-electrolyte co-fire. And while these slight improvements are notable, greater improvements are required to achieve a satisfactory working cell. The OCVs of the commercial 10Sc1CeSZ and YSZ cells were 1.121V and 1.143V respectively, with the most dense electrolyte microstructures observed for these cells. The use of Al_2O_3 as a sintering aid for the 10Sc1CeSZ system was explored to further densify the electrolyte layers to further improve the OCV. Al_2O_3 contents of 0.20, 0.55, 0.84 and 1.29 and 1.55 mol% were doped into 10Sc1CeSZ with the 0.55 mol% Al_2O_3 – 10Sc1CeSZ sample yielding the lowest porosities of 8.72% and 5.46% at 1325°C-4hrs and 1425°C-4hrs respectively. The addition of 0.55 mol% Al_2O_3 diffused well into the cubic 10Sc1CeSZ lattice without the formation of any additional phases. These results show Al_2O_3 is an effective sintering aid for 10Sc1CeSZ and the effect of the improved densification on the electrochemical performance will be examined in Chapter 7.

REFERENCES

[1] Y. Zhang, X. Huang, Z. Lu, X. Ge, J. Xu, X. Xin, X. Sha and W. Su, Effect of starting powder on screen-printed YSZ films used as electrolyte in SOFCs. *Solid State Ionics*, 2006. 177 (3–4): p. 281-287.

[2] J. Grzonka, V. Vereshchak, O. Shevchenko, O. Vasylyev and K. J. Kurzydłowski, Characterization of Sc_2O_3 & CeO_2-Stabilized ZrO_2 Powders Via Co-Precipitation or Hydrothermal Synthesis. *Microsc. Microanal.*, 2013. 19 (S5): p. 29-32.

[3] P. Ried, C. Lorenz, A. Brönstrup, T. Graule, N. H. Menzler, W. Sitte and P. Holtappels, Processing of YSZ screen printing pastes and the characterization of the electrolyte layers for anode supported SOFC. *J. Eur. Ceram. Soc.*, 2008. 28 (9): p. 1801-1808.

[4] M. R. Somalu, V. Yufit and N. P. Brandon, The effect of solids loading on the screen-printing and properties of nickel/scandia-stabilized-zirconia anodes for solid oxide fuel cells. *Int. J. Hydrogen Energy*, 2013. 38 (22): p. 9500-9510.

[5] R. K. Bordia and R. Raj, Sintering Behavior of Ceramic Films Constrained by a Rigid Substrate. *J. Am. Ceram. Soc.*, 1985. 68 (6): p. 287-292.

[6] A. Tsoga, A. Gupta, A. Naoumidis, D. Skarmoutsos and P. Nikolopoulos, Performance of a Double-Layer CGO/YSZ Electrolyte for Solid Oxide Fuel Cells. *Solid State Ionics*, 1998. 4 (3–4): p. 234-240.

[7] A. Tsoga, A. Naoumidis, A. Gupta, and D. Stöver, Microstructure and interdiffusion phenomena in YSZ-CGO composite electrolyte. *Mater. Sci. Forum*, 1999. 308-311 (1) : p. 794-799.

[8] X. Zhou, Electrical conductivity and stability of Gd-doped ceria/Y-doped zirconia ceramics and thin films. *Solid State Ionics*, 2004. 175 (1–4): p. 19-22.

[9] R. Knibbe, J. Hjelm, M. Menon, N. Pryds, M. Søgaard, H. J. Wang and K. Neufeld, Cathode-Electrolyte Interfaces with CGO Barrier Layers in SOFC. *J. Am. Ceram. Soc.*, 2010. 93 (9): p. 2877-2883.

[10] S. J. Kim and G. M. Choi, Stability of LSCF electrode with GDC interlayer in YSZ-based solid oxide electrolysis cell. *Solid State Ionics*, 2014. 262 (1): p. 303-306.

[11] A. Tsoga, A. Gupta and D. Stoever, Performance characteristics of composite film electrolytes for intermediate-temperature solid oxide fuel cells. *Solid State Ionics*, 1999. 5 (3): p. 175-182.

[12] X. Wang, J.-S. Kim and A. Atkinson, Constrained sintering of 8 mol% Y_2O_3 stabilised zirconia films. *J. Eur. Ceram. Soc.*, 2012. 32 (16): p. 4121-4128.

[13] T. J. Garino and H. K. Bowen, Kinetics of Constrained-Film Sintering. *J. Am. Ceram. Soc.*, 1990. 73 (2): p. 251-257.

[14] R. Mücke, N. H. Menzler, H. P. Buchkremer and D. Stöver, Cofiring of Thin Zirconia Films During SOFC Manufacturing. *J. Am. Ceram. Soc.*, 2009. 92 (S1): p. S95-S102.

[15] T. Yamaguchi, T. Suzuki, S. Shimizu, Y. Fujishiro and M. Awano, Examination of wet coating and co-sintering technologies for micro-SOFCs fabrication. *J. Memb. Sci.*, 2007. 300 (1–2): p. 45-50.

[16] S. Tekeli, M. Erdogan and B. Aktas, Influence of alpha-Al_2O_3 addition on sintering and grain growth behaviour of 8 mol% Y_2O_3-stabilised cubic zirconia (c-ZrO_2). *Ceram. Int.*, 2004. 30 (8): p. 2203-2209.

[17] M. Gaudon, N. H. Menzler, E. Djurado and H. P. Buchkremer, YSZ electrolyte of anode-supported SOFCs prepared from sub micron YSZ powders. *J. Mater. Sci.*, 2005. 40 (14): p. 3735-3743.

[18] Y. Zhang, X. Huang, Z. Lu, Z. Liu, X. Ge, J. Xu, X. Xin, X. Sha and W. Su, A study of the process parameters for yttria-stabilized zirconia electrolyte films prepared by screen-printing. *J. Power Sources*, 2006. 160 (2): p. 1065-1073.

[19] A. R. Hanifi, M. Zazulak, T. H. Etsell and P. Sarkar, Effects of calcination and milling on surface properties, rheological behaviour and microstructure of 8 mol% yttria-stabilised zirconia (8 YSZ). *Powder Technol.*, 2012. 231 (1): p. 35-43.

[20] S. Zürcher and T. Graule, Influence of dispersant structure on the rheological properties of highly-concentrated zirconia dispersions. *J. Eur. Ceram. Soc.*, 2005. 25 (6): p. 863-873.

[21] Y. H. Wang, X. Q. Liu and G. Y. Meng, Dispersion and stability of 8 mol.% yttria stabilized zirconia suspensions for dip-coating filtration membranes. *Ceram. Int.*, 2007. 33 (6): p. 1025-1031.

[22] T. Fengqiu, H. Xiaoxian, Z. Yufeng and G. Jingkun, Effect of dispersants on surface chemical properties of nano-zirconia suspensions. *Ceram. Int.*, 2000. 26 (1): p. 93-97.

[23] J. Zhang, F. Ye, J. Sun, D. Jiang, and M. Iwasa, Aqueous processing of fine ZrO_2 particles. *Colloids Surfaces A Physicochem. Eng. Asp.*, 2005. 254 (1–3): p. 199-205.

[24] C. G. Fonseca, R. M. F. Basaglia, M. C. Brant, T. Matencio, and R. Z. Domingues, Study of the rheological behavior of an anode slurry and the microstructural properties of an anode functional film obtained by spray coating. *Powder Technol.*, 2009. 192 (3): p. 352-358.

[25] H. Gao, J. Liu, H. Chen, S. Li, T. He, Y. Ji and J. Zhang, The effect of Fe doping on the properties of SOFC electrolyte YSZ. *Solid State Ionics*, 2008. 179 (27–32): p. 1620-1624.

[26] E. Jud, C. B. Huwiler and L. J. Gauckler, Sintering Analysis of Undoped and Cobalt Oxide Doped Ceria Solid Solutions. *J. Am. Ceram. Soc.*, 2005. 88 (11): p. 3013-3019.

[27] M. Liu, C. He, J. Wang, W. G. Wang and Z. Wang, Investigation of $(CeO_2)_x(Sc_2O_3)_{(0.11-x)}(ZrO_2)_{0.89}$ (x=0.01–0.10) electrolyte materials for intermediate-temperature solid oxide fuel cell. *J. Alloys Compd.*, 2010. 502 (2): p. 319-323.

[28] J. Van Herle and R. Vasquez, Conductivity of Mn and Ni-doped stabilized zirconia electrolyte. *J. Eur. Ceram. Soc.*, 2004. 24 (6): p. 1177-1180.

[29] M. Mori, M. Yoshikawa, H. Itoh and T. Abe, Effect of alumina on sintering behavior and electrical-conductivity of high-purity yttria-stabilized zirconia. *J. Am. Ceram. Soc.*, 1994. 77 (8): p. 2217-2219.

[30] A. A. E. Hassan, N. H. Menzler, G. Blass, M. E. Ali, H. P. Buchkremer and D. Stöver, Influence of alumina dopant on the properties of yttria-stabilized zirconia for SOFC applications. *J. Mater. Sci.*, 2002. 37 (16): p. 3467-3475.

[31] S. Tekeli, The solid solubility limit of Al_2O_3 and its effect on densification and microstructural evolution in cubic-zirconia used as an electrolyte for solid oxide fuel cell. *Mater. Des.*, 2007. 28 (2): p. 713-716.

[32] D. Hotza, A. Leo, J. Sunarso and J. C. Diniz da Costa, Effect of Nano-Al_2O_3 Addition on the Densification of YSZ Electrolytes. *J. Nano Res.*, 2009. 6 (1): p. 115-122.

[33] M. J. Verkerk, A. J. A. Winnubst and A. J. Burggraaf, Effect of impurities on sintering and conductivity of yttria-stabilized zirconia. *J. Mater. Sci.*, 1982. 17 (11): p. 3113-3122.

[34] K. C. Radford and R. J. Bratton, Zirconia electrolyte cells - Part 1 Sintering studies. *J. Mater. Sci.*, 1979. 14 (1): p. 59-65.

[35] G. Suarez and Y. Sakka, Effect of alumina addition on initial sintering of cubic ZrO_2 (8YSZ). *Ceram. Int.*, 2010. 36 (3): p. 879-885.

[36] J. H. K. Matsui, K. Tanaka and N. Enomoto, Sintering Kinetics at Constant Rates of Heating: Effect of Alumina on the Initial Sintering Stage of Yttria-Stabilized Zirconia Powders. *J. Ceram. Soc. Japan.*, 2006. 114 (1333): p. 763-768.

[37] M. P. Harmer, S. J. Bennison and C. Narayan, *Advances in Materials Characterization*, Springer, 1983.

CHAPTER 7
ELECTROCHEMICAL PERFORMANCE OF YSZ AND 10Sc1CeSZ

This chapter compares the electrical properties and cell performance of the lab grade and commercial grade Ni-YSZ and 10Sc1CeSZ systems on H_2 and CH_4.

7.1 10Sc1CeSZ AND Ni-YSZ ELECTRICAL CONDUCTIVITY

Impedance measurements were performed on bulk 10Sc1CeSZ and YSZ pellets sintered at 1500^{o}C-6hrs by researchers at IPMS (Ukraine) and the resistance values were used to plot the Arrhenius conductivities of the 10Sc1CeSZ and YSZ systems seen in Figure 7-1. Grain, grain boundary and ohmic resistance values were obtained based on the sample's semicircle characteristics at varying frequencies as a function of temperature and associating these responses to the ion mobility phenomena in the samples.

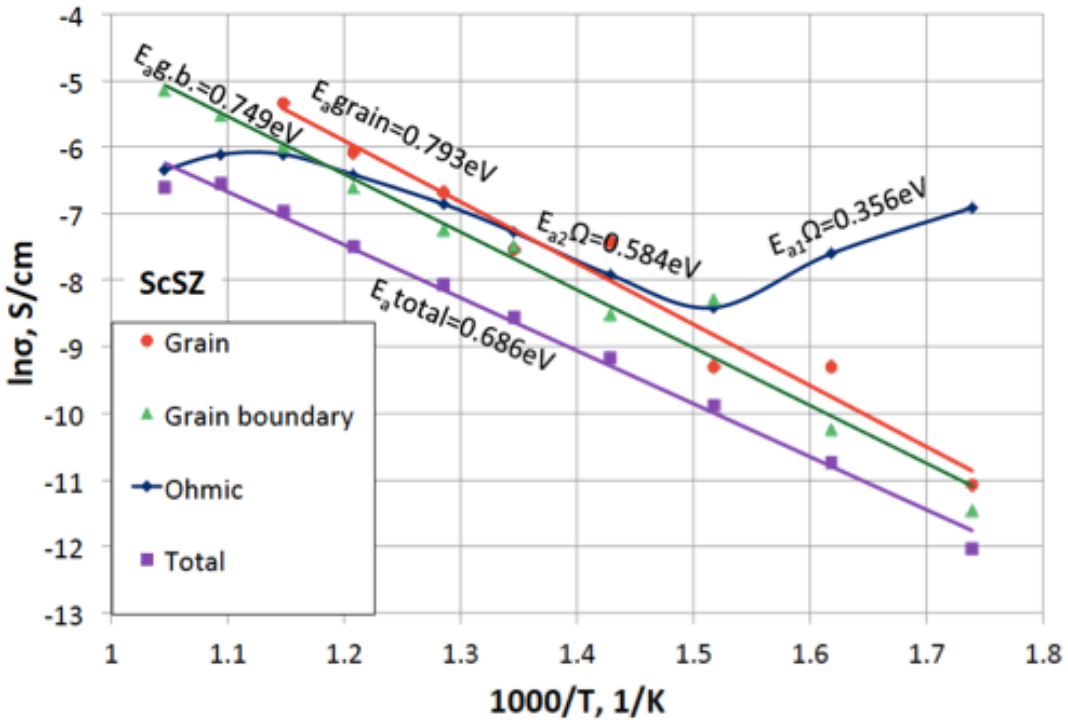

(a)

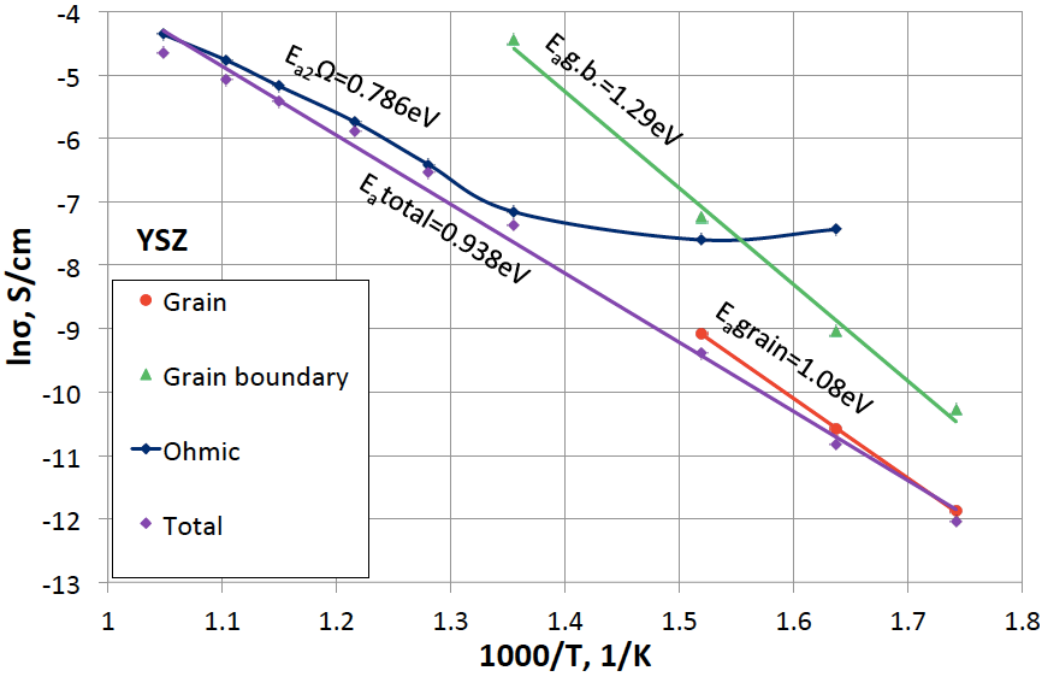

(b)

Figure 7-1: Arrhenius plots of the conductivity of a) 10Sc1CeSZ and b) YSZ

For reference, a sample impedance arc for the 10Sc1CeSZ sample at 345°C is shown in Figure 7-2. The ohmic resistance contributed to the real part (Z') intercept of the impedance data at high frequencies, the total resistance contributed to the real part (Z') intercept of the impedance data at low frequencies, the grain conductivity was ascribed to the size of the arc at the high frequency response (266kHz) and the grain boundary conductivity was associated with the size of the arc at the intermediate frequency response (1.2kHz). The phenomenon behind the third semicircle at the highest frequency of 8.8MHz is as yet still unattributed. Further discussion regarding the equivalent circuit model used for assessing sample conductivity is provided in Chapter 3, Section 3.5.4 with an explanation of the Arrhenius conductivity equation outlined in Chapter 4, Section 4.10. The activation energy (E_a) was obtained by the slope of each fitted line and for the ohmic resistance of the 10Sc1CeSZ samples (blue line) the (E_a) at high temperatures (E_a = 0.584) is different than at low temperatures (E_a = 0.386) which can be related to changes in contact or lead wire resistances. At higher temperatures Ag, which was used to make the connections, softens and sometimes shifts, which can compromise a secure connection. The remaining grain, grain boundary and total conductivity plots for the 10Sc1CeSZ system follows a single line indicating no changes in slope or conduction mechanisms. The overall (E_a) for the samples are listed in Table 7.1 where the total E_a for 10Sc1CeSZ is in close agreement with that reported by previous researchers for 8ScSZ samples in a similar temperature range [1] .

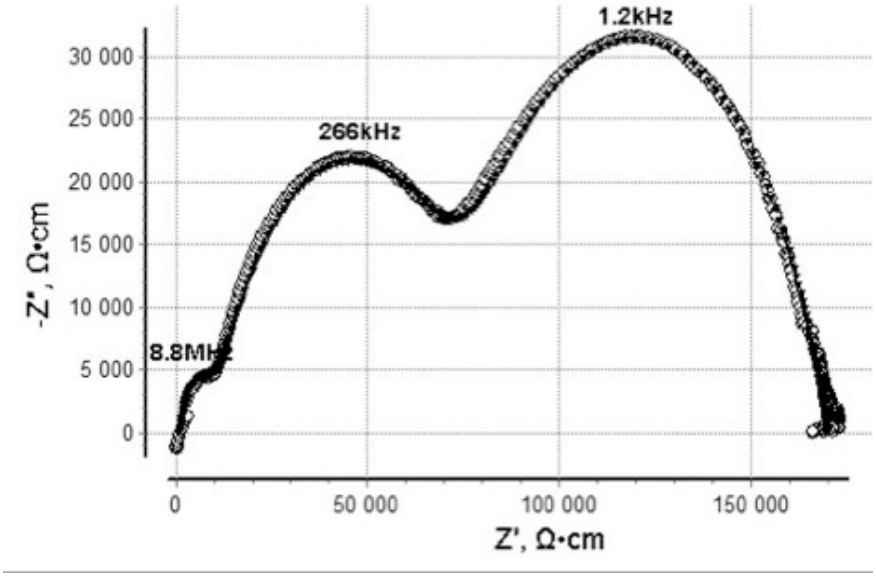

Figure 7-2: Impedance plot of a 10Sc1CeSZ bulk pellet at 345°C

The activation energies for the YSZ samples are all larger than those of the 10Sc1CeSZ samples which is attributed to the enhanced conductivity of 8 mol% Scandia-Zirconia when compared with 8 mol% Yttria-Zirconia as was reported by Yamamoto [2] and Arachi [3]. Both plots illustrate the temperature dependence of the conductivity as oxygen ion mobility increases at higher temperatures. The measured total E_a for YSZ ~ 0.938 was in agreement with values obtained by Fonseca [4]. Examination of the YSZ plot shows that the grain resistance turns to zero by 465°C, which marks the end of the data points. Grain boundary conductivities are plotted up to 500°C without any break in the slope indicating ion migration is primarily through the grain boundaries at intermediate temperature ranges. Beyond 500°C, the resistance measured is attributed only to contact resistance. The disruption in the YSZ plots is not well understood as both grain and grain boundary conductivities were obtained for the 10Sc1CeSZ system across the entire temperature range from 300 – 690°C. However, Kumar et al. suggests that decreases in grain boundary conductivity can be explained by the presence of larger grains which impede oxygen vacancy migration across the grain boundaries [5]. Factors such as grain size, density, impurity levels, intergranular thickness and porosity heavily influence grain boundary conductivity [6]. Guo et al. [7] reports that finer grains enhance grain boundary conductivity by reducing the thickness of negative space charge layers found at the grain boundaries which are formed due to yttrium ion or impurity phase segregation [8]. Doped Y_2O_3-ZrO_2 materials composed of smaller grains which typically have higher surface areas, will reduce impurity concentration at the grain boundaries when compared with doped Y_2O_3-ZrO_2 materials composed of larger grains that have the same impurity content [6], [7], [9]. Less accumulation of impurities in the grain boundary region reduces the formation of intergranular insulating layers and promotes the presence of oxygen vacancies in the space charge region. Thus, ionic conduction across the grain boundaries is enhanced due to improved ZrO_2-ZrO_2 contact and an increase in oxygen vacancy concentration and migration [10]. It is known that cubic zirconia has large grain sizes and experiences high grain growth rates during sintering [11], [12]. The impact of grain growth and larger grains sizes on the conductivity of the sintered bulk YSZ samples may have compromised intergranular contact and oxygen vacancy migration across the grain boundaries causing a disruption in the overall grain boundary conductivity. This can also explain why grain boundary measurements across the entire temperature range were obtained for the 10Sc1CeSZ sample prepared with nanoscale powders. The total conductivities for the YSZ and 10Sc1CeSZ systems at 690°C were 0.0095 $S\,cm^{-1}$ and .0013 $S\,cm^{-1}$ respectively. The measured 10Sc1CeSZ conductivity value is not in agreement with reported values of 0.18 $S\,cm^{-1}$ at 700°C [13] and there is a substantial difference in the measured conductivity for YSZ compared with literature reported values of

Table 7.1: Activation Energies for the 10Sc1CeSZ and YSZ Bulk Samples

	$E_{a\ grain}$, eV	$E_{a\ g.b.}$, eV	$E_{a\ ohmic}$, eV	$E_{a\ total}$, eV
ScSZ	0.793	0.749	0.584-0.356	0.686
YSZ	1.08	1.29	0.786	0.938

~ 0.10 $S\ cm^{-1}$ at 700°C [13]. In addition to the significant difference in the absolute values of the total conductivity, the trend of higher conductivities for the 10Sc1CeSZ samples is also not observed despite the lower total E_a. There is no clear argument for these observations. This study was performed to confirm literature results of improved conductivity with the use of 10Sc1CeSZ while supporting the use of this material to enhance SOFC performance.

7.2 PERFORMANCE OF THE YSZ AND 10Sc1CeSZ SYSTEMS OPERATING ON H_2

7.2.1 Commercial Grade YSZ and 10Sc1CeSZ Cells

In this work, anode supported YSZ and electrolyte supported 10Sc1CeSZ commercial grade cells were tested and served as reference cells to evaluate the reliability of our manufacturing and testing method. More detailed information regarding the commercial grade cells can be found in Chapter 3, Section 3.5.1. Polarisation curves for two commercial grade YSZ cells (YSZ CAS 1, YSZ CAS 2) after 5hrs and 22hrs of operation are presented in Figure 7-3. The standardised testing procedure for cells operating on H_2 is outlined in Chapter 3, Section 3.5.3. Extended time under H_2 shows improved performance for both cells with observed increases in peak power densities from 175 mW cm^{-2} to 218 mW cm^{-2} and from 128 mW cm^{-2} to 160 mW cm^{-2} for YSZ CAS 2 and YSZ CAS 1 respectively. This suggests more H_2 was electrochemically oxidised by both cells under longer exposure in the reducing environment as increased current output enhanced performance. Increased contact time may have further increased anode porosity during reduction as a result of NiO-Ni conversion which helped to promote increased H_2 diffusion, adsorption and conversion [14]. The OCVs of all cells were between 1.0 – 1.12V with minimal changes in cell OCV with extended H_2 residence time suggesting within 5hrs the anode reduction proceeded to completion. And while the NiO-Ni conversion typically occurs within an hour of reduction, further Ni particle reduction and Ni particle reassembly occurred creating a more continuous, interconnected conduction pathway which decreased cell polarisation losses improving performance [14]. The slightly lower OCV for YSZ CAS 1 compared to YSZ CAS 2 is likely due to Ag sealing imperfections though care and attention was given during the Ag application to ensure leak tight seals between the cell and the testing tube were achieved.

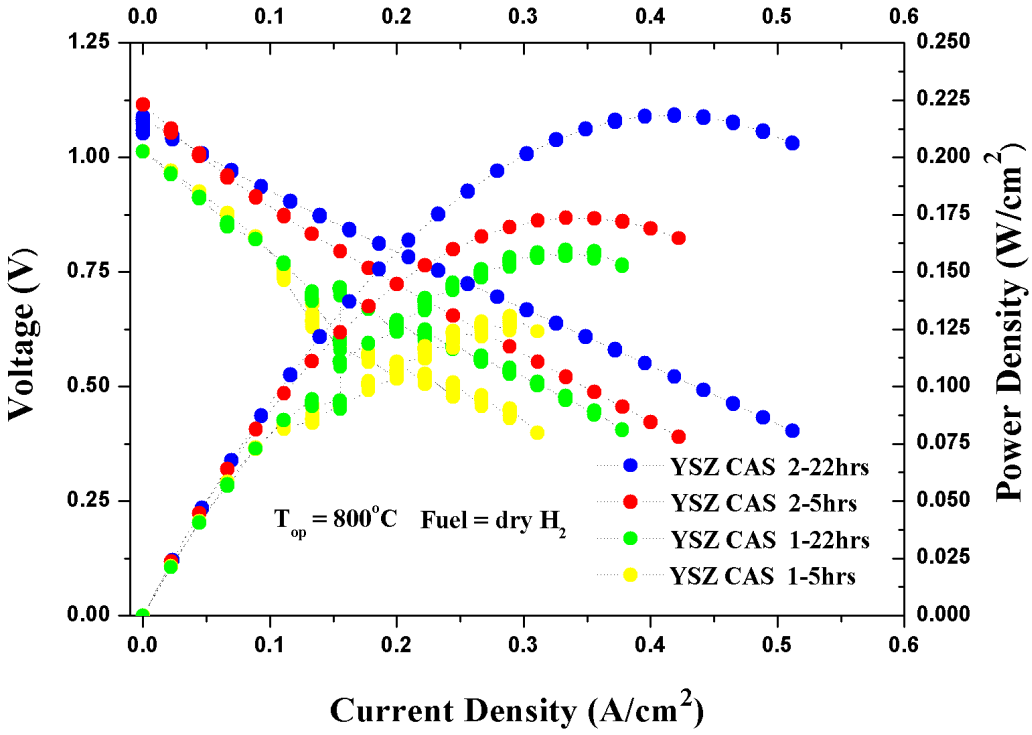

Figure 7-3: SOFC performance of two commercial grade YSZ cells after 5hrs and 22hrs testing on H_2 at 800°C

The OCV of the commercial grade 10Sc1CeSZ cells (10Sc1CeSZ CAS 1, 10Sc1CeSZ CAS 2) were between 1.09 – 1.14V, slightly higher than the OCVs of the commercial grade YSZ cells as seen in Figure 7-4, which indicates both systems contained highly dense electrolyte layers. The improvement in the OCV of the 10Sc1CeSZ cells is likely due to an even denser electrolyte achieved through the bulk ESC design. However, it is also the ESC design that contributes to high electrolyte ohmic losses at lower operating temperatures which necessitates operating temperatures between 850-950°C to offset these losses as discussed in Chapter 1, Section 1.2.2.1 [15]. This explains the relatively low power densities and why the overall performance of the 10Sc1CeSZ cells was nearly half the performance of the anode supported YSZ cells. Also, a direct comparison between the YSZ and 10Sc1CeSZ electrolyte systems and the influence of the higher ionic conductivity of the 10Sc1CeSZ electrolyte on cell performance could not be assessed as two different cell configurations were employed each having markedly different effects on current output which is largely dependent on cell operating temperature. In order to determine whether cell performance can be improved with the substitution of 10Sc1CeSZ for YSZ as the electrolyte, all variables in the cell manufacturing and testing process must remain the same. A direct comparison between the performance of the lab grade YSZ and 10Sc1CeSZ cells can be made as the cell

design, manufacturing approach and testing conditions remained the same. These results will be discussed in Section 7.2.2. Small increases in the peak power density from 102.29 mW cm^{-2} to 107.10 mW cm^{-2} for 10Sc1CeSZ CAS 1 under H_2 operation for 5hrs and 22hrs respectively suggest an improved anode microstructure with increased H_2 contact time as was seen with the commercial YSZ cells which improved mass transport and anode conductivity and enhanced performance. The increased OCV from 1.14V to 1.16V suggests a change in anode microstructure, which supports these findings. Similar results were observed for the 10Sc1CeSZ CAS 2 cells with small increases in the peak power density from 92.78 mW cm^{-2} to 97.48 mW cm^{-2} and OCV increases from 1.09V to 1.11V with extended H_2 residence time. The performance improvements of both the commercial grade YSZ and 10Sc1CeSZ cell sets with time demonstrate cell stability in the testing environment.

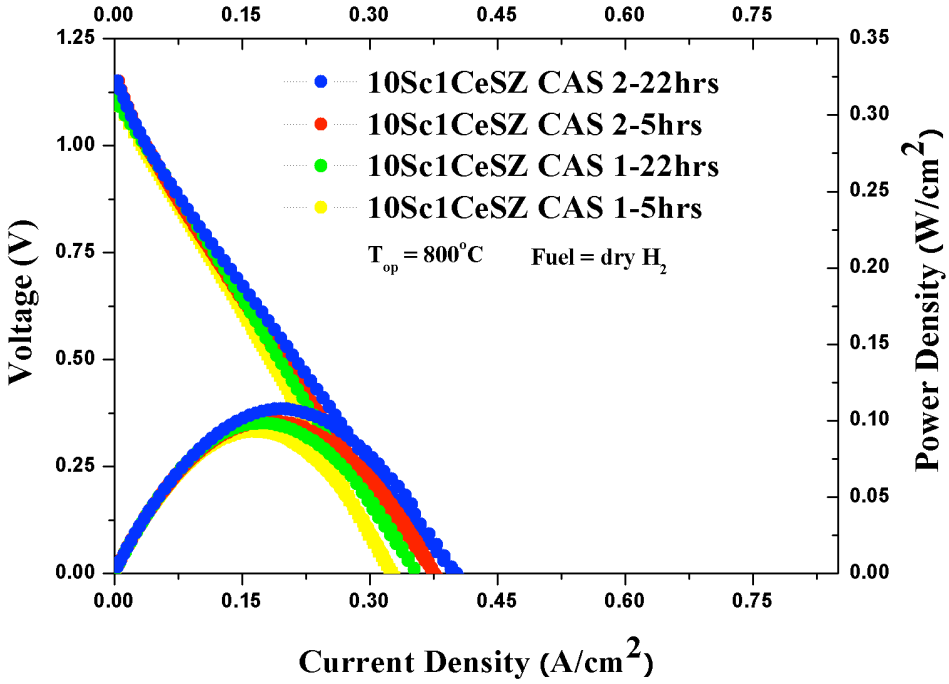

Figure 7-4: SOFC performance of two commercial grade 10Sc1CeSZ cells after 5hrs and 22hrs testing on H_2 at 800°C

7.2.2 Lab Grade YSZ and 10Sc1CeSZ Cells

Lab grade refers to the manufacturing approach employed for the fabrication of anode supported YSZ and 10Sc1CeSZ SOFCs as part of this research study. More information regarding the preparation of these cells can be found in Chapter 3, Section 3.4.2. The performance of the lab grade YSZ (YSZ1, YSZ2) and 10Sc1CeSZ (10Sc1CeSZ1, 10Sc1CeSZ2) cells are presented in Figures 7-5 and 7-6

respectively. The overall performance of the lab grade YSZ cells is comparable to the performance of the commercial grade YSZ cells with peak power densities of 231.96 mW cm^{-2} and 157.77 mW cm^{-2} achieved after 22hrs for cells YSZ2 and YSZ1 respectively. The lower OCV for cell YSZ1 (0.888V) did not result in a drop in performance, on the contrary slight increases in cell performance were observed from 139 mW cm^{-2} to 157.77 mW cm^{-2} with increased residence time under H_2 indicating an improved activity for fuel oxidation. This shows additional time in the reducing environment assisted with H_2 diffusion, consumption and current generation. The anodes of the lab grade YSZ cells had a homogenous, interconnected microstructure consisting of large pores as seen in Figure 5-15 in Chapter 5, Section 5.7.4. This is desirable for fuel transport to the reaction sites and likely contributed to performance values that were comparable to the performance of the commercial YSZ cells despite having consistently lower OCV values. The lab grade YSZ electrolyte film was uniform and dense enough to prevent significant gas leakage through the fine pores observed in the microstructure. The highest performing lab grade YSZ cell did achieve OCV values above 1.0V as discussed later in Section 7.2.3, which suggests the low OCV values for the lab grade YSZ cells seen in Figure 7-5 may also be a result of poor cell to tube sealing which can also contribute to gas leakage bringing down cell OCV.

Repetitive cell tests for the lab grade 10Sc1CeSZ cells revealed consistently low OCV values, indicative of the poor sinterability of the 10Sc1CeSZ electrolyte layer, which resulted in a porous 10Sc1CeSZ microstructure as seen in Figure 6-6 (a) in Chapter 6, Section 6.5.2. These pores were the sites of fuel leakage and responsible for the drop in OCV for the lab grade 10Sc1CeSZ cells when compared against the commercial YSZ and 10Sc1CeSZ and lab grade YSZ cells. Decreases in cell performance were observed for the lab grade 10Sc1CeSZ system with a drop in peak power densities from 120.37 mW cm^{-2} to 101.26 mW cm^{-2} for cell 10Sc1CeSZ1 after 5hrs and 22hrs respectively. 10Sc1CeSZ2 exhibited performance decreases by more than a factor of two from 136.75 mW cm^{-2} to 55.95 mW cm^{-2} after 5hrs and 22hrs respectively. Corresponding decreases in OCV for both cells were also observed. These performance decreases are contrary to what has been observed for cells that remain in the testing environment after 22hrs which means the noticeable difference in electrolyte microstructure for the lab grade 10Sc1CeSZ cells contributed significantly to these performance variations. The rate of fuel crossover through the porous electrolyte exceeded the rate of fuel supply and conversion, which resulted in waste fuel and resistive losses. Extended time under H_2 only exaggerated these losses. The linear shape of the $i - V$ curves for the lab grade 10Sc1CeSZ cells, indicate the predominant loss is attributed to fuel crossover as indicated by the voltage drop which is proportional to current density [16].

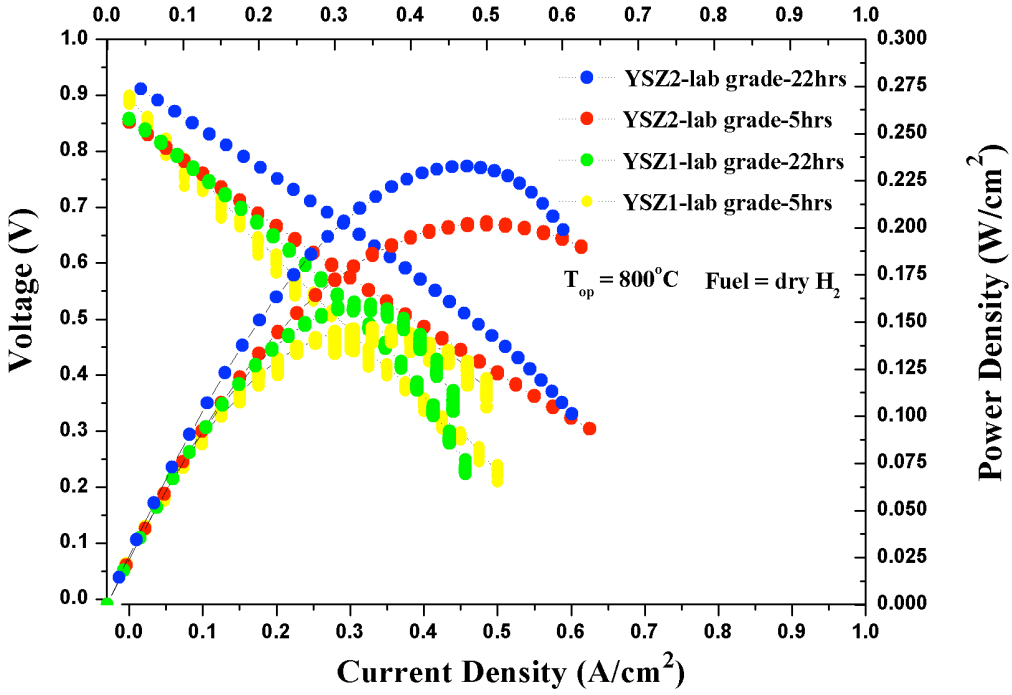

Figure 7-5: SOFC performance of two lab grade YSZ cells after 5hrs and 22hrs testing on H_2 at 800°C

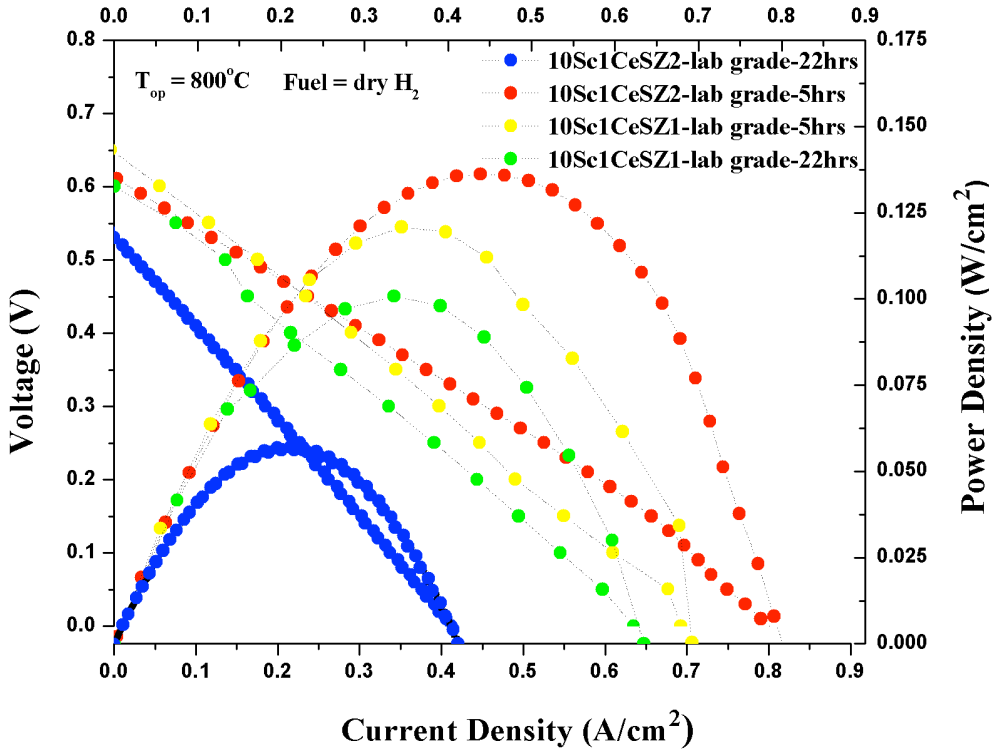

Figure 7-6: SOFC performance of two lab grade 10Sc1CeSZ cells after 5hrs and 22hrs testing on H_2 at 800°C

The notable difference in the performance between the lab grade YSZ and lab grade 10Sc1CeSZ cells show the manufacturing approach employed for the fabrication of the lab grade YSZ cell needs to be better tailored to suit the properties of the 10Sc1CeSZ system. More work is warranted to optimise the ceramic processing route for the 10Sc1CeSZ powders for improved film deposition via screen-printing. These results however demonstrate proof of concept and show the potential use of an IT-SOFC based on a 10Sc1CeSZ structure.

7.2.3 The Highest Performance for the YSZ and 10Sc1CeSZ Cells

Figure 7-7 displays the power density and polarisation curves for the lab grade and commercial grade YSZ and 10Sc1CeSZ cells that exhibited the highest performance of all tested cells. The lab grade YSZ and 10Sc1CeSZ cells were fabricated using best practice for manufacturing with performance results for tested cells in this batch obtained employing the most improved electrochemical testing method. The OCV for both the commercial YSZ and 10Sc1CeSZ cells was 1.03V and 1.15V respectively. Fuel leakage via the contact area between the cell and the testing tube due to poor sealing is assumed responsible for this OCV difference as OCVs upwards of 1.12V for commercial YSZ cells have been achieved previously. And while the OCV of the YSZ lab grade cell achieved a slightly higher OCV than the commercial grade cell of 1.06V, indicative of an improved cell sealing procedure, the relatively high current output for both cells confirmed the appropriateness of screen-printing as a manufacturing method and the reliability of the testing technique. More noticeable differences in cell performance can be seen with peak power densities of 466 mW cm^{-2} exhibited by the commercial grade YSZ cell whereas the lab grade YSZ, lab grade 10Sc1CeSZ and commercial grade 10Sc1CeSZ cells had maximum power densities of 392 mW cm^{-2}, 171 mW cm^{-2} and 90 mW cm^{-2} respectively. For ease of comparison the performance data for these cells is also listed in Table 7.2. And while peak power densities are oftentimes used to evaluate cell performance as this value indicates the maximum available power per unit area for a given cell, cells will never operate at maximum power density conditions because this means operation at low cell voltages and thus low cell efficiencies. It is typical practice to designate operating voltages to the left of the maximum power density curve (0.6 – 0.7V) where cell efficiency is high and current densities are low. For a good comparison of SOFC performance, power density as it relates to cell efficiency and the concept of area specific resistance (ASR) are both quite useful.

The area specific resistance (ASR) of the tested commercial grade and lab grade YSZ and 10Sc1CeSZ cells shown in Figure 7-7 was calculated using Equation 7.2 [14] where:

$$ASR = \frac{OCV - 0.45}{I_{0.45}} \qquad (7.2)$$

OCV is the open circuit voltage and $I_{0.45}$ is the current density at 0.45V. The ASR calculation is usually taken at low current densities (0.5 - 0.7V) such that the voltage losses over the full ohmic polarisation range can be determined.

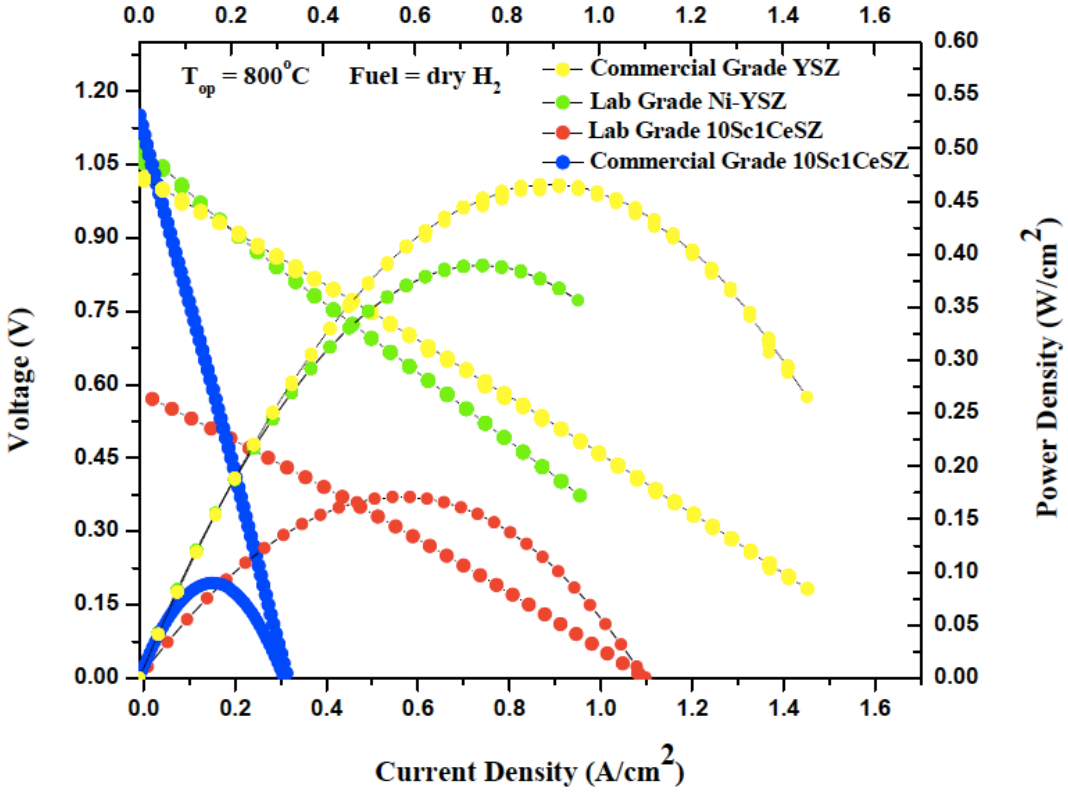

Figure 7-7: SOFC performance curves of lab grade and commercial grade YSZ and 10Sc1CeSZ cells after 22hrs testing on H_2 at 800°C

Table 7.2: Electrochemical Performance for YSZ and 10Sc1CeSZ Cells at 800°C After 22hrs

Performance	Commercial Grade YSZ	Lab Grade YSZ	Lab Grade 10Sc1CeSZ	Commercial Grade 10Sc1CeSZ
OCV (V)	1.035	1.06	0.587	1.15
PD_{max} (W cm^{-2})	0.466	0.392	0.171	0.090
ASR at 0.45V (Ω cm^2)	0.590	0.732	0.496	3.628
U_f at PD_{max}	25.37%	23.78%	19.03%	4.76%

In this case, the ASR of the cells was calculated at an operating voltage of 0.45V so the cell performances were directly comparable as the maximum OCV of the 10Sc1CeSZ cell was only 0.587V. The ASR values were 0.590 Ω cm^2, 0.732 Ω cm^2, 0.496 Ω cm^2 and 3.628 Ω cm^2, for the commercial grade YSZ, lab grade YSZ, lab grade 10Sc1CeSZ and commercial grade 10Sc1CeSZ cells respectively. Despite ASR values that exceed the acceptable value of 0.15 Ω cm^2 reported in literature [3], these results can still be used as a relative comparison of performance between cells. The increasing ASR values are in agreement with the decrease in peak power densities, though the lowest ASR value was obtained for the 10Sc1CeSZ cell despite fuel crossover via the non-dense 10Sc1CeSZ electrolyte, which limited cell potential. As the lab grade 10Sc1CeSZ cell exhibited the lowest ASR, this is indicative of lower internal electrolyte and electrode resistances as well as lower electrode-electrolyte interfacial and electrode-current collector contact resistances when compared against the other tested cells. The performance limitations associated with the lab grade 10Sc1CeSZ cell were primarily related to gas permeability via the "leaky" 10Sc1CeSZ electrolyte which suggests that if the $i - V$ curve were corrected for OCV to reflect a gas-tight 10Sc1CeSZ electrolyte, the lab grade 10Sc1CeSZ cell would outperform the YSZ system for both the commercial and lab grade cells. This assumption strongly considers ASR values as a predictor of cell performance when interpreting SOFC test data. These results represent an element of success for the 10Sc1CeSZ system and demonstrate the feasibility of an IT-SOFC based on a 10Sc1CeSZ structure.

The higher performance of the commercial grade YSZ cell compared to the lab grade YSZ cell is indicative of optimised commercial processes for the anode supported tape casted cells. The ASR values of 0.569 Ω cm^2 and 0.720 Ω cm^2 at 0.7V for the commercial grade YSZ and lab grade YSZ cells respectively, support these findings. Figure 7-7 shows an increase of 200 mW cm^{-2} in the maximum power densities of the highest performing commercial and lab grade YSZ cells when compared against the power densities of previously tested commercial and lab grade YSZ cells shown in Figures 7-3 and 7-5 respectively. This is due to enhanced current collection at the electrodes due to better contacting via improved Ag paste application as well as minor differences during cathode painting causing slight variations in effective cathode area. As these steps in the cell manufacturing process are not automated, human error will create subtle differences between cells, which can result in notable changes in cell performance. Thus, optimisation of the manufacturing process is necessary to minimise these differences.

As discussed previously, the reduction in the peak power for the commercial grade 10Sc1CeSZ cell by a factor of five is explained by the ESC configuration which requires higher operating temperatures to

yield performance results comparable to those observed for the anode supported Ni-YSZ cell within this intermediate temperature regime. And although the lab grade 10Sc1CeSZ system only attained an OCV of 0.587V, peak power densities close to twice those seen for the commercial 10Sc1CeSZ cell and nearly one third of what was observed for the commercial YSZ system were achieved. Repeated tests show stable operation for both the YSZ and 10Sc1CeSZ systems but consistently low OCVs were seen for the lab grade 10Sc1CeSZ cells which suggested porous electrolyte layers and fuel crossover compromising the oxygen partial pressures at the electrodes driving down cell potential. An examination of the 10Sc1CeSZ microstructure shown in Figure 6-6 (Chapter 6, Section 6.5.2) shows the large pores and interconnected porosity in the electrolyte layer, which supports these findings. This demonstrates a potential for improved cell performance once the manufacturing approach for the 10Sc1CeSZ electrolyte densification is standardised.

7.2.4 Impedance Spectroscopy of the Lab Grade YSZ and 10Sc1CeSZ Cells

Figure 7-8 shows Nyquist plots of the tested lab grade YSZ and 10Sc1CeSZ cells presented in Figure 7-7. The high frequency intercept of the curve with the real axis gives the value of the ohmic resistance (R_{ohm}) that includes electrolyte resistance, lead wire resistances and the overall internal resistance of the cell. The R_{ohm} for the lab grade YSZ cell (0.117 Ω cm^2) is lower than the R_{ohm} for the 10Sc1CeSZ cell (0.748 Ω cm^2) which suggests a lower conducting 10Sc1CeSZ electrolyte compared to YSZ and an overall higher internal cell resistance which is in agreement with the performance data provided in Figure 7-7. The total resistance (R_{tot}) for the YSZ cell at 0.170 Ω cm^2 is also lower than that of the 10Sc1CeSZ cell at 1.28 Ω cm^2. These results assume better ionic conductivity and better electrochemical performance for the YSZ cell when compared with the 10Sc1CeSZ cell. This is unexpected as 10Sc1CeSZ has a higher conductivity than YSZ but does agree with the performance data. For YSZ, there appears to be a single defined and dominant arc at high frequency with minimal contributions at low frequency indicating the impedance is most likely related to charge transfer reactions limiting the electrochemical process. For 10Sc1CeSZ, there are two distinct large arcs, one at high frequency and one at low frequency, which may be the result of both mass transport and charge transfer limitations to the measured impedance. The overall sizes of the impedance arcs widen with the 10Sc1CeSZ cell which may indicate some increase in electrode polarisation compared to the YSZ cell [17].

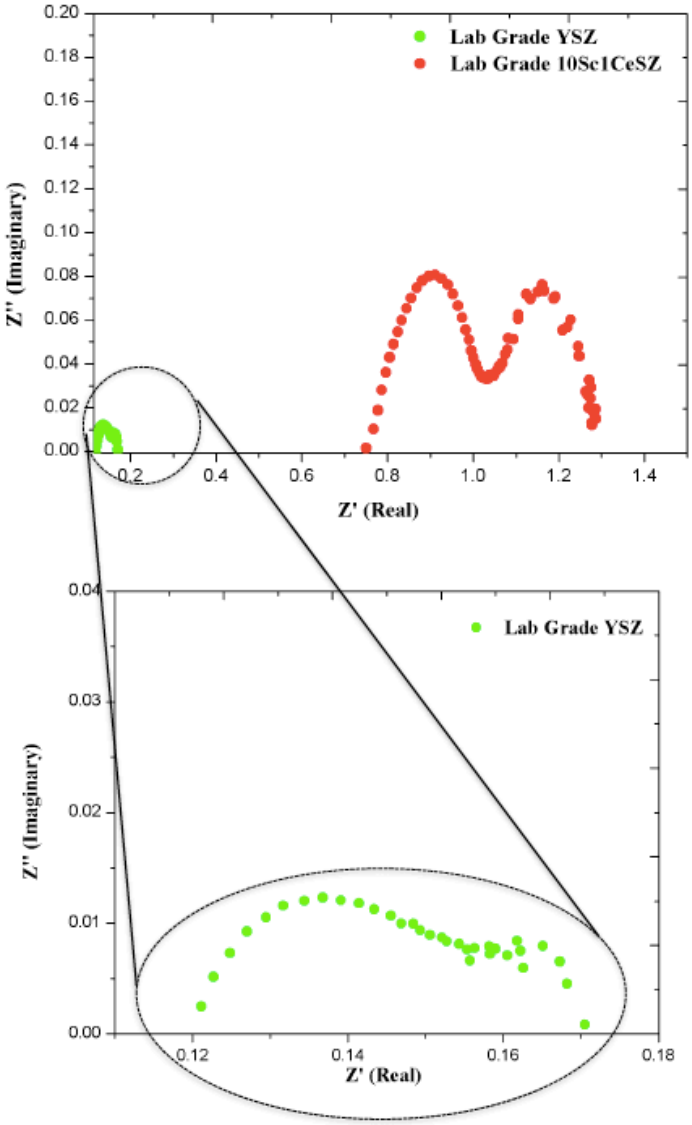

Figure 7-8: Nyquist plots for the lab grade YSZ and 10Sc1CeSZ cells

7.2.5 3D Microstructure Reconstruction of a Lab Grade Ni-10Sc1CeSZ Cell

3D image acquisitions via FIB-SEM for the reduced Ni-10Sc1CeSZ anode of the tested 10Sc1CeSZ cell presented in Figure 7-7 were obtained via the EPFL fuel cell laboratory. Quantifications were done on a sub volume sample shown in Figure 7-9 (b) due to difficulty in segmentation of the original sample volume shown in Figure 7-9 (a). The sub-volume analysis indicated a composition of 38.6% Ni, 22.9% 10Sc1CeSZ and 38.50% porosity with analysis of the solid portion at 62.8% Ni and 37.2% 10Sc1CeSZ. It can be seen in Figure 7-9 (b), the Ni particles are rather large and do not percolate. There appears to be rims around the Ni where the 10Sc1CeSZ grains gather but contact is lost which may

be brought about by the sintering or reduction process. A pre-reduction 3D analysis could have further confirmed this assumption. Figure 7-10 yields a better visualisation showing the large Ni grains, the relatively high porosity and the non-homogeneous distribution of the phases throughout the sample.

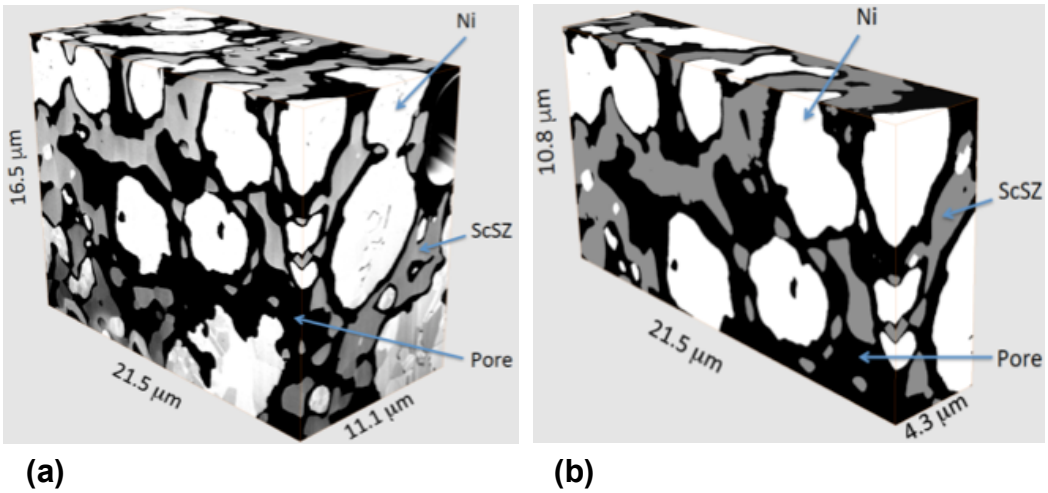

Figure 7-9: 3D microstructure of a reduced Ni-10Sc1CeSZ anode post testing in the original sample volume

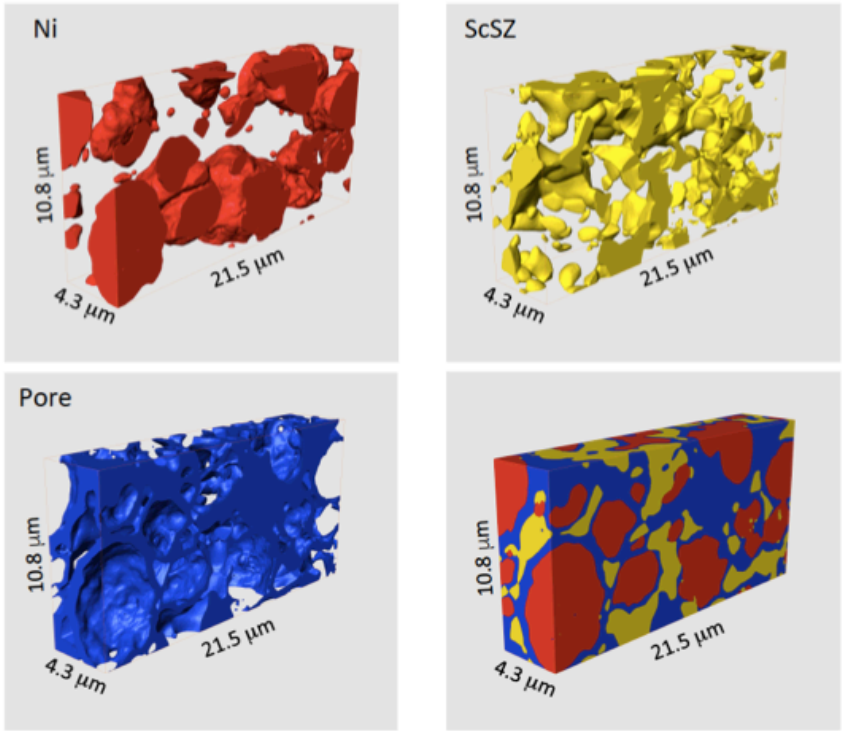

Figure 7-10: 3D microstructure of the Ni, 10Sc1CeSZ and pore phases in the sub volume cut

7.3 PERFORMANCE OF THE 0.55 mol% Al_2O_3-10Sc1CeSZ CELL

On the basis of the densification study outlined in Chapter 6, Sections 6.9.2, 6.9.3 and 6.9.4 where 0.55 mol% Al_2O_3 dopant additions were shown to improve the densification of the 10Sc1CeSZ electrolyte film, cell tests were performed to analyse the electrochemical performance of the doped samples. Power density curves are provided in Figure 7-11. Performance data for three cells prepared with screen-printed Al_2O_3-10Sc1CeSZ electrolyte films sintered at 1375°C-4hrs and 1425°C-4hrs respectively were obtained. These cells were chosen for testing, as the 1425°C-4hrs cell possessed the best microstructure of all the 0.55 mol% Al_2O_3-10Sc1CeSZ samples with the 1375°C-4hrs sample showing enhanced densification at a lower sintering temperature. The performance results of cell Al_2O_3-10Sc1CeSZ3 (5hrs) 1425°C-4hrs and a repeat test of cell Al_2O_3-10Sc1CeSZ2 are also given. For ease of comparison, the electrolyte microstructures are shown again in Figure 7-12. The Al_2O_3-10Sc1CeSZ2 and Al_2O_3-10Sc1CeSZ3 cells fired at 1425°C-4hrs exhibited the highest OCVs of 0.968V, 0.939V and 1.045V after 5hrs and 22hrs on H_2 for cell Al_2O_3-10Sc1CeSZ2 and 5hrs on H_2 for cell Al_2O_3-10Sc1CeSZ3 respectively. The Al_2O_3-10Sc1CeSZ1 cells fired at 1375°C-4hrs only had OCVs of 0.609V and 0.588V after 5hrs and 22hrs respectively. This OCV decrease is due to leakage via pinholes and pores in the electrolyte layer. Based on the promising OCV results of cell Al_2O_3-10Sc1CeSZ2 obtained during testing which only later revealed poor current output, cell Al_2O_3-10Sc1CeSZ3 (5hrs) was prepared.

Cell Al_2O_3-10Sc1CeSZ3 (5hrs) was prepared and intended for performance testing for 22hrs but initial analysis during testing showed relatively low current output so the remaining half of the test was terminated. The low current output for all of the Al_2O_3-10Sc1CeSZ cells can only be explained by possible segregation of Al_2O_3 at the grain boundaries which has been shown to occur when the solubility limit of Al_2O_3 has been exceeded [18]. This accumulation of Al_2O_3 at the grain boundaries can retard grain boundary diffusion [18] and hinder electrolyte grain boundary conductivity [19], [20]. And while our phase stability results do not indicate the formation of a separate Al_2O_3 phase for the 0.55 mol% Al_2O_3 dopant concentration and literature reports Al_2O_3 additions up to 1 mol% show fully stabilised cubic phase with no adverse effect on 10Sc1CeSZ conductivity [21], the distribution of Al_2O_3 throughout the 10Sc1CeSZ structure could have an influence on conductivity though the specific reason is not clear. The low OCV of cell Al_2O_3-10Sc1CeSZ1 has less to do with Al_2O_3 segregation and is more likely due to the low sintering temperature, which was insufficient for achieving a dense electrolyte film. The higher current outputs for the Al_2O_3-10Sc1CeSZ2 and Al_2O_3-10Sc1CeSZ3 cells are due to the improvement in

the electrolyte densities as indicated by the higher OCVs. The highest peak performance of 40 mW cm^{-2} was achieved for cell Al_2O_3-10Sc1CeSZ3 with the highest OCV.

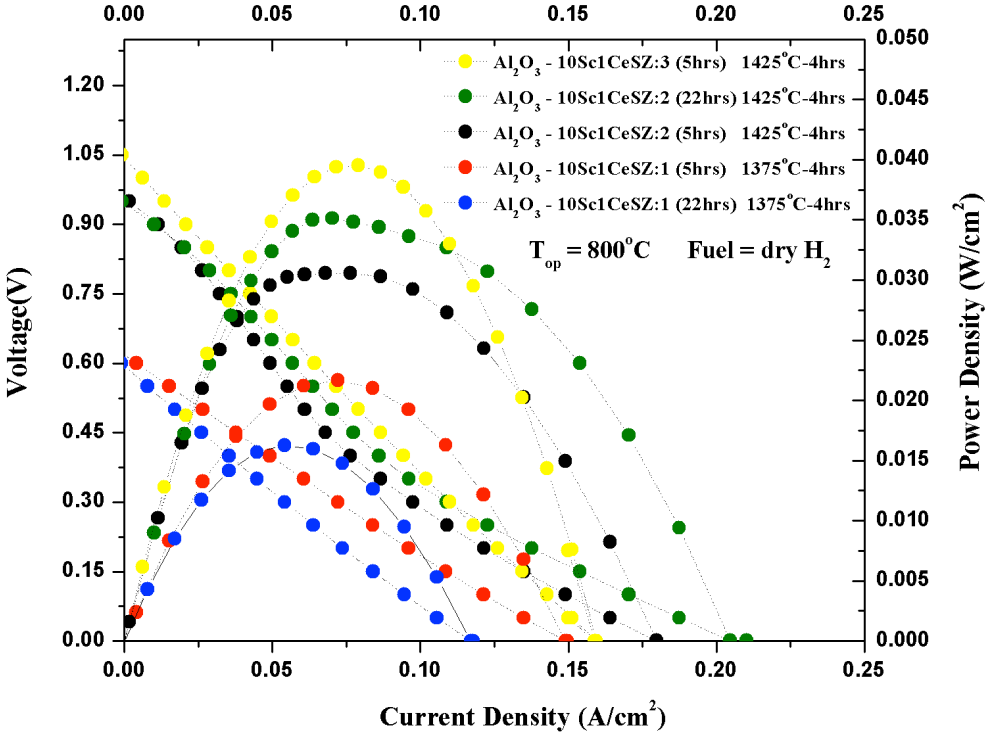

Figure 7-11: Polarisation curves for the 0.55 mol% Al_2O_3-10Sc1CeSZ cells after 5hrs and 22hrs testing on H_2 at 800°C

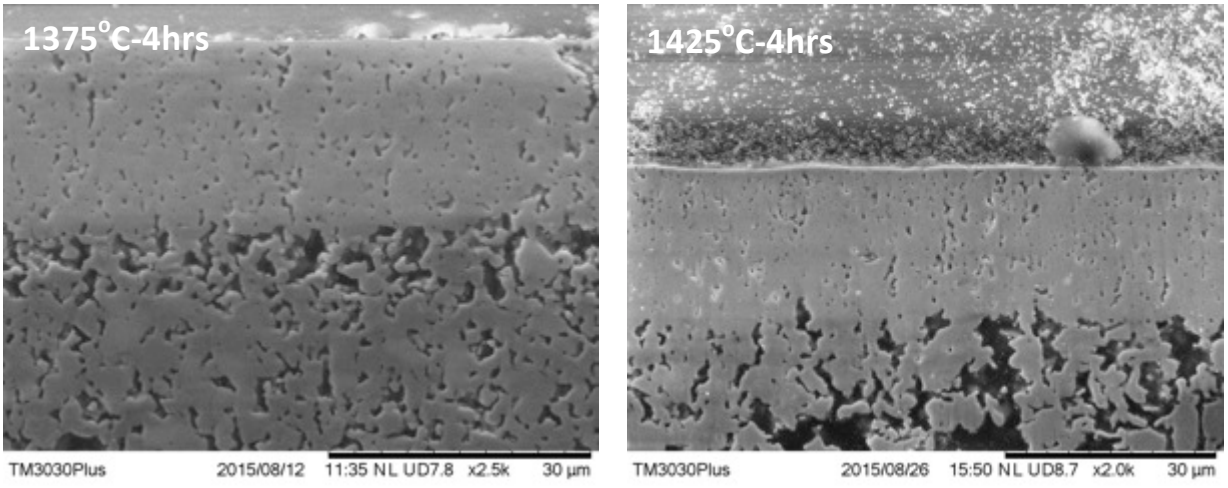

Figure 7-12: SEM microstructures of the 0.55 mol% Al_2O_3-10Sc1CeSZ electrolyte films at different sintering conditions

7.4 PERFORMANCE OF THE LAB GRADE YSZ AND 10Sc1CeSZ CELLS OPERATING ON SIMULATED BIOGAS - CH_4:CO_2

Eleven batches of YSZ and 10S1CeSZ lab grade cells were fabricated and tested at 750°C and 800°C under H_2 and CH_4:CO_2. Multiple cells were prepared to assess the reliability of the performance data though no manufacturing differences existed between the cell batches. The cell batch designation, i.e. Cell Batch 1… Cell Batch 2… etc. denotes the order in which the cells were tested. Further details regarding the test conditions can be found in Chapter 3, Sections 3.5.3 and 3.5.5. More information about the established testing procedure for simulated biogas fuelled SOFCs can be found elsewhere [22]. The OCVs of YSZ and 10Sc1CeSZ tested cells operating on H_2 after 5hrs and CH_4:CO_2 after 2hrs at 750°C under fuel flow rates of H_2:He 21:7 ml min^{-1} and CH_4:CO_2:He 14:7:7 ml min^{-1} are shown in Figures 7-13 (a) and 7-13 (b) respectively. A compiled list of the tested samples, the cell operating conditions and the corresponding OCV values can be found in Table 7.3. The cells remained in OCV mode for 2hrs under CH_4:CO_2 after the change from H_2 to CH_4:CO_2 to allow cell stabilisation in the new fuel environment and to purge any remaining H_2 from the system. OCV data for YSZ and 10Sc1CeSZ Cell Batch 1 and YSZ Cell Batch 6 could not be obtained due to test equipment malfunctions and OCV

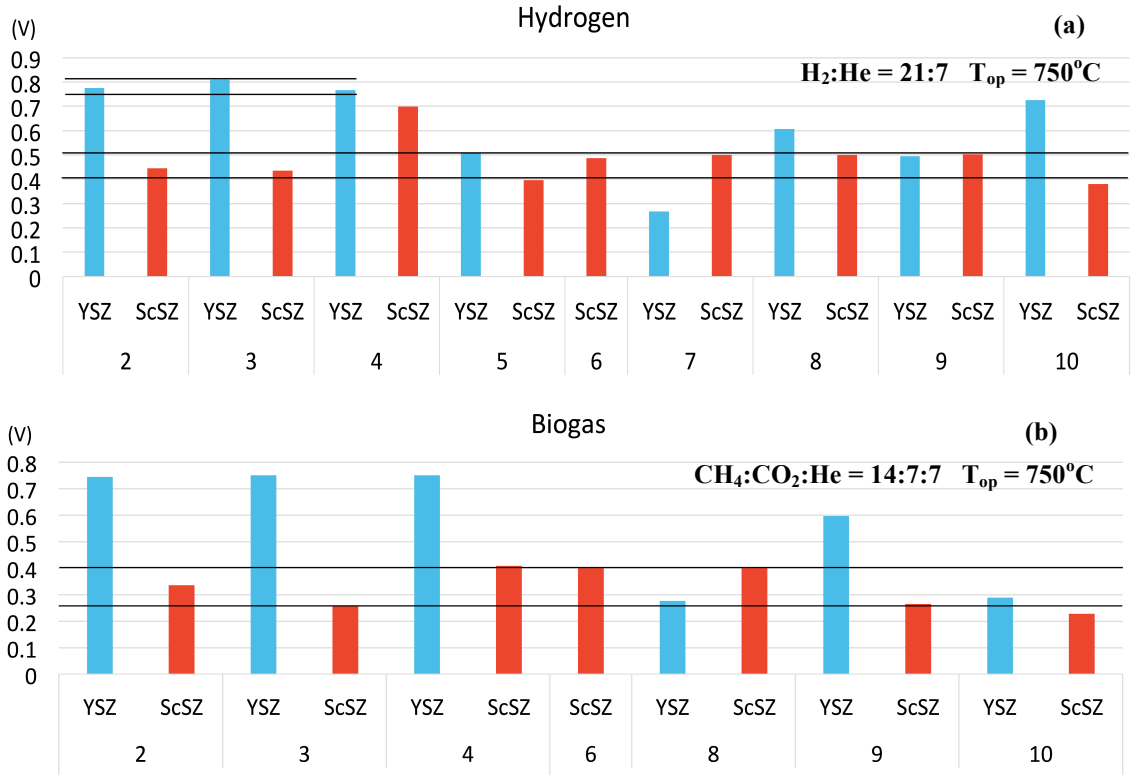

Figure 7-13: (a) Initial OCV values for YSZ and 10Sc1CeSZ tested cells operating on hydrogen after 5hrs and (b) biogas after 2hrs at 750°C

Table 7.3: Test Conditions and OCV Values for the Lab Grade YSZ and 10Sc1CeSZ Cells

Cell	OCV (V) H_2:He, 21:7 ml min^{-1} after 5hrs, 750°C	OCV (V) CH_4:CO_2:He, 14:7:7 ml min^{-1} after 2hrs, 750°C	OCV (V) H_2:He, 63:7 ml min^{-1} after 5hrs, 800°C	OCV (V) CH_4:CO_2:He, 42:21:7 ml min^{-1} after 5hrs, 800°C
YSZ Batch 2	0.775	0.744		
YSZ Batch 3	0.809	0.75		
YSZ Batch 4	0.763	0.750		
YSZ Batch 5	0.506	N/A		
YSZ Batch 7	0.267	N/A		
YSZ Batch 8	0.606	0.276		
YSZ Batch 9	0.494	0.596		
YSZ Batch 10	0.726	0.288		
YSZ Batch 11			0.682	0.679
10Sc1CeSZ 2	0.445	0.335		
10Sc1CeSZ 3	0.435	0.257		
10Sc1CeSZ 4	0.698	0.408		
10Sc1CeSZ 5	0.396	N/A		
10Sc1CeSZ 6	0.486	0.403		
10Sc1CeSZ 7	0.500	N/A		
10Sc1CeSZ 8	0.500	0.403		
10Sc1CeSZ 9	0.502	0.264		
10Sc1CeSZ 10	0.380	0.227		
10Sc1CeSZ 11	0.380		0.662	0.235

data for YSZ and 10Sc1CeSZ cell batches 5 and 7 on biogas were not obtained due to the poor electrochemical performance on H_2. The overall OCVs for both cell systems under H_2 operation were lower than what was previously reported due to the lower fuel feed flow rates. Lower fuel flow rates were used for the biogas tests so biogas could be introduced into the system gradually to monitor cell response. Flooding the cells with too much biogas fuel at the beginning can lead to early carbon formation causing a rapid decrease in performance resulting in immediate cell failure. Baseline H_2 cell performance tests were carried out first to determine whether tests would proceed on CH_4:CO_2 so lower fuel flow rates were used for the hydrogen tests to keep the molar ratio of reactant gas the same. The higher OCVs obtained with previously tested cells on H_2 under flow rates of 60 ml min^{-1} was expected since OCV is influenced by the oxygen partial pressure differences at the electrodes with greater pressure from higher fuel flow rates further increasing this difference. Better sealing onto the Al_2O_3 tubes and a more controlled cell manufacturing process, which yielded consistently denser electrolyte films, would also explain the higher OCVs of the previously tested cells. For the biogas tests, when switching from

H_2 to CH_4:CO_2, the observed decreases in OCV can be explained by poor fuel oxidation and low H_2 and CO conversion leading to higher oxygen partial pressures at the anode. The competing reactions (1) – (4) [23] that occur during the electrochemical oxidation of biogas also impact system pressure and temperature, both of which influence OCV.

$$\boldsymbol{CH_4 + CO_2 \rightarrow 2CO + 2H_2} \quad \textbf{(1)}$$
$$\boldsymbol{H_2 + O^{2-} \rightarrow H_2O + 2e^-} \quad \textbf{(2)}$$
$$\boldsymbol{CO + O^{2-} \rightarrow CO_2 + 2e^-} \quad \textbf{(3)}$$
$$\boldsymbol{CH_4 + O^{2-} \rightarrow CO + 2H_2 + 2e^-} \quad \textbf{(4)}$$

Extended residence time in the reducing environment (the cells operate on H_2 for 22hrs before CH_4:CO_2 is introduced) allows for more fuel crossover if there are cracks in the single cell system, which may also explain this decrease. For YSZ Cell Batch 9 however, an increase in OCV from 0.494V to 0.596V was observed when the reactant gas was switched from H_2 to CH_4:CO_2. This increase in OCV is likely linked to an increase in H_2 concentration brought about by improved fuel oxidation and possible changes in system pressure due to anode microstructural changes brought about by NiO-Ni reduction. The current density and power density values for these cells operating on H_2 and CH_4:CO_2 are shown in Figures 7-14 (a) and (b) respectively. Cell current density comparisons were obtained at 0.3V as the highest OCV achieved for the 10Sc1CeSZ cells was 0.5V. The current density and power density values of YSZ and 10Sc1CeSZ Cell Batches 8, 9 and 10 are featured because of all cells tested, these are the only cells that generated electrochemical performance data on both H_2:He and CH_4:CO_2:He fuels for which direct comparisons could be made. The peak power densities for both systems on hydrogen and biogas were rather modest with YSZ Cell Batch 8 exhibiting the highest peak power density of 95.16 mW cm^{-2} on H_2 for all tested systems as YSZ consistently outperformed 10Sc1CeSZ on both hydrogen and biogas. The decrease in power density on biogas relative to hydrogen for both YSZ and 10Sc1CeSZ SOFCs could be directly related to CH_4 being a heavier molecule than H_2 making fuel diffusion to the reactant sites sluggish resulting in increased concentration polarisation. Poor biogas oxidation leaving low levels of available H_2 and CO followed by the poor electrochemical oxidation of these reactant gases resulting in low current output may have also contributed. And while H_2 is the most active species for electrochemical oxidation, the electrochemical oxidation of biogas results in carbon formation over Ni-based anodes through reaction (1) via the Boudouard reaction as seen in reaction (5). These carbon deposits can block active sites on the Ni surface reducing anode catalytic activity for fuel oxidation and inhibit fuel diffusion both of which increase anode polarisation. While the simulated biogas composition

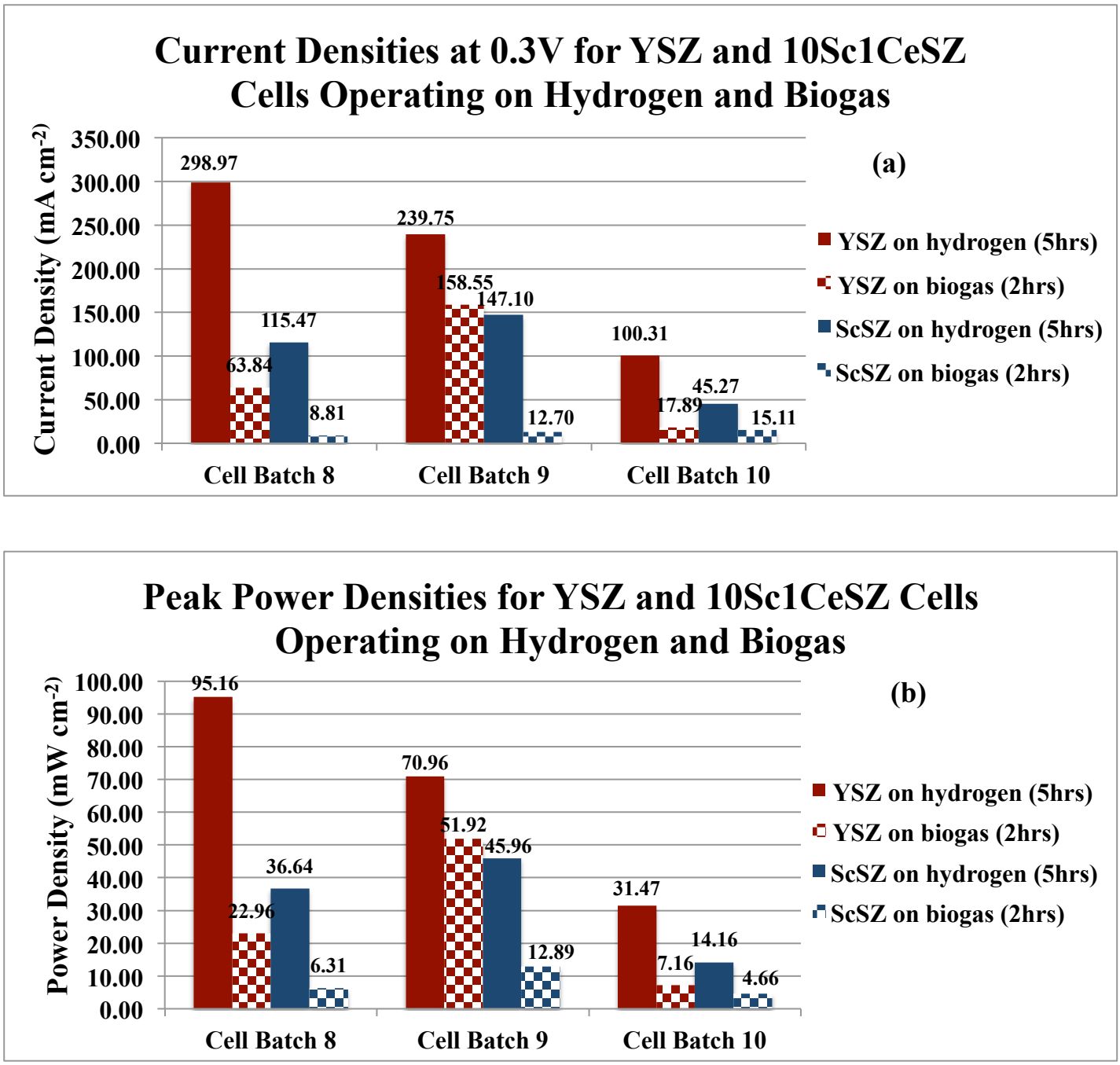

Figure 7-14: (a) Current Densities at 0.3V for YSZ and 10Sc1CeSZ tested cells operating on H_2 and CH_4:CO_2 at 750°C (b) Peak Power Densities for YSZ and 10Sc1CeSZ tested cells operating on H_2 and CH_4:CO_2 at 750°C

was expected to cause coking, no carbon was visible on the anode supports or inside the fuel inlet tubes post testing. Further work to investigate the effectiveness of 10Sc1CeSZ anodes for minimising carbon deposition under hydrocarbon operation is warranted.

$$2CO_{(ads)} \rightarrow C_{(ads)} + CO_2 \quad (5)$$

Low cell performance for the 10Sc1CeSZ cells when compared against the YSZ cells is not only due to poor fuel oxidation but also fuel crossover via the poorly dense 10Sc1CeSZ electrolyte as seen in Figure 7-15 (d) – (f) for 10Sc1CeSZ Cell Batch 8, 9 and 10 respectively making less supply fuel available. The denser YSZ electrolyte layer as shown in Figure 7-15 (a) – (c) for YSZ Cell Batch 8, 9 and 10 respectively give rise to the higher OCV values for the YSZ cells though cracks through the cathode marked with red arrows can explain the lower observed performances for Cell Batch 9 and 10.

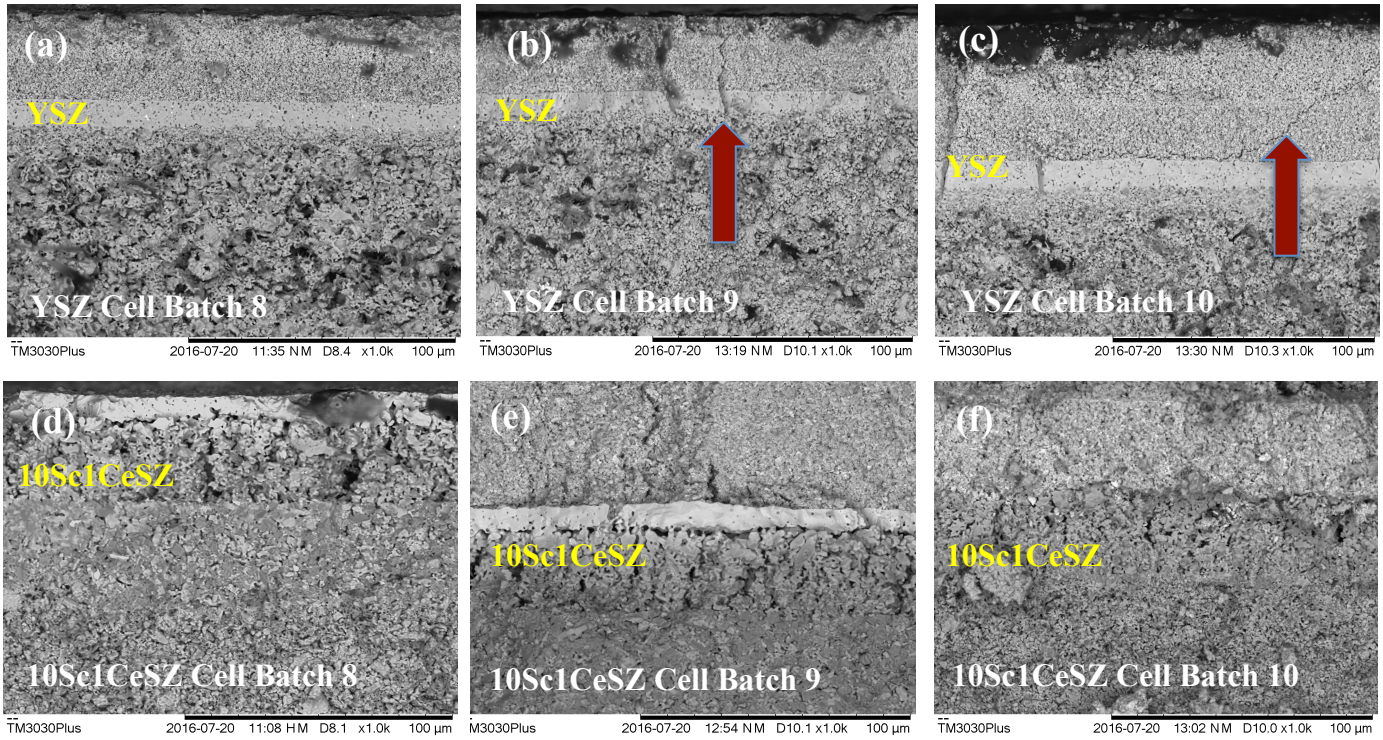

Figure 7-15: SEM fracture surfaces of post-tested (a) YSZ Cell Batch 8 (b) YSZ Cell Batch 9 (c) YSZ Cell Batch 10 (d) 10Sc1CeSZ Cell Batch 8 (e) 10Sc1CeSZ Cell Batch 9 (f) 10Sc1CeSZ Cell Batch 10 all after operation on H_2 and CH_4:CO_2 at 750°C

These preliminary results prompted an additional set of performance tests for the YSZ and 10Sc1CeSZ cells operating at 800°C and at a higher fuel flow rate of 70 ml min^{-1} with fuel feed mixtures of 63H_2:7He and 21CO:42CH_4:7He for hydrogen and biogas respectively. The objective was to enhance performance via an increased fuel supply and promote improved reaction kinetics at higher operating temperatures. Figures 7-16 and 7-17 show the performances of the YSZ and 10Sc1CeSZ cells respectively under these

new testing conditions.

The SOFC performance of YSZ and 10Sc1CeSZ after 5hrs on H_2 are comparable with peak power densities of 180.62 mW cm^{-2} and 179.97 mW cm^{-2} for YSZ Cell Batch 11 and 10Sc1CeSZ Cell Batch 11 respectively. YSZ Cell Batch 11 exhibits performance increases with extended residence time in H_2 reaching peak power densities of 200.09 mW cm^{-2} after 22hrs. For the 10Sc1CeSZ Cell Batch 11 however, increases in ASR from 0.638 Ω cm^2 to 0.967 Ω cm^2 at 0.45V are observed after 5hrs and 22hrs respectively for H_2 operation. The performance degradation is likely related to activation-polarisation losses brought about by reduced reactant concentrations (low fuel utilisations) as a result of the non-dense 10Sc1CeSZ electrolyte. The OCV decrease to 0.479V after 22hrs suggests further cell cracking and even greater fuel leakage. Initial OCV values reached upwards of 0.662V on H_2 for 10Sc1CeSZ Cell Batch 11 with large drops observed when the supply fuel was switched to biogas. The OCV for YSZ Cell Batch 11 did decrease for the 800°C operating temperature with only slight decreases in OCV from 0.682V to 0.655V throughout the entire test run on H_2, which suggests cell stability even with seal leaks and a non-fully dense electrolyte as the OCV was significantly lower than theoretical values. The higher OCV for YSZ Cell Batch 11 when compared with 10Sc1CeSZ Cell Batch 11 on biogas is likely related to a reduction in oxygen partial pressure due to a greater concentration of H_2 and CO species. Both the YSZ and 10Sc1CeSZ Cell Batch 11 cells demonstrate a high resistance for fuel oxidation under biogas operation with much lower peak power densities of 68.24 mW cm^{-2} and 9.12 mW cm^{-2} for YSZ and 10Sc1CeSZ respectively after 5hrs of testing. The presence of ceria in the 10Sc1CeSZ anode did not seem to prove effective for promoting CH_4 oxidation as the current output for the tested 10Sc1CeSZ cells on biogas were all consistently lower than what was observed for the YSZ cells. Consistently lower current outputs for the 10Sc1CeSZ cells on H_2 are also seen, with 10Sc1CeSZ Cell Batch 11 exhibiting a drop in peak power density by approximately 70% from 179.97 mW cm^{-2} after 5hrs to 53.83 mW cm^{-2} after 22hrs. In the case of the 10Sc1CeSZ cells, fuel supplied at the anode likely diffuses through the anode, permeates through the highly porous 10Sc1CeSZ electrolyte and reacts with oxygen at the cathode side which results in zero current production and decreases in OCV. The diminishing fuel supply at the anode limits the conversion of available CH_4 and H_2 and the decreased oxygen levels at the cathode reduces the energy needed to drive the electrochemical reactions forward. These challenges significantly interfere with the present investigation aimed at researching the benefits – (1) increased O^{2-} transport from the electrolyte to the anode (2) promotion of CH_4 and H_2 oxidation via enhanced oxygen storage capabilities - of employing ceria in the scandia cell anode.

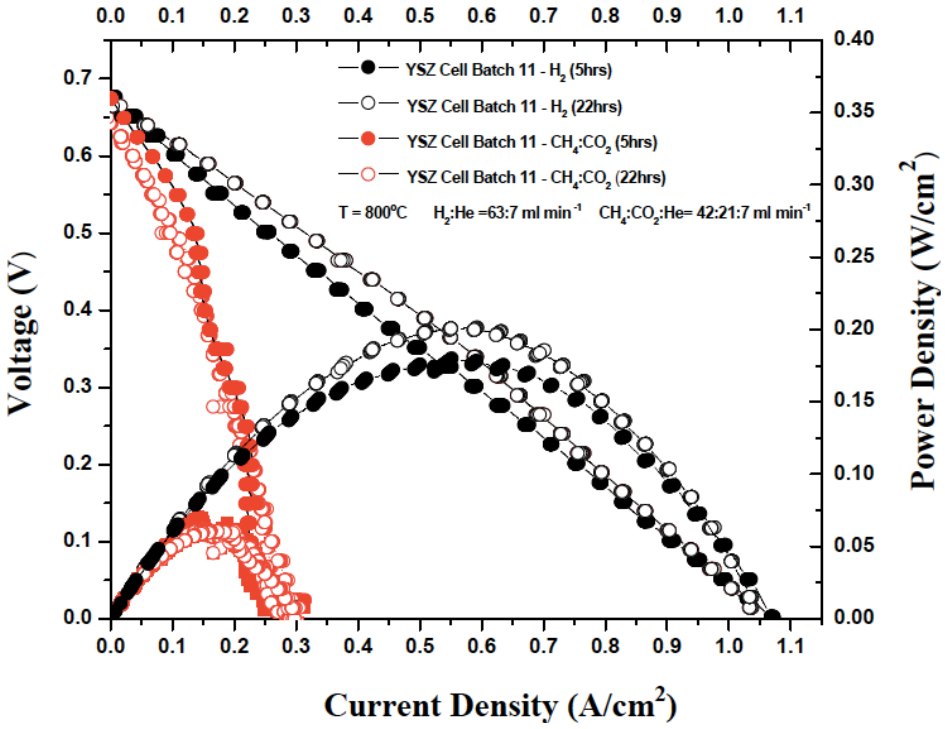

Figure 7-16: Cell performance curves for YSZ Cell Batch 11 operating on H_2 and CH_4:CO_2 at 800°C

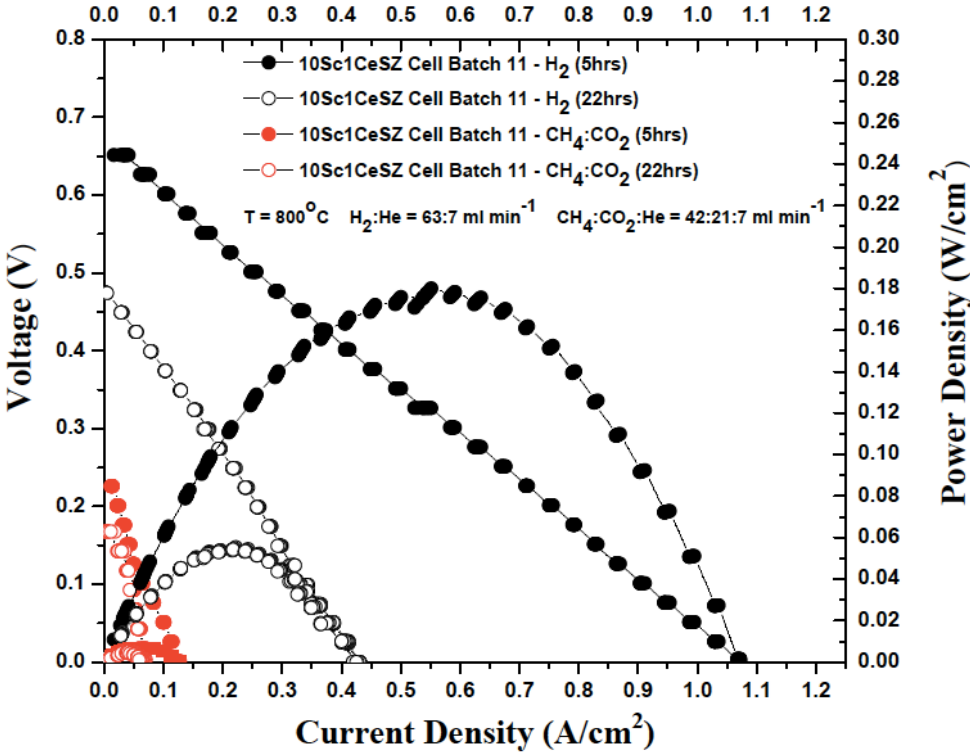

Figure 7-17: Cell performance curves for 10Sc1CeSZ Cell Batch 11 operating on H_2 and CH_4:CO_2 at 800°C

As previously discussed in Chapter 2, Section 2.3, carbon formation occurs when using Ni-based anodes during hydrocarbon operation which compromises anode activity resulting in cell failure. Sumi et al. reported the formation of rod-shaped carbon on Ni-ScSZ anodes and amorphous carbon on Ni-YSZ anodes after operation on CH_4:CO_2 = 0.5 at 1000^{o}C [24]. The amorphous carbon on the Ni-YSZ anode was reported to cause a decrease in nickel catalytic activity and inhibit gas diffusion to the reaction sites. Gunji et al. found increased temperature operation of Ni-ScSZ cells at 900^{o}C on CH_4-3%H_2O reduced carbon deposition though larger amounts of carbon were observed under OCV conditions [25]. This is because the mole fractions of CH_4-CO_2 increase under OCV as there is no current flowing through the cell leaving the supply fuel unoxidised [26]. During cell operation however, it is possible to suppress carbon deposition if high current densities (> 0.5 A cm^{-2}) are obtained as the water byproduct of the electrochemical reaction reacts with CH_4 and adsorbed CO to eliminate carbon buildup in the anode [25], [27]–[29]. For the YSZ and 10Sc1CeSZ tested cells, the decrease in power density on biogas operation relative to hydrogen operation has more to do with the much slower electrochemical oxidation of methane versus hydrogen than significant carbon deposition blocking and deactivating the anode causing performance losses. This reasoning is supported by the outlet gas profiles obtained by mass spectroscopy for the YSZ and 10Sc1CeSZ Cell Batch 11 samples during testing. Figures 7-18 and 7-19 show the mass spectra from YSZ Cell Batch 11 operating on H_2 and CH_4:CO_2 respectively. For Figure 7-18, the relative concentration represented by an arbitrary scale along the y-axis, ranges between 0.0-2.0 so that the full spectra profile is made visible. Helium was detected as denoted by the pink signal, which was expected, as helium was the carrier gas for the operation of the mass spectrometer. The blue signal represents H_2 with some oscillation and broadening levels of concentration observed. The spectra were obtained during electrochemical performance testing though a change in the H_2 concentration levels from OCV mode to current drawing mode is not clearly visible. There is an expectation of a decrease in the H_2 concentration level while obtaining $i - V$ measurements due to the electrochemical oxidation of H_2 when the cell is under load. The lack of visible change in H_2 concentration levels may be due to minimal H_2 consumption, which could explain the modest peak power density values for the YSZ Cell Batch 11. Another explanation is leakage at the cell seals and a non-fully dense YSZ electrolyte, evidenced by the OCV of 0.682V, which disrupts the measurement and generates poor quality spectra. The amber coloured peak identified as CO is more likely the presence of N_2 (the molecular mass of 28 is shared by both N_2 and CO) from air diffusing into the cell via cracks and poor seals. Only H_2 and He were supplied to this cell so there should be an absence of CO. Figure 7-19 displays smoother curves for each component in the spectra with H_2, He, CO, CO_2 and CH_4 gases detected. Steady levels of each gas are

observed throughout the cell test until just after 20hrs of operation when the relative gas concentrations drop as the fuel flow rate was reduced to 21 ml min^{-1} CH_4:CO_2 and 7 ml min^{-1} He before the test was terminated. Low levels of H_2 as represented by the blue signal are observed which indicates H_2 production via biogas oxidation was low. The highest relative concentration is observed for CH_4 at a level three times that of CO_2 as these fuels were directly fed to the fuel cell in a 3:1 CH_4:CO_2 mixture.

Figures 7-20 and 7-21 display the mass spectra profile for 10Sc1CeSZ Cell Batch 11 operating on H_2 and CH_4:CO_2 respectively. These profiles are very similar to those of YSZ Cell Batch 11 with no obvious changes in fuel concentration levels during cell operation and a much greater oscillation observed for the 10Sc1CeSZ cell fuelled by H_2 as represented by the blue signal in Figure 7-20. Again this is attributed to fuel leakage likely causing such a disruption. The detection of CO (indicated by the amber coloured peak) that is likely N_2 from air, further confirms this assumption. The expected fuel component gases of H_2, He, CO, CO_2 and CH_4 are all observed for the 10Sc1CeSZ cell operating on biogas as seen in Figure 7-21 with H_2 concentration at the lowest levels, which indicate slow methane conversion and minimal hydrogen production occurred. While the spectra obtained for both YSZ and 10Sc1CeSZ Cell Batch 11 cells are not ideal, they tend to support the findings related to slow methane conversion, low H_2 production and poor electrochemical oxidation which resulted in low SOFC performance on biogas for both systems. The low OCV values related to non-fully dense electrolytes, poor seals and cell cracks are also supported by the spectra.

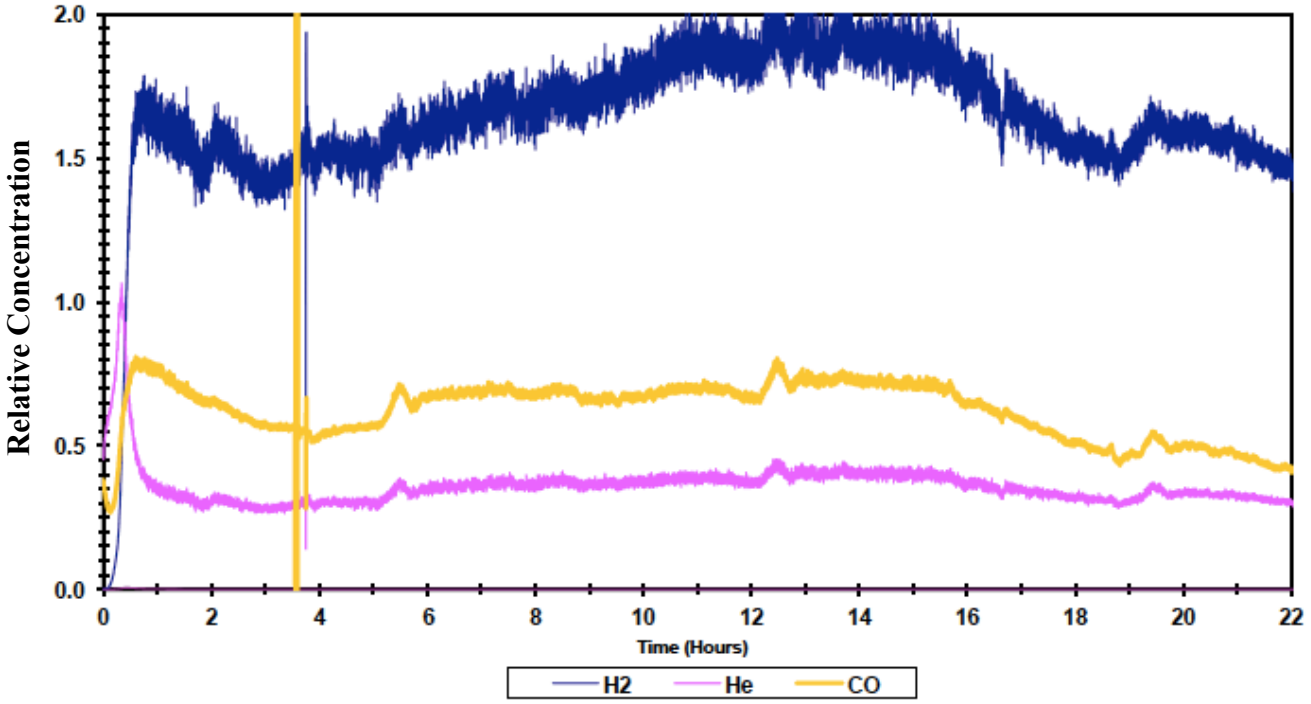

Figure 7-18: Mass spectra profile and exit gas composition for YSZ Cell Batch 11 operating on H_2 at 800°C

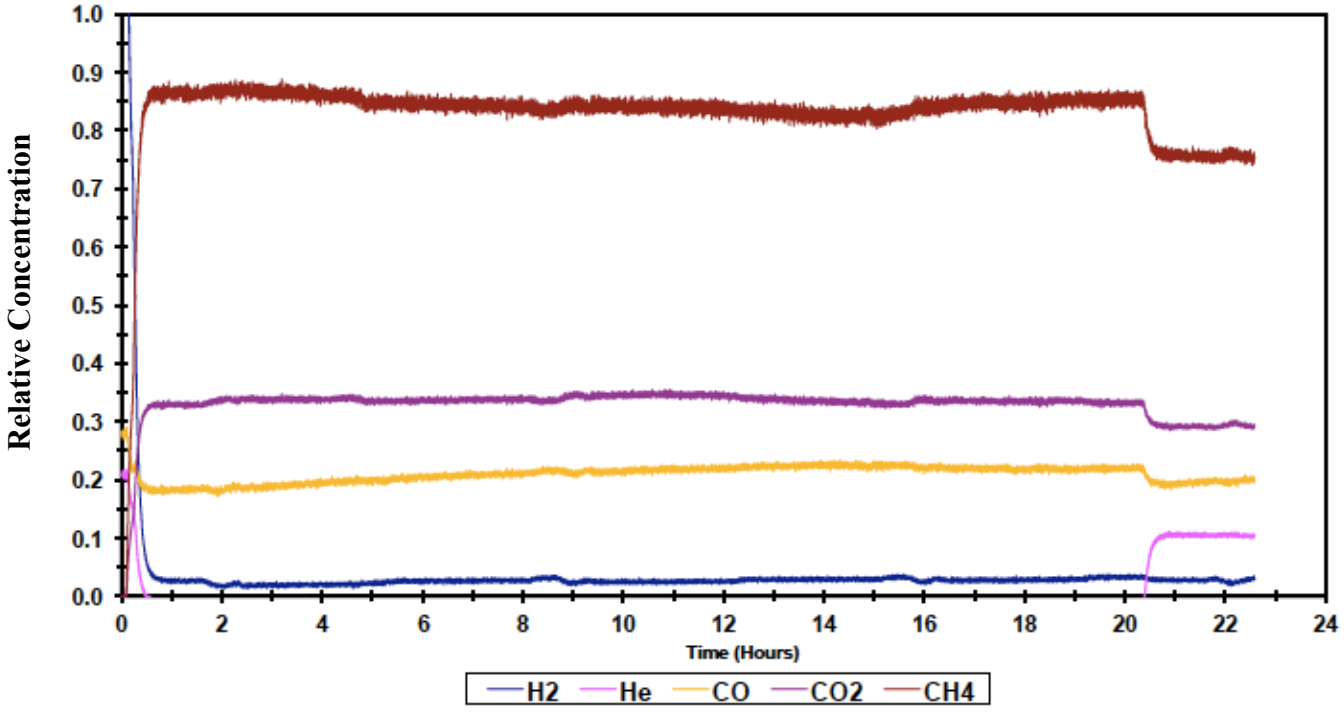

Figure 7-19: Mass spectra profile and exit gas composition for YSZ Cell Batch 11 operating on a 3:1 CH_4:CO_2 fuel mixture at 800°C

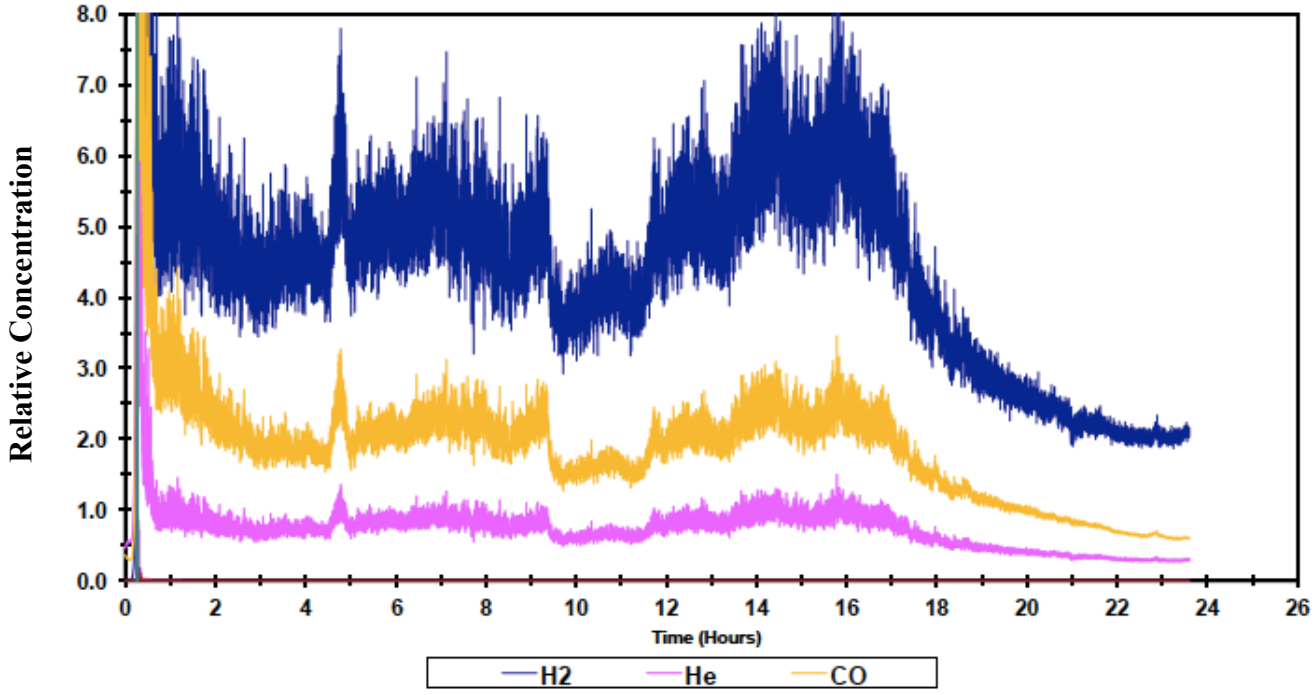

Figure 7-20: Mass spectra profile and exit gas composition for 10Sc1CeSZ Cell Batch 11 operating on H_2 at 800°C

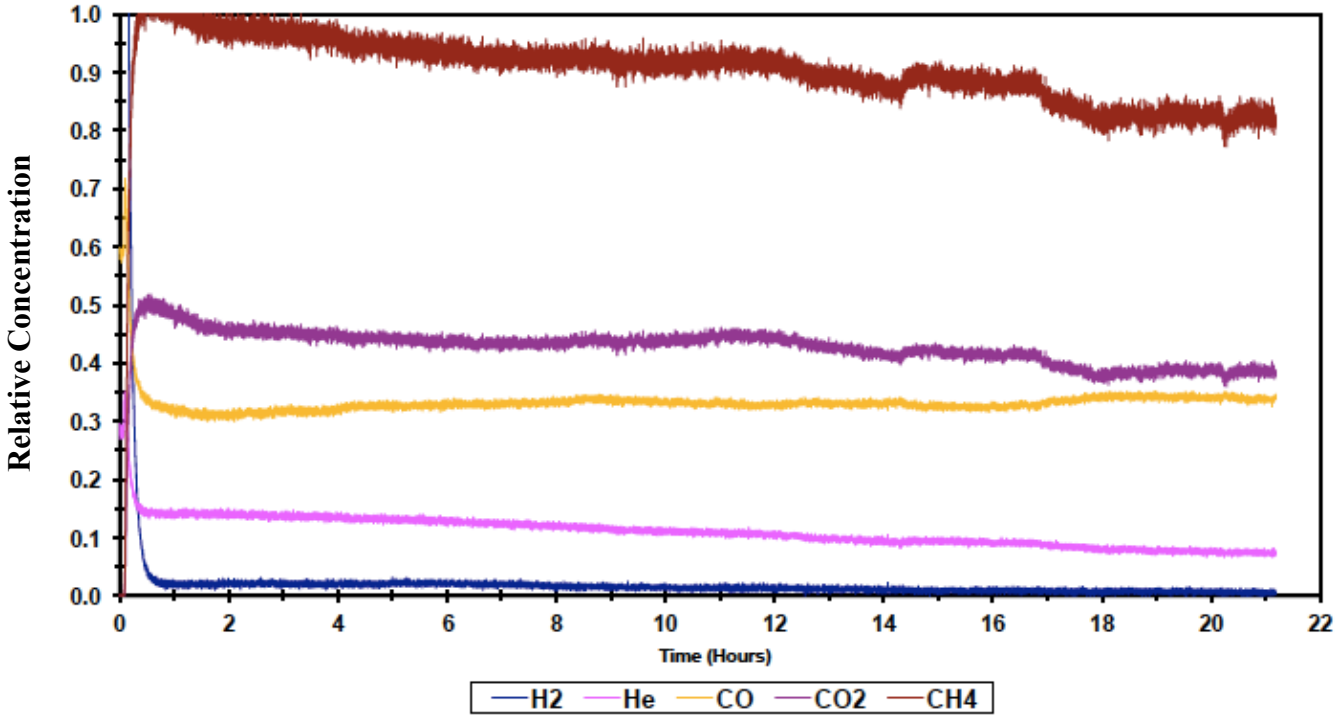

Figure 7-21: Mass spectra profile and exit gas composition for 10Sc1CeSZ Cell Batch 11 operating on a 3:1 CH_4:CO_2 fuel mixture at 800°C

7.5 SUMMARY

The successful testing of anode supported single cell YSZ and 10Sc1CeSZ SOFCs manufactured via screen-printing and co-firing operating in lower temperature regimes was demonstrated. Minimal performance differences were observed between reference commercial grade Ni-YSZ cells and baseline lab grade Ni-YSZ cells, which demonstrated the validity of the experimental technique and the reliability of the test equipment. The highest performing SOFCs had peak power densities of 466 mW cm^{-2} and 90 mW cm^{-2} for the commercial YSZ and 10Sc1CeSZ cells respectively with peak power densities of 392 mW cm^{-2} and 171 mW cm^{-2} for the lab grade YSZ and 10Sc1CeSZ cells, respectively, for operation on H_2 at 800^{o}C for all tested cells. The low current output for the commercial 10Sc1CeSZ cells was attributed to the bulk ESC design which also yielded the highest OCVs of all tested cells with values between 1.14V – 1.16V. The low OCVs of the lab grade 10Sc1CeSZ cells was due to the porous 10Sc1CeSZ electrolyte film for which a dense layer was unattainable when the nanoscale as-received powders were used during screen-printing. Despite these significantly low OCVs, the lab grade 10Sc1CeSZ cell exhibited the lowest ASR of 0.496 Ω cm^2 for all of the tested cells. 0.5 mol% Al_2O_3 additions to the 10Sc1CeSZ powders assisted in enhanced sintering and promoted densification as OCV values upwards of 1.045V were observed for the Al_2O_3-doped 10Sc1CeSZ cells. The Al_2O_3-10Sc1CeSZ cells however, exhibited poor performance with low current densities within the 10 – 40 mW cm^{-2} range seen for all tested cells. The possible segregation of Al_2O_3 at the grain boundaries may have compromised electrolyte conductivity by forming a blocking layer for oxygen ion conduction at the grain boundaries. Phase stability studies did not detect the presence of an impurity phase as XRD scans show only a single-phase cubic zirconia structure for the 0.55 mol% Al_2O_3 - 10Sc1CeSZ samples. As a result, there exist other factors that may have contributed to the low cell performance. For the lab grade YSZ and 10Sc1CeSZ cells operating on simulated biogas, very low peak power densities of 68.24 mW cm^{-2} and 9.12 mW cm^{-2} were obtained for the YSZ and 10Sc1CeSZ cells respectively. Slow biogas conversion and the poor electrochemical oxidation of H_2 were likely responsible for the overall drop in performance.

REFERENCES

[1] V. Vijaya Lakshmi, R. Bauri, A. S. Gandhi and S. Paul, Synthesis and characterization of nanocrystalline ScSZ electrolyte for SOFCs. *Int. J. Hydrogen Energy*, 2011. 36 (22): p. 14936-14942.

[2] O. Yamamoto, Electrical conductivity of stabilized zirconia with ytterbia and scandia. *Solid State Ionics*, 1995. 79 (1): p. 137-142.

[3] Y. Arachi, H. Sakai, O. Yamamoto, Y. Takeda and N. Imanishai, Electrical conductivity of the $ZrO_2 – Ln_2O_3$ (Ln =5 lanthanides) system. *Solid State Ionics*, 1999. 121 (1): p. 133-139.

[4] F. C. Fonseca and R. Muccillo, Impedance spectroscopy analysis of percolation in (yttria-stabilized zirconia)-yttria ceramic composites. *Solid State Ionics*, 2004. 166 (1–2): p. 157-165.

[5] C. N. Shyam Kumar and R. Bauri, Enhancing the phase stability and ionic conductivity of scandia stabilized zirconia by rare earth co-doping. *J. Phys. Chem. Solids*, 2014. 75 (5): p. 642-650.

[6] M. F. Han, Z. B. Yang, Z. Liu,and H. R. Le, Fabrication and Characterizations of YSZ Electrolyte Films for SOFC. *High-Performance Ceram.,* 2010. 434–435 (1): p. 705-709.

[7] X. Guo and Z. Zhang, Grain size dependent grain boundary defect structure: Case of doped zirconia. *Acta Mater.*, 2013. 51 (9): p. 2539-2547.

[8] J. Wang and H. Conrad, Contribution of the space charge to the grain boundary energy in yttria-stabilized zirconia. *J. Mater. Sci.*, 2014. 49 (17): p. 6074-6080.

[9] P. Mondal, Enhanced specific grain boundary conductivity in nanocrystalline Y_2O_3-stabilized zirconia. *Solid State Ionics*, 1999. 118 (3–4): p 331-339.

[10] X. Guo and Y. Ding, Grain Boundary Space Charge Effect in Zirconia. *J. Electrochem. Soc.*, 2004. 151 (1): p. J1-J7.

[11] A. A. Sharif, P. H. Imamura, T. E. Mitchell and M. L. Mecartney, Control of grain growth using intergranular silicate phases in cubic yttria stabilized zirconia. *Acta Mater.*, 1998. 46 (11): p. 3863-3872.

[12] S. Tekeli, M. Erdogan and B. Aktas, Influence of alpha-Al_2O_3 addition on sintering and grain growth behaviour of 8 mol% Y_2O_3-stabilised cubic zirconia (c-ZrO_2). *Ceram. Int.*, 2004. 30 (8): p. 2203-2209.

[13] J. W. Fergus, Electrolytes for solid oxide fuel cells. *J. Power Sources*, 2006. 162 (1): p. 30-40.

[14] T. Kawashima and M. Hishinuma, Analysis of Electrical Conduction Paths in Ni/YSZ Particulate Composites Using Percolation Theory. *Mater. Trans. JIM.,* 1996. 37 (7): p. 1397-1403.

[15] Z. Shao, W. Zhou and Z. Zhu, Advanced synthesis of materials for intermediate-temperature solid oxide fuel cells. *Prog. Mater. Sci.*, 2012. 57 (4): p. 804-874.

[16] J. Larminie and A. Dicks, *Fuel Cell Systems Explained*, second ed., John Wiley and Sons, 2003.

[17] S. M. M. Primdahl, Gas Diffusion Impedance in Characterization of Solid Oxide Fuel Cell Anodes. *J. Electrochem. Soc.*, 1999. 146 (8): p. 2827-2833.

[18] S. Tekeli, The solid solubility limit of Al_2O_3 and its effect on densification and microstructural evolution in cubic-zirconia used as an electrolyte for solid oxide fuel cell. *Mater. Des.*, 2007. 28 (2): p. 713-716.

[19] T. V. Dijk and A. J. Burggraaf, Grain Boundary Effects on Ionic Conductivity in Ceramic Gd_xZr_{1-x} $O_{2-(x-2)}$ Solid Solutions. *Phys. Stat. Sol.*, 1981. 63 (229): p. 229-240.

[20] M. Mori, M. Yoshikawa, H. Itoh and T. Abe, Effect of alumina on sintering behavior and electrical-conductivity of high-purity yttria-stabilized zirconia. *J. Am. Ceram. Soc.*, 1994. 77 (8): p. 2217-2219.

[21] C. Haering, A. Roosen and H. Schichl, Degradation of the electrical conductivity in stabilised zirconia systems Part II: Yttria-stabilised zirconia. *Solid State Ionics*, 2005. 176 (3): p. 253-259.

[22] L. Troskialina, *Improved Performance of Solid Oxide Fuel Cell Operating on Biogas Using Tin Anode-Infiltration*, PhD Thesis, University of Birmingham, 2016.

[23] Y. Shiratori, T. Oshima, and K. Sasaki, Feasibility of direct-biogas SOFC. *Int. J. Hydrogen Energy*, 2008. 33 (21): p. 6316-6321.

[24] H. Sumi, Y.-H. Lee, H. Muroyama, T. Matsui, and K. Eguchi, Comparison between internal steam and CO_2 reforming of methane for Ni-YSZ and Ni-ScSZ SOFC anodes. *J. Electrochem. Soc.*, 2010. 157 (8): p. B1118-B1125.

[25] A. Gunji, C. Wen, J. Otomo, T. Kobayashi, K. Ukai, Y. Mizutani, and H. Takahashi, Carbon deposition behaviour on Ni–ScSZ anodes for internal reforming solid oxide fuel cells. *J. Power Sources*, 2004. 131 (1–2): p. 285-288.

[26] J. D. Kirtley, D. a Steinhurst, J. C. Owrutsky, M. B. Pomfret, and R. a Walker, In situ optical studies of methane and simulated biogas oxidation on high temperature solid oxide fuel cell anodes. *Phys. Chem. Chem. Phys.*, 2014. 16 (1): p. 227-236.

[27] J. Liu and S. A. Barnett, Operation of anode-supported solid oxide fuel cells on methane and natural gas. *Solid State Ionics*, 2003. 158 (1–2): p. 11-16.

[28] J. B. Goodenough and Y.-H. Huang, Alternative anode materials for solid oxide fuel cells. *J. Power Sources*, 2007. 173 (1): p. 1-10.

[29] K. Ke, A. Gunji, H. Mori, S. Tsuchida, H. Takahashi, K. Ukai, Y. Mizutani, H. Sumi, M. Yokoyama, and K. Waki, Effect of oxide on carbon deposition behavior of CH_4 fuel on Ni-ScSZ cermet anode in high temperature SOFCs. *Solid State Ionics*, 2006. 177 (5–6): p. 541-547.

CHAPTER 8
SUMMARY

This chapter summarises the findings of this work and proposes future work recommendations.

8.1 CONCLUSIONS

In this work, the successful manufacture and testing of anode supported single cell SOFCs operating in lower temperature regimes was demonstrated. Half-cell design and development of an intermediate temperature SOFC (IT-SOFC) based on a Ce-doped Scandia-stabilised Zirconia (ScSZ) structure manufactured via die pressing and screen-printing was achieved. This work involved fundamental investigations and characterisation to garner a better insight into YSZ and 10Sc1CeSZ material properties and how these properties can be manipulated via manufacturing and processing and the overall influence of these parameters on microstructure, stability and performance. The consideration

of an alternate, lower temperature SOFC besides the conventional high temperature Ni-YSZ/YSZ/LSM-YSZ system was realised and the reliability of screen-printing as a deposition technique for the 10Sc1CeSZ electrolyte layer, which has yet to be reported, was also explored. A better understanding of the behaviour of the 10Sc1CeSZ system and the interplay of different factors to achieve the desired outcome is this study's contribution.

Characterisation and chemical analysis of commercial powders was carried out and provided the basis for determining how these starting materials would be used in different stages of the YSZ and 10Sc1CeSZ cell fabrication process. The findings for the 10Sc1CeSZ system were used as an indicator of cell performance and to ascertain its use as an IT-SOFC electrolyte material. The connection between starting material properties and microstructures of the final compact were made.

Preliminary screening of cells under different processing conditions was carried out to standardise the manufacturing method that yielded the desired cell properties best suited for testing. Screening studies gave more information about the variables influencing sintering behaviour, mechanical strength and porosity and correlated these findings to standardise processing conditions that yielded satisfactory performing cells with good physical properties. The results allowed a specific formulation, fabrication procedure and sintering schedule to be defined. There were different processing procedures implemented for the 10Sc1CeSZ system, as the method standardised for the conventional YSZ system was not directly transferrable to 10Sc1CeSZ. This finding further highlights how material properties strongly influence component layer characteristics and how cell features and microstructural properties govern performance.

The effect of sintering time and temperature on porosity and shrinkage were investigated for Ni-ZrO_2 supports. Analysis of system phase stability, material CTEs, half-cell sintering characteristics, substrate surface roughness, ink loading vs. printability, bulk electrolyte conductivity and the effect of Al_2O_3 doping and sintering temperature on densification were all studied. Powder particle size and distribution greatly influence sintering behaviour, which had the highest effect on microstructure and overall cell performance.

Based on the findings of this work, the following conclusions can be made:

- ✓ Ni-YSZ and Ni-10Sc1CeSZ cells were both successfully die pressed, screen-printed, co-sintered and tested over multiple trials lending consistency and reproducibility to the fabrication method. Using screen-printing to deposit the 10Sc1CeSZ electrolyte layers onto Ni-10Sc1CeSZ anode

support pellets was successful and shown to be the first time this was attempted based on literature reports.

- ✓ Minimal performance differences were observed between reference commercial grade Ni-YSZ cells and baseline lab grade Ni-YSZ cells when tested on H_2 which show proof of concept and demonstrate validity of the experimental technique and reliability of the test equipment.

- ✓ Initial data for the 10Sc1CeSZ cells showed the ceramic processing method needed to be better tailored to suit the performance requirements of the 10Sc1CeSZ system. The lab grade 10Sc1CeSZ system outperformed the lab grade YSZ system when operating on H_2 fuel, which is an element of success for this work and demonstrates the viability of a 10Sc1CeSZ structured SOFC. On-going work is required to bridge the Ni-10Sc1CeSZ system to the Ni-YSZ system and enhance the performance of both systems when operating on hydrocarbon fuels.

- ✓ Al_2O_3 additions to 10Sc1CeSZ assisted in enhanced sintering and promoted densification. Above the solubility limit (0.5 mol%) it is reported that Al_2O_3 can segregate at the grain boundaries and decrease grain boundary conductivity, resulting in an overall lower cell performance. XRD scans for the Al_2O_3-10Sc1CeSZ samples show only a single-phase cubic-zirconia structure for all of the Al_2O_3 dopant levels studied. The chosen Al_2O_3 compositions form solid solutions with 10Sc1CeSZ.

8.2 OUTLOOK

Regarding future work recommendations, bulk Al_2O_3-10Sc1CeSZ specimens should be prepared and conductivity and microstructural analysis carried out to ascertain the effect of Al_2O_3 on the microstructural evolution of 10Sc1CeSZ and the degree to which grain growth, grain boundary and bulk conductivity and Al_2O_3 segregation at the grain boundary is affected. Al_2O_3 distribution, possible diffusion into the electrodes and overall stability should also be investigated. This work will help determine the Al_2O_3 dopant levels required to densify the 10Sc1CeSZ without compromising electrical conductivity and can then be used to optimise the manufacturing method. Once optimised, the manufacturing for both the YSZ and Al_2O_3 doped 10Sc1CeSZ systems can then be used to fabricate anode supported tapes, which can be explored as part of a joint collaboration with Ukranian partners. The Ukranian collaborators will supply the powders and prepare the anode support tapes while The University of Birmingham focuses on 10Sc1CeSZ electrolyte and cathode layer deposition via screen-printing and investigates anode alloy doping for operation on biogas. The initial aim of this work was to

design an intermediate temperature SOFC based on a Ce-doped ScSZ structure and demonstrate stable SOFC operation on hydrogen and methane without significant performance losses. Despite the technical difficulties related to powder handling which contributed to the challenges of obtaining a dense 10Sc1CeSZ electrolyte layer, the overall project aim was achieved. The satisfactory performance results of the 10Sc1CeSZ system operating on H_2 as evidenced by the lower ASR values are somewhat promising and rendered this scientific investigation a success as operation of an IT-SOFC based on a Ce-doped ScSZ was illustrated. The poor performance of 10Sc1CeSZ on biogas, however, revealed the limitations of the reforming capabilities of the scandia system, which was strongly related to the manufacturing approach and warrants further cell development so improved hydrocarbon operation in intermediate temperature regimes can be explored.

LIST OF PUBLICATIONS

McDonald, N., Brodnikovskyi, Y., Brychevskyi, M., Brodnikovskyi, D., Brodnikovska, I. Polishko, I., .Kovalenko, L., Vasylyev, O., Steinberger-Wilckens, R., Belous' A.: Properties of 3.5YSZ/10Sc1CeSZ Ceramic Component for SOFC Anode Application – under review

McDonald, N., Steinberger-Wilckens, R: The Application of 10Sc1CeSZ Electrolytes in Intermediate Temperature SOFCs – A Review: manuscript in progress

McDonald, N., Brodnikovskyi, Y, Steinberger-Wilckens, R: The Use of Al_2O_3 as a Sintering Aid for the Densification of Screen-Printed 10Sc1CeSZ Films : manuscript in progress

McDonald, N. Watton, J., Dhir, A., Steinberger-Wilkens, R. The Manufacture and Testing of Ni-10Sc1Ce Anode Supported SOFCs for Intermediate Temperature Operation: 11th European SOFC and SOE Forum Conference Proceedings

Brodnikovsky,I., Vasyliv, B., Podhurska, V., Andrzejczuk, M., **McDonald, N**., Kyrpa, O., Ostash, O., O. Vasylyev, O., Steinberger-Wilckens, R., Kurzydlowski,K.: Influence of Reduction Conditions of NiO On Its Mechanical and Electrical Properties, J. Electrochem. Sci. Eng., X(Y) (2016) 0-0, doi: 10.5599/jese220

Sadykova, V.A., Eremeeva, N.F., Sadovskayaa, E.M., Bobina, A.S., Yu. Fedorovaa, E., Muzykantova, V.S., Mezentsevaa, N.V., Alikinaa, G.M., Krigera, T.A., Belyaeva, V.D., Rogova, V.A., Ulikhinc, A.S., Okhlupinc, Yu. S., Uvarovc, N.F., Bobrenokd, O.F, **McDonald, N**., Watton, J., Dhir, A., SteinbergerWilckens,R. Mertens, J., Vinke, I.C: Cathodic Materials for Intermediate-Temperature Solid Oxide Fuel Cells Based on Praseodymium Nickelates-Cobaltites, Russian Journal of Electrochemistry, 2014, Vol. 50, No.7, 669-679.

Chandan, A., Pour, M. A., **McDonald, N**., Maillard, J. G., Steinberger-Wilckens, Numerical Analysis of an SOFC Single Cell: A Multiphysics Approach, *5th European Fuel Cell Forum Conference Proceedings*.